# PRECISION CALCULATIONS IN THEORETICAL PARTICLE PHYSICS AND THE SEARCH FOR NEW PHYSICS

A dissertation submitted to the
College of Graduate and Postdoctoral Studies
in partial fulfillment of the requirements
for the degree of Doctor of Philosophy
in the Department of Physics and Engineering Physics
University of Saskatchewan
Saskatoon

By
Siyuan Li

# Permission to Use

# Disclaimer

Reference in this dissertation to any specific commercial products, process, or service by trade name, trademark, manufacturer, or otherwise, does not constitute or imply its endorsement, recommendation, or favoring by the University of Saskatchewan. The views and opinions of the author expressed herein do not state or reflect those of the University of Saskatchewan, and shall not be used for advertising or product endorsement purposes.

Requests for permission to copy or to make other uses of materials in this dissertation in whole or part should be addressed to:

Department of Physics & Engineering Physics
University of Saskatchewan
116 Science Place, Rm 163
Saskatoon, SK S7N 5E2
Canada

OR

Dean
College of Graduate and Postdoctoral Studies
University of Saskatchewan
116 Thorvaldson Building, 110 Science Place
Saskatoon, Saskatchewan S7N 5C9 Canada

# Abstract

In order to advance the understanding of fundamental particles and their interactions, precision is crucial in theoretical particle physics predictions. In quantum field theory and quantum chromodynamics (QCD), improving corrections beyond the leading order in both perturbative and non-perturbative contributions to observable quantities are key to improving theoretical results. We analyze higher-order contributions through various methodologies, such as QCD sum rules, on observables including the $2^{++}$ tensor di-gluonium two-point correlator and the hadronic vacuum polarization contributions to the muon anomalous magnetic moment. We also develop a numerical computational methodology using pySecDec, a Python-based package for the numerical calculation of dimensionally-regulated loop integrals, to evaluate loop integrals at finite temperature in the Matsubara formalism. This work refines calculational precision and scope, both phenomenologically and methodologically, to support the search for new physics phenomena.

# Acknowledgements

When the setting sun shone on my shoulders and the discussion about physics danced with accents and distant French murmurs, I felt closest to the beauty of science and the world. This moment took place in the summer of 2024, toward the end of my PhD journey, when my supervisor, Prof. Tom Steele, suggested I attend the QCD24 conference in Montpellier, France. It was a memorable experience and one of the highlights of my academic path — just one example of Tom's many thoughtful and wise suggestions that guided me through the years. Moments like these remind me that physics knows no borders, a realization only made possible through the support of many incredible people: my supervisor, Dr. Tom Steele, exemplifies kindness and brilliance, and I feel deeply fortunate to have learned from his example as both a scientist and a person; my mother, who taught me how strong, independent, and elegant a woman can be; my mentors and fellow colleagues — Dr. Derek Harnett, Dr. Jason Ho, Dr. Robin Kleiv, Dr. Alexander Palameta, Dr. Thamirys de Oliveira, Bárbara Cid Mora, Bardia Fahim, Canisius Bernard, Joshua Fenwick, Alex Magnus, Aaron Thiesen, Kurt Dixon, Masahiro Hori — you shared the challenges and joys of the theoretical physics graduate student journey with me; my partner, Ben, who has been the pillar of my life throughout my PhD and a guide to the beauty of the world. And many others that provided support to reach my academic goal — Dr. Kaori Tanaka, Dr. Rainer Dick, Dr. Masoud Ghezelbash, Dr. Zhi Wei Wang, Debbie Gjertsen, Marjorie Granrude.

Although my memory of southern France that summer may have been romanticized by all the wine, may the stone pledge against the Saint-Clément aqueduct remembers the young physicists that briefly stopped by for a post-dinner walk, as well as those who came before us and those who will follow.

To my mother and my grandmother.

# Contents

# List of Tables

# List of Figures

# List of Abbreviations

| | |
|---|---|
| BSM | Beyond Standard Model |
| FESR | Finite-Energy QCD sum rules |
| HVP | Hadronic Vacuum Polarization |
| LHS | Left Hand Side |
| LO | Leading Order |
| LQCD | Lattice Quantum Chromodynamics |
| LSR | Laplace Sum Rules |
| MDA | Minimal Duality Ansatz |
| MS scheme | Minimal Subtraction Scheme |
| $\overline{\text{MS}}$ scheme | Modified Minimal Subtraction Scheme |
| NLO | Next-to-leading Order |
| OPE | Operator Product Expansion |
| QCD | Quantum Chromodynamics |
| QCDSR | QCD (Spectral) Sum Rules |
| QED | Quantum Electrodynamics |
| QFT | Quantum Field Theory |
| RG | Renormalization Group |
| RHS | Right Hand Side |
| SM | Standard Model |
| VEV | Vacuum Expectation Value |

# 1 The Motivation for Precision

Physicists have long pondered the question, “What is matter made of?”—a curiosity that predates even the existence of physics as a formal discipline. Modern particle physics shows that matter is built from smaller building blocks with vast space between them, evolving from the ancient concept of the atom (from the Greek *atomos*, meaning “indivisible”) to the discovery of electrons, nuclei, and subatomic particles. Experiments like Thomson’s identification of the electron [1, 2], Rutherford’s $\alpha$-particle scattering [3] and Bjorken deep inelastic scattering [4, 5] revealed deeper layers of matter all the ways to nucleon substructure. Today, the Standard Model (SM) identifies 61 elementary particles, including quarks, leptons, and force carriers, as the fundamental constituents of matter and the universe [6]. Regardless of the success of the SM in providing a detailed account of particle interactions and classifications, it remains an incomplete description which only describes less than 6 percent of the universe (see Refs. [6–8] for reviews).

The search for new physical phenomena expands our understanding of the universe and often leads to groundbreaking insights especially with the advancements in particle collider experiments at facilities like CERN, Fermilab, and TRIUMF. This pursuit typically involves a critical comparison between experimental measurements and theoretical predictions. Enhancing the precision of theoretical predictions not only strengthens the reliability of these comparisons but also makes them more meaningful, paving the way for deeper exploration and discovery.

One of the “new physics” phenomena involves a class of composite particles formed from gluons, known as gluonia or glueballs. From the quark model, conventional bound states consist of mesons (quark-antiquark pairs) and baryons (three-quark or three-antiquark states) [9, 10]. However, the colour confinement property of Quantum Chromodynamics (QCD) predicts additional bound states classified as *exotic*. These include multi-quark states (e.g., tetraquarks), hybrid states (quarks bound with gluons), and the pure gluon composites called gluonia (see reviews in Refs. [11–13]). Despite significant theoretical interest, gluonia remain hypothetical due to experimental challenges in distinguishing them from ordinary mesons [11] and the perturbative and non-perturbative complexities of QCD calculations. One of our published works on a type of tensor di-gluonium improves mass prediction accuracy via extensive calculation and analysis of its correlation function [14].

Another prominent area of new physics exploration is the muon $g-2$ anomaly, investigated by the $g-2$ storage ring at Fermilab (see recent reports in Refs. [15, 16]). Precision measurements of the muon's anomalous magnetic dipole moment reveal discrepancies from SM predictions, suggesting possible Physics beyond the SM (BSM) interactions. However, theoretical calculations of the hadronic (strong interaction) contributions remain contentious, with differing results from various methodologies [17–20]. We attempt to explore this tension and presents our contributions toward resolving these discrepancies through refined theoretical approaches [21, 22].

The evaluation of particle interaction correlation functions has long been instrumental in describing observables like S-matrix elements. Improving loop integral methodologies is therefore critical for precision calculations. This thesis develops computational tools that not only enhance numerical calculations in field theory but also extend to scenarios in thermal environments and potentially, even BSM [23].

Whether by addressing missing elements in exotic particle predictions, refining theoretical models for experimental anomalies like the muon $g-2$, or developing efficient computational methodologies for field theory, this thesis is motivated to advancing precision calculations. These efforts aim to uncover new physics phenomena within and beyond the SM.

## 1.1 Thesis Outline

This manuscript-style thesis is organized into five chapters. Chapter 2 introduces the foundational theories of QCD and QCD Sum Rules (QCDSR), the primary methodology utilized in Chapters 3 and 4. Key properties such as asymptotic freedom (Sec.2.2.2) and techniques like dimensional regularization (Sec.2.3) are presented, as they are applied extensively throughout this work. The duality principle of QCDSR, which bridges theoretical QCD calculations with hadronic phenomenology, underpins this thesis (see Sec. 2.5).

In Chapter 3, we enhance the theoretical predictions of tensor di-gluonium properties using Laplace Sum Rules (LSR) to the next-to-leading order (NLO) corrections [14]. The perturbative and non-perturbative terms for each Feynman diagram are calculated and multiple renormalization schemes are applied to ensure robust results. These refinements improve the precision of their predicted masses and couplings, providing essential benchmarks for future experimental verification.

In Chapter 4, we employ higher-order corrections to Finite-Energy QCD Sum Rules (FESR) and use Hölder inequalities to establish bounds on hadronic contributions to the muon $g-2$ anomaly. To improve precision, we analyze higher-loop effects, incorporating up to five-loop perturbative corrections, along with mass corrections and condensate contributions [21, 22].

Chapter 5 presents a manuscript developing new techniques that employ the pySecDec package to numerically evaluate finite-temperature loop integrals within the Matsubara formalism, introduced earlier in the chapter. We enhance the computational capabilities of pySecDec by developing an inverse Wick rotation method, implementing dimensional regularization, and adapting the tool to handle a broad range of Feynman topologies [23].

Several appendices are included for better illustration of this thesis. Appendices A, B, C, E present, respectively, the metric conventions, SU(3) algebra properties, quantum numbers and QCD Feynman rules referenced throughout this thesis. Appendix D provides a sample code to supplement the Feynman diagram calculations discussed in Chapter 3.

Finally, Chapter 6 summarizes the three published works and highlights prospects for future research. These prospects aim to integrate novel and diverse methodologies to address complex problems in Quantum Field Theory (QFT) and QCD, thereby advancing our understanding of fundamental particles and interactions.

# 2 Introduction and Theory

## 2.1 History of the Standard Model

The rise of quantum mechanics in the early 1900s revolutionized our understanding of nature. Not only did it provide a framework to describe matter at atomic and subatomic scales, but it also introduced the discretization of physical quantities such as energy. Around the same time, Albert Einstein introduced the theory of special relativity [24], which describes the behaviour of objects moving at speeds close to the speed of light. These two groundbreaking theories were eventually interwoven into the framework of classical field theory, giving rise to QFT, which describes particles as excitations of their corresponding fields. QFT allows us to describe particles being born (creation) and dying (annihilation) in high-energy physics phenomena. It also sets the foundation for the SM of particle physics. As time progresses to the latter half of the 20th century, the collective efforts of scientists worldwide culminated in the formulation of the SM, which provides a comprehensive description of the fundamental particles in Fig. 2.1 and the forces that govern their interactions listed in Table 2.1. The success of the SM has been repeatedly confirmed through experimental verification, including the landmark discovery of the Higgs boson in 2012 at the Large Hadron Collider (LHC) [25, 26].

| | **Gravity** | **Weak** | **Electromagnetic** | **Strong** |
|---|---|---|---|---|
| **Carried by** | graviton | $W^{\pm}, Z$ | $\gamma$ (photon) | $g$ (gluon) |
| **Acts on** | all particles | quarks, leptons | quark, charged leptons, $W^{\pm}, Z$ | quarks, gluon |

**Table 2.1:** The four fundamental interactions with their corresponding for carrier bosons and involved particles. Graviton is a hypothesis whose experimental search is still ongoing.

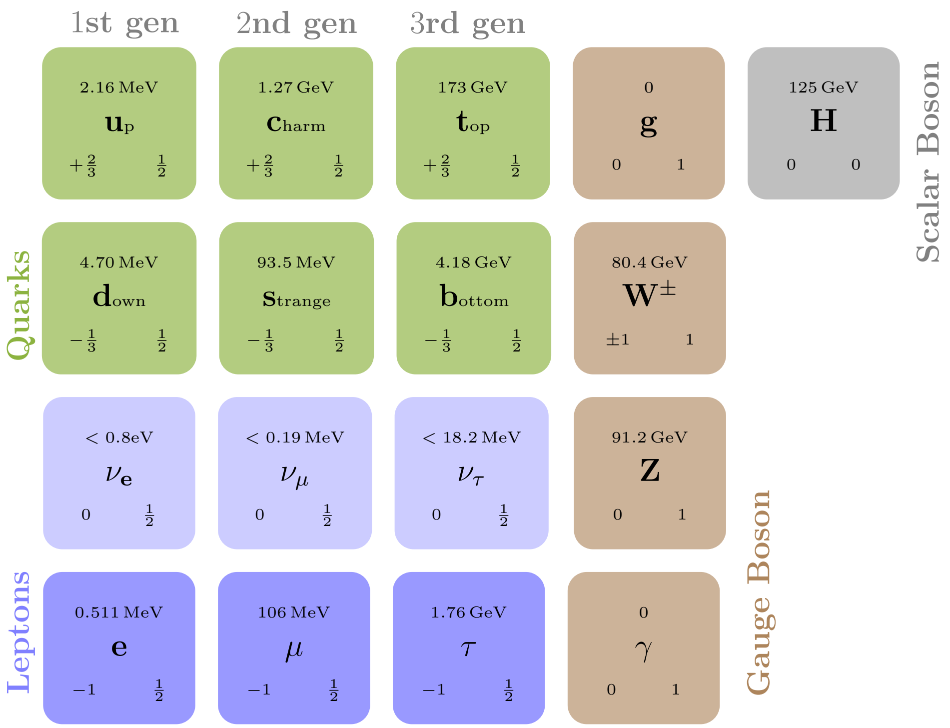

**Figure 2.1:** The Standard Model of particle physics with intrinsic properties included. The particle masses or mass bounds [7] are labelled at the top of each block with unit convention $c = \hbar = 1$ (see Appendix A). Light quark $(u, d, s)$ masses are in the $\overline{\text{MS}}$-scheme at 2 GeV scale while $c-$ and $b-$quarks masses are at their corresponding $\overline{\text{MS}}$-scheme mass scale (*e.g.*, $m_b(m_b) = m_b$). The $t-$quark mass is from $t\bar{t}$ events kinematics. The values in the bottom left corner stands for electric charges relative to elementary charge $e$. The values in the bottom right are particle spins. The first three columns corresponds to the first, second and third generation of quarks and leptons. In QCD, the involved particles are the quarks (in green) and the gluon force carrier $g$.

From the perspective of SM, all matter is built by two categories of fundamental particles:

1. Half-integer spin particles, known as fermions, obey the Pauli Exclusion Principle and follow Fermi-Dirac statistics [27] (see also *e.g.*, Ref. [28]). In the SM, spin-1/2 fermions include leptons and quarks, which serve as the fundamental building blocks of matter. There are six types (or flavors) of quarks, distinguished by their masses and the fractional electric charges they carry, as shown in Fig. 2.1: up $(u)$, down $(d)$, charm $(c)$, strange $(s)$, top $(t)$, and bottom $(b)$. Leptons, on the other hand, consist of three generations, each comprising an electrically charged particle — electron $(e)$, muon $(\mu)$, tau $(\tau)$ — along with their respective neutrinos, which are electrically neutral.

2. Integer-spin particles, known as bosons, obey Bose-Einstein statistics. The gauge

bosons shown in Fig. 2.1, represent a specific class of bosons associated with the gauge symmetries of fundamental interaction theories (*e.g.,* the photon $\gamma$ for quantum electrodynamics). These *gauge bosons* ($g, W^{\pm}, Z, \gamma$) are the force carriers, mediating the fundamental forces described by their respective gauge theories.

The Higgs Boson, the newest experimentally-confirmed member of SM, is a spin-0 (scalar) particle that plays a central role in the Higgs mechanism [29] (see also *e.g.,* Ref. [30]).

As listed in Table 2.1, all of the SM particles participate in one or more fundamental interactions among the four — strong interaction, weak interaction, electromagnetism, and gravity. The SM incorporates a collection of theories to describe these interactions (excluding gravity): quantum electrodynamics (QED) for electromagnetic interaction [6, 31]; Weinberg–Salam theory for the electroweak interaction which unifies effects from electromagnetism and weak interaction [32, 33]; and QCD, which describes the strong force responsible for binding quarks together to form hadrons (*e.g.,* protons and neutrons) [9, 10]. This thesis will be focusing on the QCD sector of the SM theory.

### 2.1.1 The Quark Model

At the early stages of particle physics, hadrons (strongly-interacting particles) such as protons ($p$) are believed to be elementary particles that could not be further divided into smaller components. However, the Bjorken deep inelastic scattering experiments, which investigated the proton's internal structure via $e^{-}p$ scattering, provided evidence for substructures within the proton, termed partons, later identified as quarks and gluons [4, 5]. These experiments demonstrated that partons possess spin-1/2 and behave as free particles at high energies, a phenomenon consistent with asymptotic freedom (discussed in detail in Sec.2.2.2). This behaviour contradicted the then-prevailing point-like proton model and necessitated a new theoretical framework. These findings laid the foundation for QCD, a non-Abelian gauge theory that describes the strong interaction between quarks and gluons, revolutionizing our understanding of hadronic structure and dynamics.

In 1964, the quark model introduced a classification scheme for hadron based on their quark content and was independently proposed by Murray Gell-Mann [9] and George Zweig [10].

In this framework, hadrons are understood as composite particles made up of quarks ($q$) and antiquarks ($\bar{q}$), specifically the $u$, $d$, and $s$ quarks (and their antiquarks). In other words, hadrons are bound states of quarks via the strong interaction. The quark model categorizes hadrons into two primary families: mesons (quark-antiquark combinations, $q\bar{q}$) and baryons (composed of three quarks or antiquarks, $qqq$ or $\bar{q}\bar{q}\bar{q}$) [9]. The properties of these hadrons are governed by their valence quark content, which determines their quantum numbers including: total angular momentum ($J$), parity symmetry ($P$), charge conjugation symmetry ($C$), hypercharge ($Y$), isospin ($I$), strangeness ($S$), electric charge ($Q$), baryon number ($B$) and more. The first three quantum numbers are often expressed as a set, $J^{PC}$ (details about this notation are provided in Appendix C).

Hadronic states are naturally organized into geometric structures known as multiplets within quantum number space. For example, the lowest baryon octet states are shown in Fig. 2.2. Baryons or mesons in the same $J^P$ set have similar properties, interact strongly, and are related by the SU(3) flavour symmetry. The organizational scheme is called the *eightfold way*, first introduced by Gell-Mann and Ne'eman [34, 35].

The colour charge was first introduced to solve the $\Delta^{++}$ baryon violation of Dirac statistics [38, 39] (see also Refs. [9, 10, 40, 41]). The Pauli exclusion principle which indicates that fermions have anti-symmetric wavefunctions under particle exchange, while $\Delta^{++}$ (which has quark content of $uuu$) requires a spin-3/2 and symmetric wavefunction. This violation is fixed with a newly added quantum number exclusive to the strong interaction (hence QCD) named colour. This colour charge has three degrees of freedom: red, green, and blue. The naming of this QCD charge is simply an analogy to distinguish between each other rather than indication of actual colour. The $\Delta^{++}$ can now be expressed as an antisymmetric wavefunction:

$$\left|\Delta^{++}\right\rangle = \frac{1}{\sqrt{6}}\epsilon^{abc}\left|u_a\uparrow, u_b\uparrow, u_c\uparrow\right\rangle, \tag{2.1}$$

where $a, b, c$ are colour indices and $\epsilon_{abc}$ is antisymmetric Levi-Civita symbol. One can also see that each quark may carry one colour charge. The formation of all hadrons must follow the *colour neutrality* requirement [9]. A combination of all three colours ($rbg$ or $\bar{r}\bar{b}\bar{g}$) or

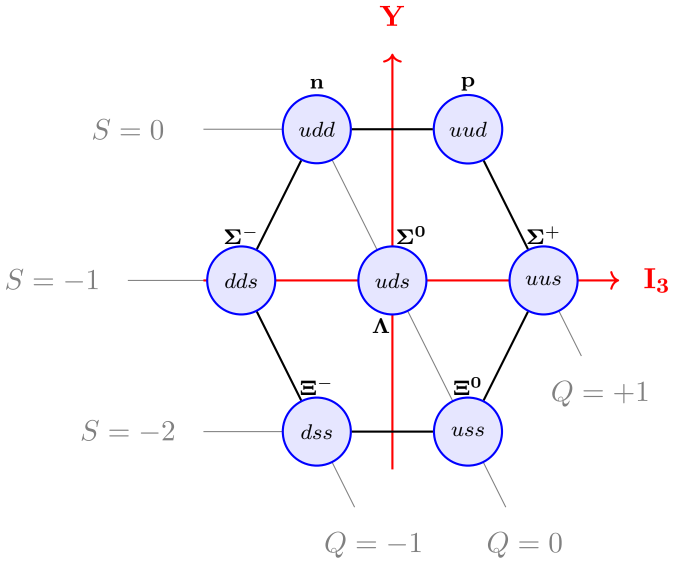

**Figure 2.2:** Baryon octet with spin $J = 1/2$ and parity $P = +1$ (*i.e.*, $J^P = \frac{1}{2}^+$) organized in two coordinates: one based on strangeness $S$ and charge $Q$ (in gray); the other based on hypercharge $Y$ and the third component of isospin $I_3$ (in red). The transformation between the two coordinate space follows the Gell-Mann-Nishijima formula: $Q = I_3 + \frac{1}{2}Y$, with $Y = B + S$ [36, 37]. The baryons in the shown octet can also be considered as the 8 resulting particles from every flavour rotation operating on $p$ reflecting $SU(3)$ symmetry. One can classify each conventional meson or baryon in their corresponding representation depending on the set's $J^P$ combination.

colour-anticolour $(r\bar{r} + g\bar{g} + b\bar{b})$ is considered colour neutral and is called a SU(3) colour singlet combination. These corresponds to baryons, antibaryons and mesons.

Additionally, QCD predicts the existence of exotic hadronic states such as tetraquarks and pentaquarks, which involve combinations of quarks and antiquarks beyond the conventional meson and baryon structures. Moreover, since gluons themselves carry colour, the strong force charge, and can self-interact, QCD also predicts gluonia, which are hypothetical bound states composed purely of gluons (e.g., Ref. [12,42]). These exotic states, particularly tensor glueballs, will be discussed in greater detail in Chapter 3.

## 2.2 Quantum Chromodynamics

We now know QCD is characterized by three colour charges of *rbg* and describes the interactions between quarks, mediated by gluons. Gluons are massless gauge bosons that are SU(3) colour singlets (colour-anticolour combination). By the exchange of gluons, quarks undergo colour changes and experience the effects of the strong force. One can find more details regarding the SU(3) symmetry group properties and the gluon colour octet in Appendix B.

### 2.2.1 QCD Lagrangian

The QCD Lagrangian is invariant under local SU(3) gauge transformation and can be written as:

$$\mathcal{L} = \sum_A \bar{q}_\alpha^A \left( i\gamma^\mu D_\mu - m_A \right) q_\alpha^A - \frac{1}{4} G_{\mu\nu}^a G_a^{\mu\nu}, \tag{2.2}$$

where:

- $q_\alpha^A$ represents the quark field with colour index $\alpha = 1, 2, 3$, and flavour index $A = 1, 2, \cdots, n_f$;
- the gauge covariant derivative is

  $$D_\mu = \partial_\mu - ig\, T_a\, \mathcal{A}_\mu^a, \tag{2.3}$$

  with $T_a$ $(a = 1, 2, \cdots, 8)$ being the SU(3)[1] generators and $g$ is the universal coupling strength;
- the gluon field strength tensor $G_{\mu\nu}^a$ is given by

  $$G_{\mu\nu}^a = \partial_\mu \mathcal{A}_\nu^a - \partial_\nu \mathcal{A}_\mu^a + g f^{abc} \mathcal{A}_\mu^b \mathcal{A}_\nu^c, \tag{2.4}$$

  where $\mathcal{A}_\mu^a(x)$ are the gluon fields and $f^{abc}$ are the SU(3) structure constants. The term $-\frac{1}{4} G_{\mu\nu}^a G_a^{\mu\nu}$ contains the kinetic term for the gluon fields that has gluon-gluon interactions. Note that $G_{\mu\nu}^a G_a^{\mu\nu}$ is gauge-invariant.

More details of the matrices and notation convention are included in Appendix A and B

---

[1] Strictly speaking, we are using su(3) algebra. In typical particle physics convention, there is usually no explicit distinction between SU(3) symmetry group and su(3) Lie algebra.

Taking the gauge fixing term and the Faddeev-Popov ghosts fields $\phi_a(x)$ [43] that obeys fermionic statistics into account, the Langrangian density can be written explicitly as [44]

$$\begin{aligned}
\mathcal{L}(x) = &- \frac{1}{2}\left[\partial_\mu A^a_\nu(x)\right]\left[\partial^\mu \mathcal{A}^\nu_a(x) - \partial^\nu \mathcal{A}^\mu_a(x)\right] - \frac{1}{2\xi}\left[\partial_\mu \mathcal{A}^\mu_a(x)\right]\left[\partial_\nu \mathcal{A}^\nu_a(x)\right] \\
&+ \frac{i}{2}\left(\bar{q}^A_\alpha(x)\gamma^\mu \partial_\mu q_\alpha(x)^A\right) - \frac{i}{2}\left[\partial_\mu \bar{q}^A_\alpha(x)\right]\gamma^\mu q^A_\alpha(x) - m\bar{q}^A_\alpha(x) q^A_\alpha(x) \\
&+ \frac{1}{2}\, g\, \bar{q}^A_\alpha(x)\lambda^a_{\alpha\beta}\gamma^\mu q^A_\beta(x)\mathcal{A}^a_\mu(x) \\
&- \frac{1}{2}\, g\, f_{abc}\left[\partial_\mu \mathcal{A}^a_\nu(x) - \partial_\nu \mathcal{A}^a_\mu(x)\right]\mathcal{A}^\mu_b(x)\mathcal{A}^\nu_c(x) \\
&- \frac{1}{4}\, g^2\, f_{abc}\, f_{ade}\mathcal{A}^b_\mu(x)\mathcal{A}^c_\nu(x)\mathcal{A}^\mu_d(x)\mathcal{A}^\nu_e(x) \\
&- \left[\partial_\mu \overline{\phi}_a(x)\right]\partial^\mu \phi_a(x) + g\, f_{abc}\left[\partial_\mu \overline{\phi}_a(x)\right]\phi_b(x)\mathcal{A}^\mu_c(x),
\end{aligned} \tag{2.5}$$

where a gauge-fixing parameter $\xi$ is introduced in the second term. The expression implies a summation over quark flavours.

Equation (2.5) includes the gauge fixing term for the gauge symmetry in a canonical covariant quantization. The process introduced unphysical particles from the theory. The self-coupling of gluon fields necessitates a new non-physical massless scalar field to eliminate the extra degrees of freedom and restore unitarity in the physical states, *i.e.,* ghost fields [43] (see also *e.g.,* [44]). The ghost field $\phi_a$ only couples to gluon field (see Appendix. E for Feynman rules involving ghost fields).

### 2.2.2 Asymptotic Freedom

The strength of the strong interaction is characterized by the dimensionless running coupling $\alpha_s(\nu)$, which depends on a reference energy scale $\nu$ (introduced by dimensional regularization in Sec. 2.3). One of the properties of QCD is asymptotic freedom, stating that the coupling decreases as the energy scale increases (or equivalently, as the distance between interacting particles decreases) [45, 46] (see also Refs. [6, 31, 44]).

The behaviour of the running coupling $\alpha_s(\nu)$ lies in the $\beta$-function which is defined as:

$$\alpha_s \beta(\alpha_s) \equiv \nu \frac{\mathrm{d}\alpha_s}{\mathrm{d}\nu}. \tag{2.6}$$

To the lowest order of $\alpha_s$, the $\beta$-function is given by [44]

$$\beta(\alpha_s) = \frac{\alpha_s}{\pi}\beta_1 + \mathcal{O}\left(\frac{\alpha_s}{\pi}\right)^2 \text{ with } \beta_1 = -\frac{11}{2} + \frac{n_f}{3} \text{ for } n_f \text{ flavours.} \tag{2.7}$$

One can solve the differential equation for $\alpha_s(\nu)$ up to one-loop order:

$$\alpha_s(\nu) = \frac{\alpha_s(\nu_0)}{1 - \frac{\alpha_s(\nu_0)}{\pi}\beta_1 \log\left(\frac{\nu}{\nu_0}\right)}, \tag{2.8}$$

where $\nu_0$ is the reference energy scale and $\alpha(\nu_0)$ is specified (*e.g.,* by experiment). Equation (2.8) reveals how the coupling decreases at high energies ($\nu \gtrsim \nu_0$) following a logarithmic relationship, and ultimately vanishes at asymptotically high energies. Figure 2.3 further demonstrates the behaviour of $\alpha_s(\nu)$ as predicted by higher-loop perturbative calculations of $\alpha_s$, capturing the phenomenon of asymptotic freedom. The dynamics of strong interactions can be accurately described through a perturbative expansion series of the running $\alpha_s(\nu)$.

At lower energy scales ($\nu \lesssim \nu_0$), however, the strong coupling strength increases and fails to converge. In this regime, perturbation theory becomes inadequate, calling for alternative methods to evaluate non-perturbative effects in the study of QCD. Later, in Sec. 2.5, we will focus on one such approach — QCDSR — that addresses the challenges brought by asymptotic freedom. Additionally, asymptotic freedom leads to another fundamental property of QCD: colour confinement.

#### 2.2.2.1 Colour Confinement

One key characteristic of QCD is called *colour confinement.* This refers to the phenomenon that no coloured state has ever been observed experimentally, *i.e.,* quarks and gluons do not exist in isolation; they are always found within colour-neutral combinations. Colour confinement is also the central concept of SU(3) colour symmetry as hadrons must be colour singlets (see algebra treatment in Appendix B.1).

The confinement theory also explains the short-range nature of the strong force. The lightest colour singlet states (*i.e.,* pions with mass $\sim 140\,\mathrm{MeV}$) gives the range of the strong interaction ($\sim$ 1 fm). If singlet gluon state exist, the massless property of the gluon will

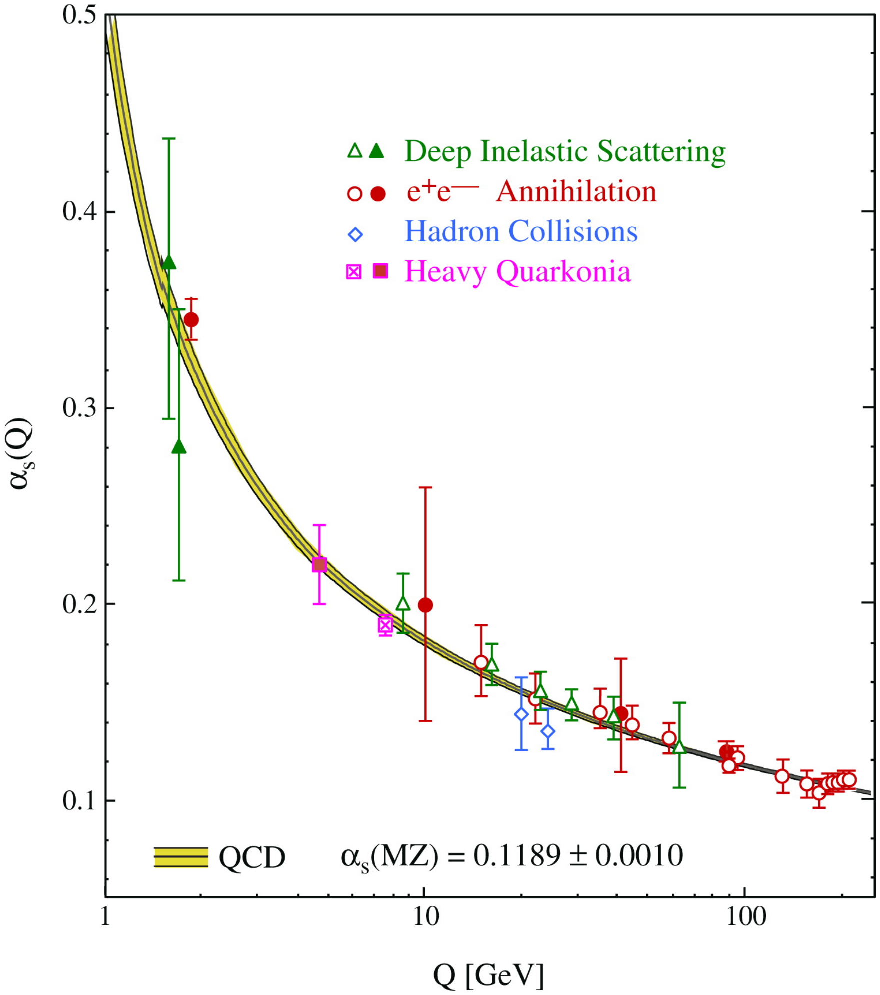

**Figure 2.3:** QCD prediction and experimental measurements of the strong coupling $\alpha_s$ with respect to energy scale $Q \equiv \nu$. The reference energy scale is $M_Z^0 \simeq 91.2\,\text{GeV}$ [7]. The QCD prediction of $\alpha_s$ is to the four-loop approximation and agrees with experiments. Figure taken from Ref. [47].

then mediate the strong interaction in infinite range, which contradicts all experimental observations. Therefore, the gluon singlet states evidently do not exist and only gluon octet are being exchanged between coloured states to realize the strong coupling [6, 48].

From the asymptotic perspective, lattice QCD (LQCD) proposed that colour confinement can be explained by the chromoelectric flux tube model [48–50] (see also *e.g.,* [51]). As the quarks within a hadron, a meson for example, are being separated away from the centre of mass of the $q\bar{q}$ system, the Coulombic bound state potential of $q\bar{q}$ increases linearly at large distance $r$ [48]:

$$V_{q\bar{q}} \sim \frac{4}{3}\frac{\alpha_s(r)}{r} + \sigma r. \tag{2.9}$$

At large enough separation distance, it is energetically possible to create an additional $q\bar{q}$ pair in the vacuum, and distribute among the two original charges, leading to the formation of new colour-neutral hadronic combinations. This can be experimentally observed through hadronic jets.

### 2.2.3 Perturbation Theory

To study a physical process, one should construct the corresponding Green's function with the appropriate particle content. This Green's function can be expressed in terms of vacuum expectation values (VEVs) of time-ordered products of finite numbers of free field operators $\phi(x_i)$ [31]:

$$\langle\Omega|\,\mathcal{T}\{\phi(x_1)\phi(x_2)\cdots\phi(x_i)\}\,|\Omega\rangle \tag{2.10}$$

where $\mathcal{T}$ denotes the time-ordering operator. The $|\Omega\rangle$ represents the ground state of the interacting theory and is replaced by $|0\rangle$ in the non-interacting (free) theory. They are distinguished in Chapter 2. In the literature referenced throughout this thesis, however, we focus exclusively on interacting theories. Therefore, all vacuum states $|\Omega\rangle$ are written as $|0\rangle$ for notation simplicity and should be understood as the interacting vacuum.

Eq. (2.10) can be evaluated using Wick's theorem [31]:

$$\mathcal{T}\{\phi(x_1)\phi(x_2)\cdots\phi(x_i)\} = :\phi(x_1)\phi(x_2)\cdots\phi(x_i) + \text{all possible contractions}:, \tag{2.11}$$

where $:\cdots:$ is the normal ordering symbol. In the simplest case of two scalar fields in the free theory (*i.e.*, $i = 2$), the contraction gives the Feynman propagator $D_F$:

$$\begin{aligned} \langle 0|\,\mathcal{T}\{\phi(x_1)\phi(x_2)\}\,|0\rangle &= \langle 0|:\phi(x_1)\phi(x_2) + \contraction{}{\phi}{(x_1)}{\phi}\phi(x_1)\phi(x_2):|0\rangle \\ &= \contraction{}{\phi}{(x_1)}{\phi}\phi(x_1)\phi(x_2) \\ &= D_F(x_1 - x_2). \end{aligned} \tag{2.12}$$

In the second line of Eq. (2.12), we used a important property that the VEV of any uncontracted operators in free-field theory results in zero:

$$\langle 0\,|:\cdots:|\,0\rangle = 0 \tag{2.13}$$

leaving only fully contracted terms. It is important to note that for the interacting-field theory vacuum $|\Omega\rangle$, the VEV for normal-ordered fields does not always vanish, leading to non-zero contributions to the correlator called condensate contributions (see more details in Sec. 2.5). Since we will be working with fermion (quark) fields $q(x)$ in the context of QCD, we employ the fermionic free field propagator $S(x_1 - x_2)$:

$$\begin{aligned} &\langle 0|\,\mathcal{T}\{q(x_1)\bar{q}(x_2)\}\,|0\rangle \equiv \\ &\qquad \contraction{}{q}{(x_1)}{\bar{q}}q(x_1)\bar{q}(x_2) = iS(x_1 - x_2) = i\int \frac{d^4k}{(2\pi)^4}\frac{\not{k} + m}{k^2 - m^2 + i\eta}e^{-ik\cdot(x_1 - x_2)}, \end{aligned} \tag{2.14}$$

where colour indices are omitted, $k$ is the internal momentum of the fermion from position $x_1$ to $x_2$. The term $\not{k} = \gamma^\mu k_\mu$ denotes the contraction of the Dirac gamma matrices with the momentum $k$ (also introduced in Appendix A). Additionally, the imaginary prescription with $\eta \to 0^+$ rises from the pole structure at $k^2 = m^2$ of the propagator. The particle-antiparticle form originates from the spinor field nature of quarks. This can also be understood through [31]:

$$\wick{\c q(x_1) \c q(x_2)} = \wick{\c{\bar{q}}(x_1) \c{\bar{q}}(x_2)} = 0. \tag{2.15}$$

Or conceptually: the $\bar{q}(x_2)$ field represents the annihilation of a quark at position $x_2$, while $q(x_1)$ represents the creation of a quark at position $x_1$. The VEV sums over all possible quantum states through which a quark at $x_2$ can propagate to $x_1$. For bosons, such as scalar bosons in Eq. (2.12), and vector bosons like gluons:

$$\begin{aligned}
\langle 0| \mathcal{T}\{\mathcal{A}^\mu(x_1)\mathcal{A}^\nu(x_2)\} |0\rangle &\equiv \wick{\c{\mathcal{A}}^\mu(x_1)\c{\mathcal{A}}^\nu(x_2)} \\
&= iD^{\mu\nu}(x_1 - x_2) \\
&= -i \int \frac{d^4k}{(2\pi)^4} \left[ g^{\mu\nu} - (1-\xi)\frac{k_\mu k_\nu}{k^2 + i\eta} \right] \frac{1}{k^2 + i\eta} e^{-ik\cdot(x_1 - x_2)},
\end{aligned} \tag{2.16}$$

with the gauge parameter $\xi$. For ghost field, its propagator is

$$\begin{aligned}
\langle 0| \mathcal{T}\{\phi(x_1)\phi(x_2)\} |0\rangle &= i\Delta^{\mu\nu}(x_1 - x_2) \\
&= -i \int \frac{d^4k}{(2\pi)^4} \frac{1}{k^2 + i\eta} e^{-ik\cdot(x_1 - x_2)},
\end{aligned} \tag{2.17}$$

which will be applied in Chapter 3 to include ghost self-energy loop in the Feynman diagrams.

As shown in Eqs. (2.14) and (2.16), a Fourier transforms is applied to obtain the final form of the propagator in momentum-space. When working with more fields in the correlator (say $i = 4$ in Eq. (2.11)), the Wick theorem applying on the four-point function for gluon fields takes the form:

$$\begin{aligned}
\mathcal{T}\{\mathcal{A}^\mu(x_1)\mathcal{A}^\nu(x_2)\mathcal{A}^\rho(x_3)\mathcal{A}^\sigma(x_4)\} =&: \mathcal{A}^\mu(x_1)\mathcal{A}^\nu(x_2)\mathcal{A}^\rho(x_3)\mathcal{A}^\sigma(x_4) : \\
&+ \wick{\c{\mathcal{A}}^\mu(x_1)\c{\mathcal{A}}^\nu(x_2)} : \mathcal{A}^\rho(x_3)\mathcal{A}^\sigma(x_4) : + \ : \mathcal{A}^\mu(x_1)\mathcal{A}^\nu(x_2) : \wick{\c{\mathcal{A}}^\rho(x_3)\c{\mathcal{A}}^\sigma(x_4)} \\
&+ \ : \wick{\c{\mathcal{A}}^\mu(x_1)\mathcal{A}^\nu(x_2)\c{\mathcal{A}}^\rho(x_3)}\mathcal{A}^\sigma(x_4) : + \ : \mathcal{A}^\mu(x_1)\wick{\c{\mathcal{A}}^\nu(x_2)\mathcal{A}^\rho(x_3)\c{\mathcal{A}}^\sigma(x_4)} : \\
&+ \ : \wick{\c{\mathcal{A}}^\mu(x_1)\mathcal{A}^\nu(x_2)\mathcal{A}^\rho(x_3)\c{\mathcal{A}}^\sigma(x_4)} : + \ : \mathcal{A}^\mu(x_1)\wick{\c{\mathcal{A}}^\nu(x_2)\c{\mathcal{A}}^\rho(x_3)}\mathcal{A}^\sigma(x_4) : \\
&+ \ : \wick{\c1{\mathcal{A}}^\mu(x_1)\c1{\mathcal{A}}^\nu(x_2)\c2{\mathcal{A}}^\rho(x_3)\c2{\mathcal{A}}^\sigma(x_4)} : + \ : \wick{\c1{\mathcal{A}}^\mu(x_1))\c2{\mathcal{A}}^\nu(x_2)\c1{\mathcal{A}}^\rho(x_3)\c2{\mathcal{A}}^\sigma(x_4)} : \\
&+ \ : \wick{\c1{\mathcal{A}}^\mu(x_1)\c2{\mathcal{A}}^\nu(x_2)\c2{\mathcal{A}}^\rho(x_3)\c1{\mathcal{A}}^\sigma(x_4)} :,
\end{aligned} \tag{2.18}$$

where any two contracted operators that are not adjacent can be rearranged to reach the form of contracted fields and/or normal ordered fields due to the commutation relations [44]:

$$\wick{: \c{\mathcal{A}}^\mu(x_1)\mathcal{A}^\nu(x_2)\c{\mathcal{A}}^\rho(x_3)\mathcal{A}^\sigma(x_4) : \;\rightarrow\; \c{\mathcal{A}}^\mu(x_1)\c{\mathcal{A}}^\rho(x_3)} : \mathcal{A}^\nu(x_2)\mathcal{A}^\sigma(x_4) :, \tag{2.19}$$

$$\wick{: \c1{\mathcal{A}}^\mu(x_1)\c2{\mathcal{A}}^\nu(x_2)\c2{\mathcal{A}}^\rho(x_3)\c1{\mathcal{A}}^\sigma(x_4) : \;\rightarrow\; \c1{\mathcal{A}}^\mu(x_1)\c1{\mathcal{A}}^\sigma(x_4)\c2{\mathcal{A}}^\nu(x_2)\c2{\mathcal{A}}^\rho(x_3)}. \tag{2.20}$$

Applying Eq. (2.13), only the fully contracted terms survive and the four-point correlation function yields

$$\begin{aligned}
&\mathcal{T}\{\mathcal{A}^\mu(x_1)\mathcal{A}^\nu(x_2)\mathcal{A}^\rho(x_3)\mathcal{A}^\sigma(x_4)\}\\
&\quad= D^{\mu\nu}(x_1-x_2)D^{\rho\sigma}(x_3-x_4)+D^{\mu\rho}(x_1-x_3)D^{\nu\sigma}(x_2-x_4)+D^{\mu\sigma}(x_1-x_4)D^{\nu\rho}(x_2-x_3).
\end{aligned} \tag{2.21}$$

Although using gluon fields as the example, Wick's theorem can be applied to any quantum fields in a similar manner.

The connected correlation function of interacting-field theory can be represented in terms of the free-field theory vacuum using the Gell-Mann-Low relation [31, 44, 52]

$$\langle\Omega|\,\mathcal{T}\{\phi(x_1)\phi(x_2)\}\,|\Omega\rangle = \lim_{t\to\infty(1-i\epsilon)} \frac{\langle 0|\,\mathcal{T}\{\phi(x_1)\phi(x_2)\exp\bigl(i\int \mathrm{d}^4x\mathcal{L}_{\text{int}}(x)\bigr)\}\,|0\rangle}{\langle 0|\,\mathcal{T}\exp\bigl(i\int \mathrm{d}^4x\mathcal{L}_{\text{int}}(x)\bigr)\,|0\rangle}, \tag{2.22}$$

where the limit of $t\to\infty(1-i\epsilon)$ provides $|\Omega\rangle$ being small perturbation of $|0\rangle$. The term $\mathcal{L}_{\text{int}}$ corresponds to the interacting part of the interacting-field theory Lagrangian. The numerator of Eq.(2.22) includes all *connected* Feynman diagrams, which link both points $x_1$ and $x_2$, as well as disconnected Feynman diagrams, also known as "vacuum bubbles" (see Fig. 2.4 for an example). All disconnected Feynman diagrams from all external points are cancelled using the exponentiation of the disconnected diagrams by the denominator of Eq. (2.22).

Equation (2.22) also provides the evaluation of the connected correlation function in perturbation expansion of power series in the coupling $g$. The exponential in the numerator

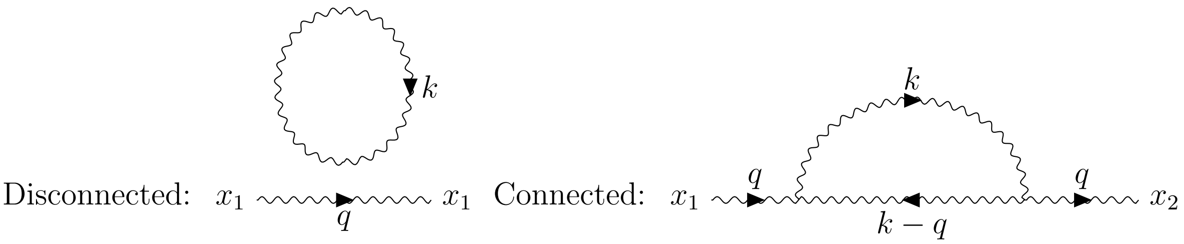

**Figure 2.4:** Feynman diagrams for gluon "vacuum bubble" (disconnected) and gluon self-energy (connected). The wavy line represent gluon field propagator.

and denominator can be written in Taylor series:

$$\exp\left(i\int \mathrm{d}^4x\mathcal{L}_{\text{int}}(x)\right) = 1 + i\int \mathrm{d}^4x\mathcal{L}_{\text{int}}(x) + \frac{1}{2}\left(i\int \mathrm{d}^4x\mathcal{L}_{\text{int}}(x)\right)^2 + \cdots . \tag{2.23}$$

Using Wick's theorem, Eq.(2.22) leads to a series of perturbative corrections, which can be illustrated diagrammatically using Feynman diagrams. In Sec.3.2, for example, we will evaluate the two-point correlation function of tensor gluonium:

$$i\int d^4x e^{iqx}\langle 0|\mathcal{T}J^g_{\mu\nu}(x)J^g_{\rho\sigma}(0)^\dagger|0\rangle \tag{2.24}$$

with $J^g_{\mu\nu}(x)$ being a gluonium current, and look for its perturbative correction to two-loop order using Feynman diagrams. Below in Fig. 2.5 are some of them for demonstration purpose.

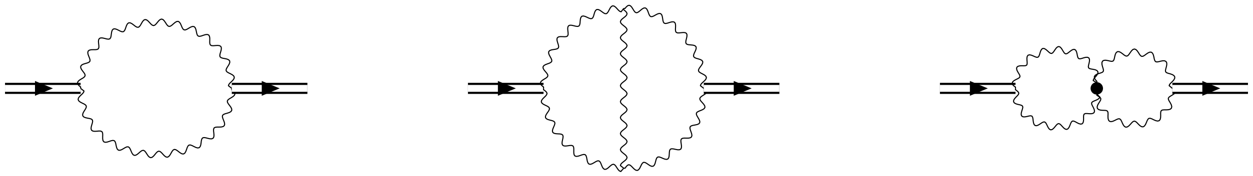

**Figure 2.5:** Feynman diagrams showing different order of corrections to the perturbative expansion of the correlation function Eq. (2.24). The double lines represent the tensor gluonium current and wavy line represent gluon field propagator. Any intersection among gluon field lines represents a gluon vertex and bring up the order of correction (power of coupling $g$, proportional to corresponding $\mathcal{L}_{\text{int}}$ terms). Thus, the first diagram is a leading-order (one-loop) perturbative correction; the second and third diagrams are NLO (two-loop) Feynman diagrams.

Feynman diagrams provide a clear and intuitive way to illustrate the correlation function, effectively organizing perturbative contributions to the correlator according to different loop-order diagrams. Each diagram's contribution can be calculated within perturbation theory using Feynman rules—a set of prescriptions that translate components of Feynman diagrams (e.g., propagators and vertices) into mathematical expressions. Basic Feynman rules for QCD are widely available in references such as [31] and [44]. For the purpose of our study, we also derived Feynman rules for specific topologies (*e.g.,* tensor-gluonium-current-to-two-gluons appeared in Fig. 2.5). These tailored and more complex Feynman rules required for our work are summarized in Appendix E.

## 2.3 Dimensional Regularization

Directly calculating correlation functions containing loop Feynman diagrams, such as ones in Fig. 2.5, in momentum space may result in divergent integrals. To address this, a set of rules is needed to regularize these divergences so that the divergent integrals are parametrized and physically meaningful [44]. For our work, we use the method of dimensional regularization [53] (see also Refs. [44, 48]).

The essential idea of dimensional regularization is to first generalize our 4-dimensional space-time integrals to $D$-dimensional, where $D = 4 \pm 2\epsilon$ (depending on the convention of choice). By expanding the integrals in $D$ dimensions as $\epsilon \to 0$, the divergences are isolated in terms proportional to $1/\epsilon$ or higher-order poles. These poles emerge at the limit of $D \to 4$ dimensions, effectively separating divergent contributions from finite contributions.

With techniques including Feynman's parametrization and Euler $\Gamma$-function (see *e.g.,* Ref. [44]), the basic formula for dimensional regularization takes the following form:

$$\begin{aligned}\Phi(D, A, B) &\equiv \int \frac{\mathrm{d}^D k}{(2\pi)^D} \frac{(k^2)^B}{(k^2 - a^2 + i\eta)^A} \\ &= \frac{i}{(4\pi)^{\frac{D}{2}}} (-1)^{B-A} \left(a^2\right)^{B-A+\frac{D}{2}} \frac{\Gamma(B + \frac{D}{2})\,\Gamma(A - B - \frac{D}{2})}{\Gamma(A)\,\Gamma\left(\frac{D}{2}\right)},\end{aligned} \tag{2.25}$$

where $A$ and $B$ are real numbers (see *e.g.,* Refs. [44, 54]). After taking the Taylor expansions in $\epsilon$ of the $\Gamma$-functions in the formula, one keeps the terms proportional to $\epsilon^{-1}$ — divergences, and $\epsilon^0$ — finite physical terms for the final result. One, sometimes, needs to keep higher-order terms in $\epsilon$ in combination with the renormalization factors, which includes $\epsilon^{-1}$ or lower orders, so that the final result will be in divergent and physical terms (application in Chapter. 3).

To illustrate, let us consider the one-loop quark self-energy. From the corresponding Feynman diagram, a *loop integral* can be constructed using the Feynman rules (listed for QCD in Appendix. E). Using the quark and gluon propagator Feynman rules from Eqs. (2.14) and (2.16), the quark self-energy loop integral in Feynman gauge ($\xi = 1$) is:

$$-i\Sigma_{\alpha\beta}(q) =$$

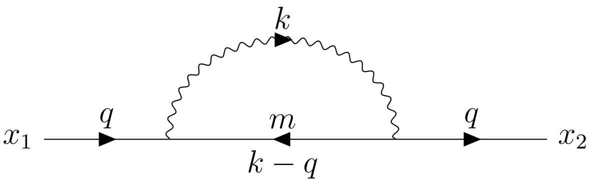

$$= -\frac{g^2}{4}\left[\lambda^a\lambda^a\right]_{\alpha\beta}\int \frac{\mathrm{d}^4k}{(2\pi)^4}\gamma^\mu \frac{\not{k}-\not{q}+m}{(k-q)^2-m^2+i\eta}\gamma^\nu \left[g^{\mu\nu}-(1-\xi)\frac{k_\mu k_\nu}{k^2+i\eta}\right]\frac{1}{k^2+i\eta}. \tag{2.26}$$

where colour indices are omitted and the integration applies over all four dimensions in infinite range. The integrand at high momentum $k$ will lead to divergent loop integral in perturbation theory, rendering them meaningless. This type of divergent behaviour in integrals is referred to as ultraviolet divergences. To address these divergences, we must safely regularize Eq.(2.26) using dimensional regularization by changing the dimension 4 to $D = 4 + 2\epsilon$, [44, 53].

$$\Sigma_{\alpha\beta}(q) = \frac{4}{3}\frac{(g\nu^\epsilon)^2}{(4\pi)^2}\left(\xi(\not{q}-m)-3m\right) \left[\left(\frac{1}{\epsilon}-\log(4\pi)+\gamma_E+\log\frac{m^2}{\nu^2}\right)+f\left(\frac{q^2}{m^2}\right)\right], \ \epsilon\to 0 \tag{2.27}$$

where $\nu$ is called the *renormalization scale* and $\gamma_E \simeq 0.577$ is the Euler's constant. The divergences are isolated in the $1/\epsilon$ pole term and $f(\frac{q^2}{m^2})$ represents the finite terms as a function of $q^2/m^2$. Note than when moving from 4-dimension to $D$-dimension, the dimensionless $g$ acquires a non-zero dimension of $[g] = -\epsilon$. In order to construct a perturbation series with a dimensionless coupling strength, an arbitrary parameter $\nu$ with dimension of mass is introduced to compensate $g$ so that the combined quantity of $g\nu^\epsilon$ remain dimensionless, *i.e.*, $[g\nu^{\epsilon}] = 0$. This leads to the definition of the dimensionless coupling:

$$\alpha_s \equiv \frac{(g\nu^{\epsilon})^2}{4\pi}, \tag{2.28}$$

which is the starting point to build the running coupling $\alpha_s(\nu)$ discussed in Sec. 2.2.2. Further details about $\alpha_s$ will be explored in Sec.2.4. To ensure consistency, a factor of $1/\nu^{\epsilon}$ must be included for every instance of $g$ appearing in loop integrals. As a result, $\left[\int \frac{\mathrm{d}^D k}{\nu^{2\epsilon}}\right] = 4$ preserves canonical dimensions in $\epsilon \to 0$ limit.

Dimensional regularization plays an important role throughout this thesis. We parametrize the divergence in tensor di-gluonium NLO correlator calculation in Chapter. 3. In Chapter 5, we use dimensional regularization to extract the divergences in both zero and finite temperature two-point correlation function and show that they can cancel each other, leading to a finite thermal effect on the target loop integral.

In the practice of explicit correlator calculation, we use the TARCER package in `MATHEMATICA` to perform dimensional regularization on our one/two loop integrals with arbitrary masses [55–58]. TARCER uses the recurrence algorithm [59, 60] to reduce the divergent tensor integrals into a combination of scalar ones, such as [58]:

$$\begin{aligned}
&\mathrm{TAI}\left[D, 0, \{\{\nu_1,\ \mathrm{m}_1\}\}\right] = \\
&\qquad \mathbf{A}_{\nu_1}^{(d)} = \frac{1}{\pi^{D/2}} \int \frac{d^D k_1}{\left[k_1^2 - m_1^2\right]^{\nu_1}},
\end{aligned} \tag{2.29}$$

$$\begin{aligned}
&\mathrm{TBI}\left[D, \mathrm{p}^2, \{\{\nu_1,\ \mathrm{m}_1\}, \{\nu_2,\ \mathrm{m}_2\}\}\right] = \\
&\qquad \mathbf{B}_{\nu_1\nu_2}^{(D)} = \frac{1}{\pi^{D/2}} \int \frac{d^D k_1}{\left[k_1^2 - m_1^2\right]^{\nu_1} \left[k_3^2 - m_2^2\right]^{\nu_2}},
\end{aligned} \tag{2.30}$$

$$\begin{aligned}
&\mathrm{TJI}\left[D, \mathrm{q}^2, \{\{\nu_1,\ \mathrm{m}_1\}, \{\nu_2,\ \mathrm{m}_2\}, \{\nu_3,\ \mathrm{m}_3\}\}\right] = \\
&\qquad \mathbf{J}_{\nu_1\nu_2\nu_3}^{(D)} = \frac{1}{\pi^{D}} \iint \frac{d^D k_1 d^d k_2}{\left[k_1^2 - m_1^2\right]^{\nu_1} \left[k_5^2 - m_2^2\right]^{\nu_2} \left[k_4^2 - m_3^2\right]^{\nu_3}},
\end{aligned} \tag{2.31}$$

which are known master integrals that can be expressed in hypergeometric function and $\Gamma$-function (see example Refs. [44,61,62]). In Sec. 3.2.3.4, the loop integral of two-loop gluonium current with fermion self-energy loop can be reduced using recursion relationships to

$$\frac{(D-2)^2(D+1)\left(9D^3-40D^2+44D-16\right)g^2q^2}{24\pi^4(D-4)(D-1)(3D-4)(3D-2)}\mathbf{J}^{(D)}_{\{1,0\}\{1,0\}\{1,0\}}, \tag{2.32}$$

followed by expansion $D = 4 + 2\epsilon$. The sample code using FeynCalc and TARCER for this topology is included in Appendix D.

## 2.4 Renormalization

Dimensional regularization extracted the divergence into isolated order terms of $1/\epsilon$ at one-loop order. The goal of theoretical predictions for observables is to compare with experimental measurements, which are finite. In this section, we will look into the theory of renormalization which remove the ultraviolet divergences in field theories for QCD is a renormalizable theory [53, 63]. We will cover two renormalization methods, conventional (Sec. 2.4.1) and diagrammatic (Sec. 2.4.2), for QCD Lagrangian. Additionally, we will revisit the running coupling (and other running parameters) in Sec. 2.4.3, only this time from the renormalization group equation of a Green's function.

### 2.4.1 Conventional Renormalization

QCD is a renormalizable theory meaning all divergences arising in Feynman integral calculations can be absorbed in finite number of bare quantities. With ultraviolet integral divergence now properly regularized using dimensional regularization in the form of $1/\epsilon$ (or higher-order) coefficients, one may use renormalization to eliminate the infinities. The conventional renormalization approach includes applying certain renormalization constants $Z_i \equiv 1 + R_i$ to the Lagrangian density (2.5), which in turn affects the correlation functions. The 1 will carry forward the bare integral, while $R_i$ introduces new counter-terms corrections aimed at cancelling the regulated divergences in the Green's function to any order in perturbation theory.

Each term in the QCD Lagrangian requires its own renormalization constant prescription:

$$
\begin{aligned}
\mathcal{L}_R(x) =& \mathcal{L}_{\text{bare}}(x) + \mathcal{L}_{\text{counter-term}}(x) \\
=& -\frac{Z_{3\mathrm{YM}}}{2}\left[\partial_\mu A^a_\nu(x)\right]\left[\partial^\mu \mathcal{A}^\nu_a(x) - \partial^\nu \mathcal{A}^\mu_a(x)\right] - \frac{Z_6}{2\xi}\left[\partial_\mu \mathcal{A}^\mu_a(x)\right]\left[\partial_\nu \mathcal{A}^\nu_a(x)\right] \\
&+ \frac{i}{2} Z_{2\mathrm{F}}\Big(\left(\bar{q}^A_\alpha(x)\gamma^\mu\partial_\mu q^A_\alpha(x)\right) - \left[\partial_\mu \bar{q}^A_\alpha(x)\right]\gamma^\mu q^A_\alpha(x)\Big) - Z_4 m \bar{q}^A_\alpha(x) q^A_\alpha(x) \\
&+ Z_{1\mathrm{F}}\frac{1}{2}\, g\, \bar{q}^A_\alpha(x)\lambda^a_{\alpha\beta}\gamma^\mu q^A_\beta(x)\mathcal{A}^a_\mu(x) \\
&- Z_{1\mathrm{YM}}\frac{1}{2}\, g\, f_{abc}\left[\partial_\mu \mathcal{A}^a_\nu(x) - \partial_\nu \mathcal{A}^a_\mu(x)\right]\mathcal{A}^\mu_b(x)\mathcal{A}^\nu_c(x) \\
&- Z_5\frac{1}{4}\, g^2\, f_{abc}\, f_{ade}\mathcal{A}^b_\mu(x)\mathcal{A}^c_\nu(x)\mathcal{A}^\mu_d(x)\mathcal{A}^\nu_e(x) \\
&- \tilde{Z}_3\left[\partial_\mu \overline{\phi}_a(x)\right]\partial^\mu \phi_a(x) + \tilde{Z}_1 g\, f_{abc}\left[\partial_\mu \overline{\phi}_a(x)\right]\phi_b(x)\mathcal{A}^\mu_c(x),
\end{aligned}
\tag{2.33}
$$

effectively rescaling all the fields, coupling, mass and parameters:

$$
\begin{aligned}
&\mathcal{A}^\mu_{a,\mathrm{B}} \equiv Z^{1/2}_{3\mathrm{YM}}\,\mathcal{A}^\mu_{a,\mathrm{R}}, && q_{\alpha,\mathrm{B}} \equiv Z^{1/2}_{2\mathrm{F}} q_{\alpha,\mathrm{R}}, && \phi_{a,\mathrm{B}} \equiv \tilde{Z}^{1/2}_3 \phi_{a,R} \\
&g_{\mathrm{YM,B}} \equiv Z_{1\mathrm{YM}}\, Z^{-3/2}_{3\mathrm{YM}}\, g_{\mathrm{R}}, && \tilde{g}_{\mathrm{B}} \equiv \tilde{Z}_1 \tilde{Z}^{-1}_3\, Z^{-1/2}_{3\mathrm{YM}}\, g_{\mathrm{R}}, && \tilde{g}_{\mathrm{F,B}} \equiv \tilde{Z}_{1\mathrm{F}}\, Z^{-1/2}_{3\mathrm{YM}}\, Z^{-1}_{2\mathrm{F}}\, g_{\mathrm{R}} \\
&g_{5,\mathrm{B}} \equiv Z_5 Z^{1/2}\, Z^{-1}_{3\mathrm{YM}}\, g_{\mathrm{R}}, && m_{\mathrm{B}} \equiv Z_4 Z^{-1}_{2\mathrm{F}}\, m_{\mathrm{R}}, && \xi_{\mathrm{B}} \equiv Z^{-1}_6 Z_{3\mathrm{YM}}\, \xi_{\mathrm{R}}
\end{aligned}
\tag{2.34}
$$

where we follow the naming convention for $Z_i$ in Ref. [44], and the notations $B$ and $R$ stand for bare and renormalized quantities. $g_{\mathrm{YM}}$, $\tilde{g}$, $g_{\mathrm{F}}$, $g_5$ correspond to couplings of three-gluon, ghost-gluon, quark-gluon and four-gluon interactions, respectively, and these bare quantities must satisfy:

$$
g_{\mathrm{YM,B}} = \tilde{g}_{\mathrm{B}} = \tilde{g}_{\mathrm{F,B}} = g_{5,\mathrm{B}} \equiv g_{\mathrm{B}}
\tag{2.35}
$$

to preserve the gauge invariance under BRST transformation [64], leading to the Salvnov-Taylor identities for related $Z_i$s:

$$
\frac{Z_{3\mathrm{YM}}}{Z_{1\mathrm{YM}}} = \frac{\tilde{Z}_3}{\tilde{Z}_1} = \frac{Z_{2\mathrm{F}}}{Z_{1\mathrm{F}}}, \qquad Z_5 = Z_{1\mathrm{YM}}\frac{Z_{1\mathrm{YM}}}{Z_{3\mathrm{YM}}}.
\tag{2.36}
$$

The renormalized Lagrangian (2.33) essentially rewrites the original bare QCD Lagrangian (2.5) in terms of renormalization constants $Z_i$ and renormalized quantities. The correlation functions using the renormalized Lagrangian (2.33) will be finite, as divergences from the bare Lagrangian are systematically removed through renormalization prescriptions. In mathematical terms, the renormalized and bare expressions of a propagator or vertex integral $D$ are related by

$$D_{\mathrm{R}}(q) = \lim_{\epsilon\to 0}\left[Z_i^{-1} D_{\mathrm{B}}(q)\right], \tag{2.37}$$

where $Z_i$ depends on the terms involved in the Lagrangian (2.33) for the integral (e.g., $Z_{3\mathrm{YM}}$ for gluon propagator). All of the renormalization constants can be derived with amputated Feynman diagrams to one-loop order (*i.e.,* tree level + one-loop correction) with varying field contents (see step-by-step derivations in Ref. [44]).

The choices of $R_i$ (hence $Z_i$) depends on the desired divergence cancellation, and different choices leading to various finite Green's functions correspond to different renormalization schemes. The minimal subtraction (MS) scheme defines $R_i$ to be a power series of $\mathcal{O}\left(\alpha_s/\pi\right)$ to cancel all the orders of poles in $\mathcal{O}\left(1/\epsilon\right)$ [65, 66]. For the quark self-energy example in Eqs. (2.27), one would have (for Feynman gauge $\xi = 1$)

$$Z_{2\mathrm{F}}^{(q)} = 1 + \frac{\alpha_s}{\pi}\frac{1}{3\epsilon},\ Z_4^{(q)} = 1 + \frac{\alpha_s}{\pi}\frac{4}{3\epsilon} \tag{2.38}$$

$$\Rightarrow \Sigma_{\mathrm{R}}(q) \sim \frac{\alpha_s}{\pi}\left[\left(-\log(4\pi) + \gamma_E + \log\frac{m^2}{\nu^2}\right) + f\left(\frac{q^2}{m^2}\right)\right] \tag{2.39}$$

free of divergence in MS scheme [44]. Another common QCD renormalization scheme is the modified minimal subtraction ($\overline{\mathrm{MS}}$) scheme [67]. As shown in the example of Eq. (2.27), $1/\epsilon$ always appear in the combination of $(1/\epsilon - \log 4\pi + \gamma_E)$. The $\overline{\mathrm{MS}}$ scheme is designed to eliminate these specific constants along with the poles by making the substitution of $\nu^2 \to \frac{\exp(\gamma_E)}{4\pi}\nu^2$. We will be using $\overline{\mathrm{MS}}$ scheme in this thesis.

The strict mathematical process of dimensional regularization and renormalization preserves the integrity of the original result and isolates the physical, finite, and measurable quantities. Therefore, the subtraction of divergences will not erase physical information. The chosen observables (*e.g.,* particle masses, cross-sections, scattering amplitudes and strong couplings) are finite after renormalization which ensure the alignment between theoretical predictions and experiments regardless the renormalization scheme of choice. One can find more detailed discussions on QCD renormalization in Refs. [44, 48, 68].

Note that all $Z_i$ in Eqs. (2.33) and (2.34) in the renormalizable theory of QCD represent local divergences, which are polynomials of $\mathcal{O}(1/q^2)$. When dealing with correlation functions of composite operators, divergences may not be simply removed by the addition of counter-term corrections ($R_i$) associated with Eqs. (2.33) and (2.34). These correlator divergences are referred to as non-local divergences, demanding the consideration of operator mixing. The renormalization for a composite operator $\mathcal{O}_i$ is

$$\mathcal{O}_{i,\mathrm{R}} = \sum_j Z_{ij}\, \mathcal{O}_{j,\mathrm{B}}, \tag{2.40}$$

where $Z_{ij}$ is the renormalization matrix, which encodes how mixing of operators $\mathcal{O}_{j,\mathrm{B}}$ contributes to the renormalization of $\mathcal{O}_{i,\mathrm{R}}$. It is also required that the dimension of $\mathcal{O}_{j,\mathrm{B}}$ must be smaller or equal to that of $\mathcal{O}_{i,\mathrm{R}}$ and that they have the same quantum numbers. As a result, $\dim(Z_{ij}) \geq 0$. The determination of $Z_{ij}$ not only includes the basic renormalization constants $Z_i$s in Eq. (2.34), but also depends on the valence quark and gluon content of the composite operator (current) in question. One needs to calculate the full Green's function including all the cross terms of bare operators with different renormalization factor combinations. For a detailed review of composite operator renormalization, see Refs. [68–71]. The counter-term corrections $R_{ij}$ from the $Z_{ij}$ matrix will lead to additional diagrams as by-products, to be included in the summation of all Feynman diagram for the prediction to be finite. In practice, the renormalization constant for gluonium current mixing with quantum number $J^{PC} = 2^{++}$ is applied in Sec. 3.2.4, generating two renormalization-induced diagrams that resolve divergences from all possible Feynman diagrams at two-loop order for the gluonium current correlator.

### 2.4.2 Diagrammatic Renormalization

Another renormalization approach is called the diagrammatic renormalization method. For each desired Feynman diagram, all possible sub-divergences of the diagram are extracted, and counter-term diagrams are constructed to be subtracted from the bare correlator. This

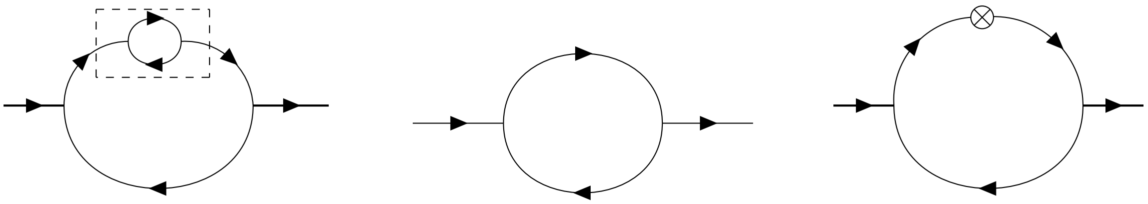

**(a)** bare diagram **(b)** sub-diagram **(c)** counter-term diagram

**Figure 2.6:** Diagrammatic renormalization procedure on fermion two-loop (NLO) diagram example. The possible sub-divergences of (a) are boxed using the dotted lines and isolated in (b). The $\otimes$ in (c) stands for the divergent part of the sub-diagram (b).

method eliminates non-local divergences, avoiding the complicated construction of renormalization factors for composite operators involving operator mixing. This method is introduced in detail in Ref. [72] for composite operator correlation functions.

In applying QCDSR (see Sec.2.5), all local divergences in loop integrals are considered. Diagrammatic renormalization targets non-local divergences which typically emerge at NLO (two-loop) correction. The procedure of diagrammatic renormalization for two-point correlation functions, in the assistance of QCDSR methodology, is outlined in Ref. [72]'s appendix. Figure 2.6 illustrates the steps of this method using a fermion self-energy two-loop diagram as an example. For each individual Feynman diagram, the process begins with constructing and evaluating all bare diagrams (see Fig. 2.6a). The dimensionally-regulated result is then filtered for non-local divergences. This involves identifying sub-parts of the diagram that carry external momentum. These sub-diagrams should includes at least one complete loop order (*e.g.,* Fig. 2.6b). If one Feynman diagram has more than one non-local divergences, all of the sub-diagram possibilities are required to be evaluated individually. From there, each sub-diagram is calculated, extracting only the divergent parts (sub-divergences). A counter-term diagram is then constructed by substituting the original sub-part with its corresponding sub-divergence, retaining finite parts and discarding the local contribution in the result (see Fig. 2.6c). Finally, the renormalized result for each Feynman diagram can be reached by subtracting counter-term diagram(s) from the bare diagram. The result of renormalized Green's function is the summation of all its renormalized Feynman diagrams. One may need to convert renormalization scale $\nu$ (from MS to $\overline{\text{MS}}$ scheme) for the running coupling and mass.

Both conventional and diagrammatic renormalization approaches are applied and compared in the case of $2^{++}$ di-gluonium NLO perturbative calculation in Sec. 3.2. The results from both approaches are identical, providing a robust verification of the calculations.

### 2.4.3 Renormalization Group Equation

The concept of renormalization group emerges from renormalization invariance, which states that the theoretical predictions of physical observables using different renormalization schemes can be transformed into each other [44]. If we expressed the relation between bare and renormalized Green's functions as

$$\mathcal{G}_{\mathrm{R}}(p_i, \alpha_s, \xi, m, \nu) = Z_{\mathcal{G}}(R_i)\, \mathcal{G}_{\mathrm{B}}(p_i, \alpha_s, \xi, m, \nu), \tag{2.41}$$

where $m$ is mass, $\xi$ is gauge parameter, $p_i = p_1, p_2, \cdots, p_N$ represents external momenta, $R_i$ is the renormalization scheme, and $\nu$ is the mass scale in the scheme. Then, the renormalized Green's functions founded in difference schemes, say $R_1$ and $R_2$, can be related to each other by $Z(R_1, R_2) \equiv Z(R_1)/Z(R_2)$.

The renormalization group (RG) equation describes how physical parameters behave at different energy scales. Since the reference energy scale $\nu$ is an artefact of dimensional renormalization, the bare Green's function is independent of $\nu$, giving:

$$\nu \frac{d}{d\nu}\, \mathcal{G}_{\mathrm{B}}(p_i, \alpha_s, \xi, m, \nu) = 0. \tag{2.42}$$

Taking derivative with respect to $\nu$ on both sides of Eq. (2.41) with the condition of (2.42) will lead to the basic RG equation

$$\left[\nu \frac{\partial}{\partial \nu} + \nu \frac{\mathrm{d}\alpha_s}{\mathrm{d}\nu} \frac{\partial}{\partial \alpha_s} + \frac{\nu}{m} \frac{\mathrm{d}m}{\mathrm{d}\nu} m \frac{\partial}{\partial m} + \nu \frac{\mathrm{d}\xi}{\mathrm{d}\nu} \frac{\partial}{\partial \xi} - \frac{1}{Z_{\mathcal{G}}} \nu \frac{\mathrm{d}Z_{\mathcal{G}}}{\mathrm{d}\nu}\right] \mathcal{G}_R(p_i, \alpha_s, \xi, m, \nu) = 0, \tag{2.43}$$

where the summation over quark flavour in $m$ is implicit. Generally, if the Green's function has $n = n_{\mathrm{YM}} + n_{\mathrm{F}} + \tilde{n}$ external lines from gluon, quark and ghost fields,

$$Z_{\mathcal{G}} = \left(Z_{3\mathrm{YM}}^{1/2}\right)^{-n_{\mathrm{YM}}} \left(Z_{2\mathrm{F}}^{1/2}\right)^{-n_{\mathrm{F}}} \left(\tilde{Z}_3^{1/2}\right)^{-\tilde{n}}. \tag{2.44}$$

A set of universal functions are introduced to compensate for the explicit $\nu$-dependence of the theory based on (2.43):

$$\nu\frac{\mathrm{d}\alpha_s}{\mathrm{d}\nu} \equiv \alpha_s\beta(\alpha_s,\xi,x), \tag{2.45}$$

$$\frac{\nu}{m}\frac{\mathrm{d}m}{\mathrm{d}\nu} \equiv -\gamma_m(\alpha_s,\xi,x), \tag{2.46}$$

$$\nu\frac{\mathrm{d}\xi}{\mathrm{d}\nu} \equiv \xi\,\delta(\alpha_s,\xi,x), \tag{2.47}$$

$$\frac{\nu}{Z_i}\frac{\mathrm{d}Z_i}{\mathrm{d}\nu} \equiv \gamma_i(\alpha_s,\xi,x), \tag{2.48}$$

where $x \equiv m/\nu$ and (2.48) depends on the field content. Equations (2.45) — (2.48) are obviously renormalization scheme dependent. All functions introduced above are independent of $x$ while $\beta$ is also gauge-independent in MS and $\overline{\text{MS}}$ schemes [44]. Suppressing all dependencies but $\alpha_s$, the RG equation can be rewritten into

$$\left[\nu\frac{\partial}{\partial\nu} + \beta(\alpha_s)\alpha_s\frac{\partial}{\partial\alpha_s} - \gamma_m(\alpha_s)m\frac{\partial}{\partial m} - \delta(\alpha_s)\xi\frac{\partial}{\partial\xi} - \gamma_{\mathcal{G}}\right]\mathcal{G}_R(p_i,\alpha_s,\xi,m,\nu) = 0, \tag{2.49}$$

with

$$\gamma_{\mathcal{G}} = -\frac{1}{2}\left[n_{\mathrm{YM}}\gamma_{\mathrm{YM}}(\alpha_s) + n_{\mathrm{F}}\gamma_{\mathrm{F}}(\alpha_s) + \tilde{n}\tilde{\gamma}(\alpha)\right], \tag{2.50}$$

where the anomalous dimensions $\gamma_{\mathrm{YM}}$, $\gamma_{\mathrm{F}}$ and $\tilde{\gamma}$ are defined by (2.48) via $Z_{3\mathrm{YM}}$, $Z_{2\mathrm{F}}$ and $\tilde{Z}_3$ respectively. The expressions of these anomalous dimensions are known and can be found such as in Refs. [44, 48].

In Sec. 2.2.2, we discussed the running coupling $\alpha_s(\nu)$ which is rooted from the RG equation. The strong coupling is dependent on the renormalization scale $\nu$ leading to the important QCD character of asymptotic freedom. Similarly, $\xi(\nu)$ and $x(\nu)$ are also running gauge parameter and running mass as functions of $\nu$ and of given initial values at certain energy. Those initial values act as boundary conditions so that one may find the running parameters at any value of energy scale. Some numerical values (in $\overline{\text{MS}}$-scheme) can be found in Ref. [7], such as

$$\begin{aligned}
&\alpha_s(M_\tau) = 0.317 \pm 0.016, \text{ with } M_\tau = 1776.93 \pm 0.09\,\text{MeV},\\
&\alpha_s(M_Z) = 0.1180 \pm 0.0009, \text{ with } M_Z = 91.1880 \pm 0.0020\,\text{GeV},\\
&m_s(\nu = 2\,\text{GeV}) = 93.5 \pm 0.8\,\text{MeV},\\
&m_c(\nu = m_c) = 1.2730 \pm 0.0046\,\text{GeV}.
\end{aligned} \tag{2.51}$$

To solve for $\beta$-function, hence the running $\alpha_s(\nu)$, in $\overline{\text{MS}}$ scheme, one needs to note that $\alpha_s$, which is defined in Eq. (2.28), subjects to its own renormalization constant $Z_\alpha$ that can be expressed with all the other $Z_i$ in the theory based on the Salvnov-Taylor identities in (2.36)

$$\alpha_s^{\text{B}} = Z_\alpha\, \alpha_s^{\text{R}}, \quad Z_\alpha = \tilde{Z}_1 \tilde{Z}_3^{-2} Z_{3\text{YM}}^{-1}. \tag{2.52}$$

Eq. (2.45) then gives [44, 48, 73]

$$\alpha_s^{\text{R}} \beta(\alpha_s^{\text{R}}, \epsilon) = \nu \frac{\mathrm{d}\alpha_s^{\text{R}}}{\mathrm{d}\nu} = \nu \frac{\mathrm{d}}{\mathrm{d}\nu}\left(\alpha_s^{\text{B}} Z_\alpha^{-1}\right) = 2\epsilon\, \alpha_s^{\text{R}} - \alpha_s^{\text{R}} \frac{1}{Z_\alpha} \nu \frac{\mathrm{d}Z_\alpha}{\mathrm{d}\nu} \tag{2.53}$$

in $\overline{\text{MS}}$ scheme. Since $Z_\alpha$ is indirectly dependent on $\nu$ through $\alpha_s^{\text{R}}$,

$$\beta(\alpha_s^{\text{R}}, \epsilon) = 2\epsilon - \frac{1}{Z_\alpha} \alpha_s^{\text{R}}\, \beta(\alpha_s^{\text{R}}, \epsilon)\, \frac{\partial Z_\alpha}{\partial \alpha_s^{\text{R}}}. \tag{2.54}$$

General expression of the coupling renormalization constant can be written in terms of pole expansion:

$$Z_\alpha = 1 + \sum_{n=1}^{\infty} Z_{\alpha,n}(\alpha_s^{\text{R}})/\epsilon^n. \tag{2.55}$$

Combining with [44]

$$\alpha_s^{\text{R}} \beta(\alpha_s^{\text{R}}, \epsilon) = 2\alpha_s^{\text{R}} \epsilon + \alpha_s^{\text{R}} \beta(\alpha_s^{\text{R}}) \tag{2.56}$$

due to QCD being a renormalizable theory, one finds to $1/\epsilon$ order,

$$\beta(\alpha_s^{\mathrm{R}}) = -2\,\alpha\,\frac{\partial Z_{\alpha,1}(\alpha_s^{\mathrm{R}})}{\partial \alpha_s^{\mathrm{R}}} \tag{2.57}$$

which can be used to find $\beta(\alpha_s^{\mathrm{R}})$. Using Eq. (2.52) to find $Z_\alpha$ to $1/\epsilon$ order:

$$Z_\alpha = 1 + \frac{\alpha_s^{\mathrm{R}}}{\pi}\left(\frac{11}{4} - \frac{n_f}{6}\right)\frac{1}{\epsilon} + \mathcal{O}\left(\frac{1}{\epsilon}\right)^2 \tag{2.58}$$

resulting $\beta$-function to the lowest order shown in Eq. (2.7). The mass anomalous dimension can be found in the similar manner

$$\gamma_m\left(\alpha_s\right) = \frac{\alpha_s}{\pi}\gamma_1 + \mathcal{O}\left(\frac{\alpha_s}{\pi}\right)^2, \quad \gamma_1 = 2. \tag{2.59}$$

Eq. (2.46) can be solved for the quark mass in leading order (see *e.g.,* Ref. [74])

$$m(\nu) = m(\overline{m})\left[\frac{\alpha_s(\nu)}{\alpha_s(\overline{m})}\right]^{\frac{12}{33-2n_f}}, \tag{2.60}$$

where $\overline{m}$ typically corresponds to $m(\overline{m})$ for heavy quarks or $2\,\mathrm{GeV}$ for light quarks, and the running coupling $\alpha_s(\nu)$ is shown in (2.8). The dependence of $n_f$ flavour states the running parameters also depends on the heaviest quark content of the target hadron in QCDSR (Sec. 2.5). For instance, $\alpha_s(M_\tau)$ in (2.51) corresponds to $n_f = 4$ energy region as $M_\tau$ is larger than $u, d, s, c$ quark masses, whereas for $n_f = 3$ range, the energy scale needs to satisfy $m_s \leq \overline{m} \leq m_c$. In Chapter 4, both the running coupling and the running of quark mass are studied across different $n_f$ regimes, as well as transitions between various energy regions, to identify the optimal energy scale that yields correlation function results providing the most restrictive constraints for the muon magnetic moment anomaly.

## 2.5 QCD Sum Rules

Due to asymptotic freedom, the QCD coupling $\alpha(\nu)$ is small at high energy scale (and short distance). The interaction can be described using perturbation theory as the perturbative contributions of the correlation function, which is proportional to $\mathcal{O}(\alpha_s/\pi)^{n-1}$, will converge quickly. Here $n$ stands for the number of loop correction order. Conversely, $\alpha_s(\nu)$ becomes large at a low energy scale, leading to the non-perturbative region of QCD. We, therefore, are in need to find a comprehensive approach that includes the large-distance interactions. Among many methods trying to tackle the low energy scales region including LQCD [75, 76] which discretizes spacetime into a lattice enabling numerical computation of path integral for quark and gluon fields with high-performance computing [75]. Effective field theories, on the other hand, use symmetries and relevant degrees of freedom to capture non-perturbative QCD effects. Examples include chiral perturbation theory [77] and heavy quark effective theory [78, 79]. There are also approaches such as topological solutions of instantons [80] and anti-de Sitter/conformal field theory correspondence [81], which provide approximate models for low energy QCD dynamics.

In the works included in this thesis, we will be using QCD spectral sum rules (or QCDSR) [82, 83] to obtain hadronic properties with parameters called *condensates*. Spectral sum rules, in general, relate integrals over spectral functions of hadronic correlators to QCD quantities using dispersion relations, which are rooted in principles of analyticity and causality. Such methods were employed even prior to the advent of QCD [84–86]. In the late 1970s, Shifman, Vainshtein and Zakhorov (SVZ) formulated the QCDSR [82, 83] by using operator product expansion (OPE) and applying the dispersion relations on current correlators. Reviews of QCDSR methodology can be found in Refs. [48, 87–89]. QCDSR relates the theoretical QCD quantities to the phenomenological hadronic quantities. This ability of QCDSR is called quark-hadron duality. The theoretical quark side of the relationship can be written in OPE of a hadronic two-point function consisted of a QCD perturbative series and non-perturbative contributions, the latter represented by condensates. The hadronic side is dependent on spectral functions, typically extracted from experimental data (*e.g.,* physical observables such as spectral densities reflecting resonances). Using this duality relation, one can determine physical quantities, such as hadron masses and current-hadron couplings, as demonstrated in the work presented in Chapter 3.

### 2.5.1 Operator Product Expansion (OPE)

A hadronic current, usually denoted $J(x)$, is a composite operator that encodes the valence quark and gluon field content and reflects hadronic quantum numbers $J^{PC}$. A composite operator is built by quantum fields of valence content at a space-time position, *e.g.,* $x$. A hadronic current relates QCD operators to hadronic states with same quantum numbers in order to evaluate the amplitude for the particle propagation or excitation between two positions. For a generic hadronic current $J(x)$, we have the two-point correlation function in momentum space as

$$\Pi(Q^2) = i \int d^4x e^{iq\cdot x} \langle\Omega| \mathcal{T} J(x) J(0)^\dagger |\Omega\rangle \,, \quad Q^2 \equiv -q^2 < 0, \tag{2.61}$$

similar to what we have seen in Eq. (2.24) for tenor gluonium current. While the high-energy regime of QCD can be effectively described using perturbation theory, the larger value of $\alpha_s$ at low-energy scales requires a non-perturbative approach. QCDSR uses OPE [44, 90]:

$$\langle\Omega| : O_1(x) O_2(y) : |\Omega\rangle = \lim_{x\to y} \sum_n C_n(x-y) \langle\Omega| : \mathcal{O}_n(y) : |\Omega\rangle \,, \tag{2.62}$$

to parametrize the non-perturbative effects by writing the uncontracted fields (such as $O_1(x)$ and $O_2(y)$) in Eq. (2.61) with non-zero vacuum expectation values (VEVs) as a series of local operator $\mathcal{O}_n$, which are called QCD condensates [44, 48]. All of these condensates are gauge-invariant and Lorentz-invariant which preserves the underlying symmetries of QCD [44]. The OPE applies for free scalar and spinor field theories, as well as renormalized interacting-field theories to all order in perturbation theory [44]. Here $C_n$ are c-number functions (also called Wilson coefficients) with $n$ indicating the canonical (mass) dimension of the local operator $\mathcal{O}_n$:

$$[\mathcal{O}_n] = M^n. \tag{2.63}$$

One can consider the high-energy region as the term with $\mathcal{O}_n \to \mathbf{I}$ (the unit operator), thus giving pure perturbative results. For example in Chapter 4, the two-point correlation

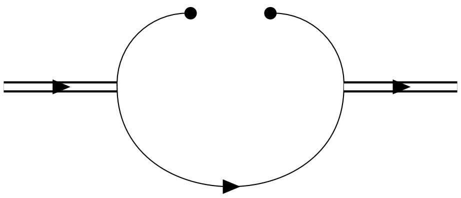

**Figure 2.7:** Example diagram for non-perturbative quark condensate contribution correspond to Eq. (2.64c). The bottom connected quark propagator corresponds to the contracted perturbative calculation. The disconnected nodes on the top half reflects the non-perturbative quark condensate $\langle \bar{q}q \rangle$.

function for the light quark vector current has the form of $J_\mu(x) = \bar{q}(x)\gamma_\mu q(x)$, the time-ordered product from the two point correlation function (2.61) can evaluated as below:

$$\mathcal{T}\{\bar{q}(x)q(x)q(0)\bar{q}(0)\} = \,:\bar{q}(x)q(x)q(0)\bar{q}(0): \qquad \text{disconnected diagram} \tag{2.64a}$$

$$+ :\wick{\c1{\bar{q}}(x)\c2{q}(x)\c1{q}(0)\c2{\bar{q}}(0)}: + \cdots \qquad \text{fully contracted} \tag{2.64b}$$

$$+ \wick{\c1{\bar{q}}(x)\c1{q}(0)} : q(x)\bar{q}(0) : + \cdots . \qquad \text{partially contracted} \tag{2.64c}$$

When sandwiched between fixed inital and final states, (2.64a) corresponds to the disconnected diagram, which is not of interest as discussed in Sec.2.2.3. The fully contracted terms (2.64b) provide pure perturbative contribution (*e.g.,* product of two quark-field propagators, $i^2 S(x)S(x)$) in the OPE. These are represented by the c-number function $C_0$ with the trivial : $\mathcal{O}_0 := \mathbf{I}$. Lastly, the partially contracted terms (2.64c) leave behind normal-ordered components, *i.e.,* condensates, with their time-ordered contracted components forming the c-number functions, such as:

$$C_4 \langle \Omega | : q(x)\bar{q}(0) : | \Omega \rangle \text{, with } C_4 = iS(x). \tag{2.65}$$

In Feynman diagrams, the normal-ordered condensates are represented with disconnected field lines (see Fig. 2.7).

The normal-ordered product in Eq. (2.65) can be expressed as a power series expansion in $x^\mu$

$$\langle \Omega | : q(x)\bar{q}(0) : | \Omega \rangle = \langle \Omega | : q(0)\bar{q}(0) : | \Omega \rangle + x^\mu \langle \Omega | : \partial_\mu q(0)\bar{q}(0) : | \Omega \rangle + \cdots . \tag{2.66}$$

The ordinary derivative $\partial_\mu$ in (2.66) is not gauge invariant contrary to the condensates. This can be solved using the fixed-point gauge technique [91, 92]

$$x^\mu \mathcal{A}^a_\mu(x) = 0, \text{ where } \mathcal{A}^a_\mu(x) = \int_0^1 \mathrm{d}a\, a\, G^a_{\rho\mu}(ax) x^\rho. \tag{2.67}$$

In this gauge $\mathcal{A}^a_\mu(x)$ can be written in terms of the gluon field strength tensor. With the fixed-point gauge simplification, $\mathcal{A}^a_\mu(x)$ can be expressed in an expansion with respect to $G^a_{\rho\mu}(ax)$ around $x^\mu = 0$. Because $\mathcal{A}_\omega(0) = 0$, we have the gauge condition

$$\partial_\omega G_{\omega\mu}(0) = x^\omega \left[D_\omega(0), G_{\omega\mu}(0)\right], \tag{2.68}$$

which allows us to rewrite the the expansion series with covariant derivatives as opposed to ordinary derivatives [44]. A similar approach can be applied to the quark field resulting in Taylor expansions with only covariant derivatives [93]. And there is no conflict between fixed-point gauge and covariant gauge approaches [94].

Higher order of $x^\mu$ terms in (2.66) correspond to higher dimensional condensates. In momentum space, the non-perturbative effect introduces power corrections of $1/Q^{2n}, (n \geq 1)$ to the perturbative contribution. This means higher dimensional condensate terms have smaller contribution to the correlator OPE at large enough energy. The condensates are low-energy contributions because they become important as $Q^2$ decreases. In our works, we typically truncate after dimension six condensate contributions (see Secs. 3.4 and 4.3). The important non-zero VEVs of the lowest dimension scalar operators includes [44]:

$$\begin{aligned}
&\text{Dimension 4:} \qquad && m_q\langle\bar{q}q\rangle \equiv \langle\Omega| : m_a \bar{q}^A_\alpha(0) q^A_\alpha(0) : |\Omega\rangle && \text{(2.69a)}\\
& && \langle\alpha_s G^2\rangle \equiv \langle\Omega| : \alpha_s G^{\mu\nu}_a(0) G^a_{\mu\nu}(0) : |\Omega\rangle && \text{(2.69b)}\\
&\text{Dimension 6:} && \langle G^3\rangle \equiv \langle\Omega| : f^{abc}\, G^{\mu\nu}_a(0)\, G^b_{\nu\rho}(0)\, G^{c\,\rho}_\mu(0) : |\Omega\rangle && \text{(2.69c)}\\
& && \langle\bar{q}q\rangle^2 \equiv \langle\Omega| : \bar{q}^A \gamma_\mu \lambda^a q^A \sum_B \bar{q}^B \gamma^\mu \lambda^a q^B : |\Omega\rangle && \text{(2.69d)}\\
& && \cdots &&
\end{aligned}$$

Of course, we also have the dimension zero unit operator **I** mentioned earlier in this section.

Note that the quark-antiquark dimension-four ($D = 4$) condensate (2.69a) only includes light quark contribution as the heavy quark current tends to contribute through perturbative or effective theory approaches due to their short lifetime and large mass comparing to the QCD scale $\Lambda_{\rm QCD}$ [95, 96]. Heavy quarks can show up in hybrid currents with gluon fields such as heavy quarkonium hybrids (*e.g.,* Refs. [51, 97]).

The values of the condensates in (2.69) can be found with a combination of QCD theory and experimental results. For example, the quark condensate (2.69a) can be found using the Gell-Mann–Oakes–Renner (GOR) relation $m_q\langle\bar{q}q\rangle = -\frac{1}{2}f_\pi^2 m_\pi^2$ for non-strange quarks by using current algebra and the assumption of partially conserved axial vector current [98]. The values of pion mass and decay constant are experimentally found and given in Table. 4.2 and Ref. [7]. The $\cdots$ in the last line refers to other higher dimension ($D > 4$) condensates such as the dimension-five quark-gluon mixed condensate $\langle\bar{q}\sigma_{\mu\nu}T^a G^{a\,\mu\nu}q\rangle$ and dimension-eight gluon condensates $\langle\big(f^{abc}G_a^{\mu\nu}G^b_{\rho\sigma}\big)^2\rangle$ and $\langle\big(f^{abc}G_a^{\mu\nu}G^b_{\nu\rho}\big)^2\rangle$ [44, 48].

Those condensate contributions in VEV form represents the non-perturbative components in the OPE. For the tensor di-gluonium correlator, its OPE in Ref. [14] is expressed as

$$q_{\rm T}(q^2) = iP_{\mu\nu\rho\sigma}\int d^4x e^{iq\cdot x}\,\langle\Omega|\,\mathcal{T}J^g_{\mu\nu}(x)J^g_{\rho\sigma}(0)^\dagger\,|\Omega\rangle \tag{2.70}$$

$$= C_1(q^2)\mathbf{I} + C_4(q^2)\langle\alpha_s G^2\rangle + C_6(q^2)\langle G^3\rangle + \cdots \tag{2.71}$$

where $J^g_{\mu\nu}$ is the gluonic current, $P_{\mu\nu\rho\sigma}$ is the projection operator, $C_1(q^2)$ is the perturbative contribution, $C_4(q^2)$ and $C_6(q^2)$ correspond to the c-number functions for $D = 4$ and $D = 6$ condensates. $C_n$ can be calculated perturbatively. In Chapter 3 while calculating the dimension-four condensate contributions, We also used the lowest-order expansions of the non-zero VEVs [94, 99–101],

$$
\begin{aligned}
\langle\Omega| : G^a_{\mu\rho}(x) G^b_{\nu\sigma}(0) : |\Omega\rangle &= \frac{\delta^{ab}}{8}\left\langle G^2\right\rangle \frac{1}{D^2-D}\left(g_{\mu\nu}g_{\rho\sigma}-g_{\mu\sigma}g_{\rho\nu}\right)\\
\langle\Omega| : f^{nmt} G^n_{\mu\nu}(x) G^m_{\rho\sigma}(y) G^t_{\omega\tau}(0) : |\Omega\rangle &= \left\langle G^3\right\rangle \frac{1}{D(D-1)(D-2)}\left(g_{\mu\rho}g_{\nu\omega}g_{\sigma\tau}-g_{\nu\rho}g_{\mu\omega}g_{\sigma\tau}\right.\\
&\quad - g_{\mu\sigma}g_{\nu\omega}g_{\rho\tau}+g_{\nu\sigma}g_{\mu\omega}g_{\rho\tau}-g_{\mu\rho}g_{\nu\tau}g_{\sigma\omega}\\
&\quad \left.+g_{\nu\rho}g_{\mu\tau}g_{\sigma\omega}+g_{\mu\sigma}g_{\nu\tau}g_{\rho\omega}-g_{\nu\sigma}g_{\mu\tau}g_{\rho\omega}\right)\\
\langle\Omega| : \left[D_\mu,\left[D_\nu,G_{\rho\sigma}\right]\right] G_{\omega\tau} : |\Omega\rangle &= -\frac{g^3\left\langle G^3\right\rangle}{2D\left(D^2-4\right)}\left(2g_{\mu\nu}\left(g_{\rho\omega}g_{\sigma\tau}-g_{\sigma\omega}g_{\rho\tau}\right)\right.\\
&\quad + g_{\nu\tau}\left(g_{\rho\omega}g_{\sigma\mu}-g_{\sigma\omega}g_{\rho\mu}\right)-g_{\nu\omega}\left(g_{\rho\tau}g_{\sigma\mu}-g_{\sigma\tau}g_{\rho\mu}\right)\\
&\quad \left.-\frac{3}{D-1}\left(g_{\mu\tau}\left(g_{\rho\omega}g_{\sigma\nu}-g_{\sigma\omega}g_{\rho\nu}\right)-g_{\mu\omega}\left(g_{\rho\tau}g_{\sigma\nu}-g_{\sigma\tau}g_{\rho\nu}\right)\right)\right).
\end{aligned}
\tag{2.72}
$$

### 2.5.2 Dispersion Relation

The methodology of QCDSR is based on a Källén-Lehmann dispersion relation [102–104] and will be derived analytically in this section. For a more detailed derivation, see Ref. [88]. Beginning with the two-point correlation functions of the composite operators, we use the residue theorem for the contour integral $\Pi(Q^2)$ with chosen contour $C$ shown in Fig. 2.8:

$$
\begin{aligned}
\Pi(Q^2) &= \oint_C \frac{\mathrm{d}z}{2\pi i}(Q^2)^n \frac{\Pi(z)}{z^n(z-Q^2)}\\
&= \frac{(Q^2)^n}{2\pi i}\left(\oint_{|z|=R\to\infty} \mathrm{d}z\,\frac{\Pi(z)}{z^n(z-Q^2)}+\oint_{|z|=\delta}\mathrm{d}z\,\frac{\Pi(z)}{z^n(z-Q^2)}\right.\\
&\quad \left.+\int_0^{R\to\infty}\mathrm{d}z\,\frac{\Pi(z-i\epsilon)-\Pi(z+i\epsilon)}{z^n(z-Q^2)}\right), \quad \epsilon\to 0^+.
\end{aligned}
\tag{2.73}
$$

As the radius $R$ of the first subcontour in $Q^2$-space goes to infinity, the first term (large circle part) in the second line of (2.73) will vanish. The second integral involves the subcontour of a small circle around the origin with radius $\delta \to 0^+$ and leads to $Q^2$ polynomials to order of $n$ at the origin. For the integral in the third line (above and below the branch cut),

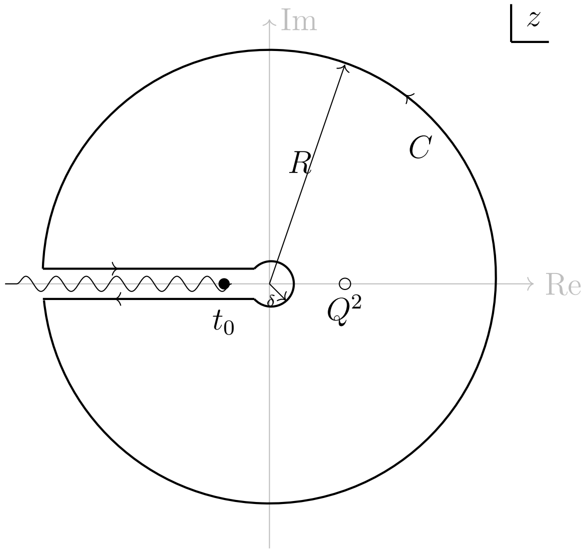

**Figure 2.8:** The integral contour $C$ in the complex $z = Q^2$ plane for the Källén-Lehmann dispersion relation derivation. The integral poles $\{0, Q^2\}$; large circular contour radius $R$; small circular contour with radius $\delta$ are marked. The wavy line represents the correlator branch cut with hadronic threshold $t_0$ as the branch point.

we can use the Schwarz reflection [105] (also indicated by the contour figure), which gives

$$\underbrace{\Pi(z - i\epsilon)}_{\text{bottom}} - \underbrace{\Pi(z + i\epsilon)}_{\text{top}} = i2\,\mathrm{Im}\Pi(z). \tag{2.74}$$

Therefore, we have the dispersion relation

$$\begin{aligned}\Pi(Q^2) = &\underbrace{\Pi(0) + Q^2\Pi'(0) + \frac{1}{2}Q^4\Pi''(0) + \cdots + \frac{1}{n}Q^{2n}\Pi^{(n)}(0)}_{\text{subtraction terms}} \\ &+ (-Q^2)^{n+1}\frac{1}{\pi}\int_{t_0}^{\infty} dt\frac{\mathrm{Im}\,\Pi(t)}{t^{n+1}(t+Q^2)},\end{aligned} \tag{2.75}$$

where the $(-1)^{n+1}$ in the last term is from the change of integration variable $t = -z$, $\Pi^{(n)}(0) = \frac{\mathrm{d}^n}{\mathrm{d}(Q^2)^n}\Pi(Q^2)|_{Q^2=0}$ and $t_0$ is the hadronic threshold. The subtraction terms are polynomials of $Q^2$. The number of the subtraction terms (as in how big $n$ is needed to be) depends on the asymptotic behaviour of $\Pi(Q^2)$. The faster $\Pi(Q^2)$ falls at large $Q^2$, the fewer subtractions are needed.

The relationship between the hadronic spectral function $\rho^{\mathrm{had}}(t)$ and the imaginary part of the correlation function can be introduced in the framework of quark-hadron duality: [48,88]

$$\frac{1}{\pi}\mathrm{Im}\Pi(t) = \rho^{\mathrm{had}}(t), \tag{2.76}$$

which enable the relation of $\mathrm{Im}\,\Pi(t)$ through hadronic physics.

For an intermediate conclusion, one has the a dispersion relation from Eqs. (2.75) and (2.76) that can be related to the OPE form Sec 2.5.1:

$$\begin{aligned} C_1(Q^2)\mathbf{I} + C_{4q}(Q^2)m_q\langle\bar{q}q\rangle + C_{4g}(Q^2)\langle\alpha_s G^2\rangle + C_{6g}(Q^3)g^3\langle G^3\rangle + \cdots \\ = \Pi(0) + Q^2\Pi'(0) + \frac{1}{2}Q^4\Pi''(0) + \cdots + \frac{1}{n}Q^{2n}\Pi^{(n)}(0) \\ + (-Q^2)^{n+1}\int_{t_0}^{\infty} dt\frac{\rho^{\mathrm{had}}(t)}{t^{n+1}(t+Q^2)}, \end{aligned} \tag{2.77}$$

where $C_{4q}, C_{4g}, C_{6g}$ are c-number functions for dimension-four and six quark/gluon condensates. Equation (2.77) has the correlation function with suitable composite operators calculated by OPE on the LHS and hadronic spectral function from experimental model representing the phenomenological side of the equation on RHS. The dispersion relation hence encode the quark-hadron duality in QCDSR.

### 2.5.3 Hadronic Spectral Function

Typically, the hadronic spectral function $\rho^{\mathrm{had}}(t)$ is related to the particle process at hand. For example, for light quark vector current $J_\mu(x) = \bar{q}\gamma_\mu q$ appearing in Chapter 4, the spectral function is related to the $e^+e^- \to$ Hadrons total cross section through optical theorem with hadronic $R$-ratio [106, 107]:

$$R(t) = \frac{\sigma(e^+e^- \to \mathrm{Hadrons})}{\sigma(e^+e^- \to \mu^+\mu^-)} \propto \mathrm{Im}\,\Pi(t). \tag{2.78}$$

Figure 2.9 shows the experimental measurement $R(t)$ in the light quark energy sector. One can depict the $R(t)$ behaviour using resonance models for $\rho^{\mathrm{had}}$. The minimal duality ansatz (MDA), also known as single narrow resonance model, parametrizes the hadronic

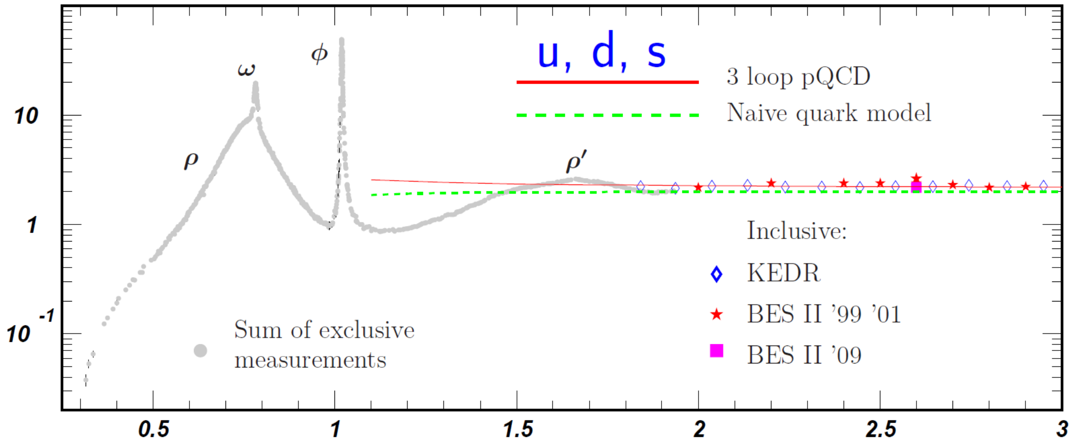

**Figure 2.9:** Total cross section ratio $R(t)$ in the light-flavour threshold region verses $e^+e^-$ collision energy $\sqrt{t}$ in GeV figure from Ref. [108]. The plot in gray is experimental data. The continuum threshold $s_0$ locates around 1.4 GeV separating the resonance region ($2m_\pi < s_0 < \mathcal{O}(1.4)$ GeV) and continuum region ($\mathcal{O}(1.4)$ GeV $< s_0 < 3$ GeV). Notice that the QCD continuum region also includes some higher-energy excitations (*e.g.*, $\rho'$ hadron). The resonance region includes peaks corresponding to $\rho$, $\omega$ and $\phi$ hadron masses. The red line is 3-loop perturbative QCD prediction which gives a good description of the continuum $R(t)$. The gap between $\phi$ and $\rho$ resonances are included in the QCD prediction in the sense of global integrated average, reflecting the quark-hadron duality nature of QCDSR.

spectral function to isolate the mass and coupling properties of the ground state [89]:

$$\rho^{\text{had}} = \rho^{\text{res}}(t) + \rho^{\text{cont}}(t)\Theta(t - s_0),\ \rho^{\text{cont}} = \frac{1}{\pi}\,\text{Im}\,\Pi^{\text{QCD}}(t), \tag{2.79}$$

where $\Theta(t - s_0)$ is a Heaviside step function, $s_0 > t_0$ is the threshold of the lowest continuum state, and the relation between continuum part of spectral function and imaginary part of correlator is from the optical theorem [31]. $\rho^{\text{had}}(t)$ is separated into two parts based on energy sector:

- a resonance piece $\rho^{\text{res}}(t)$ reflecting low-energy region describing resonance phenomenology;
- and a QCD continuum piece with $\rho^{\text{cont}} = \frac{1}{\pi}\,\text{Im}\,\Pi^{\text{QCD}}(t)$ reflecting behaviour in higher-energy sector above $s_0$ (*i.e.*, $s_0 < t < \infty$), which is explicitly marked here showing it can be evaluated using OPE through QCD [48].

$\rho^{\text{res}}(t)$ can be modelled based on the hadronic process in study, or measured experimentally.

For instance, MDA represents the pole in spectral density as a narrow resonance using

$$\rho^{\mathrm{res}}(t) = f_H^2 M_H^{2d} \delta(t - M_H^2), \tag{2.80}$$

where $f_H$ is the hadronic coupling with mass dimension of the hadronic current's ground state, $d$ is the power of $t$ in the spectral function asymptotic behaviour, and $M_H$ is the resonance mass for the ground state.

### 2.5.4 Borel Transform

The dispersion relation (2.77) bridges theoretical and phenomenological aspects of the correlation function. In order to retrieve hadronic parameters of target particle processes, such as masses and couplings, one ought to solve two problems. First, the terms $\Pi^{(n)}(0)$ are divergent subtraction constants that do not contribute physically to the QCDSR and are, in general, unknown. Those $Q^2$ polynomials are called local divergences and need to be eliminated. Secondarily, LHS of (2.77) are typically considered in the limit $Q^2 \to 0$ in order to capture the non-perturbative effects by condensates, yet the RHS is only a good approximation in $Q^2 \to \infty$ limit. When QCDSR is appropriately averaged, one can find a compromise middle-ground value (*e.g.*, $Q^2 \simeq 1\,\mathrm{GeV}^2$). To further refine the approximation and eliminate subtraction terms, one can apply both sides of the sum rule the Borel transformation [83]:

$$\hat{\mathcal{B}} \equiv \lim_{\substack{Q^2\to\infty, N\to\infty, \\ Q^2/N = M_B^2}} \frac{1}{\Gamma(N)} (-Q^2)^N \left(\frac{\mathrm{d}}{\mathrm{d}Q^2}\right)^N, \tag{2.81}$$

where $M_B$ is called Borel mass and is a fixed value. This transformation removes the $Q^2$-polynomial subtraction terms by taking sufficient derivatives with respect to the Euclidean momentum $Q^2$. Hence the Borel transform is perfect for this purpose and it has the following identities [44]

$$\hat{\mathcal{B}}[Q^{2k}] = 0, \quad \hat{\mathcal{B}}\left[\frac{1}{(t+Q^2)^k}\right] = \tau^k \frac{1}{\Gamma(k)} e^{-t\tau}, \quad \hat{\mathcal{B}}\left[\frac{Q^{2k}}{t+Q^2}\right] = \tau(-t)^k e^{-t\tau}, \tag{2.82}$$

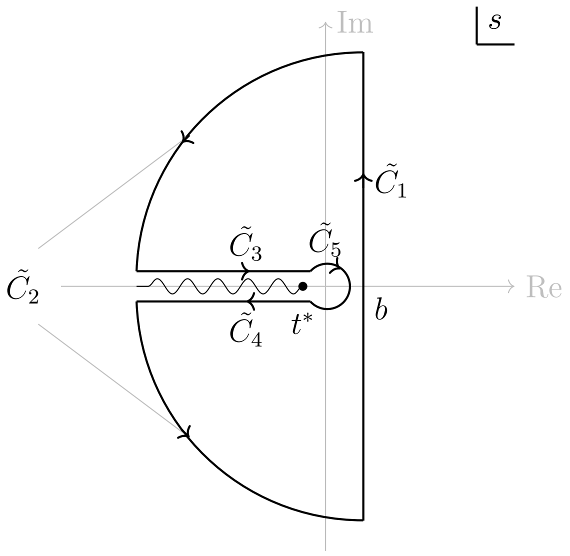

**Figure 2.10:** The integral contour $\tilde{C}$ in the complex $s = Q^2$ plane for the inverse LSR integral. The wavy line represents the branch cut with QCD threshold $t^*$ as the branch point.
Contour $\tilde{C}$ are divided into five sections: $\tilde{C}_1$ straight line at $Re(Q^2) = b$ that goes from negative to positive in imaginary space; $\tilde{C}_2$ large circular contour with radius $R$; $\tilde{C}_3$ and $\tilde{C}_4$ line contour above and below the branch cut with their imaginary parts $\epsilon \to 0$; $\tilde{C}_5$ small circular contour with radius $\delta$.
The line integral in (2.85) corresponds to contour section $\tilde{C}_1$ can be found using the integration over the remaining pieces of the contour based on Cauchy's theorem:
$\oint_{\tilde{C}} ds\, e^{\tau s} f(s) = 0 \Rightarrow \int_{\tilde{C}_1} ds\, e^{\tau s} f(s) = -\sum_{i=2}^{5} \int_{\tilde{C}_i} ds\, e^{\tau s} f(s)$.

where Borel parameter $\tau = 1/M_B^2$ and $k > 0$. Applying the Borel transform on Eq. (2.77) using identities in Eq. (2.82)

$$\frac{\hat{\mathcal{B}}}{\tau} \left[ (-Q^2)^k \Pi(Q^2) \right] = \int_{t_0}^{\infty} t^k e^{-t\tau} \rho^{\text{had}}(t) \text{d}t, \tag{2.83}$$

we reach a more convenient form of QCDSR with local divergences removed and hadronic spectral function being weighted by an exponential function $e^{-t\tau}$ emphasizing lower-energy region and suppressing continuum contribution to study the ground state resonance. This exponential function is playing the role of a Kernel function $K(\tau, t)$ which varies depending on the category of the spectral sum rule of interest.

### 2.5.5 Laplace Sum Rules

Eq. (2.83) is also known as Borel/Laplace sum rules (LSR):

$$\mathcal{L}_k(\tau) = \int_{t_0}^{\infty} t^k e^{-t\tau} \rho^{\text{had}}(t) \mathrm{d}t, \quad k \geq 0. \tag{2.84}$$

The name comes from the relation between Borel transform and inverse Laplace transform $\mathcal{L}^{-1}$ [44, 109, 110]

$$\frac{\hat{\mathcal{B}}}{\tau} \left[ f(s) \right] = \mathcal{L}^{-1} \left[ f(s) \right] = \frac{1}{2\pi i} \int_{b-i\infty}^{b+i\infty} \mathrm{d}s \, e^{\tau s} f(s), \tag{2.85}$$

where $b$ here is chosen to be larger than any pole or branch structure of the correlation function so that the contour of the LSR integral can be evaluated in the similar manner as Eq. (2.73) with Cauchy's theorem (see contour $\tilde{C}$ in Fig. 2.10).

Substituting (2.79) into (2.84):

$$\mathcal{L}_k(\tau) = \int_{t_0}^{\infty} t^k e^{-t\tau} \rho^{\text{res}} \, \mathrm{d}t + \int_{s_0}^{\infty} t^k e^{-t\tau} \frac{1}{\pi} \, \mathrm{Im} \, \Pi^{\text{QCD}}(t) \, \mathrm{d}t \,, \tag{2.86}$$

where both $\mathcal{L}_k(\tau)$ and the QCD continuum contribution can be theoretically determined through QCD. Rearranging them, we reach another common form of the sum rule:

$$\mathcal{R}_k(\tau, s_0) \equiv \mathcal{L}_k(\tau) - \int_{s_0}^{\infty} t^k e^{-t\tau} \frac{1}{\pi} \, \mathrm{Im} \, \Pi^{\text{QCD}}(t) \, \mathrm{d}t \tag{2.87}$$

$$= \int_{t_0}^{\infty} t^k e^{-t\tau} \rho^{\text{res}}(t) \, \mathrm{d}t \,, \quad k \geq 0, \tag{2.88}$$

where the QCD quantity $\mathcal{R}_k(\tau, s_0)$ is related to phenomenological $\rho^{\text{had}}$, $s_0$ separates the resonance parameters and continuum sectors, and $t_0$ is the threshold of the minimum energy squared required for the physical process to occur. When working with light quark vector currents in Chapter 4, $t_0$ is set to $t_0 = 2m_\pi^2$, as two pions are the lightest possible state that can be created. When evaluating tensor di-gluonium in Chapter 3, a specific value for $t_0$ is not needed in the LSR analysis, as we adopted the narrow resonance model.

The upper bound of (2.88) is sometimes taken as $s_0$ such as in Ref. [21] to express a cut-off before continuum in energy spectrum for analysis. If one is using the narrow resonance model (2.79), then the choice of the upper limit between $s_0$ and $\infty$ will not make any significant difference. In other $\rho^{\text{had}}$ models, such as a Breit-Wigner (first used in Ref. [111]) or a Gaussian distribution model (*e.g.,* Ref. [112]), the resonance width is much larger and $\rho^{\text{res}}$ contribution may bleed into the continuum region.

Applying the MDA parametrization in Eqs. (2.79) and (2.80) on (2.88), we get

$$\mathcal{R}_k(\tau, s_0) = f_H^2 M_H^{2d+2k} e^{-M_H^2 \tau}. \tag{2.89}$$

This combination of duality model and sum rule is very useful to extract hadronic mass by using adjacent weights $k$

$$\frac{\mathcal{R}_{k+1}(\tau, s_0)}{\mathcal{R}_k(\tau, s_0)} = M_H^2. \tag{2.90}$$

A strict upper bound for $M_H$ can be found by taking $s_0 \to \infty$: $M_H^2 \leq \mathcal{R}_{k+1}(\tau, \infty)/\mathcal{R}_k(\tau, \infty)$ [83, 113]. One can also easily isolate the coupling constant $f_H$ from (2.88) for analysis:

$$f_H^2 = e^{M_H^2 \tau} \mathcal{R}_k(\tau)/M_H^{2d+2k}, \tag{2.91}$$

with $M_H$ determined by Eq. (2.90).

### 2.5.6 Optimization Criterion

Although one has a rough idea on finding hadronic mass and current resonance coupling using $\sqrt{\mathcal{R}_{k+1}/\mathcal{R}_k}$ (2.90) and $\mathcal{R}_k$ (2.88), the involved QCDSR are functions dependent on key variables: the QCD continuum threshold $s_0$, which characterizes the structure of the hadronic spectral function, and the Borel parameter $\tau$, introduced through the Borel transform. These two free parameters play a crucial role in setting restrictions on the sum rule, ensuring the accuracy and reliability of the results.

With a given $s_0$ value, one can find a range for $\tau$ using two requirements from each side of QCDSR:

- On the QCD side, OPE terms should converge. One needs to ensure the OPE convergence when higher-dimensional non-perturbative term are considered. That means the OPE should be dominated by perturbation theory calculation and condensate contribution should weigh lesser as their dimension goes higher. Since condensate contribution correspond to low-energy region, *i.e.,* small $M_B$ values, it is suitable to set an upper bound for $\tau = 1/M_B^2$ based on when condensate remain as relatively small corrections to OPE.

- On the hadronic side of QCDSR, one wants to avoid large uncertainties introduced by continuum approximation. Thus, the resonance contribution for the ground state should be larger than the continuum contribution. Since the QCD continuum becomes more significant at high-energy scale, or large $M_B$ values, one can find a lower bound for $\tau$ given a value of $s_0$.

The constraint formed by above upper and lower bounds on $\tau$ is called *the Borel window*, in which QCDSR is considered to be reliable with reasonable continuum and condensate contributions to the sum rule. In the original SVZ sum rule papers, these bounds $(\tau_{\min}, \tau_{\max})$ are found by numerically setting fixed values for contribution percentage [82, 83]. They can also be determined using Hölder Inequalities [114]:

$$\mathcal{R}_0\left(\omega\tau_{\min} + (1-w)\tau_{\max}, s_0\right) \leq \mathcal{R}_0^{\omega}\left(\tau_{\min}, s_0\right)\mathcal{R}_0^{1-\omega}\left(\tau_{\max}, s_0\right), \tag{2.92}$$

$$\mathcal{R}_1\left(\omega\tau_{\min} + (1-w)\tau_{\max}, s_0\right) \leq \mathcal{R}_1^{\omega}\left(\tau_{\min}, s_0\right)\mathcal{R}_1^{1-\omega}\left(\tau_{\max}, s_0\right), \tag{2.93}$$

where $0 \leq \omega \leq 1$, $\tau_{\min} \leq \tau_{\max}$, and sum rules' weights $0 < k < 2$ are favoured to avoid introducing poorly understood higher dimensional QCD condensates.

Within the Borel window for $\tau$, one can look at the other free parameter $s_0$ from phenomenology and search for its value where optimal resonance information can be extracted from sum rule. The $\tau$-stability condition

$$\frac{\mathrm{d}}{\mathrm{d}\tau} M_H(\tau, s_0) = 0 \tag{2.94}$$

gives the minimum value for $s_0$ at which $M_H(\tau, s_0)$ depends least on the Borel parameter. In practice, the sum rule doesn't always have a good minimum within Borel window and one can choose an inflexion point reflecting optimal resonance information, which also satisfies the stability condition. Within a stable sum rule, the upper bound of continuum threshold can be found when $M_H(\tau, s_0)$ presents stability with respect to $s_0$ given a $\tau$ inside the Borel window (for a review, see *e.g.,* Refs. [48, 89, 115, 116]).

Technically speaking, there is one more free parameter that affects the sum rule optimization: the subtraction point $\mu$ in perturbative QCD at which the series from perturbation theory are evaluated. This $\mu$ is related to QCD renormalization and taken as $\mu^2 = 1/\tau$ in the light-quark systems (see *e.g.,* Ref. [117]). There are more complicated behaviour of $\mu^2$ that affects sum rule analysis when involve heavy-quark content (see *e.g.,* Refs. [118, 119]).

In Chapter 3, both mass and coupling of the ground state of $J^{PC} = 2^{++}$ tensor digluonium were computed and analysed using LSR with MDA parametrization.

In Chapter 4, an approach using QCD LSR is performed to find constraints on muon anomalous magnetic moment in Sec. 4.3.4. Although the results are weaker than our primary approach of Finite-Energy sum rules, the additional LSR analysis ensures the robustness of our methodology.

### 2.5.7 Finite-Energy Sum Rules

The definition of finite-energy sum rules can be derived from LSR at $\tau \to 0$ limit (equivalently, the high-energy limit $M_B \to \infty$). By taking a small $\tau$ expansion for Eq. (2.88):

$$F_k(s_0) = \int_{t_0}^{s_0} \mathrm{d}t\, t^k \frac{1}{\pi} \mathrm{Im}\Pi^{\mathrm{H}}(t), \tag{2.95}$$

where $k \geq 0$ is the weight (or degree) of the sum rule. FESR is a type of spectral sum rules that exists before its application to QCD (*e.g.,* see Refs. [120–122]). It can also be derived using, again, Cauchy's theorem with the same contour $C$ in Fig. 2.8 with the integrals below [123]:

$$\frac{1}{2\pi i}\oint_C \mathrm{d}z\, z^n \Pi(z) = 0, \quad n = 0, 1, \cdots \tag{2.96}$$

$$\frac{1}{2\pi i}\left(\oint_{|z|=R} \mathrm{d}z\, z^n \Pi(z) + \oint_{|z|=\delta} \mathrm{d}z\, z^n \Pi(z) + \int_0^R \mathrm{d}z\, z^n\, 2i\, \mathrm{Im}\,\Pi(z)\right) = 0. \tag{2.97}$$

Only this time, we don't have the $Q^2$ pole and we take $R = s_0$. Similar to the process in Eqs. (2.73) and (2.74), the last term in (2.97) is form the paths above and below the branch cut on real axis which lead to the $\Pi(Q^2)$ discontinuity and application of the Schwarz reflection. The smaller circular integral goes to zero at $\delta \to 0$ limit. The FESR then yields

$$F_k(Q^2) \equiv \int_0^{R=s_0} \mathrm{d}t\, t^k \frac{1}{\pi}\, \mathrm{Im}\,\Pi(t) = \frac{(-1)^{k+1}}{2\pi} s_0^{k-1} \int_{-\pi}^{+\pi} \mathrm{d}\theta\, e^{i(k+1)\theta}\, \Pi(Q^2), \qquad \text{with } Q^2 = s_0\, e^{i\theta} \tag{2.98}$$

where RHS is from the large circular contour with radius $s_0$ which must be larger than any quark mass in $\Pi(Q^2)$ calculation [48, 124, 125]. The matching of LHS and RHS of Eq.(2.98) results in the sum rule. Comparing to LSR as an exponential sum rule, FESR has a polynomial Kernel function and is governed by high $s_0 = |Q^2|$ region on the real axis, especially when $k$ increases. When applying the sum rules to correlation functions, the FESR will typically give higher QCD continuum threshold $s_0$ than LSR because the higher-mass resonances in LSR are exponentially suppressed compared to FESR (see examples in Refs. [48, 126]). One ought to proceed with caution at high-energy part of the spectral function when using FESR.

In Chapter 4, we are interested in the structural similarity between FESR (2.95) and the approximate form of leading-order hadronic vacuum polarization contribution to muon anomalous magnetic moment ($a_\mu^{\mathrm{HVP,LO}}$), which we utilize to relate $a_\mu^{\mathrm{HVP,LO}}$ to sum rule analysis in order to find its constraints with QCDSR methodology.

# 3 $J^{PC} = 2^{++}$ Tensor Di-gluonium

The publication presented in this chapter is Ref. [14]:

$2^{++}$ ***Tensor di-gluonium from Laplace sum rules at NLO***
**Siyuan Li, Stephan Narison, Tom Steele, Davidson Rabetiarivony,**
**Phys. Lett. B 849, 138454 (2024), doi:10.1016/j.physletb.2024.138454**

This published research improves the accuracy in $2^{++}$ tensor di-gluonium mass predictions via the correlator, and thus to help interpreting experimentally-observed $J^{PC} = 2^{++}$ tensor mesons $f_2(2010, 2300, 2340)$ listed by the Particle Data Group.

A brief research motivation is included in Sec. 3.1. In Sec. 3.2, required Feynman rules are calculated and the $J^{PC} = 2^{++}$ tensor di-gluonium two-point correlator is evaluated to the NLO perturbative corrections. The results for all the NLO Feynman diagrams are renormalized using both conventional and diagrammatic renormalization, and the agreement between these approaches provides a robust verification of our findings. In the following Sec. 3.3, the dimension-four and dimension-six condensate contributions are calculated using plane-wave, coordinate-space, and RG equation methods, with the consistency among these different techniques further confirming the reliability of the results. The manuscript of Ref. [14] is included in Sec. 3.4. Results from Secs. 3.2 and 3.3 are reflected in Sec. 3.4.3-3.4.5 of the publication.

My contributions to Ref. [14] relate heavily to the perturbation theory. For the target two-point function, I derived the necessary Feynman rules and constructed the Feynman integrals. Using conventional and diagrammatic renormalization approaches, I calculated, compared, and confirmed the perturbative contribution to the NLO corrections, designed the result table and edited the manuscript. Additionally, I also performed dimension-four and dimension-six gluon condensates calculation using the three techniques mentioned above.

## 3.1 Motivation for Tensor Di-gluonium

In QCD, gluonium is a hadronic configuration exclusively composed of gluons due to the nature of gluons carrying colour charges (see Refs. [11–13] for reviews on glueballs). The name of "tensor di-gluonium" suggests:

1. It is a bound state composed of two gluons ($gg$), each carrying spin-1.

2. It has spin quantum number $S = 2$ yielding $J = 2$, corresponds to a rank-2 tensor (*e.g.,* polarizations states, QCDSR operators).

This can be understood through the definitions of orbital, spin, and total angular momenta (see Appendix C). To have both positive parity ($P$) and positive charge conjugation ($C$), one finds $L = 0$. Thus, $J^{PC} = 2^{++}$ is expected to be the ground state of the spin-2 gluon systems.

The spin-2 state, $J = 2$, is the first non-trivial spin for di-gluonium (compared to $J = 0$), and it holds significant experimental relevance. Spin-0 particles are challenging to detect because they share the same spin as the vacuum, making $J = 2$ particles more observable due to their distinct angular distributions (and corresponding decay products) [12, 127].

The existence of gluonia remains theoretical, with experimental and theoretical searches ongoing, heavily due to the mixing of gluonium states with nearby meson states. Radiative $J/\Psi$ decays have proven to be a promising method to investigate gluonium, as theoretical predictions suggest the lowest-lying mass for gluonia to be between $1 - 3$ GeV [128–131]. A recent experimental determination by BESIII [132] identified the $X(2370)$ particle as a pseudoscalar gluonium candidate with quantum numbers $J^{PC} = 0^{-+}$ also using the $J/\psi$ decay mechanism. For our research, the PDG lists three resonances for $J^{PC} = 2^{++}$ tensor mesons — $f_2(2010, 2300, 2340)$[1] [7, 108].

Building on the work of [133] on the $2^{++}$ tensor di-gluonium, we have extended the calculation to the NLO corrections of perturbative QCD and to dimension-eight gluon condensates. The primary motivation for this research is that tensor gluonium with quantum

---

[1] see Appendix. C.1 for PDG naming scheme.

number $2^{++}$ is one of the few gluonium particles that have not been studied in QCDSR beyond LO perturbation theory, primarily due to the complexity of its calculation. Our goal is to advance the theoretical understanding of tensor gluonia and fill in this last missing piece of the gluonium puzzle.

## 3.2 Perturbative Contribution Calculation

### 3.2.1 Feynman rules for Tensor Gluonium

In order to study the $2^{++}$ gluonium, we shall start with its two-point correlator [131]:

$$\begin{aligned}\psi^T_{\mu\nu\rho\sigma} &\equiv i\int d^4x e^{iqx}\left\langle 0\left|\mathcal{T} J^g_{\mu\nu}(x) J^g_{\rho\sigma}(0)^\dagger\right| 0\right\rangle \\ &= P_{\mu\nu\rho\sigma}\psi_T\left(q^2\right) + \cdots ,\end{aligned} \tag{3.1}$$

where $\cdots$ stands for the possible lower spins' contributions, $P_{\mu\nu\rho\sigma}$ is the spin-2 projection operator (see (3.3) below) and $J^g_{\mu\nu}(x)$ is the gluonic currents that are built from the gluon fields [131]:

$$J^g_{\mu\nu} = -G_\mu^{\ \alpha,a} G_{\nu\alpha,a} + \frac{1}{4} g_{\mu\nu} G^a_{\alpha\beta} G^{\alpha\beta}_a . \tag{3.2}$$

Extending of the 4-dimensional results in [134], the D-dimensional version of the projection operator shown in [131] and [128] has the form

$$P_{\mu\nu\rho\sigma} = \eta_{\mu\rho}\eta_{\nu\sigma} + \eta_{\mu\sigma}\eta_{\nu\rho} - \frac{2}{D-1}\eta_{\mu\nu}\eta_{\rho\sigma}, \text{ with } \eta_{\mu\nu} \equiv g_{\mu\nu} - \frac{q_\mu q_\nu}{q^2}, \tag{3.3}$$

whose normalization factor is

$$P_{\mu\nu\rho\sigma}P^{\mu\nu\rho\sigma} = 2\left(D^2 - D - 1\right). \tag{3.4}$$

Note that we are only interested in the self-interaction of gluons, thus the two-point correlator in Eq. (3.1) containing only the gluonic current $J^g_{\mu\nu}$ to probe the gluonium state. There are conventional mesons with quantum number $2^{++}$ which would be probed by the quark current

$J^q_{\mu\nu}$.

We will be using a `MATHEMATICA` package called Feyncalc [135–137] for Feynman diagram evaluation and algebraic calculations throughout this research. Feyncalc includes numerous, powerful functions for Feynman diagram/integral analysis in quantum field theory, including Lorentz index contraction, colour factor calculation and Passarino-Veltman reduction which will all be applied later in Sec. 3.2.3. As introduced in Chapter 2, we will also apply TARCER package [58] in our codes along with FeynCalc to reduce two-loop propagator integral expressions to basic integrals in `MATHEMATICA`.

The Feynman rules for gluon propagator, fermion (quark) propagator, ghost propagator and vertices involving these three fields are known (*e.g.,* Refs. [31, 44, 138, 139]). Yet there are two specific diagram components required in gluonic current calculation that are not included in the basic Feynman rules of QCD: gluonic-current-to-2-gluon and gluonic-current-to-3-gluon. In this section, both of these topologies will be evaluated for its Feynman rules from their corresponding Green's function and application of Wick's theorem.

### 3.2.1.1 Feynman Rule for Current-to-2-gluon

To find the Feynman rule of gluonic-current-to-2-gluon, we will start with Green's function.

$$\mathcal{G}_{\mu\nu}{}^{\rho\sigma} \equiv i \int d^4x\, d^4y\, d^4z\, e^{irx}\, e^{iq(y-x)}\, e^{ip(z-x)} \left\langle 0 \left| \mathcal{T} J^g_{\mu\nu}(x) \mathcal{A}^\rho_a(y) \mathcal{A}^\sigma_b(z) \right| 0 \right\rangle . \tag{3.5}$$

Eq. (3.5) is associated with the topology in the form of a gluonic-current-to-2-gluon vertex with two gluon propagators connected to the external legs of the vertex:

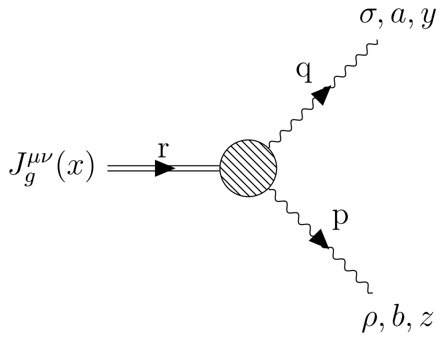

$$= Z^{\mu\nu\sigma'\rho'}_{a'b'}(p,q) D^{\sigma'\sigma}_{a'a}(q) D^{\rho'\rho}_{b'b}(p), \tag{3.6}$$

where $D^{\mu\nu}_{ab}(q)$ are the gluon propagators and $Z^{\mu\nu\sigma\rho}_{ab}(p,q)$ (represented as ▨ here) stands for the current-to-2-gluon vertex Feynman rule we are looking for:

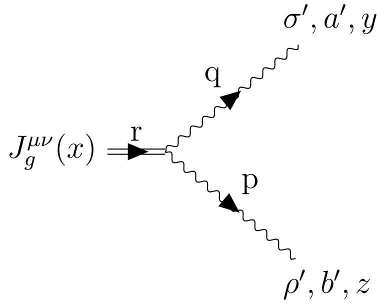

$$= Z^{\mu\nu\sigma'\rho'}_{a'b'}(p,q). \tag{3.7}$$

From Eqs. (3.2), (2.4) and (3.5), we have the current-to-2-gluon two-point function in the form of gluonic fields:

$$\begin{aligned} &\left\langle 0 \left| \mathcal{T} J^g_{\mu\nu}(x) \;\; \mathcal{A}^\rho_a(y) \mathcal{A}^\sigma_b(z) \right| 0 \right\rangle \\ &\qquad = \left\langle 0 \middle| \mathcal{T} \left( -G_\mu{}^{\alpha,c} G_{\nu\alpha,c} + \frac{1}{4} g_{\mu\nu} G^c_{\alpha\beta} G^{\alpha\beta}_c \right) \mathcal{A}^\rho_a(y) \mathcal{A}^\sigma_b(z) \middle| 0 \right\rangle , \\ &\qquad\qquad \text{with } G^c_{\alpha\beta} = \partial_\alpha \mathcal{A}^c_\beta - \partial_\beta \mathcal{A}^c_\alpha + g f^{cde} \mathcal{A}^d_\alpha \mathcal{A}^e_\beta . \end{aligned} \tag{3.8}$$

As one can easily observe, the third term ($f^{cde}\mathcal{A}^d_\alpha\mathcal{A}^e_\beta$) in each gluon field strength tensor would lead to two types of contractions in Wick's theorem [31]. One of the permutations is contracting with three other gluon fields and the other is with another double-gluon. One will then have five/six gluon fields in the operator of the Green's function while the current-2-to-gluon Feynman rule at tree level only requires four gluon fields. When calculating Feynman rules, we are always evaluating a Green's function where the field content matches the operator content of the Lagrangian so that the result Feynman rule is at the lowest order of interaction. Therefore, we will ignore the last (non-abelian) term in $G^c_{\alpha\beta}$ and proceed to expand Eq. (3.8).

$$\begin{aligned}
&\langle 0\left|\mathcal{T}J^g_{\mu\nu}(x)\ \ \mathcal{A}^\rho_a(y)\mathcal{A}^\sigma_b(z)\right|0\rangle \\
&\qquad = \left\langle 0\middle|\mathcal{T}\Big(-\left(\partial_\mu\mathcal{A}^{\alpha,c}(x)-\partial^\alpha\mathcal{A}^c_\mu(x)\right)\left(\partial_\nu\mathcal{A}_{\alpha,c}(x)-\partial_\alpha\mathcal{A}_{\nu,c}(x)\right)\right. \\
&\qquad \left.+\frac{1}{4}g_{\mu\nu}\left(\partial_\alpha\mathcal{A}^c_\beta(x)-\partial_\beta\mathcal{A}^c_\alpha(x)\right)\left(\partial^\alpha\mathcal{A}^\beta_c(x)-\partial^\beta\mathcal{A}^\alpha_c(x)\right)\Big)\mathcal{A}^\rho_a(y)\mathcal{A}^\sigma_b(z)\middle|0\right\rangle ,
\end{aligned} \tag{3.9}$$

which has 16 terms in total. Two of these will be demonstrated below as examples of the calculations performed to find the Green's function of the current-to-2-gluon Feynman rule (Eq. (3.5)). The first example of Green's function term is:

$$i\int d^4x\,d^4y\,d^4z\,e^{irx}\,e^{iq(y-x)}\,e^{ip(z-x)}\,\langle 0\,|\mathcal{T}\{\partial_\mu\mathcal{A}^\alpha_c(x)\partial_\nu\mathcal{A}_{\alpha,c}(x)\mathcal{A}^\rho_a(y)\mathcal{A}^\sigma_b(z)\}|\,0\rangle\,. \tag{3.10}$$

After applying Wick's theorem, there are two possible contractions:

$$\begin{aligned}
&i\int d^4x\,d^4y\,d^4z\,e^{irx}\,e^{iq(y-x)}\,e^{ip(z-x)} \\
&\Big(
\contraction[2ex]{\langle 0\,|\partial_\mu}{\mathcal{A}^\alpha_c}{(x)\partial_\nu\mathcal{A}_{\alpha,c}(x)\mathcal{A}^\rho_a(y)}{\mathcal{A}^\sigma_b}
\contraction{\langle 0\,|\partial_\mu\mathcal{A}^\alpha_c(x)\partial_\nu}{\mathcal{A}_{\alpha,c}}{(x)}{\mathcal{A}^\rho_a}
\langle 0\,|\partial_\mu\mathcal{A}^\alpha_c(x)\partial_\nu\mathcal{A}_{\alpha,c}(x)\mathcal{A}^\rho_a(y)\mathcal{A}^\sigma_b(z)|\,0\rangle
+
\contraction{\langle 0\,|\partial_\mu}{\mathcal{A}^\alpha_c}{(x)\partial_\nu\mathcal{A}_{\alpha,c}(x)}{\mathcal{A}^\rho_a}
\contraction[2ex]{\langle 0\,|\partial_\mu\mathcal{A}^\alpha_c(x)\partial_\nu}{\mathcal{A}_{\alpha,c}}{(x)\mathcal{A}^\rho_a(y)}{\mathcal{A}^\sigma_b}
\langle 0\,|\partial_\mu\mathcal{A}^\alpha_c(x)\partial_\nu\mathcal{A}_{\alpha,c}(x)\mathcal{A}^\rho_a(y)\mathcal{A}^\sigma_b(z)|\,0\rangle
\Big) \\
&=\int d^4r\,d^4p\,d^4q\left(q^\alpha g^{\mu\sigma'}D^{\sigma'\sigma}_{bc}(q)p^\alpha g^{\rho'\nu}D^{\rho'\rho}_{ac}(p)+p^\alpha g^{\rho'\mu}D^{\rho'\rho}_{ac}(p)q^\alpha g^{\sigma'\nu}D^{\sigma'\sigma}_{bc}(q)\right) \\
&=\delta_{a'b'}\int d^4r\,d^4p\,d^4q\,\left(g^{\mu\sigma'}g^{\rho'\nu}+g^{\rho'\mu}g^{\sigma'\nu}\right)(q\cdot p)\,D^{\rho'\rho}_{b'b}(p)D^{\sigma'\sigma}_{a'a}(q),
\end{aligned} \tag{3.11}$$

where in the last line the sensitivity of covariant and contravariant indices label is omitted in the Einstein notation for the Lorentz indices.

The second example term from Eq. (3.9) is

$$
\begin{aligned}
&i\int d^4x\, d^4y\, d^4z\, e^{irx}\, e^{iq(y-x)}\, e^{ip(z-x)} \left\langle 0 \left| \mathcal{T}\{\frac{1}{4} g_{\mu\nu}\partial_\alpha \mathcal{A}_{\beta c}(x)\partial^\alpha \mathcal{A}_c^\beta(x)\mathcal{A}_a^\rho(y)\mathcal{A}_b^\sigma(z)\} \right| 0 \right\rangle \\
&\xrightarrow{\text{Wick's theorem}} \frac{i}{4}\int d^4x\, d^4y\, d^4z\, e^{irx}\, e^{iq(y-x)}\, e^{ip(z-x)} \\
&\Big( \langle 0\, | g_{\mu\nu}\partial_\alpha \mathcal{A}_{\beta,c}(x)\partial^\alpha \mathcal{A}_c^\beta(x)\mathcal{A}_a^\rho(y)\mathcal{A}_b^\sigma(z) |\, 0\rangle + \langle 0\, | g_{\mu\nu}\partial_\alpha \mathcal{A}_{\beta,c}(x)\partial^\alpha \mathcal{A}_c^\beta(x)\mathcal{A}_a^\rho(y)\mathcal{A}_b^\sigma(z) |\, 0\rangle \Big) \\
&= \frac{1}{2}\delta_{a'b'}\int d^4r\, d^4p\, d^4q\ (q\cdot p)\, g^{\mu\nu} g^{\rho'\sigma'} D_{b'b}^{\rho'\rho}(p) D_{a'a}^{\sigma'\sigma}(q).
\end{aligned}
\tag{3.12}
$$

Based on the sample calculations given in Eqs. (3.11) to (3.12), the complete results for the Green's function can be expressed in terms of the gluon propagators $D^{\sigma'\sigma}(q)$ and $D^{\rho'\rho}(p)$:

$$
\begin{aligned}
\mathcal{G}^{\mu\nu\rho\beta} = \delta_{a'b'} \int & d^4r\, d^4p\, d^4q\, \delta_{a'b'}\, [\, (-g^{\mu\sigma'} g^{\nu\rho'} - g^{\mu\rho'} g^{\nu\sigma'} + g^{\mu\nu} g^{\sigma'\rho'})\, p\cdot q \\
& + g^{\mu\sigma'}\, q^{\rho'}\, p^\nu + g^{\mu\rho'}\, p^{\sigma'}\, q^\nu + g^{\nu\rho'}\, q^\mu\, p^{\sigma'} + g^{\nu\sigma'}\, p^\mu\, q^{\rho'} \\
& - g^{\sigma'\rho'}\, q^\mu\, p^\nu - g^{\rho'\sigma'}\, p^\mu\, q^\nu - g^{\mu\nu}\, p^{\sigma'}\, q^{\rho'}\ ]\ D_{b'b}^{\rho'\rho}(p) D_{a'a}^{\sigma'\sigma}(q)
\end{aligned}
\tag{3.13}
$$

which corresponds to $\int Z_{a'b'}^{\mu\nu\sigma'\rho'}(p,q) D_{a'a}^{\sigma'\sigma}(q) D_{b'b}^{\rho'\rho}(p)$. Cleaning up the indices, we, therefore, have the Feynman rule for gluonic-current-to-2-gluon from Eq. (3.7) as shown below:

$$
\begin{aligned}
Z_{ab}^{\mu\nu\sigma\rho}(p,q) = -\delta_{ab}\, [ & (-g^{\mu\sigma} g^{\nu\rho} - g^{\mu\rho} g^{\nu\sigma} + g^{\mu\nu} g^{\sigma\rho})\, p\cdot q \\
& + g^{\mu\sigma}\, q^\rho\, p^\nu + g^{\mu\rho}\, p^\sigma\, q^\nu + g^{\nu\rho}\, q^\mu\, p^\sigma \\
& + g^{\nu\sigma}\, p^\mu\, q^\rho - g^{\sigma\rho}\, q^\mu\, p^\nu - g^{\rho\sigma}\, p^\mu\, q^\nu - g^{\mu\nu}\, p^\sigma\, q^\rho\ ]
\end{aligned}
\tag{3.14}
$$

#### 3.2.1.2 Feynman Rule for Current-to-3-gluon

In some tensor gluonium NLO diagrams (*e.g.,* diagrams f, g and h in Sec. 3.2.2), we will encounter a diagram piece that connects gluonic current to three gluon propagators. The process to find the Feynman rule for such topology is very similar to what we just did for the current-to-2-gluon piece, only more cumbersome. One will start with the Green's function which has an additional gluon field compared to Eq. (3.5):

$$i\int d^4w\, d^4x\, d^4y\, d^4z\, e^{irw}\, e^{ip(w-x)}\, e^{ik(w-y)}\, e^{iq(w-z)} \left\langle 0 \left| \mathcal{T} J^g_{\mu\nu}(w) \mathcal{A}^\rho_a(x) \mathcal{A}^\lambda_b(y) \mathcal{A}^\sigma_c(z) \right| 0 \right\rangle . \tag{3.15}$$

The topology is therefore:

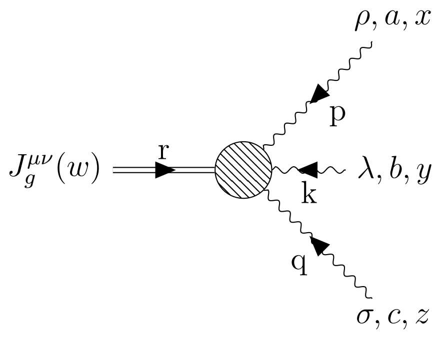

$$= E^{\mu\nu\rho'\lambda'\sigma'}_{a'b'c'}(p,q,k) D^{\rho\rho'}_{aa'}(p) D^{\sigma\sigma'}_{bb'}(q) D^{\lambda\lambda'}_{cc'}(k) \tag{3.16}$$

where $E^{\mu\nu\rho\lambda\sigma}_{abc}(p,q,k)$ stands for the current-to-3-gluon vertex Feynman rule:

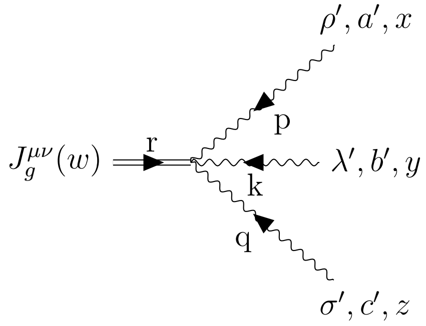

$$= E^{\mu\nu\rho'\lambda'\sigma'}_{a'b'c'}(p,q,k). \tag{3.17}$$

Substituting in expression for gluonic currents and gluon field strength tensors in Eq. (3.15),

$$i\int d^4w\, d^4x\, d^4y\, d^4z\, e^{irw}\, e^{ip(w-x)}\, e^{ik(w-y)}\, e^{iq(w-z)} \\ \left\langle 0 \left| \mathcal{T} \left( -G_\mu{}^\alpha G_{\nu\alpha} + \frac{1}{4} g_{\mu\nu} G_{\alpha\beta} G^{\alpha\beta} \right) \mathcal{A}^\rho_a(x) \mathcal{A}^\lambda_b(y) \mathcal{A}^\sigma_c(z) \right| 0 \right\rangle , \tag{3.18}$$

To find the tree-level Feynman rule for current-to-3-gluon, one will need six gluon fields in Green's function for fully contracted vacuum expectation values of time-ordered products of gluon field operators. Using Wick's theorem, one will eventually reach the Feynman rule for current-to-3-gluon as below.

$$
\begin{aligned}
&E_{abc}^{\mu\nu\rho\lambda\sigma}(p,q,k) = \\
&-igf_{abc}\Big[(p-q)^{\lambda}\left(g^{\mu\nu}g^{\rho\sigma}-g^{\rho\mu}g^{\sigma\nu}-g^{\sigma\mu}g^{\rho\nu}\right)+(k-p)^{\sigma}\left(g^{\mu\nu}g^{\lambda\rho}-g^{\rho\mu}g^{\lambda\nu}-g^{\lambda\mu}g^{\rho\nu}\right) \\
&+(q-k)^{\rho}\left(g^{\mu\nu}g^{\sigma\lambda}-g^{\lambda\mu}g^{\sigma\nu}-g^{\sigma\mu}g^{\lambda\nu}\right)+g^{\rho\lambda}\left(g^{\sigma\nu}\left(p-k\right)^{\mu}+g^{\sigma\mu}\left(p-k\right)^{\nu}\right) \\
&+g^{\rho\sigma}\left(g^{\lambda\nu}\left(q-p\right)^{\mu}+g^{\lambda\mu}\left(q-p\right)^{\nu}\right)+g^{\sigma\lambda}\left(g^{\rho\nu}\left(k-q\right)^{\mu}+g^{\rho\mu}\left(k-q\right)^{\nu}\right)\Big]
\end{aligned}
\tag{3.19}
$$

Both Feynman rules found in this section are listed in Appendix E along with other non-abelian gauge theory Feynman rules that occur in this research. In principle, one can also derive a current-to-4-gluon Feynman rule by forming a Green's function with eight gluon fields. This current-to-4-gluon Feynman rule would contribute at 3-loop or 2-loop level diagrams. The latter leads to a massless tadpole topology that is zero in dimensional regularization (see a tadpole example in Sec. 3.2.3.1).

### 3.2.2 Tensor Di-gluonium Diagrams to NLO

In this section, one can find all the LO and NLO diagrams for tensor gluonium which will be heavily referred to in this chapter. The LO self-energy diagram is shown in diagram (a) below, whereas the NLO diagrams are shown in diagram (b)-(i). Note that the diagram labeling in Sec. 3.2 is self-contained and unrelated to the manuscript, particularly Table 3.1.

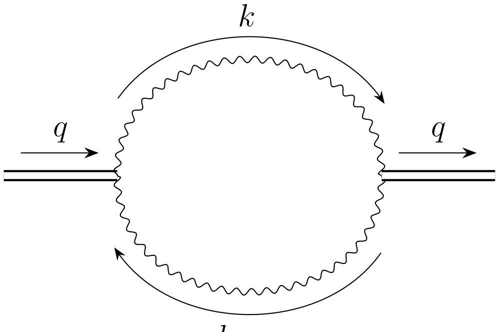

(a) Tensor Gluonium LO Self-energy Diagram

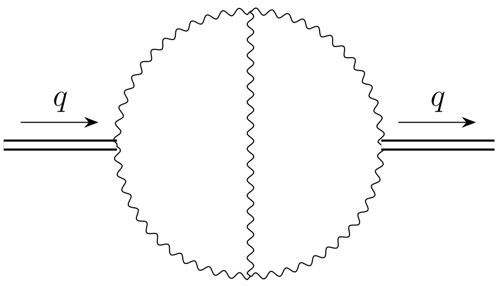

(b) NLO Gluon Exchange Diagram

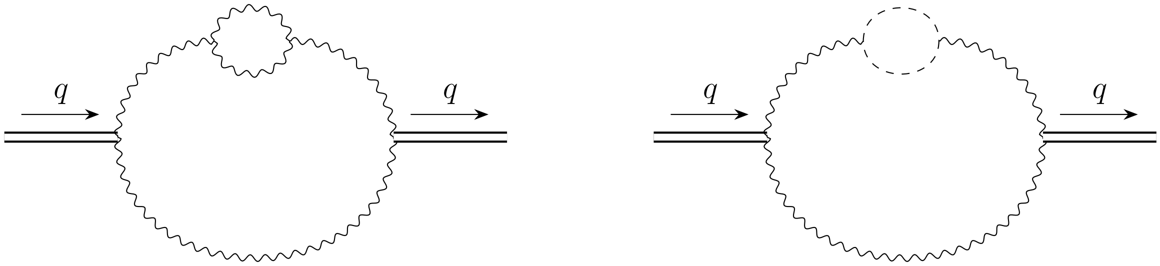

(c) NLO Gluon Self-Energy with Gluonic Loop

(d) NLO Gluon Self-Energy with Ghost Loop

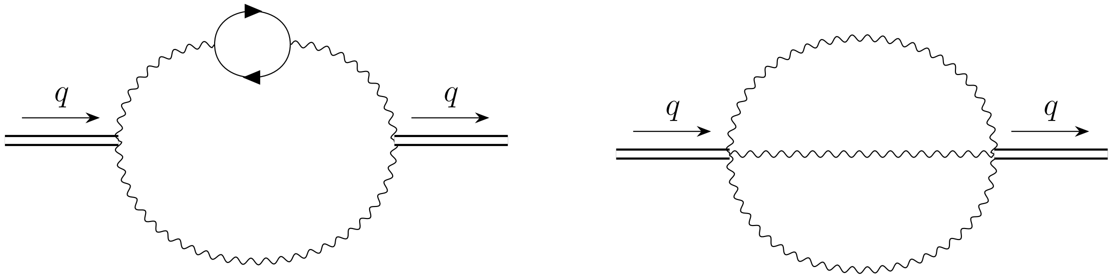

(e) NLO Gluon Self-Energy with Quark Loop

(f) NLO Sunrise Diagram

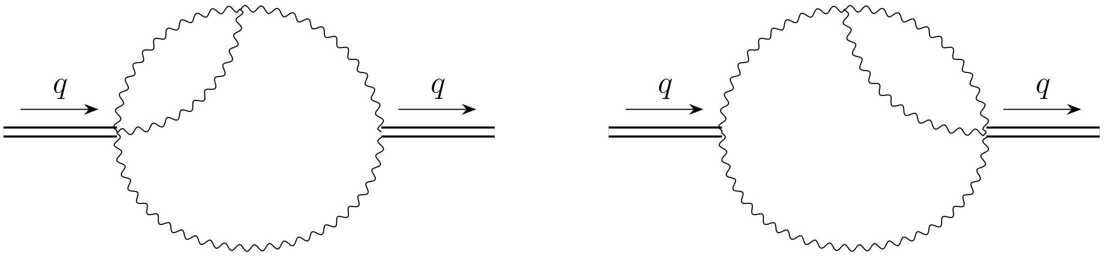

(g) NLO Vertex Diagram 1

(h) NLO Vertex Diagram 2

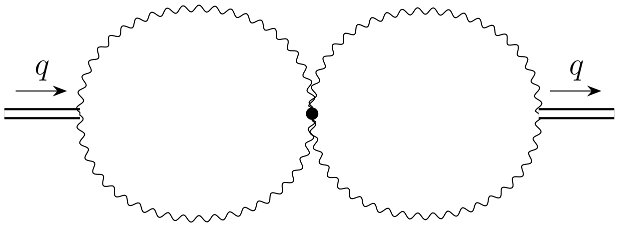

(i) NLO Butterfly

The conventional renormalization method requires renormalization-induced diagrams (diagram j and k) for calcualtion. These two diagrams will be eveluated and applied in section 3.2.4.

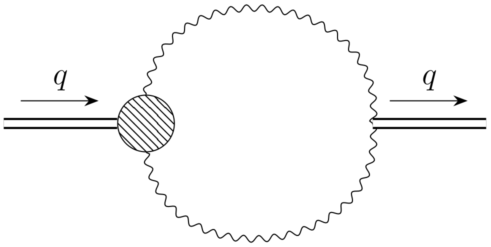

(j) NLO Renormalization-Induced Diagram 1

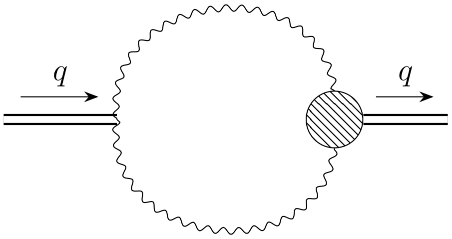

(k) NLO Renormalization-Induced Diagram 2

### 3.2.3 Method of Diagrammatic Renormalization

As outlined in Sec. 2.4.2, diagrammatic renormalization is an alternative method as opposed to the conventional renormalization processes for QCD correlation functions. In this section, NLO diagrams (b)-(i) will be evaluated perturbatively, and the non-local divergences will be renormalized in the perturbative expansion of each bare correlation function diagram following the methods of Ref. [72]. This will be achieved by subtracting all counter-term diagrams $\gamma$ for each divergent sub-diagram of bare diagram $x$:

$$\Pi^{(x)}_{renorm} = \Pi^{(x)}_{bare} - \sum_{\gamma} \Pi^{(x)\gamma}_{ct}, \tag{3.20}$$

where $\Pi^{(x)\gamma}_{ct}$ will be built by replacing the sub-diagram $\gamma$ with its divergent part.

All of the bare correlation function calculation results will be given in arbitrary gauge with gauge parameter $\xi$. As will be seen in Section 3.2.3.8, the gauge parameter cancels in the sum of all NLO bare correlators showing gauge parameter independence and thus providing consistency check on our calculation. Hence, the diagrammatic renormalization process will be implemented in Feynman gauge ($\xi = 1$).

#### 3.2.3.1 Sunrise Topology (diagram f)

In the case of the NLO sunrise diagram, we have the topology and the bare projected correlator calculated in arbitrary gauge and as shown below.

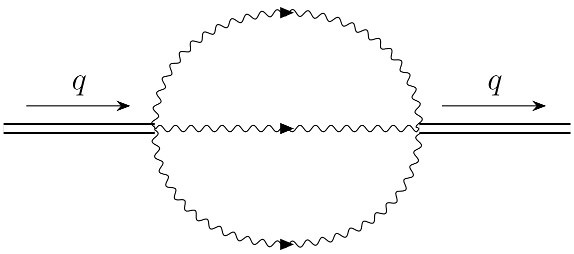

$= \Pi^{(f)}_{bare}$

$$\begin{aligned}\Pi^{(f)}_{bare}(Q^2 \equiv -q^2) =& iP^{\mu\nu\rho\sigma}(q) \int \frac{d^Dk}{(2\pi)^D} \int \frac{d^Dp}{(2\pi)^D}\, E^{\mu\nu\alpha\beta\gamma}_{abc}(-k, -p, -q+k+p) \\ & D^{\alpha\lambda}_{ad}(k)\; D^{\beta\theta}_{be}(p)\; D^{\gamma\phi}_{ch}(q-k-p)\; E^{\rho\sigma\lambda\theta\phi}_{deh}(k, p, q-k-p) \\ =& -\frac{\alpha_s Q^4}{160\pi^3}\left(3\xi^2 - 3\xi + 10\right) L,\; L = \log\left(\frac{Q^2}{\nu^2}\right)\end{aligned} \tag{3.21}$$

where all correlation function diagrams are calculated in $\overline{\text{MS}}$ scheme and in dimensional regularization scheme of $D = 4+2\epsilon$. The renormalization factor of $1/\nu^{2\epsilon}$ is implicit for each loop in the NLO diagrams. This applied to all correlators evaluated in Sec. 3.2.3. Equation (3.21) neglects the non-physical polynomial subtraction-constant terms in the dispersion relation of $\Pi(Q^2)$, which correspond to local divergences that do not enter QCDSR. This approach will be consistently applied to all subsequent NLO diagrams without repetitive explanation. The possible sub-divergences of diagram (f) are isolated in the dotted box ⬚ in the Feynman diagram as the following sub-diagram.

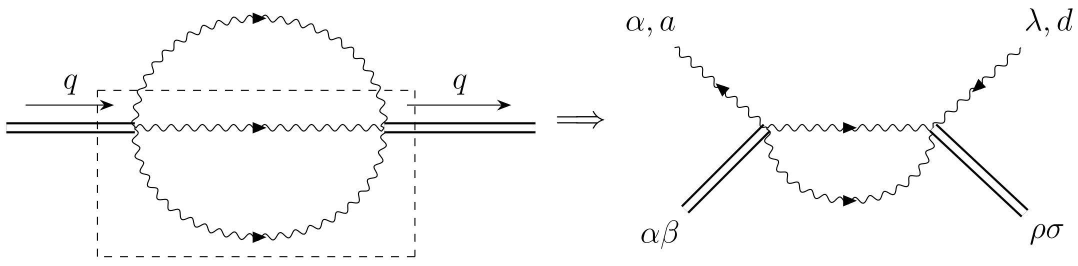

$$= X_{ad}^{\alpha\beta\rho\sigma\gamma\chi}$$

$$
\begin{aligned}
X_{ad}^{(f)\mu\nu\rho\sigma\gamma\chi}(q,k) = &\int \frac{d^D p}{(2\pi)^D} \\
&E_{abc}^{\mu\nu\alpha\beta\gamma}(-k,-p,-q+k+p)\ \ D_{be}^{\beta\theta}(p)\ D_{ch}^{\gamma\phi}(q-k-p)\ E_{deh}^{\rho\sigma\lambda\theta\phi}(k,p,q-k-p).
\end{aligned}
\tag{3.22}
$$

The sunrise diagram now has the counter-term diagram expression

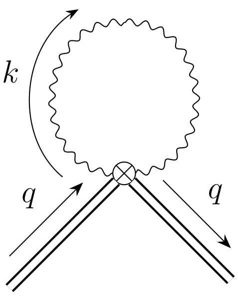

$$= iP^{\mu\nu\rho\sigma}(q) \int \frac{d^D k}{(2\pi)^D}\ X_{ad}^{(f)\mu\nu\rho\sigma\alpha\lambda}(q,k) D_{ad}^{\alpha\lambda}(k). \tag{3.23}$$

where $\otimes$ stands for the divergent part of the sub-diagram $X_{ad}^{\mu\nu\rho\sigma\alpha\lambda}$ as in Eq. (3.22). In the counter-term diagram in Eq. (3.23), the topology is a *tadpole* with a massless gluon propagator. The loop integral of such topology is zero in dimensional regularization [44]. Even in the case of a massive tadpole, the external momentum $q$ wouldn't enter the loop integral of Eq. (3.23) — a disconnected diagram. Thus this counter-term diagram corresponds to a subtraction constant in the QCD sum-rules dispersion relation Eq. (2.77), representing a local divergence.

From Eq. (3.21), we can see the bare correlation function of the NLO sunrise topology has no divergent term (e.g. logarithmic divergence) which agrees with the absence of a physical contribution from Eq. (3.23).

#### 3.2.3.2 Gluon Self-Energy with Gluonic Loop (diagram c)

In the case of NLO gluon self-energy with gluonic loop diagram, there is a topology which is not included in Sec. 3.2.2:

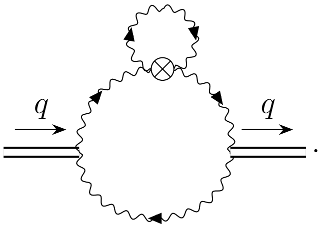

. (3.24)

The NLO gluon self-energy diagram in (3.24) includes a massless gluon tadpole and is therefore zero in dimensional regularization as discussed above. We will focus on the non-zero case in this section (diagram c):

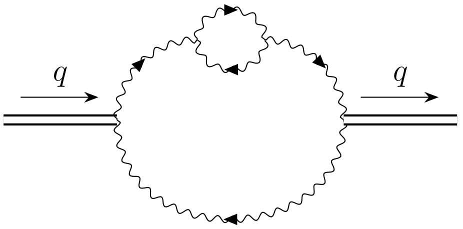

$$= \Pi^{(c)}_{bare}. \tag{3.25}$$

Here the bare two-point correlation function $\Pi^{(c)}_{bare}$ will be calculated by evaluating the following Feynman integral:

$$\begin{aligned}
\Pi^{(c)}_{bare}(Q^2 \equiv -q^2) &= iP^{\mu\nu\rho\sigma}(q) \int \frac{d^D k}{(2\pi)^D} \int \frac{d^D p}{(2\pi)^D} Z^{\mu\nu\alpha\beta}_{ab}(p, q-p)\, D^{\alpha\gamma}_{ac}(p) \\
&\quad V^{\gamma\theta\eta}_{cde}(k-p, -k)\, D^{\eta\phi}_{ef}(k)\, V^{\phi\lambda\chi}_{fhj}(k, p-k, -p)\, D^{\theta\lambda}_{dh}(p-k) \\
&\quad D^{\chi\tau}_{jl}(p)\, D^{\beta\zeta}_{bm}(q-p)\, Z^{\rho\sigma\tau\zeta}_{lm}(-p, p-q) \\
&= \frac{\alpha_s Q^4}{2400\pi^3} \left[ (375 - 90\xi) L^2 + \left( -45\xi^2 - \frac{90\xi}{\epsilon} + 144\xi + \frac{375}{\epsilon} - 1420 \right) L \right] \\
&= \frac{19\, \alpha_s\, Q^4}{1600\pi^3} L \left( 10L - \frac{2642}{57} + \frac{10}{\epsilon} \right), \; L = \log\left( \frac{Q^2}{\nu^2} \right), \\
&\quad \{\xi = 1 \text{ Feynman gauge}\}
\end{aligned} \tag{3.26}$$

where $V^{\mu\nu\lambda}_{abc}(p,q,r)$ stands for the triple-gluon vertex and its chosen notation convention can be referred in Appendix E. In the gluonic loop case, the local divergence is shown by

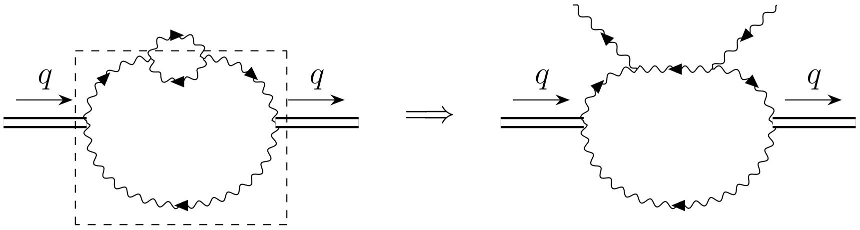

$$, \qquad (3.27)$$

corresponding to a counter-term diagram in the form of a gluon tadpole with gluonic loop topology:

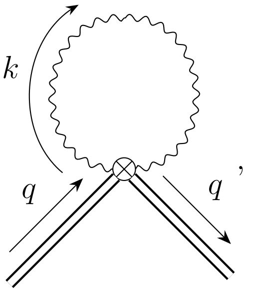

$$, \qquad (3.28)$$

where $\otimes$ stands for the divergent part of sub-diagram shown in Eq. (3.27). Similar to Eq. (3.23), the counter-term diagram in Eq. (3.28) is another local divergence.

The only non-local sub-divergence of $\Pi^{(c)}_{bare}$ is located in the gluonic self-energy with gluon loop topology, which is isolated by the dotted box as shown in the following diagrams:

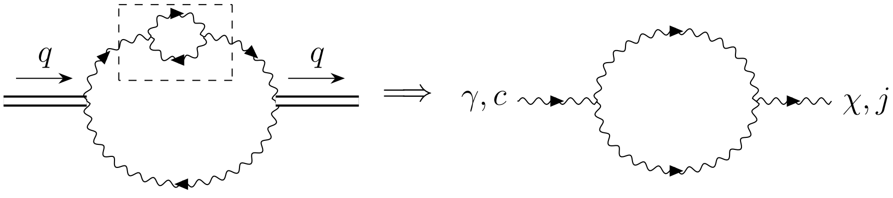

$$= X^{(c)\gamma\chi}_{cj}. \qquad (3.29)$$

Only the divergent $(\frac{1}{\epsilon})$ part of $X^{\gamma\chi}$ will be extracted to form the counter-term diagram:

$$\begin{aligned} X^{(c)\gamma\chi}_{cj}(p) &= \int \frac{d^D k}{(2\pi)^D} V^{\gamma\theta\eta}_{cde}(k-p,-k)\; D^{\eta\phi}_{ef}(k)\; V^{\phi\lambda\chi}_{fhj}(k,p-k,-p)\; D^{\theta\lambda}_{dh}(p-k) \\ &\xrightarrow{1/\epsilon} i\delta^{cj}\frac{g^2}{64\pi^2\epsilon}\left(22q^\gamma p^\chi - 19p^2 g^{\gamma\chi}\right). \end{aligned} \qquad (3.30)$$

Note that as mentioned in Sec. 2.4.2, the $\frac{1}{\epsilon}$ divergence subtraction are performed in MS scheme. So the renormalized result will need conversion to $\overline{\text{MS}}$ scheme using $\nu^2 \to \exp(\gamma_E)\nu^2/4\pi$. Now we can use the sub-divergence result in Eq. (3.30) to form the counter-term for diagram (c) by substituting the gluonic loop with tensor $X_{cj}^{\gamma\chi}$ both diagrammatically and algebraically.

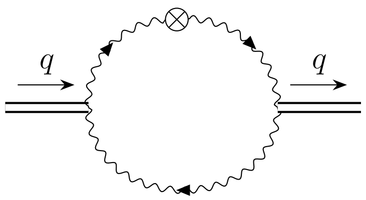

$$= \Pi_{ct}^{(c)}$$

$$\begin{aligned}\Pi_{ct}^{(c)}(Q^2 \equiv -q^2) =& iP^{\mu\nu\rho\sigma}(q) \int \frac{d^D p}{(2\pi)^D} Z_{ab}^{\mu\nu\alpha\beta}(p, q-p)\ D_{ac}^{\alpha\gamma}(p) \\ & X_{cj}^{(c)\gamma\chi}(p)\ D_{jl}^{\chi\tau}(p)\ D_{bm}^{\beta\zeta}(q-p)\ Z_{lm}^{\rho\sigma\tau\zeta}(-p, p-q) \\ =& \frac{19\,\alpha_s\,Q^4}{1600\pi^3} L\left(5L - 9 + \frac{10}{\epsilon}\right),\ L = \log\left(\frac{Q^2}{\nu^2}\right). \end{aligned} \tag{3.31}$$

The non-local divergent $L/\epsilon$ terms from Eq. (3.26) and (3.31) are identical. According to the diagrammatic renormalization method, the renormalized correlator can be found subtracting the counter-term diagram in Eq. (3.31) from the bare diagram (c) [72]. Since the divergent pieces from both are the same, the subtraction will eliminate the divergence from the correlator. The diagrammatic renormalization method gives the renormalized result for diagram (c):

$$\Pi_{renorm}^{(c)}(Q^2) = \Pi_{bare}^{(c)}(Q^2) - \Pi_{ct}^{(c)}(Q^2) = \frac{\alpha_s Q^4}{4800\pi^3} L\left(285L - 2129\right),\ L = \log\left(\frac{Q^2}{\nu^2}\right). \tag{3.32}$$

#### 3.2.3.3 Gluon Self-Energy with Ghost Loop (diagram d)

The second gluonic self-energy diagram we are going to discuss has a ghost loop. The bare correlator has the following form:

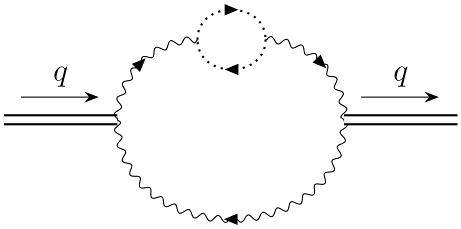

$$= \Pi^{(d)}_{bare},$$

where

$$\Pi^{(d)}_{bare}(Q^2 \equiv -q^2) = iP^{\mu\nu\rho\sigma}(q) \int \frac{d^Dk}{(2\pi)^D} \int \frac{d^Dp}{(2\pi)^D}$$
$$Z^{\mu\nu\alpha\beta}_{ab}(p, q-p)\; D^{\alpha\gamma}_{ac}(p)\; Y^{\gamma}_{ecd}(k)\; \Delta^{ef}(k)\; Y^{\chi}_{hjf}(k-p)$$
$$\Delta^{dh}(p-k)\; D^{\chi\tau}_{jl}(p)\; D^{\beta\zeta}_{bm}(q-p)\; Z^{\rho\sigma\tau\zeta}_{lm}(-p, p-q) \tag{3.33}$$

$$= \frac{\alpha_s Q^4}{160\pi^3} L \left( L + \frac{1}{\epsilon} - \frac{79}{15} \right),\; L = \log\left(\frac{Q^2}{\nu^2}\right),$$

where $\Delta^{ab}(k)$ stands for ghost field propagator and $Y^{\mu}_{abc}(p)$ stands for gluon-ghost vertex. Diagram (d) has identical topology as to diagram (c), which is analyzed in Section 3.2.3.2 in detail, except for the ghost internal lines. Therefore, diagram (d) has a similar form of non-local divergence which is isolated by the dotted box as shown in the following diagrams.

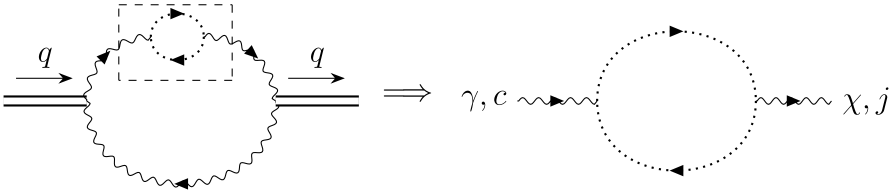

$$= X^{(d)\gamma\chi}_{cj} \tag{3.34}$$

The counter-term diagram for the gluon self-energy with ghost loop will be constructed with the divergent part ($\frac{1}{\epsilon}$) of Eq. (3.34):

$$
\begin{aligned}
X_{cj}^{(d)\gamma\chi}(p) = \int \frac{d^Dk}{(2\pi)^D}\, Y_{ecd}^{\gamma}(k)\, \Delta^{ef}(k)\, Y_{hjf}^{\chi}(k-p)\, \Delta^{dh}(p-k) \\
\xrightarrow{1/\epsilon} -i\delta^{cj}\frac{g^2}{64\pi^2\epsilon}\left(p^2 g^{\gamma\chi} + 2p^\gamma p^\chi\right) .
\end{aligned}
\tag{3.35}
$$

Now the counter-term for diagram (d) can be found by substituting the divergent part of the sub-diagram Eq. (3.35) in the gluonic self-energy with ghost loop diagram, resulting in the following counter-term diagram.

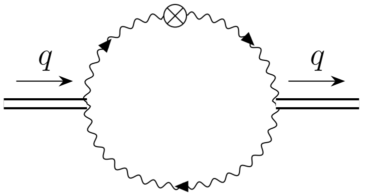

$$= \Pi_{ct}^{(d)}$$

$$
\begin{aligned}
\Pi_{ct}^{(d)}(Q^2 \equiv -q^2) = iP^{\mu\nu\rho\sigma}(q) \int \frac{d^Dp}{(2\pi)^D}\, Z_{ab}^{\mu\nu\alpha\beta}(p, q-p)\, D_{ac}^{\alpha_s\gamma}(p)\, X_{cj}^{(d)\gamma\chi}(p) \\
D_{jl}^{\chi\tau}(p)\, D_{bm}^{\beta\zeta}(q-p)\, Z_{lm}^{\rho\sigma\tau\zeta}(-p, p-q)
\end{aligned}
\tag{3.36}
$$

$$= \frac{\alpha_s Q^4}{1600\pi^3} L\left(5L - 9 + \frac{10}{\epsilon}\right),\ L = \log\left(\frac{Q^2}{\nu^2}\right) .$$

The logarithmic terms representing the non-local divergence of diagram (d) from Eq. (3.33) and (3.36) are identical. Therefore, the subtraction between the bare diagram Eq. (3.33) and the counter-term diagram result Eq. (3.36) will eliminate the non-local divergence. The diagrammatic renormalization method gives the renormalized result for diagram (d):

$$\Pi_{renorm}^{(d)}(Q^2) = \Pi_{bare}^{(d)}(Q^2) - \Pi_{ct}^{(d)}(Q^2) = \frac{\alpha_s Q^4}{4800\pi^3} L\left(15L - 131\right),\ L = \log\left(\frac{Q^2}{\nu^2}\right) . \tag{3.37}$$

#### 3.2.3.4 Gluon Self-Energy with Quark Loop (diagram e)

Another case of the NLO gluonic self-energy topology is with a quark loop, whose bare two-point correlation function diagram has the following form:

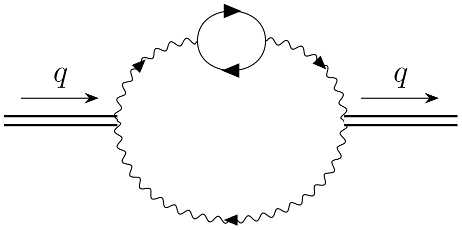

$$= \Pi^{(e)}_{bare},$$

where

$$\begin{aligned}\Pi^{(e)}_{bare}(Q^2 \equiv -q^2) = iP^{\mu\nu\rho\sigma}(q) \int \frac{d^Dk}{(2\pi)^D} \int \frac{d^Dp}{(2\pi)^D} Z^{\mu\nu\alpha\beta}_{ab}(p, q-p)\; D^{\alpha\gamma}_{ac}(p)\; \Gamma^{\gamma}_{c}\; S(k) \\ \Gamma^{\chi}_{j}\; S(p-k)\; D^{\chi\tau}_{jl}(p)\; D^{\beta\zeta}_{bm}(q-p)\; Z^{\rho\sigma\tau\zeta}_{lm}(-p, p-q)\end{aligned} \tag{3.38}$$

$$= n_f \frac{\alpha_s Q^4}{60\pi^3} L \left[-L + \frac{64}{15} - \frac{1}{\epsilon}\right],\; L = \log\left(\frac{Q^2}{\nu^2}\right),$$

with $\Gamma^{\mu}_{a}$ standing for gluon-fermion vertex Feynman rule and $n_f$ representing the number of light quark flavours.

Isolating the non-local sub-divergence of $\Pi^{(e)}_{bare}$,

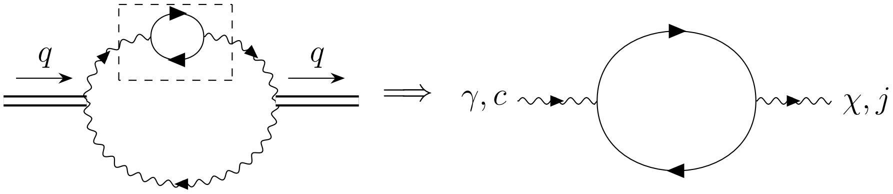

$$= X^{(e)\gamma\chi}_{cj}, \tag{3.39}$$

where the divergent part of $X^{(e)\gamma\chi}_{cj}$ will be extracted:

$$\begin{aligned}X^{(e)\gamma\chi}_{cj}(p) &= \int \frac{d^Dk}{(2\pi)^D}\; \Gamma^{\gamma}_{c}\; S(k)\; \Gamma^{\chi}_{j}\; S(p-k) \\ &\xrightarrow{1/\epsilon} -i\delta^{cj} \frac{g^2}{24\pi^2\epsilon} \left(p^{\gamma}p^{\chi} - p^2 g^{\gamma\chi}\right).\end{aligned} \tag{3.40}$$

The counter-term for diagram (e) can then be formed by substituting the quark loop with the divergent part of the sub-diagram $X_{cj}^{(e)\gamma\chi}(p)$:

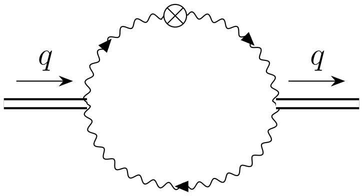

$$= \Pi_{ct}^{(e)}$$

$$\begin{aligned}
&\Pi_{ct}^{(e)}(Q^2 \equiv -\, q^2) \\
&\qquad = i P^{\mu\nu\rho\sigma}(q) \int \frac{d^D p}{(2\pi)^D} Z_{ab}^{\mu\nu\alpha\beta}(p, q-p)\; D_{ac}^{\alpha_s \gamma}(p)\; X_{cj}^{(e)\gamma\chi}(P) \\
&\qquad\quad D_{jl}^{\chi\tau}(p)\; D_{bm}^{\beta\zeta}(q-p)\; Z_{lm}^{\rho\sigma\tau\zeta}(-p, p-q) \qquad (3.41) \\
&\qquad = n_f \frac{\alpha_s Q^4}{60\pi^3} L \left( -\frac{L}{2} + \frac{9}{10} - \frac{1}{\epsilon} \right),\ L = \log\left(\frac{Q^2}{\nu^2}\right).
\end{aligned}$$

We now have the renormalized result for diagram (e) from the bare diagram Eq. (3.38) and the counter-term diagram Eq. (3.41) by applying the diagrammatic normalization method:

$$\Pi_{renorm}^{(e)}(Q^2) = \Pi_{bare}^{(e)}(Q^2) - \Pi_{ct}^{(e)}(Q^2) = n_f \frac{\alpha_s Q^4}{1800\pi^3} L\left(-15L + 101\right),\ L = \log\left(\frac{Q^2}{\nu^2}\right). \quad (3.42)$$

The non-local divergence (logarithmic term) cancels in Eq. (3.42) as required.

#### 3.2.3.5 Gluon Exchange (diagram b)

Moving on to the NLO gluon exchange diagram,

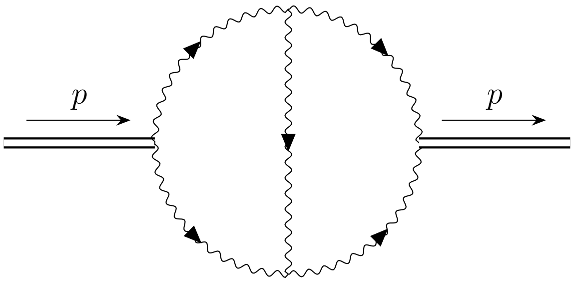

$$= \Pi_{bare}^{(b)},$$

where the diagram (b) bare correlation function is

$$
\begin{aligned}
\Pi^{(b)}_{bare}(Q^2 \equiv -q^2) = i P^{\mu\nu\rho\sigma}(q) \int \frac{d^D k}{(2\pi)^D} \int \frac{d^D p}{(2\pi)^D} \\
Z^{\mu\nu\alpha\beta}_{ab}(p, q-p)\ D^{\alpha\gamma}_{ac}(p) D^{\beta\zeta}_{bm}(q-p)\ V^{\gamma\phi\eta}_{ced}(-p, p-k, k) \\
D^{\phi\xi}_{eh}(p-k)\ V^{\xi\zeta\theta}_{hmi}(k-p, p-q, q-k) \\
D^{\eta\lambda}_{df}(k)\ D^{\theta\tau}_{ij}(q-k)\ Z^{\rho\sigma\lambda\tau}_{fj}(-k, k-q) \\
= \frac{\alpha_s Q^4}{480\pi^3} L \left[ (36\xi - 43)L + \left( \frac{36}{\epsilon} - \frac{513}{5} \right) \xi + \frac{9173}{60} - \frac{43}{\epsilon} \right] \\
= \frac{7\, \alpha_s\, Q^4}{28800\, \pi^3} L \left( -60L + 431 - \frac{60}{\epsilon} \right),\ L = \log\left( \frac{Q^2}{\nu^2} \right). \\
\{\xi = 1 \text{ Feynman gauge}\}
\end{aligned}
\tag{3.43}
$$

For diagram (b) topology, one of the two possible sub-divergences is isolated in the dotted box in the Feynman diagram as shown below in Eq. (3.44).

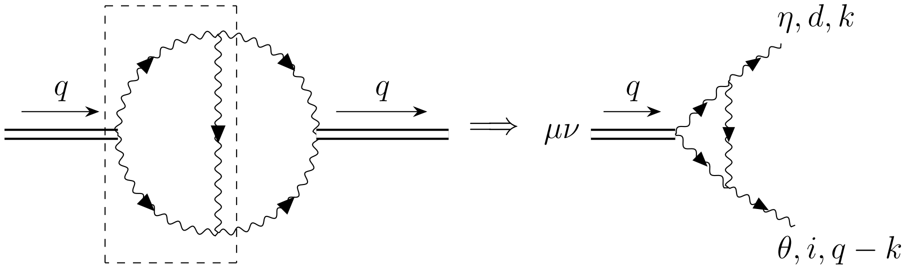

$$= X^{(b1)\mu\nu\eta\theta}_{di}, \tag{3.44}$$

where

$$
\begin{aligned}
X^{(b1)\mu\nu\eta\theta}_{di}(q,k) = \int \frac{d^D p}{(2\pi)^D}\ Z^{\mu\nu\alpha\beta}_{ab}(p, q-p)\ D^{\alpha\gamma}_{ac}(p)\ D^{\beta\zeta}_{bm}(q-p)\ V^{\gamma\phi\eta}_{ced}(-p, p-k, k) \\
D^{\phi\xi}_{eh}(p-k)\ V^{\xi\zeta\theta}_{hmi}(k-p, p-q, q-k).
\end{aligned}
\tag{3.45}
$$

One can see that the tensor $X^{(b1)\mu\nu\eta\theta}_{di}$ has four Lorentz indices and two colour indices. The integral can not be simply reduced into TARCER notation with `FeynCalc` built-in functions [58]. Instead, we used the `FeynCalc` built-in TID function to reduce Eq. (3.45) to the

Passarino-Veltman scalar integrals such as $A_0$, $B_0$, $C_0$ etc [44,140]. In our case, these scalar integrals, which has been introduced in Sec. 2.3, take forms as shown below:

$$A_0 = \frac{1}{i\pi^{D/2}} \int d^D p \, \frac{1}{p^2} \xrightarrow{1/\epsilon} 0 \tag{3.46}$$

$$B_0(q) = \frac{1}{i\pi^{D/2}} \int d^D p \, \frac{1}{p^2 \, (p+q)^2} \xrightarrow{1/\epsilon} -\frac{1}{16\pi^4 \epsilon} \tag{3.47}$$

$$C_0(k, q, k-q) = \frac{1}{i\pi^{D/2}} \int d^D p \, \frac{1}{p^2 \, (p+k)^2 \, (p+q)^2 \, (p+k-q)^2} \xrightarrow{1/\epsilon} 0 \tag{3.48}$$

As indicated in the above integrals, $A_0$ (Eq. (3.46)) is the loop integral of a massless tadpole which is zero and $C_0$ (Eq. (3.48)) is convergent. Therefore neither $A_0$ nor $C_0$ integrals will be contributing to the extraction of $\frac{1}{\epsilon}$ divergence for constructing the counter-term diagram of diagram (b). Only $B_0$ integrals gives divergent $\frac{1}{\epsilon}$ contribution to the result of $X_{di}^{(b1)\mu\nu\eta\theta}$. Specifically, each $B_0$ integral contributes a $-\frac{1}{16\pi^4\epsilon}$ to the divergent terms. Substituting all $B_0$ integrals with $-\frac{1}{16\pi^4\epsilon}$ and eliminating all the terms involving $A_0$ and $C_0$ integrals, we have the divergent part for the sub-diagram of Eq. (3.45):

$$\begin{aligned}
X_{di}^{(b1)\mu\nu\eta\theta}(q,k) \xrightarrow{1/\epsilon} -\frac{1}{16\pi\epsilon}\alpha_s \delta^{di} \Big[ & -26k^\theta k^\mu g^{\eta v} + 72k^\mu k^\nu g^{\eta\theta} - 26k^\theta k^\nu g^{\eta\mu} \\
& + 12k^2 g^{\eta v} g^{\theta\mu} + 12k^2 g^{\eta\mu} g^{\theta v} - 24k^2 g^{\eta\theta} g^{\mu v} - 36k^\mu q^\nu g^{\eta\theta} \\
& + 16k^\theta q^\mu g^{\eta v} - 36k^\nu q^\mu g^{\eta\theta} + 16k^\theta q^\nu g^{\eta\mu} \\
& + q^\eta \left(-21k^\theta g^{\mu v} + 26k^\mu g^{\theta v} + 26k^\nu g^{\theta\mu} + 7q^\theta g^{\mu v} - 12q^\mu g^{\theta v} - 12q^\nu g^{\theta\mu}\right) \\
& + k^\eta \left(26k^\theta g^{\mu v} - 26k^\mu g^{\theta v} - 26k^\nu g^{\theta\mu} - 5q^\theta g^{\mu v} + 10q^\mu g^{\theta v} + 10q^\nu g^{\theta\mu}\right) \\
& - 12g^{\eta v} g^{\theta\mu}(k\cdot q) - 12g^{\eta\mu} g^{\theta v}(k\cdot q) + 24g^{\eta\theta} g^{\mu v}(k\cdot q) - 2q^\theta q^\mu g^{\eta v} \\
& -2q^\theta q^\nu g^{\eta\mu} + 16q^\mu q^\nu g^{\eta\theta} + 2q^2 g^{\eta v} g^{\theta\mu} + 2q^2 g^{\eta\mu} g^{\theta v} - 5q^2 g^{\eta\theta} g^{\mu v} \Big].
\end{aligned} \tag{3.49}$$

The next step of diagrammatic renormalization is substituting the sub-diagram in Eq. (3.44) with the divergent part of $X^{(b1)}$:

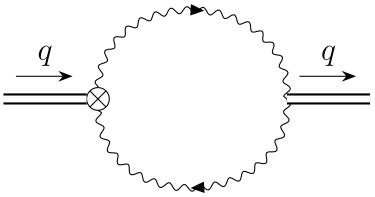

$$= \Pi_{ct}^{(b1)}$$

$$\begin{aligned}
&\Pi_{ct}^{(b1)}(Q^2 \equiv -\, q^2) \\
&\qquad = i P^{\mu\nu\rho\sigma}(q) \int \frac{d^D k}{(2\pi)^D}\; X_{di}^{(b1)\mu\nu\eta\theta}(q,k)\; D_{df}^{\eta\lambda}(k)\; D_{ij}^{\theta\tau}(q-k)\; Z_{fj}^{\rho\sigma\lambda\tau}(-k,k-q) \qquad (3.50)\\
&\qquad = \frac{7\,\alpha_s\,Q^4}{28800\,\pi^3} L \left(-15L + \frac{2084}{7} - \frac{30}{\epsilon}\right),\; L = \log\left(\frac{Q^2}{\nu^2}\right).
\end{aligned}$$

Now we have the first counter-term for diagram (b), generated from the sub-divergence located in the left half of the topology (Eq. (3.44)).

There is another sub-divergence in diagram (b). Since diagram (b) is perfectly symmetric upon the change of external momentum direction, it has a similar sub-diagram as Eq. (3.44):

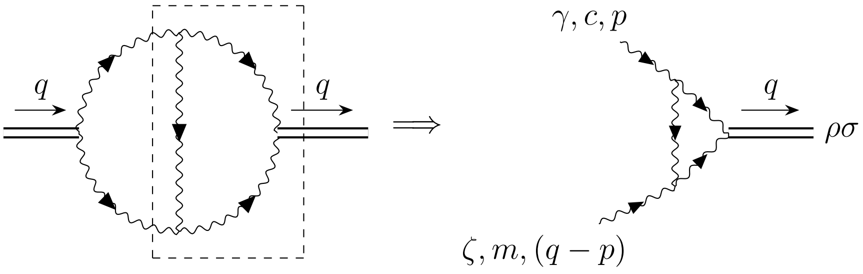

$$= X_{cm}^{(b2)\rho\sigma\gamma\zeta}(q,p), \quad (3.51)$$

$$\begin{aligned}
X_{cm}^{(b2)\rho\sigma\gamma\zeta}(q,p) = \int \frac{d^D k}{(2\pi)^D} V_{ced}^{\gamma\phi\eta}(-p,p-k,k)\; D_{eh}^{\phi\xi}(p-k)\; V_{hmi}^{\xi\zeta\theta}(k-p,p-q,q-k) \\
D_{df}^{\eta\lambda}(k)\; D_{ij}^{\theta\tau}(q-k)\; Z_{fj}^{\rho\sigma\lambda\tau}(-k,k-q)
\end{aligned} \qquad (3.52)$$

$$
\begin{aligned}
&X_{cm}^{(b2)\rho\sigma\gamma\zeta}(q,p) \\
&\xrightarrow{1/\epsilon} -\delta^{cm}\frac{\alpha_s}{16\pi\epsilon}\Big[-2q^\zeta q^\rho g^{\gamma\sigma} + 16q^\rho q^\sigma g^{\gamma\zeta} - 2q^\zeta q^\sigma g^{\gamma\rho} + 2q^2 g^{\gamma\sigma} g^{\zeta\rho} + 2q^2 g^{\gamma\rho} g^{\zeta\sigma} \\
&- 5q^2 g^{\gamma\zeta} g^{\rho\sigma} + 16q^\rho p^\zeta g^{\gamma\sigma} - 36q^\rho p^\sigma g^{\gamma\zeta} + 16q^\sigma p^\zeta g^{\gamma\rho} - 36q^\sigma p^\rho g^{\gamma\zeta} \\
&+ p^\gamma\left(-5q^\zeta g^{\rho\sigma} + 10q^\rho g^{\zeta\sigma} + 10q^\sigma g^{\zeta\rho} + 26p^\zeta g^{\rho\sigma} - 26p^\rho g^{\zeta\sigma} - 26p^\sigma g^{\zeta\rho}\right) \\
&+ q^\gamma\left(7q^\zeta g^{\rho\sigma} - 12q^\rho g^{\zeta\sigma} - 12q^\sigma g^{\zeta\rho} - 21p^\zeta g^{\rho\sigma} + 26p^\rho g^{\zeta\sigma} + 26p^\sigma g^{\zeta\rho}\right) \\
&- 12g^{\gamma\sigma} g^{\zeta\rho}(q\cdot p) - 12g^{\gamma\rho} g^{\zeta\sigma}(q\cdot p) + 24g^{\gamma\zeta} g^{\rho\sigma}(q\cdot p) \\
&-26p^\zeta p^\rho g^{\gamma\sigma} - 26p^\zeta p^\sigma g^{\gamma\rho} + 72p^\rho p^\sigma g^{\gamma\zeta} + 12p^2 g^{\gamma\sigma} g^{\zeta\rho} + 12p^2 g^{\gamma\rho} g^{\zeta\sigma} - 24p^2 g^{\gamma\zeta} g^{\rho\sigma}\Big],
\end{aligned}
\tag{3.53}
$$

where the divergence result of $X^{(b2)}$ is found using the same method as for $X^{(b1)}$ by utilizing the divergence properties of the Passarino-Veltman scalar integrals. Substituting the sub-diagram in Eq. (3.51) with the result of $X^{(b2)}$ generates the second counter-term for diagram (b):

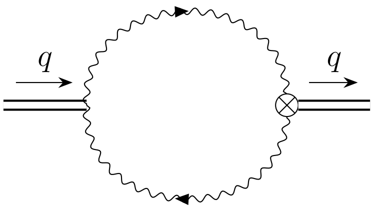

$= \Pi_{ct}^{(b2)}$

$$
\begin{aligned}
&\Pi_{ct}^{(b2)}(Q^2 \equiv -\,q^2) \\
&\qquad = iP^{\mu\nu\rho\sigma}(q)\int \frac{d^D p}{(2\pi)^D} Z_{ab}^{\mu\nu\alpha\beta}(p,q-p)\; D_{ac}^{\alpha\gamma}(p)\; D_{bm}^{\beta\zeta}(q-p)\; X_{cm}^{(b2)\rho\sigma\gamma\zeta}(q,p) \\
&\qquad = \frac{7\,\alpha_s\,Q^4}{28800\,\pi^3} L\left(-15L + \frac{2084}{7} - \frac{30}{\epsilon}\right),\; L = \log\left(\frac{Q^2}{\nu^2}\right).
\end{aligned}
\tag{3.54}
$$

We now have the symmetric counter-term diagram. The counter-term diagrams from both $X^{(b1)}$ (Eq. (3.50)) and $X^{(b2)}$ (Eq. (3.54)) divergences are identical as expected because the diagram correlators are only dependent on the squared product of the external momentum ($q^2$), thus the change in direction of $q$ in the NLO gluon exchange diagram would not affect the result of its counter-term diagram correlation functions.

For the diagrammatic renormalization method, one is required to subtract all counter-term diagrams from the corresponding bare diagram as introduced in Eq. (3.20). Hence, both counter-term diagrams $\Pi_{ct}^{(b1)}$ (Eq. (3.50)) and $\Pi_{ct}^{(b2)}$ (Eq. (3.54)) need to be subtracted from the bare diagram (b) $\Pi_{bare}^{(b)}$ (Eq. (3.43)) to completely cancel the $\frac{L}{\epsilon}$ divergence from the bare correlator.

$$\begin{aligned}\Pi_{renorm}^{(b)} &= \Pi_{bare}^{(b)} - \sum_{\gamma=1}^{2} \Pi_{ct}^{(b\gamma)} \\ &= \frac{\alpha_s Q^4}{28800\pi^3} L\left(-210L - 1151\right),\ L = \log\left(\frac{Q^2}{\nu^2}\right)\end{aligned} \tag{3.55}$$

#### 3.2.3.6 Butterfly Topology (diagram i)

Our second to last case is the butterfly topology. The bare correlation function for diagram (i) is found by calculating its corresponding Feynman integral:

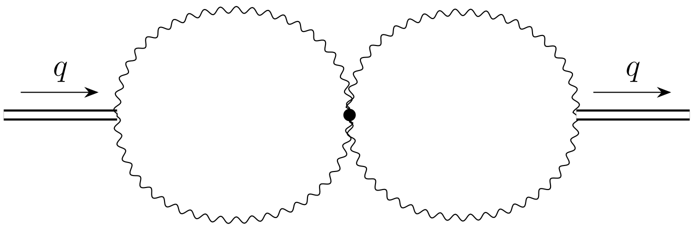

$$= \Pi_{bare}^{(i)},$$

$$\begin{aligned}\Pi_{bare}^{(i)} = iP^{\mu\nu\rho\sigma}(q) \int \frac{d^D k}{(2\pi)^D} \int \frac{d^D p}{(2\pi)^D}\, & Z_{ab}^{\mu\nu\alpha\beta}(q-k,k)\ D_{ac}^{\alpha\gamma}(q-k)\ D_{bd}^{\beta\zeta}(k)\ H_{cedf}^{\gamma\phi\zeta\lambda} \\ & D_{eg}^{\phi\chi}(q-p)\ D_{fh}^{\lambda\tau}(p)\ Z_{gh}^{\rho\sigma\chi\tau}(p-q,-p)\end{aligned} \tag{3.56}$$

$$= \frac{\alpha_s\, Q^4}{36\pi^3} L\left(3L + \frac{3}{\epsilon} - 10\right),\ L = \log\left(\frac{Q^2}{\nu^2}\right), Q^2 \equiv -q^2.$$

The butterfly topology has two symmetric non-local divergences. One of which is isolated in the dotted box in the Feynman diagram as shown below in Eq. (3.57),

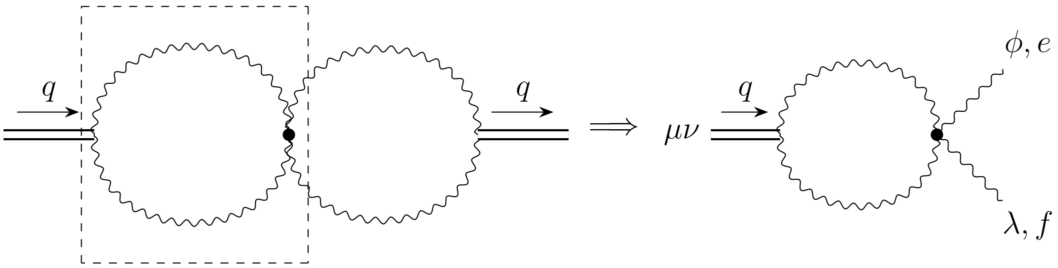

$$= X_{ef}^{(i1)\mu\nu\phi\lambda}, \tag{3.57}$$

where the divergent part of $X^{(b1)}$ is extracted using the technique invovling the Passarino-Veltman scalar integrals as introduced in section 3.2.3.5:

$$\begin{aligned} X_{ef}^{(i1)\mu\nu\phi\lambda}(q) &= \int \frac{d^D k}{(2\pi)^D}\, Z_{ab}^{\mu\nu\alpha\beta}(q-k,k)\, D_{ac}^{\alpha\gamma}(q-k)\, D_{bd}^{\beta\zeta}(k)\, H_{cedf}^{\gamma\phi\zeta\lambda} \\ &\xrightarrow{1/\epsilon} -\frac{\alpha_s}{16\pi\epsilon}\delta^{ef}\Big(2q^\lambda\left(q^\mu g^{v\phi} + q^\gamma g^{\mu\phi} - q^\phi g^{\mu v}\right) \\ &+g^{\lambda\phi}\left(q^2 g^{\mu v} + 4q^\mu q^v\right) + 2g^{\lambda v}\left(q^\mu q^\phi - 2q^2 g^{\mu\phi}\right) + 2g^{\lambda\mu}\left(q^v q^\phi - 2q^2 g^{v\phi}\right)\Big). \end{aligned} \tag{3.58}$$

Substituting the sub-diagram in Eq. (3.57) with the divergent part of $X^{(b1)}$, one have the first counter-term for diagram (i):

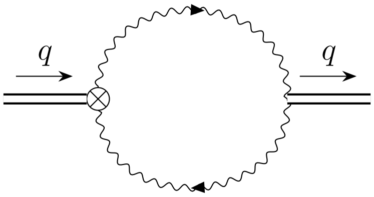

$$= \Pi_{ct}^{(i1)}$$

$$\begin{aligned} &\Pi_{ct}^{(i1)}(Q^2 \equiv -q^2) \\ &= iP^{\mu\nu\rho\sigma}(q)\int \frac{d^D p}{(2\pi)^D}\, X_{ef}^{(i1)\mu\nu\phi\lambda}(q)\, D_{eg}^{\phi\chi}(q-p)\, D_{fh}^{\lambda\tau}(p)\, Z_{gh}^{\rho\sigma\chi\tau}(p-q,-p) \\ &= \frac{\alpha_s\, Q^4}{144\,\pi^3} L\left(3L + \frac{6}{\epsilon} - 10\right),\ L = \log\left(\frac{Q^2}{\nu^2}\right). \end{aligned} \tag{3.59}$$

Eq. (3.59) gives the counter-term diagram generated from the sub-divergence embedded in the left half of diagram (i) (Eq. (3.57)). There is also a symmetric sub-divergence located in the right half of the diagram (i) topology shown below:

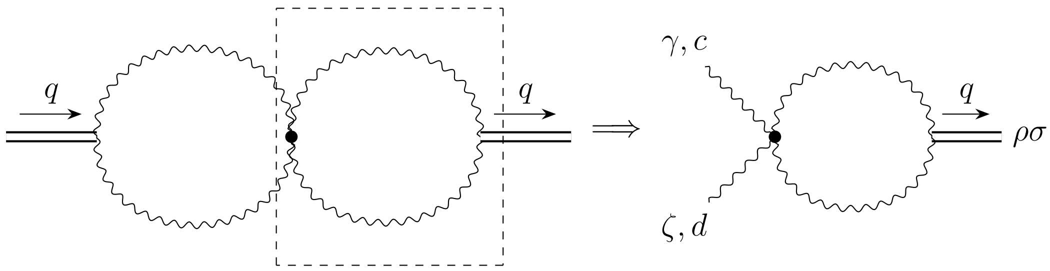

$$= X_{cd}^{(i2)\rho\sigma\gamma\zeta}, \tag{3.60}$$

$$X_{cd}^{(i2)\rho\sigma\gamma\zeta}(q) = \int \frac{d^D p}{(2\pi)^D}\, H_{cedf}^{\gamma\phi\zeta\lambda}\, D_{eg}^{\phi\chi}(q-p)\, D_{fh}^{\lambda\tau}(p)\, Z_{gh}^{\rho\sigma\chi\tau}(p-q,-p)$$

$$\xrightarrow{1/\epsilon} -\frac{\alpha_s}{16\pi\epsilon}\delta^{cd}\Bigg(2q^\zeta q^\sigma g^{\gamma\rho} + 4q^\rho q^\sigma g^{\gamma\zeta} + 2q^\gamma\left(-q^\zeta g^{\rho\sigma} + q^\rho g^{\xi\sigma} + q^\sigma g^{\zeta\rho}\right) \tag{3.61}$$

$$-4q^2 g^{\gamma\rho} g^{\zeta\sigma} + q^2 g^{\gamma\zeta} g^{\rho\sigma} + 2g^{\gamma\sigma}\left(q^\zeta q^\rho - 2q^2 g^{\zeta\rho}\right)\Bigg).$$

Hence, one may construct the second counter-term diagram for diagram (i) by replacing the sub-divergence in Eq. (3.60) with $X^{(i2)}$:

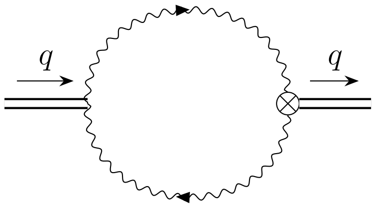

$$= \Pi_{ct}^{(i2)}$$

$$\Pi_{ct}^{(i2)}(Q^2 \equiv -q^2)$$

$$= iP^{\mu\nu\rho\sigma}(q)\int \frac{d^D k}{(2\pi)^D}\, Z_{ab}^{\mu\nu\alpha\beta}(q-k,k)\, D_{ac}^{\alpha\gamma}(q-k)\, D_{bd}^{\beta\zeta}(k)\, X_{cd}^{(i2)\rho\sigma\gamma\zeta}(q) \tag{3.62}$$

$$= \frac{\alpha_s Q^4}{144\,\pi^3}L\left(3L + \frac{6}{\epsilon} - 10\right),\ L = \log\left(\frac{Q^2}{\nu^2}\right).$$

The symmetric divergences $X^{(i1)}$ (Eq. (3.58)) and $X^{(i2)}$ (Eq. (3.61)) are identical as expected, similarly to the gluon exchange diagram (b) in section 3.2.3.5. Subtracting all the possible counter-term diagrams (Eqs. (3.59) and (3.62)) from the bare diagram (i) (Eq. (3.56)), the diagrammatic renormalization method gives the renormalized the correlator for the butterfly topology:

$$\begin{aligned}\Pi^{(i)}_{renorm} &= \Pi^{(i)}_{bare} - \sum_{\eta=1}^{2} \Pi^{(i\eta)}_{ct} \\ &= \frac{\alpha_s Q^4}{72\pi^3} L\left(3L - 10\right),\ L = \log\left(\frac{Q^2}{\nu^2}\right).\end{aligned} \tag{3.63}$$

#### 3.2.3.7 Vertex Diagrams (diagram g and h)

Finally, we have the vertex diagrams to finish our analysis and calculations on NLO tensor di-gluonium diagrams. Starting with diagram (g), the bare correlation function for NLO vertex diagram (g) is:

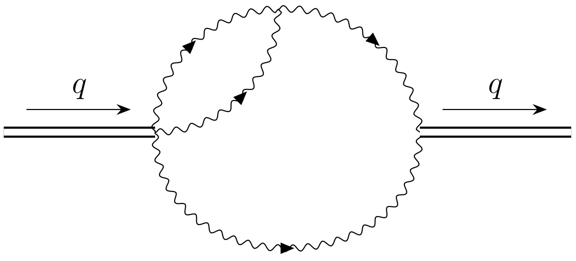

$$= \Pi^{(g)}_{bare},$$

$$\begin{aligned}\Pi^{(g)}_{bare}(Q^2 \equiv -q^2) &= iP^{\mu\nu\rho\sigma}(q) \int \frac{d^D k}{(2\pi)^D} \int \frac{d^D p}{(2\pi)^D} E^{\mu\nu\alpha\beta\gamma}_{abc}(-k, k-p, p-q)\ D^{\alpha\theta}_{ad}(k) \\ &\quad D^{\beta\phi}_{be}(p-k)\ V^{\theta\phi\chi}_{def}(-k, k-p, p)\ D^{\chi\lambda}_{fh}(p)\ D^{\gamma\tau}_{cj}(q-p)\ Z^{\rho\sigma\lambda\tau}_{hj}(-p, p-q) \\ &= \frac{3\alpha_s Q^4}{160\pi^3}\left[\left(-\xi - \frac{25}{6}\right)L^2 + \left(\xi^2 + \left(\frac{18}{5} - \frac{1}{\epsilon}\right)\xi + \frac{467}{24} - \frac{25}{6\epsilon}\right)L\right] \\ &= \frac{31\,\alpha_s\,Q^4}{320\pi^3} L\left(-L - \frac{1}{\epsilon} + \frac{2887}{620}\right),\ L = \log\left(\frac{Q^2}{\nu^2}\right), \quad \{\xi = 1 \text{ Feynman gauge}\}.\end{aligned} \tag{3.64}$$

We also have a local divergence isolated by a dotted box as shown in Eq. (3.65):

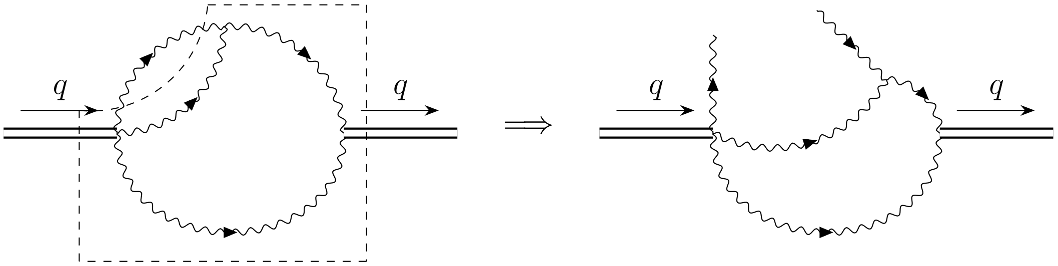

. (3.65)

The above sub-divergence will lead to a counter-term diagram which has the same tadpole topology as shown in Eq. (3.28), hence no physical contribution.

The only non-local sub-divergence in diagram (g) is isolated in the dotted box shown below in Eq. (3.66):

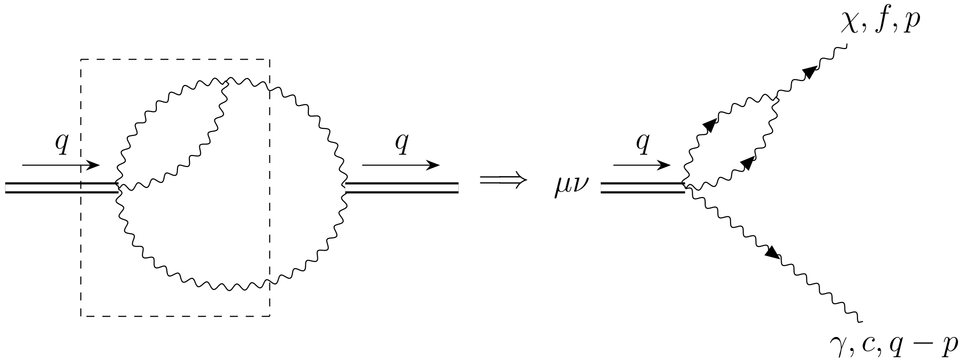

$$= X^{(g)\mu\nu\chi\gamma}_{cf}(q,p), \tag{3.66}$$

$$\begin{aligned}
X^{(g)\mu\nu\chi\gamma}_{cf}(q,p) &= \int \frac{d^D k}{(2\pi)^D}\, E^{\mu\nu\alpha\beta\gamma}_{abc}(-k,k-p,p-q)\; D^{\alpha\theta}_{ad}(k) \\
&\qquad D^{\beta\phi}_{be}(p-k)\; V^{\theta\phi\chi}_{def}(-k,k-p,p) \\
&\xrightarrow{1/\epsilon} \frac{1}{8\pi\epsilon}\alpha_s\delta^{cf}\bigg(-18q^\nu p^\mu g^{\gamma\chi} + 18q^\chi\left(p^\nu g^{\gamma\mu} + p^\mu g^{\gamma v} - p^\gamma g^{\mu v}\right) + 18q^\nu p^\gamma g^{\mu\chi} \\
&- 2p^\nu\left(9q^\mu g^{\gamma\chi} + 12p^\chi g^{\gamma\mu} - 28p^\mu g^{\gamma\chi} + 14p^\gamma g^{\mu\chi}\right) + 18q^\mu p^\gamma g^{\gamma\chi} \\
&- 18g^{\gamma v}g^{\mu\chi}(q\cdot p) + 18g^{\gamma\chi}g^{\mu v}(q\cdot p) - 18g^{\gamma\mu}g^{\gamma\chi}(q\cdot p) - 24p^\mu p^\chi g^{\gamma v} \\
&+22p^2 g^{\gamma v}g^{\mu\chi} + 26p^\gamma p^\chi g^{\mu\nu} - 28p^\gamma p^\mu g^{\gamma\chi} - 25p^2 g^{\gamma\chi}g^{\mu\nu} + 22p^2 g^{\gamma\mu}g^{\gamma\chi}\bigg).
\end{aligned} \tag{3.67}$$

The calculation of the above tensor $X^{(g)}$ requires taking contractions of 17 possible tensor combinations and solving the resulting 17 equations for their respective pre-factors. Then the counter-term diagram of the NLO vertex diagram (g) can then be found as shown below:

$$\begin{aligned}\Pi_{ct}^{(g)}(Q^2 \equiv -\, q^2) = i P^{\mu\nu\rho\sigma}(q) \int \frac{d^D p}{(2\pi)^D}\; & X_{cf}^{(g)\mu\nu\chi\gamma}(q,p) D_{fh}^{\chi\lambda}(p) \\ & D_{cj}^{\gamma\tau}(q-p)\; Z_{hj}^{\rho\sigma\lambda\tau}(-p, p-q) \end{aligned} \tag{3.68}$$

$$= \frac{31\, \alpha_s\, Q^4}{320\, \pi^3} L \left( -\frac{L}{2} + \frac{256}{465} - \frac{1}{\epsilon} \right),\; L = \log\left(\frac{Q^2}{\nu^2}\right).$$

The renormalized correlator for diagram (g) is:

$$\Pi_{renorm}^{(g)}(Q^2) = \Pi_{bare}^{(g)}(Q^2) - \Pi_{ct}^{(g)}(Q^2) = \frac{\alpha_s Q^4}{19200\pi^3} L\,(-930L + 7637)\,,\; L = \log\left(\frac{Q^2}{\nu^2}\right) \tag{3.69}$$

Looking at our vertex diagrams (g and h) shown below, we can see that they are completely symmetric. Since the results of the correlation functions for both topologies are only dependent on $q^2$ (as well as all our NLO diagrams discussed in this research), the change in the sign of the external momentum from $q$ to $-q$ would not affect the Feynman integral results. Thus, $\Pi^{(g)}$ should have the same result as $\Pi^{(h)}$. This property has been explicitly verified in our calculation.

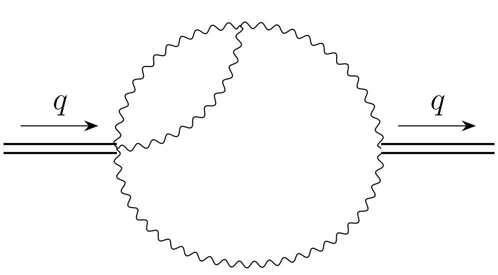

(g)

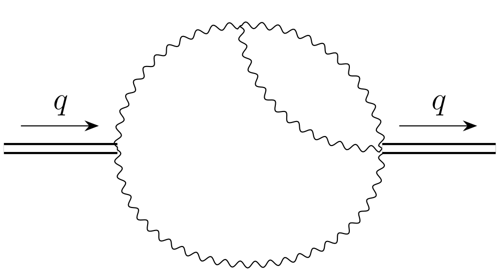

(h)

The bare, counter-term and renormalized correlators for the NLO vertex diagram (h) are listed below in Eqs. (3.70)-(3.72):

$$\Pi^{(h)}_{bare}(Q^2) = \frac{3\alpha_s Q^4}{160\pi^3}\left[\left(-\xi - \frac{25}{6}\right)L^2 + \left(\xi^2 + \left(\frac{18}{5} - \frac{1}{\epsilon}\right)\xi + \frac{467}{24} - \frac{25}{6\epsilon}\right)L\right]$$

$$= \frac{31\,\alpha_s\,Q^4}{320\pi^3}L\left(-L - \frac{1}{\epsilon} + \frac{2887}{620}\right), \quad \{\xi = 1 \text{ Feynman gauge}\} \tag{3.70}$$

$$\Pi^{(h)}_{ct}(Q^2) = \frac{31\,\alpha_s\,Q^4}{320\,\pi^3}L\left(-\frac{L}{2} + \frac{256}{465} - \frac{1}{\epsilon}\right), \tag{3.71}$$

$$\begin{aligned}\Pi^{(g)}_{renorm}(Q^2) &= \Pi^{(h)}_{bare}(Q^2) - \Pi^{(h)}_{ct}(Q^2)\\ &= \frac{\alpha_s Q^4}{19200\pi^3}L\left(-930L + 7637\right),\ L = \log\left(\frac{Q^2}{\nu^2}\right), Q^2 \equiv -q^2.\end{aligned} \tag{3.72}$$

With the above results for the last NLO diagram addressed, we have all of the 8 bare and renormalized $2^{++}$ tensor gluonium correlation function diagrams to NLO.

#### 3.2.3.8 Gauge Dependency and Summation

In section 3.2.3.1-3.2.3.7, we discussed and calculated all 8 possible non-zero NLO diagrams for $2^{++}$ tensor gluonium. To find the NLO contribution for the correlation function, one simply needs to sum all the diagrams up. Therefore, the complete NLO $2^{++}$ tensor gluonium correlation function can be found by using the results listed: Eqs. (3.43), (3.26), (3.33), (3.38), (3.21), (3.64) and (3.70).

$$\begin{aligned}\Pi^{NLO}(Q^2)_{bare} &= \sum_{m=b}^{i}\Pi^{(m)}_{bare}\\ &= -\frac{\alpha_s}{900\pi^3}Q^4\log\left(\frac{Q^2}{\nu^2}\right)\left[\left(15\log\left(\frac{Q^2}{\nu^2}\right) + \frac{15}{\epsilon} - 64\right)n_f - 75\right],\end{aligned} \tag{3.73}$$

where the bare NLO $2^{++}$ tensor gluonium correlation function is independent of the gauge parameter $\xi$. $\Pi^{NLO}$ is in $\overline{MS}$ scheme, dimensional regularization scheme of $D = 4 + 2\epsilon$ and chiral limit of $n_f$ light quark flavours.

To find the total NLO $2^{++}$ tensor gluonium renormalized correlation function diagrams, one needs to sum all the results from different NLO renormalized diagrams:

$$\begin{aligned}\Pi^{NLO}_{renorm}(Q^2) &= \sum_{m=b}^{i} \Pi^{(m)}_{renorm} \\ &= \frac{\alpha_s}{1800\pi^3} Q^4 \log\left(\frac{Q^2}{\nu^2}\right)\left[\left(101 - 15\log\left(\frac{Q^2}{\nu^2}\right)\right) n_f + 150\right].\end{aligned} \tag{3.74}$$

The contributions of each diagram are organized in Table. 3.1.

We also calculated and verified the LO correlator of tensor gluonium $\Pi^{LO} = -\frac{Q^4}{20\pi^2}\log\left(\frac{Q^2}{\nu^2}\right)$ from [131]. The renormalized correlator corrected to NLO using the diagrammatic renormalization method can be written in the form of correction to $\Pi^{LO}$ as follows:

$$\begin{aligned}\Pi_{renorm} &= \Pi^{NLO}_{renorm} + \Pi^{LO} \\ &= \Pi^{LO}\left[1 + \frac{\alpha_s}{\pi}\left(\frac{n_f}{6}\log\left(\frac{Q^2}{\nu^2}\right) - \frac{101 n_f + 150}{90}\right)\right].\end{aligned} \tag{3.75}$$

In the next section, we will demonstrate the equivalence of the result (3.75) using conventional renormalization method.

### 3.2.4 Method of Renormalization-Induced Diagrams

As one can see from Sec. 3.2.3, the diagrammatic renormalization method requires multiple steps of calculation for each diagram. It is a good method for the renormalization of individual diagrams. Since we are looking for the overall NLO contribution to tensor di-gluonium $2^{++}$, there is another approach to implementing renormalization-induced diagrams. Referring to [128], the renormalized meson-gluonium currents have the following forms:

$$\begin{aligned}J^{\mu\nu}_{q,R} &= Z_{11} J^{\mu\nu}_{q,B} + Z_{12} J^{\mu\nu}_{g,B}, \\ J^{\mu\nu}_{g,R} &= Z_{21} J^{\mu\nu}_{q,B} + Z_{22} J^{\mu\nu}_{g,B},\end{aligned} \tag{3.76}$$

where the renormalization constants $Z_{ij}$ are in $\overline{\mathrm{MS}}$ scheme ($D = 4 + 2\epsilon$, converted from [128] convention of $D = 4 - \epsilon$) and $J^{\mu\nu}_{q,B}$ is the bare quark current:

$$J^{\mu\nu}_{q,B} = i\,\overline{q}\left(\gamma^{\mu} D^{\nu} + \gamma^{\nu} D^{\mu}\right) q. \tag{3.77}$$

Since any crossed term involving $J^{\mu\nu}_{q,B}$ in $\langle J^{\mu\nu}_{g,R}(x_1) J^{\mu\nu}_{g,R}(x_2)\rangle$ will lead to higher-order contribution at $\mathcal{O}\left(\alpha_s/\pi\right)^2$ [128], the only renormalization constant needed is $Z_{22}$ that connects the bare gluon current $J^{\mu\nu}_{g,B}$ to renormalized gluon current $J^{\mu\nu}_{g,R}$:

$$Z_{22} = 1 + R_{22} = 1 - \frac{\alpha_s}{6\pi\epsilon} n_f. \tag{3.78}$$

The first term of 1 in Eq. (3.78) will simply carry the bare gluonium diagrams forward. And the second term $R_{22} = -\frac{\alpha_s}{6\pi\epsilon} n_f$ will construct a new diagram term to renormalize the divergences from the carried bare diagrams. These new diagrams built with the renormalization constants are called renormalization-induced diagrams. Due to the symmetry of the tensor gluonium LO diagram, we will have two renormalization-induced diagrams (diagram j and k), where the renormalization constant will be embedded in a term which is proportional to the current-to-2-gluon vertex. Starting from calculating the Feynman diagram j as shown below with the renormalization constant $R_{22}$ is represented as the shaded circle ▨:

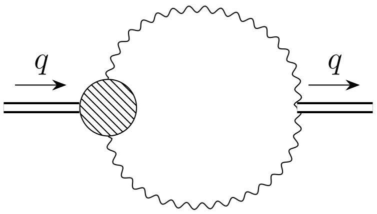

$$= \Pi^{(j)}_{bare},$$

$$\begin{aligned}
\Pi^{(j)}_{bare}(Q^2 \equiv -q^2) = iP^{\mu\nu\rho\sigma}(q) \int \frac{d^D k}{(2\pi)^D} \Big(R_{22}\; Z^{\mu\nu\alpha\beta}_{ab}(q-k,k)\Big) \\
D^{\alpha\gamma}_{ac}(q-k)\; D^{\beta\zeta}_{bd}(k)\; Z^{\rho\sigma\gamma\zeta}_{cd}(k-q,-k) \\
= \frac{\alpha_s Q^4}{1200\pi^3} n_f L \left(5L + \frac{10}{\epsilon} - 9\right),\; L = \log\left(\frac{Q^2}{\nu^2}\right).
\end{aligned} \tag{3.79}$$

Similarly, $R_{22}$ can also be built in the current-to-2-gluon on the right side of the diagram as follows:

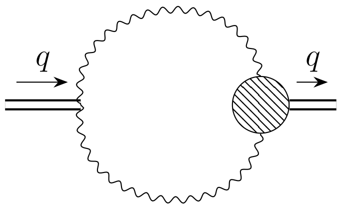

$$= \Pi^{(k)}_{bare},$$

$$\Pi^{(k)}_{bare}(Q^2 \equiv -q^2) = iP^{\mu\nu\rho\sigma}(q) \int \frac{d^D k}{(2\pi)^D}$$
$$Z^{\mu\nu\alpha\beta}_{ab}(q-k,k)\ D^{\alpha\gamma}_{ac}(q-k)\ D^{\beta\zeta}_{bd}(k)\ \left(R_{22} Z^{\rho\sigma\gamma\zeta}_{cd}(k-q,-k)\right) \tag{3.80}$$
$$= \frac{\alpha_s Q^4}{1200\pi^3} n_f L \left(5L + \frac{10}{\epsilon} - 9\right),\ L = \log\left(\frac{Q^2}{\nu^2}\right).$$

Both renormalization-induced diagrams have the same results as they are, again, symmetric under the change of external momentum $q$'s direction and both diagrams are only dependent on $q^2$. Now based on Eq. (3.78), we should have the renormalized tensor di-gluonium current by summing the NLO bare diagrams and the renormalization-induced diagrams found with $R_{22}$:

$$\Pi^{NLO}_{R}(Q^2) = \sum_{m=b}^{k} \Pi^{(m)}_{bare} = \frac{\alpha_s}{1800\pi^3} Q^4 \log\left(\frac{Q^2}{\nu^2}\right)\left[\left(101 - 15\log\left(\frac{Q^2}{\nu^2}\right)\right) n_f + 150\right]. \tag{3.81}$$

Comparing Eqs. (3.74) and (3.81), we reached the same result in renormalizing the tensor gluonium $2^{++}$ with both methods. This is a powerful check on the accuracy of our NLO renormalized correlator results.

## 3.3 Non-perturbative Contribution

QCD condensates, as detailed in Sec. 2.5.1, described the low-energy non-perturbative sector of QCD vacuum in the method of QCDSR. In this section, two techniques are used to evaluate the contribution to specific gluon condensate terms ($D = 4$ and 6) in the OPE:

1. The plane-wave method extracts the gluon condensate by applying one-gluon states to the current operators (*e.g.,* $|\epsilon, k\rangle$) [82,141]. The non-trivial term involving both quark and gluon fields from the correlation function is annihilated by the process of vacuum averaging in the method [94,142]. This step of averaging over the momentum direction is designed to simulate the effect of vacuum. Using Wilson's operator identity [90], the condensate coefficients $C_n$ are calculated perturbatively.
2. The coordinate-space method [44,141,143], on the other hand, expands the condensate terms in coordinate space after the Wick's expansion in OPE. Since the gluon condensate contribution is gauge invariant (so does the correlator), the results from both methods will be in agreement even though the coordinate-space method does not rely on operator identities.

The two techniques for OPE are reviewed in depth regarding their equivalency and respective advantages in Ref. [94]. We also used the RG invariance property of $\langle \alpha_s G^2 \rangle$ to find $D = 4$ NLO condensate contribution.

### 3.3.1 Dimension-Four Gluon Condensates $\langle G^2 \rangle$

To find LO contribution of dimension-four condensates $\langle \alpha_s G^2 \rangle \equiv \alpha_s \langle \Omega \left| : G^a_{\mu\nu} G^{\mu\nu}_a : \right| \Omega \rangle$ using plane-wave method, one may refer to the methodology processes in Ref. [94]. The gluonic dimension-four condensate contribution are represented by the coefficient $C_4$ from the two-point correlation function OPE shown in Eq. (2.62). This coefficient can be extracted by applying a gluon state $|\epsilon, k\rangle$ to the composite operators:

$$\psi(q^2) = P_{\mu\nu\rho\sigma} \int d^4x \, e^{iqx} \left\langle \epsilon, k \left| \mathcal{T} J^g_{\mu\nu}(x) J^g_{\rho\sigma}(0)^\dagger \right| \epsilon, k \right\rangle , \tag{3.82}$$

the normalized projection $\psi(q^2)$ is then

$$\psi(q^2) = 4\, C_4 \left( \epsilon^2 k^2 - (\epsilon \cdot k)^2 \right) + \cdots , \tag{3.83}$$

where $\cdots$ denotes the terms annihilated during the vacuum averaging step.

The LO condensate diagram shown in Fig. 3.2 (Sec. 3.4.4) is calculated using the FeynCalc. Averaging over external momentum $q$ by expanding then contracting with $k_\gamma$ and $k_\theta$, where $\gamma, \theta$ are randomly chosen Lorentz indices. The LO condensate contribution for $2^{++}$ tensor digluonium contribution is

$$C_4 = \frac{2}{(D-1)D}, \tag{3.84}$$

which disappears in later Laplace sum rules analysis when taking derivatives of two-point functions.

The LO contribution was also evaluated using the coordinate-space method [94]. We applied Wick's theorem on the two-point function:

$$\begin{aligned} &\langle 0 \left| \mathcal{T} J^g_{\mu\nu}(x) J^g_{\rho\sigma}(0)^\dagger \right| 0 \rangle \\ &\qquad = \left\langle 0 \left| \mathcal{C}^{\alpha\beta\gamma\delta}_{\mu\nu} \, \mathcal{C}^{\eta\omega\lambda\tau}_{\rho\sigma} \mathcal{T} \left( \overline{G^a_{\alpha\beta}(x) G^b_{\gamma\delta}(x) G^c_{\eta\omega}}(0) G^d_{\lambda\tau}(0) \right) \right| 0 \right\rangle \\ &\qquad = \mathcal{C}^{\alpha\beta\gamma\delta}_{\mu\nu} \, \mathcal{C}^{\eta\omega\lambda\tau}_{\rho\sigma} \left\langle 0 \left| \mathcal{T} \left( G^a_{\alpha\beta}(x) G^c_{\eta\omega}(0) \right) \right| 0 \right\rangle \left\langle 0 \left| : G^b_{\gamma\delta}(x) G^d_{\lambda\tau}(0) : \right| 0 \right\rangle , \end{aligned} \tag{3.85}$$

where $\mathcal{C}^{\alpha\beta\gamma\delta}_{\mu\nu}$ acts as a projection operator for the gluonic currents so that it can be written as $J^g_{\mu\nu}(x) = \mathcal{C}^{\alpha\beta\gamma\delta}_{\mu\nu} \, G_{\alpha\beta}(x) \, G_{\gamma\delta}(x)$. The fully contracted term can be found with the gluon field strength tensor and gluon propagator expression [144]:

$$\overline{G^a_{\alpha\beta}(x) G^c_{\eta\omega}}(0) \equiv -i \int \frac{d^D p}{(2\pi)^D} \frac{\delta^{ac}}{p^2} e^{-ip\cdot x} \left( g_{\beta\omega} p_\alpha p_\eta + g_{\alpha\eta} p_\beta p_\omega - g_{\beta\eta} p_\alpha p_\omega - g_{\alpha\omega} p_\beta p_\eta \right), \tag{3.86}$$

while the normal ordering VEV term is also expressed in terms of a linear combination of metric tensors [44]:

$$\begin{aligned} \left\langle 0 \left| : G^b_{\gamma\delta}(x) G^d_{\lambda\tau}(0) : \right| 0 \right\rangle &= \frac{\delta^{bd}}{8} \langle G^2 \rangle \frac{1}{D^2 - D} \left( g_{\delta\gamma} g_{\gamma\tau} - g_{\gamma\lambda} g_{\delta\tau} \right) \\ &\qquad \text{with } \left\langle G^2 \right\rangle \equiv \left\langle 0 \left| : G^a_{\mu\nu}(0) G^a_{\mu\nu}(0) : \right| 0 \right\rangle . \end{aligned} \tag{3.87}$$

The result of Eq. (3.85) summed with its other 3 possible permutations agrees with the plane-wave method result in (3.84).

We used a different approach, the RG equation, to evaluate the NLO gluon condensate contribution. Following the method of Ref. [145], the dimension-four gluon condensate term $\Pi_{G^2} = C_4^{\text{all orders}}\langle\alpha_s G^2\rangle$ obeys RG equation:

$$\left\{\nu\frac{\partial}{\partial\nu} + \beta(\alpha)\alpha\frac{\partial}{\partial\alpha_s} - 2\gamma_\rho\right\}\Pi_{G^2} = 0, \tag{3.88}$$

where taking the leading order contributions for the anomalous dimension $\gamma_\rho = \gamma_1\frac{\alpha_s}{\pi} = -\frac{n_f}{3}\frac{\alpha_s}{\pi}$ [14] and beta function $\beta(\alpha_s) = \beta_1\frac{\alpha_s}{\pi}$. The condensate contribution of the correlation function in Eq. (3.88) to NLO is

$$\Pi_{G^2} = \langle\alpha_s G^2\rangle\left[\frac{b_{00}}{\alpha_s} + b_{10} + b_{11}\log\left(\frac{Q^2}{\nu^2}\right)\right], \tag{3.89}$$

where $b_{00}, b_{10}, b_{11}$ are prefactors for each term. One can tell from the order of $\alpha_s$ that $b_{00}$ corresponds to LO result giving $\frac{2}{(D-1)D} = \frac{1}{6}$ from above. Substituting Eq. (3.89) in Eq. (3.88), we solve for

$$b_{11} = -\frac{b_{00}}{2\pi}(\beta_1 + 2\gamma_1). \tag{3.90}$$

Since only $b_{11}$ logarithmic term will remain non-zero after Borel transform, the NLO condensate contribution to $2^{++}$ tensor digluonium is

$$\Pi_{G^2}^{\text{NLO}} = \frac{\alpha_s}{\pi}\langle G^2\rangle\left(\frac{11}{24} + \frac{n_f}{36}\right)\log\left(\frac{Q^2}{\nu^2}\right). \tag{3.91}$$

### 3.3.2 Dimension-Six Gluon Condensates $\langle G^3\rangle$

One can again use the coordinate-space method to evaluate dimension-six di-gluonium condensate LO contribution with modification from Section 3.3.1. There are three types of LO Feynman diagrams to take into consideration for $\langle G^3\rangle$ which are listed in Fig 3.3. We start calculating the diagram type in the first row and third row of Fig. 3.3. Apart from the gluon propagator and other required Feynman rules (see Appendix E), one needs an additional

VEV operator for $\langle G^3\rangle$. We are using a derived expression from Ref. [100]:

$$\begin{aligned} &f^{nmt}\left\langle : G^n_{\mu\nu}G^m_{\rho\sigma}G^t_{\omega\tau} :\right\rangle \\ &\qquad = \langle G^3\rangle \frac{1}{D(D-1)(D-2)}\left(g_{\mu\rho}g_{\nu\omega}g_{\sigma\tau} - g_{\nu\rho}g_{\mu\omega}g_{\sigma\tau} - g_{\mu\sigma}g_{\nu\omega}g_{\rho\tau} + g_{\nu\sigma}g_{\mu\omega}g_{\rho\tau}\right. \\ &\qquad\qquad \left. - g_{\mu\rho}g_{\nu\tau}g_{\sigma\omega} + g_{\nu\rho}g_{\mu\tau}g_{\sigma\omega} + g_{\mu\sigma}g_{\nu\tau}g_{\rho\omega} - g_{\nu\sigma}g_{\mu\tau}g_{\rho\omega}\right). \end{aligned} \tag{3.92}$$

We also need an propagator from abelian gluon tensor $G^a_{\mu\rho}(x)$ to gluonic field $A^b_\lambda(y)$ from Ref. [144] to construct our Feynman integral:

$$\overline{G^a_{\mu\rho}(x)A^b_\lambda}(y) = -\int \frac{d^Dp}{(2\pi)^D}\frac{\delta^{ab}}{p^2}e^{-ip\cdot(y-x)}\left(g_{\lambda\sigma}p_\nu - g_{\lambda\nu}p_\sigma\right). \tag{3.93}$$

Including all possible index permutations of contracted fields and normal ordering, the calculation process does not differ much from dimension-four condensate calculation only lengthier.

The diagrams in the second row of Fig. 3.3 are called equations of motion diagrams. We need a VEV operator that includes two gluonic fields and two gluonic strength tensors [100]:

$$\begin{aligned} &\mathrm{Tr}\left[\langle : [D_\mu,[D_\nu,G_{\rho\sigma}]]\,G_{\omega\tau} :\rangle\right] \\ &\quad = -\frac{g^3\langle G^3\rangle}{2d\,(d^2-4)}\left(2g_{\mu\nu}\left(g_{\rho\omega}g_{\sigma\tau} - g_{\sigma\omega}g_{\rho\tau}\right) \quad + g_{\nu\tau}\left(g_{\rho\omega}g_{\sigma\mu} - g_{\sigma\omega}g_{\rho\mu}\right)\right. \\ &\quad \left. - g_{\nu\omega}\left(g_{\rho\tau}g_{\sigma\mu} - g_{\sigma\tau}g_{\rho\mu}\right) - \frac{3}{d-1}\left(g_{\mu\tau}\left(g_{\rho\omega}g_{\sigma\nu} - g_{\sigma\omega}g_{\rho\nu}\right) - g_{\mu\omega}\left(g_{\rho\tau}g_{\sigma\nu} - g_{\sigma\tau}g_{\rho\nu}\right)\right)\right). \end{aligned} \tag{3.94}$$

All topologies in Fig. 3.3 considered, the total sum of dimension six condensates LO contribution is zero.

The equation of motion diagram also has a gluon propagator that gives a single denominator. Therefore, it cannot be computed with the plane-wave method due to the singularity it possesses [146]. However, in the plane-wave method, the other two types of diagram (first and third row of Fig. 3.3) still produce results that sum to zero. Therefore, the results from the plane-wave method and the coordinate-space method are still in agreement.

Having evaluated both the perturbative (Sec.3.2) and non-perturbative (Sec.3.3) contributions to the $2^{++}$ tensor- di-gluonium correlation function, the following sections summarize the published manuscript in *Phys. Lett. B* **849** (2024) 138454 (see also Ref. [14]).

## 3.4 Manuscript: $2^{++}$ Tensor di-gluonium from Laplace sum rules at NLO

**Abstract:** We evaluate the next-to-leading (NLO) corrections to the perturbative (PT) and $\langle\alpha_s G^2\rangle$ condensate and the LO constant term of the $\langle G^3\rangle$ contributions to the $2^{++}$ tensor di-gluonium two-point correlator. Using these results into the inverse Laplace transform sum rules (LSR) moments and their ratio, we estimate the mass and coupling of the lowest ground state. We obtain : $M_T = 3028(429)$ MeV and the renormalization group invariant (RGI) coupling $\hat{f}_T = 167(40)$ MeV within a vacuum saturation estimate of the $D = 8$ dimension gluon condensates ($k_G = 1$). We study the effect of $k_G$ on the result and find: $M_T = 3188(405)$ MeV and $\hat{f}_T = 164(28) MeV$ for $k_G = (3 \pm 2)$. Our result does not favour the pure gluonia/glueball nature of the observed $f_2(2010, 2300, 2340)$ states.

### 3.4.1 Introduction

Since the pioneering work of Novikov et al. (NSVZ) [133], some efforts have been made for improving the determination of the $2^{++}$ tensor di-gluonium mass and coupling either using a least-square fit method [147] or stability criteria [115, 131].[2] To Lowest Order (LO) of perturbative QCD (PT) and including the dimension $D = 8$ condensates estimated by (SVZ) [82] using vacuum saturation, the up-to-date results are [131][3]:

$$\begin{aligned} f_T|_{LO} &= 113(20) \text{ MeV}, \\ M_T|_{LO} &= 2.0(1) \text{ GeV}, \quad M_T|_{LO} \leq 2.7(4) \text{ GeV}. \end{aligned} \tag{3.95}$$

In this paper, we shall improve these LO results by including NLO corrections and checking the effect of the violation of vacuum saturation on the results.

---

[2] For recent reviews on the status of gluonia/glueballs, see *e.g.,* [108] and references quoted therein.

[3] Tachyonic gluon mass contribution though important for recovering the universal scale of the gluonia channels does not contribute in the unsubtracted sum rule analysis as it has no imaginary part [148]. We have rescaled the normalization of the coupling by a factor $\sqrt{2}$.

### 3.4.2 The QCD $2^{++}$ di-gluonium two-point function

We shall be concerned with the two-point function [4]:

$$\psi_T^{\mu\nu\rho\sigma}(q^2) \equiv i\int d^4x\, e^{iqx}\langle 0|\theta_G^{\mu\nu}(x)\,(\theta_G^{\rho\sigma})^\dagger\,(0)|0\rangle$$
$$= \left(P^{\mu\nu\rho\sigma} \equiv \eta^{\mu\rho}\eta^{\nu\sigma} + \eta^{\mu\sigma}\eta^{\nu\rho} - \frac{2}{n-1}\eta^{\mu\nu}\eta^{\rho\sigma}\right)\psi_T(q^2), \tag{3.96}$$

built from the gluon component of the energy-momentum tensor [5]:

$$\theta_G^{\mu\nu} = \alpha_s\Big[-G^{\mu,a}_{\alpha}G^{\nu\alpha}_{a} + \frac{1}{4}g^{\mu\nu}G^{a}_{\alpha\beta}G^{\alpha\beta}_{a}\Big]\,. \tag{3.97}$$

with:

$$\eta^{\mu\nu} \equiv g^{\mu\nu} - q^\mu q^\nu/q^2\ \ : \qquad P_{\mu\nu\rho\sigma}P^{\mu\nu\rho\sigma} = 2(n^2-n-2)\ , \tag{3.98}$$

where: $n = 4 + 2\epsilon$ is the space-time dimension used for dimensional regularization and renormalization. To LO and up to dimension $D = 8$ gluon condensates, the QCD expression is [133]:

$$\psi_T|_{LO}(q^2 \equiv -Q^2) = a_s^2\Big[-\frac{Q^4}{20}\log\frac{Q^2}{\nu^2} + \frac{5}{3}\pi^3\alpha_s\langle 2O_1 - O_2\rangle\Big], \tag{3.99}$$

where $a_s \equiv \alpha_s/\pi$ and :

$$O_1 = (f_{abc}G_{\mu\alpha}G_{\nu\alpha})^2\,, \qquad O_2 = (f_{abc}G_{\mu\nu}G_{\alpha\beta})^2\,. \tag{3.100}$$

Using the vacuum saturation hypothesis ($k_g = 1$), it reads [133]:

$$\langle 2O_1 - O_2\rangle \simeq -k_G\left(\frac{3}{16}\right)\langle G^2\rangle^2. \tag{3.101}$$

---

[4] For relations among different form factors, see e.g. [148].

[5] Notice the extra-factor $\alpha_s$ compared to the current used in Ref. [131] and references quoted therein.

We shall test the effect of this assumption by taking :

$$k_G \neq 1, \tag{3.102}$$

for an eventual violation of the factorization assumption like the one found for the $D = 6$ four-quark condensates (see e.g. [48,115,116,149]) where this assumption is violated by about a factor 5-6.

### 3.4.3 PT expression of the two-point function up to NLO

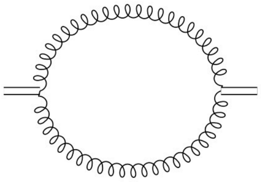

**Figure 3.1:** LO perturbative contribution to $\psi_T(Q^2)$.

- *Lowest Order (LO) contribution*

  It comes from the diagram in Fig. 3.1 and reads:

$$\psi_T^{pert}|_{LO} = -a_s^2 \frac{Q^4}{20} \log \frac{Q^2}{\nu^2} \tag{3.103}$$

- *Next-to-Leading (NLO) contribution*

  We use two approaches to perform the calculation:

  ◇ *Diagrammatic renormalization*

  This approach has been initiated in [72] for QCD sum-rule correlation functions. It requires an isolation of the sub-divergences arising from the one-loop sub-diagram(s) of an individual bare NLO diagram (see e.g., Ref. [68]) . Counter-term diagrams generated from the sub-divergences are then calculated and subtracted from the bare diagram to obtain the renormalized diagram. A self-consistency check of the method is the cancellation of non-local divergences in each diagram.

| Label | NLO Diagrams | Conventional |  | Diagrammatic |  |
|---|---|---|---|---|---|
|  |  | $A$ | $B$ | $A$ | $B$ |
| a) | 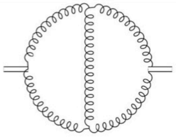 | $-\frac{7}{30}$ | $\frac{3017}{1800} - \frac{7}{30\epsilon}$ | $-\frac{7}{60}$ | $-\frac{1151}{1800}$ |
| b) | 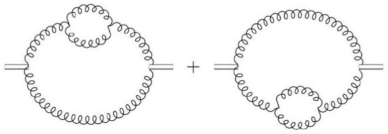 | $\frac{19}{10}$ | $-\frac{1321}{150} + \frac{19}{10\epsilon}$ | $\frac{19}{20}$ | $-\frac{2129}{300}$ |
| c) | 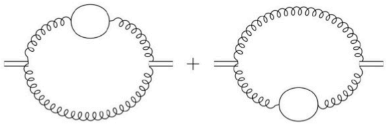 | $-\frac{4}{15}n_f$ | $\frac{256}{225}n_f - \frac{4}{15\epsilon}n_f$ | $-\frac{2}{15}n_f$ | $\frac{202}{225}n_f$ |
| d) | 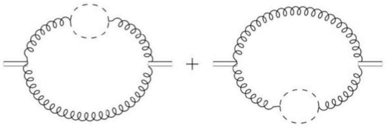 | $\frac{1}{10}$ | $-\frac{79}{150} + \frac{1}{10\epsilon}$ | $\frac{1}{20}$ | $-\frac{131}{300}$ |
| e) | 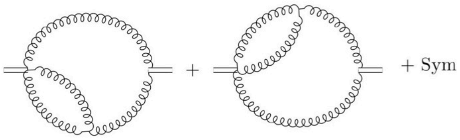 | $-\frac{31}{10}$ | $\frac{2887}{200} - \frac{31}{10\epsilon}$ | $-\frac{31}{20}$ | $\frac{7637}{600}$ |
| f) | 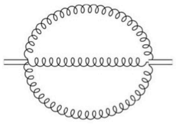 | $0$ | $-1$ | $0$ | $-1$ |
| g) | 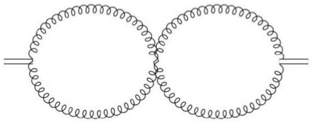 | $\frac{4}{3}$ | $-\frac{40}{9} + \frac{4}{3\epsilon}$ | $\frac{2}{3}$ | $-\frac{20}{9}$ |
| h) | 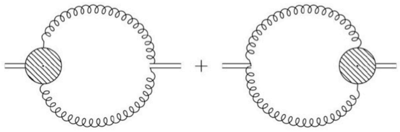 | $\frac{2}{15}n_f$ | $-\frac{6}{25}n_f + \frac{4}{15\epsilon}n_f$ | N/A | N/A |
| Total |  | $-\frac{2}{15}n_f$ | $\frac{202}{225}n_f + \frac{4}{3}$ | $-\frac{2}{15}n_f$ | $\frac{202}{225}n_f + \frac{4}{3}$ |

**Table 3.1:** NLO perturbative contribution to $\psi_T(Q^2)$ in conventional and diagrammatic renormalization methods. The quantities $A$ and $B$ are defined in Eq. (3.104). Diagrams h) are only used in conventional renormalization but are not applicable (N/A) in the diagrammatic method.

We shall be concerned with the bare diagrams a–g listed in Table 3.1 and their corresponding individual diagrammatically-renormalized contributions parametrized in Feynman gauge as:

$$\psi_T^{pert}|_{NLO}^{diag}(Q^2) = a_s^3 \left(\frac{Q^4}{16}\right) \log\frac{Q^2}{\nu^2}\left[A \log\frac{Q^2}{\nu^2} + B\right] \tag{3.104}$$

with : $a_s \equiv \alpha_s/\pi$. The sum of the contributions of the bare diagrammatically-renormalized diagrams a–g in Table 3.1 leads to the renormalized NLO two-point function for $n_f$ flavours:

$$\psi_T^{pert}|_{NLO}^{R}(Q^2) = a_s^3 \left(\frac{Q^4}{16}\right) L\left[-\frac{2}{15}n_f L + \left(\frac{4}{3} + \frac{202}{225}n_f\right)\right], \tag{3.105}$$

with: $L = \log\frac{Q^2}{\nu^2}$. Note that diagram h from Table 3.1 is not used in the diagrammatic renormalization method, but is crucial in the conventional renormalization approach for the cancellation of the non-local $(1/\epsilon)\log(Q^2/\nu^2)$ as we shall see in the next section.

◇ *The conventional approach*

Here, we calculate each QCD diagram using the standard Feynman approach (see e.g. [48,73,115]). We consider the renormalization of the gluonic current using the renormalization constant obtained in Ref. [128] for the current $\theta_g^{\mu\nu}/\alpha_s$:

$$Z_\psi = 1 - \left(\frac{n_f}{3}\right)\frac{a_s}{2\epsilon} \tag{3.106}$$

for $n = 4 + 2\epsilon$ dimensions to which corresponds the anomalous dimension:

$$\gamma_\psi \equiv \left(\gamma_1 = \frac{n_f}{3}\right) a_s + \cdots . \tag{3.107}$$

Taking into account the renormalization of $\alpha_s$:

$$Z_{\alpha_s} = 1 + \beta(\alpha_s)\frac{1}{2\epsilon}, \tag{3.108}$$

one can deduce the anomalous dimension of the current $\theta_g^{\mu\nu}$:

$$\gamma_\psi^\theta \equiv \left(\gamma_1^\theta = -\frac{11}{2}\right) a_s + \cdots \ . \tag{3.109}$$

The diagrams appearing in Table 3.1e) to g) are due to the non-abelian property of QCD where:

$$G_{\mu\nu}^{(a)} = \partial_\mu A_\nu^{(a)} - \partial_\nu A_\mu^{(a)} + g f^{abc} A_\mu^{(b)} A_\nu^{(c)} \tag{3.110}$$

The diagram in Table 3.1h) is induced by the off-diagonal term which arises due to the mixing of the $\bar{q}q$ and $G^2$ currents. Following [128, 150], such terms are necessary to cancel the non-local $(1/\epsilon)$ log $(Q^2/\nu^2)$ divergent terms appearing in the calculations given in Table 3.1. It is remarkable to notice that there is a systematic factor two difference for the coefficient A of diagrams a) to g) from the two approaches. The sum of the individual diagrams in Table 3.1 gives for the current normalized in Eq. 3.97 :

$$\psi_T^{RI}|_{NLO}(Q^2) = \frac{a_s^3}{600} Q^4 \log\frac{Q^2}{\nu^2}\, n_f \left[5\left(\log\frac{Q^2}{\nu^2} + \frac{2}{\epsilon}\right) - 9\right] \tag{3.111}$$

◇ *NLO PT results*

We have shown in the previous sections, that the diagrammatic and conventional approaches lead to the same result. The renormalized two-point function for $n_f$ flavours reads :

$$\begin{aligned} \psi_T^{pert}|_{NLO}^R(Q^2) \quad &\equiv \psi_T^{pert}|_{LO} + \psi_T^{pert}|_{NLO}^B + \psi_T^{RI}|_{NLO} \\ &= \psi_T^{pert}|_{LO}\left[1 + a_s\left(\frac{n_f}{6}\log\frac{Q^2}{\nu^2} - \frac{101 n_f + 150}{90}\right)\right], \end{aligned} \tag{3.112}$$

where $\psi_T^{pert}|_{LO}$ can be deduced from Eq. (3.99). One can notice that for gluodynamics $(n_f = 0)$, we recover the earlier result of [151].

### 3.4.4 Dimension-four gluon $\langle\alpha_s G_{\mu\nu}^a G_a^{\mu\nu}\rangle$ condensate

One can notice from Eq. 3.99 that, unlike the case of scalar and pseudoscalar gluonia [133], the contributions of the gluon condensates are only due to the $D = 8$ dimension.

- *LO contribution*

From the diagram in Fig. 3.2, we have checked that to LO the leading log-term does not contribute to the two-point function. The LO contribution comes from the constant term:

$$\psi_T^{G^2}|_{LO} = \frac{\alpha_s}{6}\langle\alpha_s G^2\rangle, \tag{3.113}$$

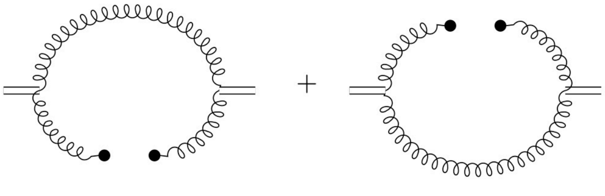

**Figure 3.2:** LO $\alpha_s G^2$ contribution to $\psi_T(Q^2)$.

where we have used two different approaches (plane wave and conventional one using the projection in Eq. 3.96). The non-zero value of this constant term raises the question of the validity of the null result obtained in Ref. [152] based on instantons for dual/antidual background fields. However, this term is harmless in the LSR analysis as it will disappear when one takes the different derivatives of the two-point functions.

- *NLO contribution*

The leading-log. contribution at NLO, can be derived from the renormalization group equation (RGE). Using the fact that the $\langle\alpha_s G^2\rangle$ obeys the RGE [145] (see different applications in section 4.4 of [73]) [6] :

$$\left\{-\frac{\partial}{\partial t}+\beta(a_s)\,a_s\frac{\partial}{\partial a_s}-2\gamma_\psi^\theta\right\}\psi_T^{G^2}=0 \tag{3.114}$$

where $t \equiv (1/2)\log(Q^2/\nu^2)$ and $\gamma_\psi^\theta$ is the anomalous dimension defined in Eq. 3.109. Writing the $\alpha_s$ expansion as:

$$\psi_T^{G^2} = \left(g_0\alpha_s^2 + 2g_1\alpha_s^2 a_s\,t + g_1'\alpha_s^2 a_s - 2\gamma_\psi^\theta\alpha_s^2 + \cdots\right)\langle G^2\rangle, \tag{3.115}$$

---

[6] We take into account the overall $\alpha_s$ factor appearing in the definition of the energy-momentum tensor current.

and considering that $\langle\alpha_s G^2\rangle$ is a constant, one deduces :

$$g_1 = g_0\left(\frac{\beta_1}{2} - \gamma_1^\theta\right) = \frac{1}{24}\left(11 + \frac{2n_f}{3}\right) \qquad \text{with :} \quad g_0 = \frac{1}{6}. \tag{3.116}$$

### 3.4.5 Dimension-six $g\langle f_{abc}G^a_{\mu\nu}G^b_{\nu\rho}G^c_{\rho\mu}\rangle$ gluon condensate

- *LO contribution*

We calculate the coefficients of the $\langle gG^3\rangle$ contribution using the conventional approach and the projection in Eq. 3.98. We show the different contributions in Fig. 3.3 where the total sum is zero (log . coefficient and constant term) in agreement with the result of [152].

| Diagrams | $\psi_T(Q^2)$ |
|---|---|
| 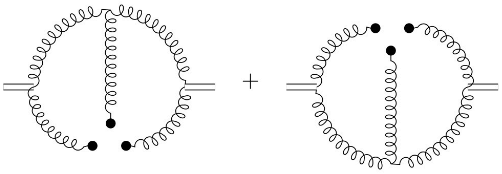 | $= -\frac{1}{12Q^2}\langle gG^3\rangle$ |
| 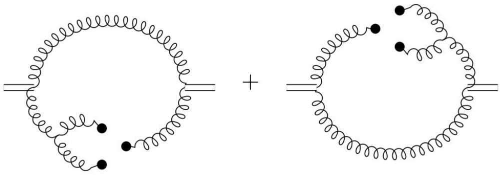 | $= 0$ |
| 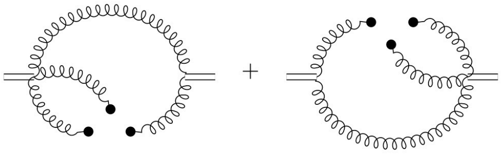 + Sym | $= +\frac{1}{12Q^2}\langle gG^3\rangle$ |

**Figure 3.3:** LO $g\langle G^3\rangle$ contribution to $\psi_T(Q^2)/\alpha_s^2$.

- *Check of the result*

We recompute the $G^3$ coefficient of the scalar gluonium two-point function using the same method. We recover the result of Ref. [133] which is an indirect test of our result.

### 3.4.6 Laplace Sum Rule (LSR) analysis

- *QCD expression*

Collecting the previous results, we obtain for $n_f = 3$ flavours to order $\alpha_s$ and up to dimension-8 condensates:

$$\begin{aligned}\tilde{\psi}_T(Q^2) &\equiv \frac{\psi_T(Q^2)}{\alpha_s^2}\\ &= -\frac{1}{20\pi^2}Q^4\log\frac{Q^2}{\nu^2}\left[1+a_s\left(\frac{1}{2}\log\frac{Q^2}{\nu^2}-\frac{151}{30}\right)\right]\\ &\quad +\frac{13}{24\pi}\langle\alpha_s G^2\rangle\log\frac{Q^2}{\nu^2}-\frac{5\pi}{16}\frac{k_G\alpha_s\langle G^2\rangle^2}{Q^4}.\end{aligned} \tag{3.117}$$

We shall be concerned with the following inverse Laplace transform moments and their ratio [82, 89, 153–155]:

$$\begin{aligned}\mathcal{L}^c_{0,1}(\tau,\mu) &= \int_{t>}^{t_c} dt\ t^{(0,1)}e^{-t\tau}\frac{1}{\pi}\mathrm{Im}\,\tilde{\psi}_T(t,\nu)\ ,\\ \mathcal{R}^c_{10}(\tau) &\equiv \frac{\mathcal{L}^c_1}{\mathcal{L}^c_0}=\frac{\int_{t>}^{t_c} dt\ e^{-t\tau}t\,\mathrm{Im}\,\tilde{\psi}_T(t,\nu)}{\int_{t>}^{t_c} dt\ e^{-t\tau}\mathrm{Im}\,\tilde{\psi}_T(t,\nu)},\end{aligned} \tag{3.118}$$

To get the lowest moment $\mathcal{L}^c_0$, we take the 3rd derivative of the two-point function which is superconvergent while for the $\mathcal{L}^c_1$ moment, we take the 4th derivative of $Q^2\tilde{\psi}_T(Q^2)$. The NLO QCD expressions of the moments for $n_f = 3$ flavours are:

$$\mathcal{L}^c_0=\frac{\tau^{-3}}{10\pi^2}\left\{\left[1-a_s\left(\frac{53}{15}+\gamma_E\right)\right]\rho^c_2-\frac{65\pi}{12}\langle\alpha_s G^2\rangle\tau^2\rho^c_0-\frac{\pi^2}{a_s}\left(\frac{25}{8}\right)k_G\langle\alpha_s G^2\rangle^2\tau^4\right\}, \tag{3.119}$$

and

$$\mathcal{L}^c_1=\frac{3\tau^{-4}}{10\pi^2}\left\{\left[1-a_s\left(\frac{16}{5}+\gamma_E\right)\right]\rho^c_3-\frac{65\pi}{36}\langle\alpha_s G^2\rangle\tau^2\rho^c_1+\frac{\pi^2}{a_s}\left(\frac{25}{24}\right)k_G\langle\alpha_s G^2\rangle^2\tau^4\right\}, \tag{3.120}$$

from which one can deduce the ratio $\mathcal{R}^c_{10}(\tau)$. $\gamma_E = 0.5772...$ is the Euler constant and:

$$\rho^c_n = 1-e^{-t_c\tau}\left(1+(t_c\tau)+\cdots+\frac{(t_c\tau)^n}{n!}\right)\ . \tag{3.121}$$

- *Strategies*

◇ *Parametrization of the spectral function*

To a first approximation, we have parametrized the spectral function using the minimal duality ansatz (MDA):

$$\frac{1}{\pi}\mathrm{Im}\,\tilde{\psi}(t) = f_T^2 M_T^4 \delta(t - M_T^2) + \theta\,(t\_t_c)\ \text{“QCD continuum”}, \tag{3.122}$$

where we assume that the QCD expression of the spectral function above the continuum threshold $t_c$ smears all radial excitation contributions. $f_T$ is normalized as $f_\pi = 132$ MeV. In the MDA parametrization:

$$\mathcal{R}_{10}^c \simeq M_T^2. \tag{3.123}$$

◇ *Optimization procedure*

One can notice that there are three free parameters in the analysis, namely the LSR variable $\tau$, the continuum threshold $t_c$ and the perturbative subtraction constant $\nu$. The later quantity is eliminated when one works with different derivatives of the two-point function for taking its inverse Laplace transform and working with the running QCD parameters. The optimal results will be extracted at the minimum or inflexion points in $\tau$ while we shall fix the range of $t_c$ in a conservative region from the beginning of $\tau$-stability until the (approximate) $t_c$-stability.

◇ *QCD input parameters*

We shall work with the QCD input parameters [116, 149]:

$$\Lambda = 340(28)\,\mathrm{MeV}, \quad \langle \alpha_s G^2 \rangle = (6.49 \pm 0.35)10^{-2}\ \mathrm{GeV}^4, \tag{3.124}$$

and use the parametrization of the $D = 8$ gluon condensates given in Eq. 3.101.

- *Di-gluonium mass and coupling at Lowest Order (LO)*

In this section, we redo the analysis in Ref. [131] using the expression in Eq. 3.99 that one shall explicitly compare with the one including the new NLO terms.

◇ We show the determination of $M_T$ from $\mathcal{R}_{10}^c$ in Fig. 3.4, where the vacuum saturation

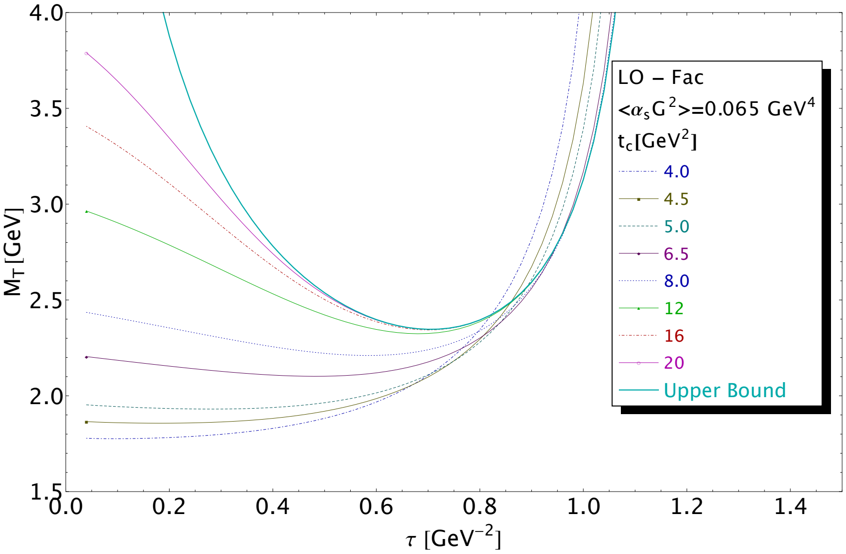

**Figure 3.4:** Behaviour of the $2^{++}$ tensor di-gluonium mass from the ratio of moments $\mathcal{R}^c_{10}$ versus $\tau$ for different values of $t_c$ at LO.

estimate of the $D = 8$ gluon condensates is assumed. We show the $t_c$-behaviour of the optimal values on $\tau$ in Fig. 3.5. The final optimal results are obtained for the set $(\tau, t_c)$ from (0.18,4.5) to (0.68,12) (GeV$^{-2}$, GeV$^2$) and are respectively 1857 and 2324 MeV. They lead to the mean :

$$M_T = 2091(234)_{t_c}(24)_{G^2}\text{MeV} \quad \multimap\!\!\!\rightarrow \quad t_c \simeq \left(6.5^{+5.5}_{-2.0}\right)\text{GeV}^2. \tag{3.125}$$

◇ We show the analysis of the coupling $f_T$ from the moment $\mathcal{L}^c_0$ in Fig. 3.6.

– One obtains:

$$f_T = 156(9)_{t_c}(0.4)_{G^2}(22)_{M_T}\ \text{MeV} \quad \multimap\!\!\!\rightarrow \quad t_c \simeq \left(7.0^{+5.0}_{-0.5}\right)\text{GeV}^2. \tag{3.126}$$

These results agree within the errors with the ones in Eq. 3.95 obtained at slightly low value of $t_c \simeq 5.5$ GeV$^2$. The large error obtained here is due to the most conservative choice of the $t_c$-range.

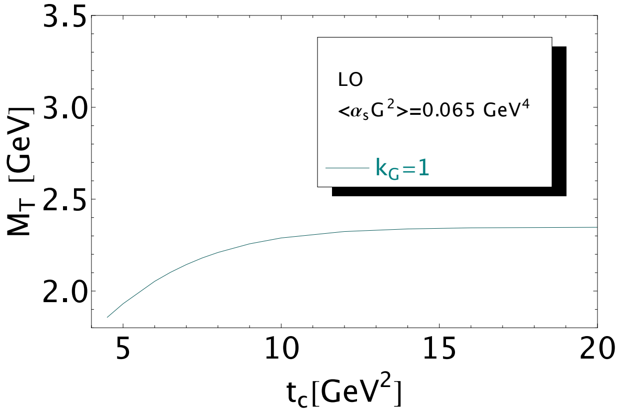

**Figure 3.5:** $t_c$-behaviour of the $2^{++}$ tensor di-gluonium LO mass at the $\tau$ minimum.

– We obtain the upper bounds:

$$M_T \leq 2347 \text{ MeV}, \qquad f_T \leq 174 \text{ MeV}. \tag{3.127}$$

The bound on the mass is comparable with the one in Eq. 3.95.

- *The $2^{++}$ ground state di-gluonium mass at NLO*

  ◇ *Factorization of the $D = 8$ gluon condensates ($k_G = 1$)*

The behaviour of the mass is shown in Fig 3.7 where we have assumed the factorization of the dimension 8 gluon condensates. The stabilities in $\tau$ are reached for the set $(\tau, t_c) = (0.12, 9.5)$ to (0.36,20) (GeV$^{-2}$,GeV$^2$) to which correspond the mass values 2746 and 3309 MeV.

– We deduce the mean value:

$$\begin{aligned}\langle M_T\rangle &= 3028(281)_{t_c}(1)_\tau(34)_\Lambda(47)_{G^2}(243)_{PT}(207)_{PT_{G^2}}(0)_{OPE}\text{MeV}\\ &= 3028(429)\text{MeV} \quad \multimap\!\!\!\rightarrow \quad t_c \simeq \left(12.6^{+7.4}_{-3.1}\right)\text{GeV}^2.\end{aligned} \tag{3.128}$$

We have added some systematic errors: the last 5th and 6th errors come from an estimate of the higher order (HO) $\alpha_s$ corrections to the PT and $\langle\alpha_s G^2\rangle$ contributions where the $\alpha_s^n$ coefficients are assumed to increase geometrically [153]. The last 7th error comes from the high-dimension condensates estimated to be about $(\Lambda^2\tau)$ times the $\langle G^4\rangle$ contributions.

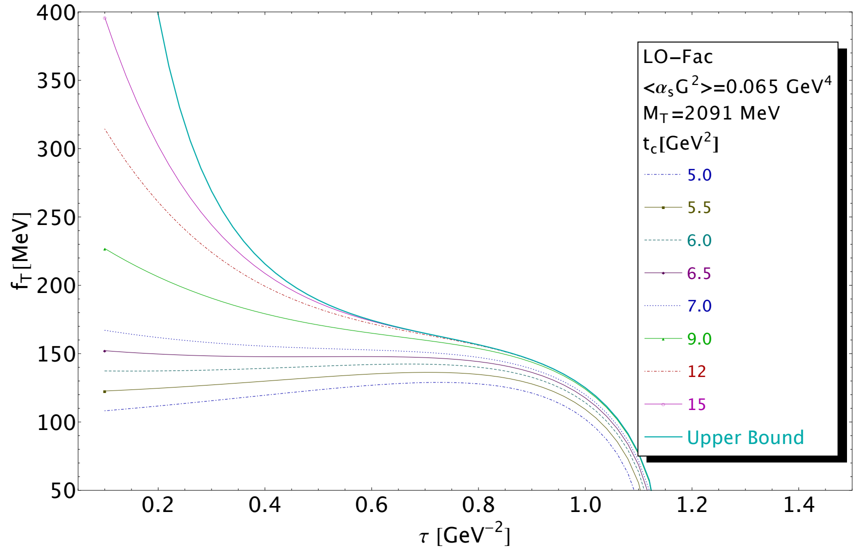

**Figure 3.6:** Behaviour of the $2^{++}$ tensor di-gluonium coupling from the moment $\mathcal{L}_0^c$ versus $\tau$ for different values of $t_c$ at LO assuming a factorization of the $D = 8$ condensates ($k_G = 1$).

– From Fig. 3.7, one can also deduce the optimal upper bound from the positivity of the ratio of moments. We obtain:

$$\begin{aligned} M_T &\leq 3376(26)_\Lambda(42)_{G^2}(240)_{PT}(286)_{PT_{G^2}} \\ &\leq 3376(377)\text{MeV} \end{aligned} \tag{3.129}$$

◇ *Comparison with the LO results within factorization*

We notice that the PT NLO corrections increase the central value of the mass by 561 MeV from its LO value while the $\langle\alpha_s G^2\rangle$ ones provide an additional increase of 376 MeV.

◇ *Comparison with some other LSR results*

– In Ref. [156], the result:

$$M_T = 1.86^{+014}_{-0.17}\ \text{GeV} \tag{3.130}$$

has been obtained to LO PT but including the NLO $\langle\alpha_s G^2\rangle$ term and the LO constant term of the $\langle gG^3\rangle$ condensates. Unfortunately, our results summarized in Eq. 3.117 do not agree with the coefficients of these condensates. The difference of these coefficients may come from

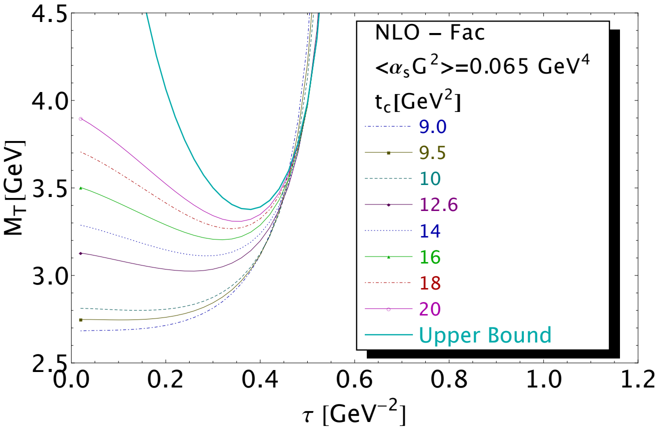

**Figure 3.7:** Behaviour of the $2^{++}$ tensor di-gluonium mass from the ratio of moments $\mathcal{R}^c_{10}$ versus $\tau$ for different values of $t_c$ at NLO assuming a factorization of the $D = 8$ condensates ($k_G = 1$).

the different current used by Ref. [156].

– Result within instanton liquid model is about 1525 MeV [157] which is lower than the above result.

⋄ *Effect of the* $D = 8$ *condensates*

Now, we study the effect of the estimate of the $D = 8$ gluon condensates on the mass determination assuming that the factorization can be violated like in the case of the four-quark condensate. The analysis is similar to the one in Fig. 3.7. We show the optimal results in Fig. 3.8 versus $t_c$ for different values of the violation factor $k_G$.

One can notice that the value of the mass is a smooth increasing function of $k_G$. From the vacuum saturation estimate ($k_G = 1$) to 5 (if one takes the same value as the violation of the four-quark condensate), the value of the mass moves from 3028(287) MeV to 3347(295) MeV thus an increase of about 319 MeV.

⋄ *Final estimate of the mass at NLO*

For definiteness, we shall work with the conservative range :

$$k_G = (3 \pm 2). \tag{3.131}$$

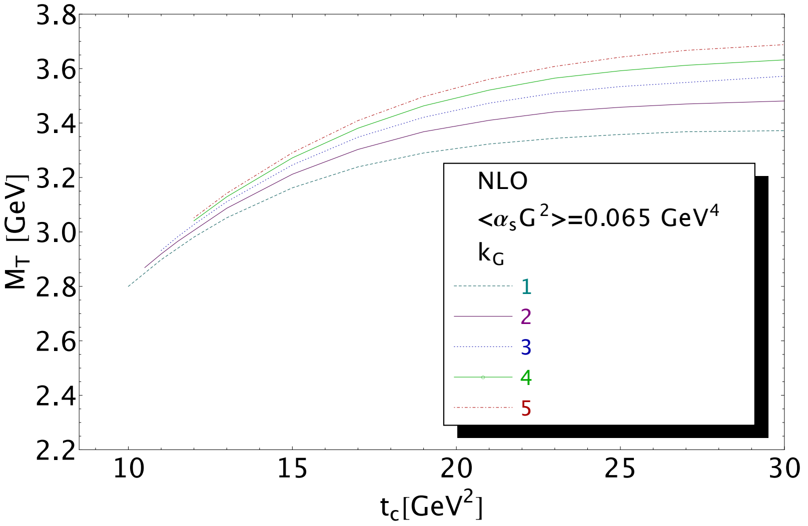

**Figure 3.8:** Behaviour of the $2^{++}$ tensor di-gluonium mass versus $t_c$ for different values of the factorization factor $k_G$.

– Then, we deduce the final estimate :

$$\begin{aligned}\langle M_T\rangle &= 3188(291)_{t_c}(34)_\Lambda(47)_{G^2}(159)_{k_G}(157)_{PT}(162)_{PT_G}(2)_{OPE}\text{MeV}\\ &= 3188(405)\text{MeV},\end{aligned} \tag{3.132}$$

which corresponds to $t_c \approx \left(14.1^{+7.9}_{-3.1}\right)\,\text{GeV}^2$.

– The related absolute upper bound is:

$$\begin{aligned}M_T &\leq 3580(17)_\Lambda(45)_{G^2}(168)_{k_G}(210)_{PT}(198)_{PT_{G^2}}(8)_{OPE}\text{MeV}\\ &\leq 3580(338)\text{MeV}.\end{aligned} \tag{3.133}$$

Our result for the ground state mass is in line with the ones from some other approaches [12] and ADS/QCD [158] where its mass is expected to be above 2 GeV. It is slightly higher than recent lattice calculations in the range $(2.27 \sim 2.67)$ GeV [130, 159, 160].

- *The* $2^{++}$ *ground state di-gluonium coupling at NLO*

We introduce the renormalization group invariant (RGI) coupling $\hat{f}_T$ which is related to the running coupling $f_T(\nu)$ associated to the two-point correlator $\tilde{\psi}_T$ as:

$$f_T(\nu) = \frac{\hat{f}_T}{\left(\log \frac{\nu}{\Lambda}\right)^{\frac{\gamma_1}{-2\beta_1}}} \qquad : \qquad \gamma_1 = \frac{n_f}{3}. \tag{3.134}$$

We shall extract the coupling from the lowest moment $\mathcal{L}_0^c$.

$\diamond$ *Factorization of the* $D = 8$ *gluon condensates* ($k_G = 1$)

– The NLO analysis is shown in Fig 3.9 . One can notice that, in the presence of the NLO terms (PT and $\langle \alpha_s G^2 \rangle$), the curves present more pronounced minimum and inflexion points. The curves present a minimum 201 and 246 MeV for the set $(\tau, t_c)$ equals to (0.2,11) and (0.3,22) (GeV$^{-2}$,GeV$^2$). One obtains to NLO:

$$\begin{aligned} \hat{f}_T\Big|_{NLO} &= 167(25)_{t_c}(1)_\tau(1.5)_\Lambda(1)_{G^2}(25)_{M_T}(16)_{PT}(11)_{PT_{G^2}}(0)_{OPE}\text{MeV} \\ &= 167(40)\text{MeV} \quad \mathrel{-\!\!\!\circ\!\!\!\rightarrow} \quad t_c \simeq \left(14^{+8}_{-3}\right)\text{GeV}^2 \end{aligned} \tag{3.135}$$

and the optimal upper bound at the minimum $\tau \simeq 0.3$ GeV$^{-2}$:

$$\begin{aligned} \hat{f}_T\Big|_{NLO} &\leq 186(1)_\Lambda(2)_{G^2}(32)_{M_T}(2)_{PT}(11)_{PT_{G^2}}(0)_{OPE}\text{MeV} \\ &\leq 186(34)\text{MeV} \end{aligned} \tag{3.136}$$

where we have used the mass value in Eq. (3.128).

– Comparing with the LO result, one can notice that the change of the mass from 2091 to 3028 MeV has increased the coupling by a huge amount of about 58 MeV while fixing the mass at its LO value, the NLO corrections have only increased the coupling by 13 MeV.

$\diamond$ *Beyond the factorization of the* $D = 8$ *gluon condensates*

We extract the value of the coupling corresponding to the $k_G$-factor in Eq. 3.131. The curves are shown in Fig. 3.10. One obtains for the set of $(\tau, t_c)$ : (0.12, 12) and (0.30, 22) in (GeV$^{-2}$, GeV$^2$) the values 156.6 and 173.6 MeV which give:

$$\begin{aligned} \hat{f}_T &= 164(8)_{t_c}(3)_\Lambda(1.3)_{G^2}(3)_{k_G}(20)_{M_T}(16)_{PT}(5)_{PT_{G^2}}(0)_{OPE}\text{MeV} \\ &= 164(28)\text{MeV} \quad \mathrel{-\!\!\!\circ\!\!\!\rightarrow} \quad t_c \simeq \left(12.5^{+9.5}_{-0.5}\right)\text{GeV}^2 \end{aligned} \tag{3.137}$$

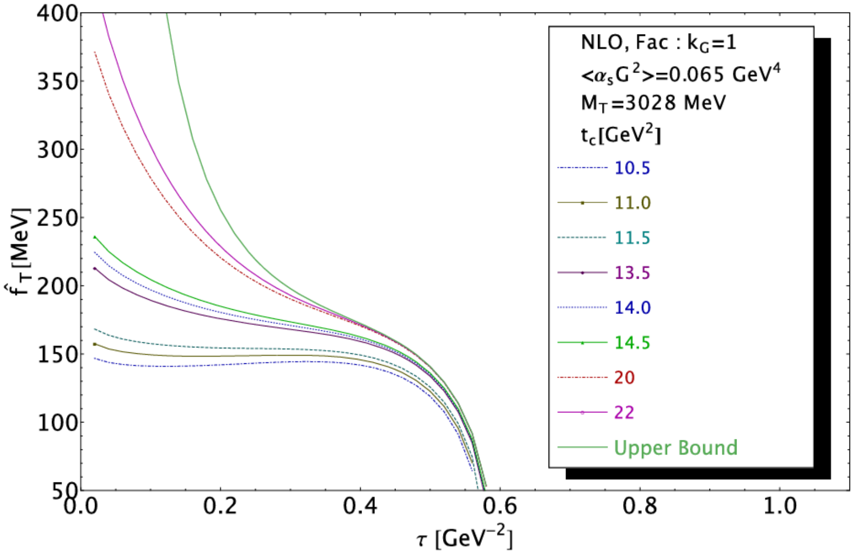

**Figure 3.9:** Behaviour of the $2^{++}$ tensor di-gluonium RGI coupling from the moment $\mathcal{L}_0^c$ versus $\tau$ for different values of $t_c$ at NLO within factorization.

and the optimal upper bound at the inflexion point $\tau \simeq 0.3\text{GeV}^{-2}$:

$$\begin{aligned} \hat{f}_T\Big|_{NLO} &\leq 203(5)_\Lambda(2)_{G^2}(5)_{k_G}(28)_{M_T}(19)_{PT}(11)_{PT_{G^2}}(0)_{OPE}\text{MeV} \\ &\leq 203(36)\text{MeV}. \end{aligned} \tag{3.138}$$

We notice that,like the mass, the value of the coupling is weakly affected by the value of the $D = 8$ gluon condensates.

### 3.4.7 Summary and conclusions

◇ We have computed the perturbative and $\langle\alpha_s G^2\rangle$ NLO corrections to the $2^{++}$ tensor di-gluonium two-point correlator and use the method of Laplace transform sum rules (LSR) to revisite the estimate of the mass and coupling of the lowest ground state.

◇ We find that the LO $\langle\alpha_s G^2\rangle$ coefficient has no imaginary part like found by NSVZ [133] but the constant term is not zero in contrast to NSVZ who have used dual/anti-dual field arguments. Thus, the use of the RGE allows to fix its $\log(Q^2/\nu^2)$ NLO coefficient from this LO constant term.

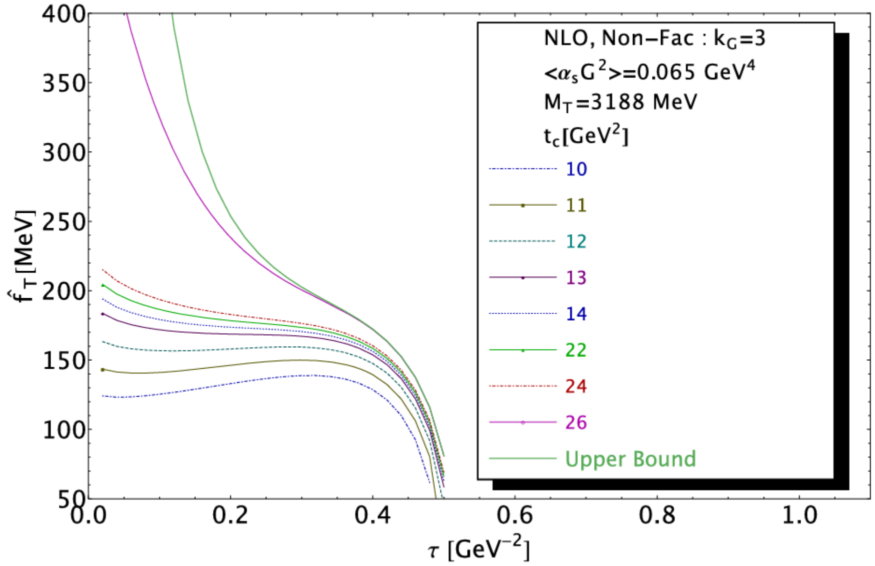

**Figure 3.10:** Behaviour of the $2^{++}$ tensor di-gluonium RGI coupling from the moment $\mathcal{L}_0^c$ versus $\tau$ for different values of $t_c$ at NLO without factorization.

◇ We note that our LO coefficient of $\langle g^3G^3\rangle$ disagrees with the one of Ref. [156] but agrees with the one of NSVZ. This disagreement may be related to the choice of current. As an indirect check of our result, we recalculate the $\langle g^3G^3\rangle$ coefficient in the scalar gluonium channel and recover the one of NSVZ.

◇ Assuming vacuum saturation for the estimate of the $D = 8$ gluon condensates, we found the lowest ground state mass $M_T = 3028(429)$ MeV (Eq. (3.128)) and RGI coupling $\hat{f}_T = 167(40)$ MeV (Eq. (3.135)). We also obtain the absolute upper bounds related to the positivity of the spectral function: $M_T \leq 3376(377)$ MeV (Eq. (3.129)) and $\hat{f}_T \leq 186(34)$ MeV (Eq. (3.136)).

◇ We study the effect of the estimate of the $D = 8$ gluon condensates. We find $M_T = 3188(405)$ MeV (Eq. (3.132)) and $\hat{f}_T = 164(28)$ MeV (Eq. (3.137)) for the violation factor $k_G = (3 \pm 2)$. We also deduce the upper bounds: $M_T \leq 3580(338)$ MeV (Eq. (3.133)) and $\hat{f}_T \leq 203(36)$ MeV (Eq. (3.138)).

◇ Our result is in line with the ones from some other approaches [12] and ADS/QCD [158] where its mass is expected to be above 2 GeV. However, the central value of our mass is slightly higher than lattice calculations in the range $(2.27 \sim 2.67)$ GeV [130, 159, 160].

⋄ Our result does not favour the interpretation of the observed $f_2(2010, 2300, 2340)$ states as pure gluonia/glueball candidates (see e.g. [161]). Moreover, we do not expect that an eventual meson-gluonium mixing will affect our result as this mixing is expected to be small $(\theta \simeq -10^0)$ [128].

### Acknowledgments

TGS is grateful for research funding from the Natural Sciences & Engineering Research Council of Canada (NSERC).

## 3.5 Next Step

This research advances the theoretical understanding of the $2^{++}$ tensor di-gluonium by applying QCDSR methodology at NLO, offering improved predictions that can aid future experimental searches for theoretical gluonia. The inclusion of NLO corrections from both the perturbative contributions (3.112) and the condensate contributions (3.115) and (3.116) provides substantial refinements over the LO results, showing the importance of precision calculation performed in this research. Moreover, a promising new direction has emerged in the investigation of the negative-parity tensor di-gluonium ($J^{PC} = 2^{-+}$), while a parallel research project on QCDSR calculation and analysis of scalar tri-gluonium ($J^{PC} = 0^{++}$) is also underway. These efforts collectively contribute to the pursuit of precision calculations and the potential discovery of new physics.

# 4 Muon Anomalous Magnetic Moment $a_\mu^{\mathrm{HVP,LO}}$

As one of the important current topics in the field of particle physics, the muon $g-2$ experiment provides updating high-precision measurements that can potentially lead to the discovery of new physics within and/or beyond the SM. In Chapter 3, we advanced the QCD prediction of the $2^{++}$ tensor gluonium and attempted to match the theoretically evaluated properties to potential particle candidates from the Particle Data Group [7].

For muon anomalous magnetic moment ($a_\mu \equiv (g-2)/2$), the experimental measurement from Fermilab [15] disagrees with theory [17] to the "new physics" threshold of $5.0\sigma$, inviting us to investigate a resolution for the tension. One can find an overview of the current landscape for the $a_\mu$ search in Sec. 4.1, as well as a more detailed motivation for our research in Sec. 4.2. Details in the flavour transitions for the running QCD parameters and RG analysis are detailed in Sec. 4.4 and 4.5, respectively. The manuscript presented in Sec. 4.3 of this chapter is published as Ref [21]:

***QCD bounds on leading-order hadronic vacuum polarization contributions to the muon anomalous magnetic moment***

**Siyuan Li, T.G. Steele, J. Ho, R. Raza, K. Williams, R.T. Kleiv**

**Phys. Rev. D 110 (2024) 1, 014046, doi:10.1103/PhysRevD.110.014046**

My role in this work includes Hölder inequalities derivation for $F_{-2}(s_0)$ lower bound, higher-loop perturbative corrections calculation, acquiring QCD inputs, performing numerical calculations for the FESR, conducting running parameters analysis, and analysing RG effects or condensate contributions. Additionally, I cross-checked the methodology used to determine the upper bound of the QCD contribution to $a_\mu$. I also contributed to the writing and editing of the manuscript.

In the 27th High-energy Physics International Conference in Quantum Chromodynamics (QCD24), I presented the above work and led in the writing and editing of the conference proceeding, which is peer-reviewed and published in Ref. [22]:

***Bounds on $a_\mu^{\text{HVP,LO}}$ using Hölder's inequalities and finite-energy QCD sum rules***

**Siyuan Li, T.G. Steele, J. Ho, R. Raza, K. Williams, R.T. Kleiv**

**Nucl. Part. Phys. Proc. 347 (2024), 6-11,**

**doi:10.1016/j.nuclphysbps.2024.09.002**

## 4.1 What is Muon Anomalous Magnetic Moment?

Muon is one of the fundamental particles in the SM. It has the same electric charge and quantum spin (1/2) as the electron. Due to its charge and quantum spin, the muon has a magnetic moment:

$$\vec{\mu} = g\frac{e}{2m_\mu}\vec{S}, \tag{4.1}$$

where $g$ is called the $g$-factor, $e$ is the elementary electric charge, $m_\mu$ represents the muon mass, and $\vec{S}$ is the muon spin-1/2 operator. The muon's magnetic moment is often represented by its $g$-factor, or gyromagnetic ratio, denoted as $g$. In the non-relativistic limit for a spin-1/2 particle in an electromagnetic field, the Dirac equation reduces to the Pauli equation [162] (also see Ref. [163]):

$$i\frac{\mathrm{d}\psi}{\mathrm{d}t} = \left[\frac{1}{2m}\left(-i\nabla - e\vec{A}\right)^2 + e\phi - \frac{e}{2m}\vec{\sigma}\cdot\vec{B}\right]\psi, \tag{4.2}$$

where $m$ is particle mass, $\psi$ is the particle's spinor wavefunction, $\vec{A}$ and $\phi$ represent the vector and Coulomb potentials, respectively, $\vec{B} = \nabla\times\vec{A}$ is the magnetic field and $\vec{\sigma} = \hat{S}$ is the Pauli spin vector (with Pauli spin matrices $\sigma_i, i = 1, 2, 3$) representing the spin. The spin field interaction term thus relates to the magnetic moment as follows:

$$-\frac{e}{2m}\vec{\sigma}\cdot\vec{B} = -\vec{\mu}\cdot\vec{B} \tag{4.3}$$

$$\Rightarrow \vec{\mu} = \frac{e}{2m}\hat{S}. \tag{4.4}$$

Comparing Eqs. (4.1) and (4.4), we see that the Dirac equation predicts $g = 2$ for spin-1/2 particles including muon. The classical prediction of the $g$-factor accounts for the kinetic term of the free particle as well as its interactions with the applied field. However, as a charged particle, muon tends to self-interact in vacuum and results in the production of virtual particles that only exist for a short time. Those virtual particles can range in mass, such as massless photons, light electrons, or heavier $W$, $Z$ and Higgs bosons. When we observe a muon, we see it surrounded by a cluster of virtual particles, constantly being created around it. The measured $g$-factor deviates away from the predicted value of 2 by a fraction and that difference is called the muon anomalous magnetic moment, also called muon $g-2$ or $a_\mu$:

$$a_\mu = (g-2)_\mu/2. \tag{4.5}$$

$a_\mu$ can also be interpreted as the quantum loop effects.

The vacuum environment where a muon is producing the virtual particles, which includes all known and undiscovered particles, serves as an ideal environment for physicists to study particle processes and explore uncharted regions in particle physics.

Muon $g-2$ can be accurately measured and tremendous effort has been invested into its experimental measurement. From the first experiment with the Synchrocyclotron at CERN in 1961 (*e.g.,* Refs. [164,165]) to the Brookhaven National Laboratory Muon E821 experiment, which ran until 2001 (*e.g.,* Ref. [166]), and to the ongoing Fermilab collaboration preparing to release their final result in the near future [15,16], muon $g-2$ measurement has come a long way and is providing promising insights for SM as well as BSM studies.

Among the potential spin-1/2 candidates with the same magnetic anomaly mechanism, the muon is much heavier than the electron (approximately 207 times), which is more prone to electromagnetic interactions [167], making the muon much more sensitive to heavier particles from BSM. Muon also has a lifetime long enough to be observed before decaying into electrons/positrons ($10^7$ times longer than $\tau$). All of these properties make it a suitable target for the $g-2$ experiment.

To make muon $g-2$ an even better observable for particle physics studies, $a_\mu$ in Eq. (4.5) can be directly measured. The following measuring mechanism for muon $g-2$ is based on

Fermilab's Muon $g-2$ collaboration (*e.g.,* see Refs. [16, 168]). Beginning with directing accelerated protons into a fixed target to produce pions, these pions then quickly decay into muons and neutrinos via the weak interaction. The muon beam is then directed into a storage ring, where it encounters a strong, uniform magnetic field $\vec{B}$. The moving particles is therefore moving in a circle at the cyclotron frequency:

$$\omega_c = \frac{2B}{m_\mu}. \tag{4.6}$$

As a muon is injected into an external magnetic field $\vec{B}$, a torque will be exerted on the muon spin by the magnetic field ($\vec{\mu} \times \vec{B}$) causing the spin axis to rotate, or precess, about the magnetic field at a muon spin precession frequency:

$$\omega_s = \frac{\mu}{S} B = g\frac{eB}{2m_\mu} = (1+a_\mu)\frac{eB}{2m_\mu}, \tag{4.7}$$

where the $g$-factor stands for the gyration rate of the muon when placed in a magnetic field. The rate of spin precession relative to momentum precession is thus

$$\omega_a = \omega_s - \omega_c = a_\mu \frac{e}{m_\mu} B, \tag{4.8}$$

called the muon anomalous precession frequency which can be directly measured. The simplified model described above omitted the weakly focusing quadrupole electric field $\vec{E}$ and the relativistic effect. $\omega_a$ can be more completely represented as [16] (or see the relativistic equation of motion for spin in uniform external fields from Ref. [169]):

$$\vec{\omega}_a = -a_\mu \frac{e}{m_\mu}\vec{B} + \frac{e}{m_\mu}\left[\left(a_\mu - \frac{1}{\gamma_\mu^2 - 1}\right)\frac{\vec{\beta}\times\vec{E}}{c} + a_\mu\left(\frac{\gamma_\mu}{\gamma_\mu + 1}\right)\left(\vec{\beta}\cdot\vec{B}\right)\vec{\beta}\right], \tag{4.9}$$

where $\vec{\beta}$ is the muon velocity relative to the speed of light and $\gamma_\mu$ stands for muon's Lorentz factor. The second term can be eliminated by adopting a "magic momentum" of $p_0 \simeq 3.094\,\mathrm{GeV}$ for the muon, deriving from $\gamma_\mu = \sqrt{1 + 1/a_\mu}$. The third term is zero if there is no vertical betatron motion, leading back to Eq. (4.8).

The properties of muon particles allow the determination of the spin direction. In the muon storage ring, muons will decay through the following weak interactions almost exclusively [7]:

$$\mu^+ \to e^+ + \nu_e + \bar{\nu}_\mu, \quad \mu^- \to e^- + \bar{\nu}_e + \nu_\mu, \tag{4.10}$$

with positive/negative muons $\mu^\pm$, electron neutrinos $\nu_e$ and muon neutrinos $\nu_\mu$ with their antiparticles. The decay product $e^+$ with maximum allowed kinetic energy will travel in the direction aligned with the muon spin when it decayed ($e^-$ will travel in the opposite directions) due to helicity alignment constraints imposed by the weak interaction [170]. And those $e^{+/-}$ can be detected by calorimeters located on the inner radius of the storage ring [171]. The number of weighed positrons detected with respect to time elapsed fits a sinusoidal wave function with decaying amplitude and vertical shift [15]. The angular frequency of the sinusoidal wave fit is our anomalous precession frequency $\omega_a$ in Eq. (4.8). The most recent experimental world average for muon anomalous magnetic moment is [7]:

$$a_\mu^{\text{exp}} = 116592061(41) \times 10^{-11}. \tag{4.11}$$

## 4.2 Motivation for $a_\mu^{\text{QCD}}$

According to SM, $a_\mu$ has three types of contribution:

$$a_\mu^{\text{SM}} = a_\mu^{\text{QED}} + a_\mu^{\text{EW}} + a_\mu^{\text{Had}} \tag{4.12}$$

where

- The electromagnetic contributions from photon and lepton loops (see Fig. 4.1a) have been calculated to 10th order correction in perturbative QED expansion $a_\mu^{\text{QED}} \simeq 116584719(0.1) \times 10^{-11}$ [7, 17].

- The electroweak contributions are from $W^\pm$, $Z$ and Higgs loops collectively (see Fig. 4.1c). The numerical evaluation finds negligible results at 3-loop order, giving $a_\mu^{\text{EW}} = 153.6(1.0) \times 10^{-11}$ [7, 17, 172, 173]. Among the three parts of Eq. (4.11), electroweak loop contri-

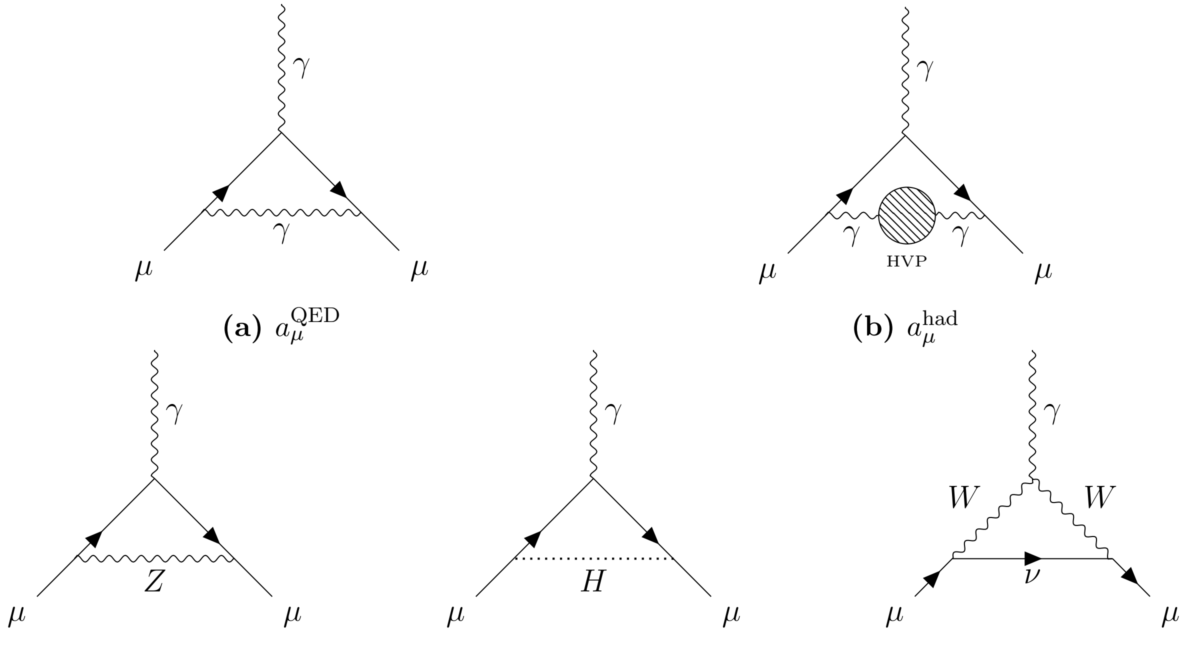

**(a)** $a_\mu^{\text{QED}}$ **(b)** $a_\mu^{\text{had}}$

**(c)** $a_\mu^{\text{EW}}$

**Figure 4.1:** LO contributions to QED, hadronic vacuum polarization and electroweak Feynman diagrams for $a_\mu^{\text{SM}}$.

butions are the smallest and order of magnitudes smaller than QED and hadronic contributions.

- The hadronic loops are mainly from hadronic vacuum polarization (HVP) $a_\mu^{\text{HVP}}$ which is the largest contribution to $a_\mu^{\text{had}}$ (see LO HVP Feynman diagram in Fig. 4.1b). It is also the main source of theoretical uncertainty for $a_\mu$ in general. This comes from when the photon in the vacuum around the muon briefly transforms into $q\bar{q}$ pairs and then back into a photon before disappearing. During the described process, the virtual hadrons produced may interact with muon differently compared to the original photon, leading to a shift in $a_\mu$. Besides HVP, there is also the hadronic light-by-light [17] (also see *e.g.,* Refs. [7, 174]) contribution which is smaller than $a_\mu^{\text{HVP}}$.

The difficulties in calculating $a_\mu^{\text{HVP}}$ lie in the non-perturbative QCD effects at low energies where quarks are bound into hadrons. For the LO HVP contribution ($a_\mu^{\text{HVP,LO}}$), one may use the dispersion integral from the data-driven dispersive method [17, 107, 175]. The dispersion relation relates the real part of the polarization function, which contributes to

$a_\mu$, to the experimentally accessible imaginary part. By experimental measurements of the $e^+e^- \to$ hadrons cross section, one can calculate $a_\mu^{\text{HVP}}$ by integrating the spectral function over energy. The lattice QCD (LQCD) community is also actively contributing to muon $g-2$ prediction, though the methodology is still developing in precision for $a_\mu$. However, the predictions for $a_\mu^{\text{HVP,LO}}$ using different dispersive methods disagree with the recent, more precise experimental measurement from Fermilab [15, 16], showing discrepancies of $5.0\sigma$ [17] and $0.9\sigma$ [18]. These predictions also do not align with LQCD results within their respective error ranges [19, 20].

The theoretical discrepancy in $a_\mu^{\text{HVP,LO}}$ among different methods motivates us to look for fundamental bounds with QCDSR methodology. Here we provided our upper and lower bounds for $a_\mu^{\text{HVP,LO}}$ by using Hölder inequalities and FESR. We relate the dispersion integral for $a_\mu^{\text{HVP,LO}}$ [17, 107, 175] to the structure of FESR [124, 126, 176, 177], specifically a newly-developed lower and upper bounds of theoretical FESR quantity $F_{-2}(s_0)$ with parameter $s_0$ in the unit of energy-squared allowing us to adjust our theoretical prediction. We can then extend Hölder inequalities to FESR. Hence, providing bounds for $a_\mu^{\text{HVP,LO}}$. Our calculation and analysis focus on the light-quark vector current correlation function (see Fig. 4.2 for the one-loop order Feynman diagram), including both perturbative and non-perturbative (condensates) contributions calculated with QCD sum rules. The upper and lower bounds values bridge the results from LQCD and data-driven approaches [17]. It is crucial to understand that our choices of $s_0$ in the final results represent the energy scale value that provides the most restrictive lower and upper bounds. It is not a cut-off for QCD contribution nor a duality threshold. That said, the convergence property for chosen $s_0$'s (in Table. 4.3) as we went higher order (up to five-loop) in perturbative contributions was also ensured during the analysis [21]. For the FESR with weight $k = 0, 1, 2$ (see Eqs. (4.53),(4.54),(4.55)), the perturbative contributions are calculated to an unprecedented high order of corrections to five loops, as shown in Fig. 4.3. The non-perturbative contribution terms are also compared and, as expected, are much smaller than the perturbative ones.

The following section presents the published manuscript in *Phys. Rev. D* **110** (2024) 1, 014046 (see also Ref. [21]).

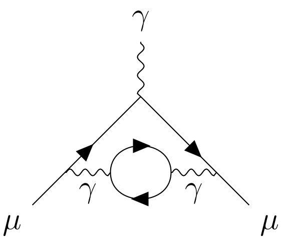

**Figure 4.2:** $a_\mu^{\rm HVP,LO}$ Feynman diagram representing one-loop contribution.

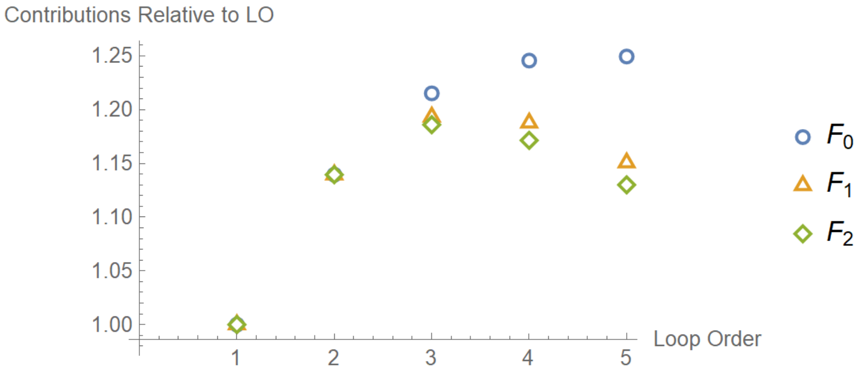

**Figure 4.3:** The perturbative contributions from LO (one loop) to five loops, relative to the LO value, for $F_1(s_0)$, $F_2(s_0)$, and $F_3(s_0)$ at the non-strange energy scale value $s_0 = 1.09\text{GeV}^2$ (see Table 4.3), show convergence at higher-loop orders and highlight the importance of higher-order corrections in QCDSR precision calculations.

## 4.3 Manuscript: QCD bounds on leading-order hadronic vacuum polarization contributions to the muon anomalous magnetic moment

**Abstract:** QCD bounds on the leading-order (LO) hadronic vacuum polarization (HVP) contribution to the anomalous magnetic moment of the muon ($a_\mu^{\rm HVP,LO}$, $a_\mu = (g-2)_\mu/2$) are determined by imposing Hölder inequalities and related inequality constraints on systems of Finite-Energy QCD sum-rules. This novel methodology is complementary to lattice QCD and data-driven approaches to determining $a_\mu^{\rm HVP,LO}$. For the light-quark $(u, d, s)$ contributions up to five-loop order in perturbation theory in the chiral limit, LO in light-quark mass corrections, next-to-leading order in dimension-four QCD condensates, and to LO in dimension-six QCD condensates, we find that $(657.0 \pm 34.8) \times 10^{-10} \le a_\mu^{\rm HVP,LO} \le (788.4 \pm 41.8) \times 10^{-10}$, bridging the range between lattice QCD and data-driven values.

### 4.3.1 Introduction

In the summer of 2023, the Muon $g-2$ experiment at Fermilab announced an updated result to the measurement of $a_\mu \equiv (g-2)_\mu/2$, increasing the precision of their previous measurement by a factor of two [15] (see also *e.g.,* Ref. [16]). This updated experimental result reinforces the tension between experimental measurements and predictions from the Standard Model using data-driven and dispersive methods, pushing the disagreement between this new experimental observation and the prediction from theory [17] up to $5.0\sigma$ [15]. In addition to this new experimental evidence, recent precision measurements of the pion form factor by CMD-3 have been used to calculate the lowest-order hadronic contributions to $a_\mu$ [18], and found agreement with [15] to within $0.9\sigma$. Furthermore, a recent calculation by the Budapest–Marseille–Wuppertal (BMW) collaboration using lattice QCD (LQCD) reached sub-percent levels of precision competitive with data-driven and dispersive methods [19]. This high-precision LQCD calculation of $a_\mu$ is in significantly better agreement with current experimental measurements. While efforts are ongoing by the LQCD community to produce new calculations of sub-percent precision [20], the results of the BMW collaboration produced a new tension between theoretical methods.

Currently, contributions to $a_\mu$ from the hadronic vacuum polarization (HVP) dominate the uncertainties in the Standard Model calculation. In the data-driven approach, the leading-order (LO) dispersion integral for the contributions to $a_\mu$ from HVP (*i.e.,* $a_\mu^{\mathrm{HVP,LO}}$) is given by [17, 107, 175]

$$a_\mu^{\mathrm{HVP,LO}} = \frac{1}{4\pi^3}\int_{4m_\pi^2}^{\infty} \sigma^H(t)K(t)\,\mathrm{d}t \tag{4.13}$$

where $\sigma^H$ is the $e^+e^-$ to hadrons cross section and $K(t)$, the kernel function, is given by

$$K(t) = \int_0^1 dx\,\frac{x^2(1-x)}{x^2+(1-x)t/m_\mu^2}\,, \tag{4.14}$$

where $m_\mu$ is the muon mass. Using the hadronic $R$-ratio

$$R(t) = \frac{\sigma^H\,(t)}{\sigma\,(e^+e^- \to\, \mu^+\mu^-)}\,, \tag{4.15}$$

with

$$\sigma\left(e^+e^-\to\,\mu^+\mu^-\right)=\frac{4\pi\alpha^2}{3t^2}\left(t+2m_\mu^2\right)\sqrt{1-\frac{4m_\mu^2}{t}}=\frac{4\pi\alpha^2}{3t}+\mathcal{O}\left(\frac{1}{t^3}\right)\,, \tag{4.16}$$

where $\alpha$ is the fine-structure constant, Eq. (4.13) can be expressed as

$$a_\mu^{\text{HVP,LO}}=\frac{\alpha^2}{3\pi^2}\int_{4m_\pi^2}^{\infty}\frac{1}{t}R(t)K(t)\,\mathrm{d}t\,, \tag{4.17}$$

where the approximation associated with (4.16) is negligible. Since the hadronic $R$-ratio can be expressed in terms of the hadronic vacuum polarization spectral function $R(t)=12\pi\text{Im}\Pi^H(t)$ [106, 107], a QCD expression for Eq. (4.13) can be written in terms of the hadronic spectral function $\text{Im}\Pi^H(t)$,

$$a_\mu^{\text{QCD}}=\frac{4\alpha^2}{\pi}\int_{4m_\pi^2}^{\infty}\frac{1}{t}\text{Im}\Pi^H(t)K(t)\,\mathrm{d}t\,. \tag{4.18}$$

We can relate (4.17) and (4.18) to QCD sum-rule methods by approximating Eq. (4.14) as

$$K(t)\approx\frac{m_\mu^2}{3t}=K_{\text{approx}}(t) \tag{4.19}$$

to obtain

$$a_\mu^{\text{QCD}}\approx\frac{4m_\mu^2\alpha^2}{3\pi}\int_{4m_\pi^2}^{\infty}\frac{1}{t^2}\text{Im}\Pi^H\left(t\right)\mathrm{d}t\,, \tag{4.20}$$

where the effects of the approximation associated with (4.19) will be discussed below. The challenges of a QCD determination of $a_\mu^{\text{HVP,LO}}$ arise from the $1/t^2$ behaviour in (4.20) that emphasizes the low-energy region.

QCD sum-rules [82, 83] (see *e.g.,* [48, 88, 141, 178] for reviews) implement quark-hadron duality by relating a QCD prediction to an integrated hadronic spectral function, and hence (4.20) suggests the possibility of using QCD sum-rules for determining $a_\mu^{\text{HVP,LO}}$. In particular, the structure of (4.20) is such that it can be written in terms of a FESR defined by [124, 126, 176, 177]

$$F_k\left(s_0\right) = \int_{t_0}^{s_0} \frac{1}{\pi} \mathrm{Im}\Pi^H\left(t\right) t^k \, \mathrm{d}t \,, \tag{4.21}$$

where $k$ is an integer that indicates the weight of the sum-rule and $t_0$ is a physical threshold. In (4.21), the left-hand side is obtained from a QCD prediction, and hence the FESRs relate a QCD prediction to an integrated hadronic spectral function. Writing (4.20) in terms of (4.21) gives

$$a_\mu^{\mathrm{QCD}} \approx \frac{4m_\mu^2\alpha^2}{3} F_{-2}\left(\infty\right) \geq \frac{4m_\mu^2\alpha^2}{3} F_{-2}\left(s_0\right) \,. \tag{4.22}$$

In the last step of Eq. (4.22), positivity of the hadronic spectral function has been used to obtain a lower bound. As outlined below, the presence of the parameter $s_0$ allows optimization of our theoretical prediction. Unfortunately, determining a field-theoretical expression for $F_{-2}\left(s_0\right)$ requires knowledge of low-energy constants, and hence a direct theoretical prediction is not possible. Various QCD sum-rule approaches have been used to circumvent this issue (see *e.g.,* Refs. [106, 107, 179, 180]). In this paper we examine the fundamental properties of the field theoretical result (4.22) through the application of the Hölder, Cauchy-Schwarz, and related inequalities to obtain QCD lower and upper bounds on the LO hadronic vacuum polarization contribution to the anomalous magnetic moment of the muon $a_\mu^{\mathrm{HVP,LO}}$.

In Section 4.3.2 the fundamental inequalities for lower and upper bounds are developed. Section 4.3.3 provides the necessary QCD expressions and input parameters for light-quark $(u, d, s)$ contributions up to five-loop order in perturbation theory in the chiral limit, LO in light-quark mass corrections, next-to-leading order (NLO) in dimension-four QCD condensates, and to LO in dimension-six QCD condensates. Analysis methodology and results for $a_\mu^{\mathrm{HVP,LO}}$ are presented in Section 4.3.4, and the Appendix updates the Laplace sum-rule bounds on $a_\mu^{\mathrm{HVP,LO}}$ in Ref. [107] with current determinations of the necessary QCD input parameters, five-loop perturbative corrections, and NLO dimension-four condensate contributions.

### 4.3.2 QCD Finite-Energy Sum Rule Bounds on $a_\mu^{\rm HVP,LO}$

#### 4.3.2.1 Lower Bounds

Hölder inequalities have previously been developed for QCD Laplace [114] and Gaussian sum-rules [181], and their application can be used to constrain the region of sum-rule parameter space in the study of hadronic systems (see *e.g.,* Refs. [114, 181–185]). Extending this Hölder inequality methodology to FESRs allows us to establish fundamental bounds on the theoretically-undetermined FESR $F_{-2}\left(s_0\right)$, leading to a constraint on $a_\mu^{\rm QCD}$ via (4.22).

The Hölder inequality is expressed generally as [186, 187]

$$\left|\int_{t_1}^{t_2} f\left(t\right) g\left(t\right) {\rm d}\mu\right| \leq \left(\int_{t_1}^{t_2} \left|f\left(t\right)\right|^p {\rm d}\mu\right)^{\frac{1}{p}} \left(\int_{t_1}^{t_2} \left|g\left(t\right)\right|^q {\rm d}\mu\right)^{\frac{1}{q}}\,, \quad \frac{1}{p}+\frac{1}{q}=1\,. \tag{4.23}$$

With careful choice of functions $f(t)$, $g(t)$, and using positivity of ${\rm Im}\Pi^H\left(t\right)$ to define the measure ${\rm d}\mu = \frac{1}{\pi}{\rm Im}\Pi^H\left(t\right){\rm d}t$ our Hölder inequality becomes

$$\left|\int_{t_0}^{s_0} t^{\alpha+\beta}\frac{1}{\pi}{\rm Im}\Pi^H\left(t\right){\rm d}t\right| \leq \left(\int_{t_0}^{s_0} \left|t^\alpha\right|^p \frac{1}{\pi}{\rm Im}\Pi^H\left(t\right){\rm d}t\right)^{\frac{1}{p}} \left(\int_{t_0}^{s_0} \left|t^\beta\right|^q \frac{1}{\pi}{\rm Im}\Pi^H\left(t\right){\rm d}t\right)^{\frac{1}{q}}\,. \tag{4.24}$$

Because the QCD quantity $F_k\left(s_0\right)$ in Eq. (4.21) must inherit the properties associated with the hadronic spectral function, Eq. (4.24) can be expressed in terms of the FESRs

$$F_{\alpha+\beta}\left(s_0\right) \leq \left[F_{\alpha\,p}\left(s_0\right)\right]^{\frac{1}{p}}\left[F_{\beta\,q}\left(s_0\right)\right]^{\frac{1}{q}} \;\rightarrow\; F_{\alpha+\beta}\left(s_0\right) \leq \left[F_{\alpha\,p}\left(s_0\right)\right]^{\frac{1}{p}}\left[F_{\frac{\beta\,p}{p-1}}\left(s_0\right)\right]^{\frac{p-1}{p}}\,. \tag{4.25}$$

Eq. (4.25) results in a family of inequalities which can be used to place a lower bound on $F_{-2}\left(s_0\right)$. These are restricted due to the conditions from the Hölder inequality [Eq. (4.23)], as well due to the requirement from FESRs $F_k\left(s_0\right)$ that the weight $k$ be an integer. By restricting our attention to inequalities that give a lower bound on $F_{-2}\left(s_0\right)$ through a combination of positive-weight FESR expressions, we derive the following inequalities:

$$F_{-2} \geq \frac{F_0^2}{F_2}\,, \tag{4.26}$$

$$F_{-2} \geq \frac{F_0^3}{F_1^2}\,, \tag{4.27}$$

$$F_{-2} \geq \frac{F_1^4}{F_2^3}\,, \tag{4.28}$$

where we have suppressed the $s_0$ dependence in each FESR. These inequalities place a lower bound on $F_{-2}\left(s_0\right)$ through a combination of FESRs that have weights low enough ($0 \leq k \leq 2$) to avoid dependence on unknown higher dimension QCD condensates as outlined below.

Having determined the lower bounds (4.26)–(4.28), we next determine which is the strongest restriction on $F_{-2}$. Starting from Eq. (4.25), we apply the substitutions $\alpha = \frac{k+1}{2}$ and $\beta = \frac{k-1}{2}$, and consider the Cauchy-Schwarz inequality (*i.e.,* the Hölder inequality in Eq. (4.25) with $p = q = 2$). This gives

$$F_k \leq F_{k+1}^{1/2} F_{k-1}^{1/2} \;\rightarrow\; F_k^2 \leq F_{k+1} F_{k-1}\,. \tag{4.29}$$

Rearranging this gives us a relationship between ratios of FESRs,

$$\frac{F_k}{F_{k+1}} \leq \frac{F_{k-1}}{F_k}\,. \tag{4.30}$$

Applying this to our constraints (4.26)-(4.28), we find the following hierarchy,

$$F_{-2} \geq \frac{F_0^3}{F_1^2} \geq \frac{F_0^2}{F_2} \geq \frac{F_1^4}{F_2^3}\,. \tag{4.31}$$

The most restrictive lower bound on $F_{-2}\left(s_0\right)$ is therefore provided by

$$F_{-2} \geq \frac{F_0^3}{F_1^2}\,. \tag{4.32}$$

From this, taking Eqs. (4.22) and (4.32), we can relate this inequality to a bound on $a_\mu^{\mathrm{QCD}}$,

$$a_\mu^{\mathrm{QCD}} \geq \frac{4m_\mu^2\alpha^2}{3}\frac{F_0^3\left(s_0\right)}{F_1^2\left(s_0\right)}\,. \tag{4.33}$$

In obtaining the lower bound (4.33) on $a_\mu^{\mathrm{QCD}}$, the approximation in Eq. (4.19) has been used. The resulting lower bound (4.33) is only valid if this approximation is also a lower bound on $K(t)$. However, the approximation (4.19) provides an upper bound on $K(t)$, and $K_{\mathrm{approx}}(t)$ must therefore be re-scaled by a factor $\xi$ to obtain a valid lower bound

$$K_\xi(t) = \xi K_{\mathrm{approx}}(t) = \xi\frac{m_\mu^2}{3t}\,. \tag{4.34}$$

The crucial energy region for determining $\xi$ is the low-energy region from threshold to the $\rho,\omega$ peak. A naive Breit-Wigner $\sigma^{\mathrm{BW}}$ for the $\rho,\omega$ is non-zero at threshold and provides an overestimate of $\sigma^H(t)$ in the low-energy region. Thus $\xi$ can be determined by the constraint

$$\int_{4m_\pi^2}^{m_\rho^2} K(t)\sigma^{\mathrm{BW}}(t)\,\mathrm{d}t \geq \int_{4m_\pi^2}^{m_\rho^2} K_\xi(t)\sigma^{\mathrm{BW}}(t)\,\mathrm{d}t\,. \tag{4.35}$$

The inequality (4.35) is saturated by $\xi = 0.83$, and as shown in Fig. 4.4, this value of $\xi$ also results in a lower bound $K_\xi(t) \leq K(t)$ beyond the $\rho,\omega$ peak,

$$\int_{4m_\pi^2}^{\infty} K(t)\sigma^H(t)\,\mathrm{d}t \geq \int_{4m_\pi^2}^{\infty} K_\xi(t)\sigma^H(t)\,\mathrm{d}t\,. \tag{4.36}$$

Hence (4.33) is modified to our final form

$$a_\mu^{\mathrm{QCD}} \geq \xi\frac{4m_\mu^2\alpha^2}{3}\frac{F_0^3\left(s_0\right)}{F_1^2\left(s_0\right)}\,,\ \xi = 0.83\,. \tag{4.37}$$

It should be noted from Fig. 4.4 that the approximate form $K_\xi(t)$ clearly underestimates the exact $K(t)$ above the $\rho,\omega$ peak, and hence the final bound in Eq. (4.37) is expected to be a conservative lower bound. Finally, the utility of the parameter $s_0$ appearing in (4.37) is now evident, because it can be varied to find the strongest possible QCD bound.

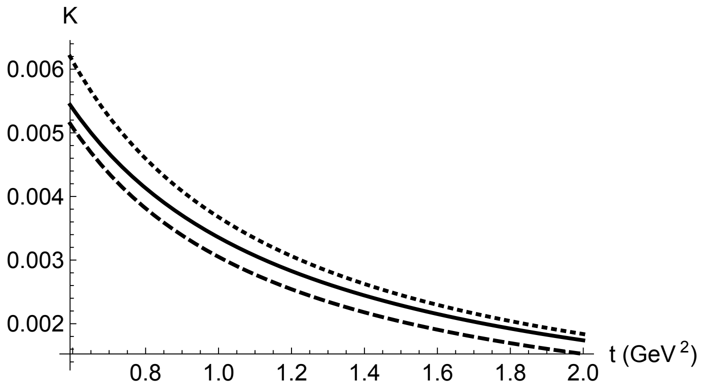

**Figure 4.4:** The exact $K(t)$ (solid line) compared to the approximate form $K_\xi(t)$ with $\xi = 0.83$ (lower dashed line) and with $\xi = 1$ (upper dotted line).

#### 4.3.2.2 Upper Bounds

Because the kernel $K(t)$ decreases monotonically with increasing energy and $K(t) < K_{\text{approx}}(t)$ (see Fig. 4.4), the following upper bound can be obtained from (4.18) and (4.20)

$$a_\mu^{\text{QCD}} \le \frac{4m_\mu^2\alpha^2}{3\pi}\int_{t_0}^{\infty}\frac{1}{t^2}\text{Im}\Pi^H(t)\,\text{d}t \le \frac{4m_\mu^2\alpha^2}{3\pi}\frac{1}{t_0^2}\int_{t_0}^{\infty}\text{Im}\Pi^H(t)\,\text{d}t\,,\ t_0 = 4m_\pi^2\,. \tag{4.38}$$

However, this bound can be improved by adapting and extending the techniques outlined in Ref. [188]. Ultimately, the goal is to construct an upper bound on $F_{-2}(s_0)$, but we illustrate the method of Ref. [188] with the necessary step of an upper bound on $F_{-1}(s_0)$ via the following relation based on positivity of the hadronic spectral function

$$\int\limits_{t_0}^{s_0}\frac{1}{t}\left[1 + At\right]^2\text{Im}\Pi^H(t)\ \text{d}t \ge 0\,. \tag{4.39}$$

By extremizing $A$ to obtain the most stringent relation we find

$$F_{-1} \le F_{-1}^{(B)} = \frac{F_0}{t_0} - \frac{\left(F_1/t_0 - F_0\right)^2}{\left(F_2/t_0 - F_1\right)}\,, \tag{4.40}$$

$$F_2/t_0 - F_1 > 0\,, \tag{4.41}$$

where the FESR dependence on $s_0$ has been suppressed and the subsidiary condition (4.41) is required for the validity of (4.40).

An upper bound on $F_{-2}$ can then be obtained by extremizing the relation

$$\int_{t_0}^{s_0} \frac{1}{t^2}\left[1+At\right]^2 \mathrm{Im}\Pi^H(t)\,\mathrm{d}t \le \frac{1}{t_0}\int_{t_0}^{s_0} \frac{1}{t}\left[1+At\right]^2 \mathrm{Im}\Pi^H(t)\,\mathrm{d}t\,, \tag{4.42}$$

to find

$$F_{-2} \le \frac{F_{-1}^{(B)}}{t_0} - \frac{\left(F_0/t_0 - F_{-1}^{(B)}\right)^2}{\left(F_1/t_0 - F_0\right)}\,, \tag{4.43}$$

$$F_1/t_0 - F_0 > 0\,, \left(F_0/t_0 - F_{-1}^{(B)}\right)^2 < \left(F_0/t_0 - F_0^2/F_1\right)^2\,, \tag{4.44}$$

where the inequality $F_{-1} \ge F_0^2/F_1$ [see (4.29)] has been used as part of the subsidiary condition (4.44) for the validity of (4.43). An alternative upper bound on $F_{-2}$ can be obtained by extremizing

$$\int_{t_0}^{s_0} \frac{1}{t^2}\left[1+At\right]^2 \mathrm{Im}\Pi^H(t)\,\mathrm{d}t \le \frac{1}{t_0^2}\int_{t_0}^{s_0} \left[1+At\right]^2 \mathrm{Im}\Pi^H(t)\,\mathrm{d}t \tag{4.45}$$

to obtain

$$F_{-2} \le F_0/t_0^2 - \frac{\left(F_1/t_0^2 - F_{-1}^{(B)}\right)^2}{\left(F_2/t_0^2 - F_0\right)}\,, \tag{4.46}$$

$$F_2/t_0^2 - F_0 > 0\,, \left(F_1/t_0^2 - F_{-1}^{(B)}\right)^2 < \left(F_1/t_0^2 - F_0^2/F_1\right)^2\,, \tag{4.47}$$

where the inequality $F_{-1} \ge F_0^2/F_1$ [see (4.29)] has again been used as part of the subsidiary condition (4.47) for the validity of (4.46).

Thus the upper QCD bound that is complimentary to the lower bound (4.33) is

$$a_\mu^{\mathrm{QCD}} \le \frac{4m_\mu^2\alpha^2}{3}\begin{cases} F_{-1}^{(B)}/t_0 - \frac{\left(F_0/t_0 - F_{-1}^{(B)}\right)^2}{F_1/t_0 - F_0} \\ F_0/t_0^2 - \frac{\left(F_1/t_0^2 - F_{-1}^{(B)}\right)^2}{F_2/t_0^2 - F_0} \end{cases}\,, \tag{4.48}$$

where either (4.43) or (4.46) is used for a QCD upper bound on $F_{-2}$. Both forms lead to identical numerical values despite the distinct pathways used to obtain them. Note that similar to the lower bound on $F_{-2}$ in (4.32), the $F_{-2}$ upper bounds (4.43) and (4.46) all depend on the well-determined QCD FESRs $\{F_0, F_1, F_2\}$, and similarly the parameter $s_0$ can be varied to find the strongest possible QCD bound. Combining (4.37) and (4.48), our $a_\mu^{\mathrm{QCD}}$ bounds emerging from fundamental QCD sum-rule inequalities are

$$\xi\frac{4m_\mu^2\alpha^2}{3}\frac{F_0^3\left(s_0\right)}{F_1^2\left(s_0\right)} \le a_\mu^{\mathrm{QCD}} \le \frac{4m_\mu^2\alpha^2}{3}\begin{cases} F_{-1}^{(B)}/t_0 - \frac{\left(F_0/t_0 - F_{-1}^{(B)}\right)^2}{F_1/t_0 - F_0} \\ \\ F_0/t_0^2 - \frac{\left(F_1/t_0^2 - F_{-1}^{(B)}\right)^2}{F_2/t_0^2 - F_0} \end{cases}, \ \xi = 0.83\,, \tag{4.49}$$

where the parameter $s_0$ can be varied independently on both sides of the inequality to find the strongest possible bounds.

### 4.3.3 Finite-Energy Sum-Rules: QCD Inputs

To generate a bound on $a_\mu^{\mathrm{QCD}}$ from the FESRs in Eq. (4.49), correlation functions for the light quark vector current $j_\mu(x) = \bar{q}(x)\gamma_\mu q(x)$ provide the QCD prediction related to the hadronic spectral function in (4.21). The original LO calculation of the QCD correlation function $\Pi(Q^2)$ up to dimension-six in the operator-product expansion [82, 83, 189] (see also Refs. [44, 48, 107, 189]) has been extended to NLO in the dimension-four QCD condensates [184, 190, 191] and $\overline{\mathrm{MS}}$-scheme perturbative contributions up to five loop order in the chiral limit [192–198] (see also Refs. [199, 200])

$$\begin{aligned} \Pi\left(Q^2\right) = & \frac{1}{4\pi^2}\Pi^{\mathrm{pert}}\left(Q^2\right) - \frac{3m_q^2(\nu)}{2\pi^2 Q^2} + 2\langle m_q\bar{q}q\rangle\frac{1}{Q^4}\left(1 + \frac{1}{3}\frac{\alpha_s(\nu)}{\pi}\right) \\ & + \frac{1}{12\pi}\langle\alpha_s G^2\rangle\frac{1}{Q^4}\left(1 + \frac{7}{6}\frac{\alpha_s(\nu)}{\pi}\right) - \frac{224}{81}\pi\alpha_s\langle\bar{q}\bar{q}qq\rangle\frac{1}{Q^6}\,. \end{aligned} \tag{4.50}$$

In addition, $\Pi\left(Q^2\right)$ also requires an additional pre-factor of the quark charge $Q_q^2$. The perturbative contributions in (4.50) are given by

$$\frac{1}{\pi}\mathrm{Im}\Pi^{\mathrm{pert}}\left(t,\nu\right)=S\left[x(\nu),L(\nu)\right]=1+\sum_{n=1}^{\infty}x^n\sum_{m=0}^{n-1}T_{n,m}L^m\,, \tag{4.51}$$

$$x(\nu)\equiv\frac{\alpha_s(\nu)}{\pi}\,,\;L(\nu)\equiv\log\left(\frac{\nu^2}{t}\right)\,, \tag{4.52}$$

where the coefficients $T_{n,m}$ given in Table 4.1 are implicitly a function of $n_f$, the number of active quark flavours. As outlined below, the energy range in our analysis results in a renormalization scale appropriate to $n_f=3$ and $n_f=4$. The QCD parameters necessary for Eqs. (4.21) and (4.50) are listed in Table 4.2.

| $n_f=4$ | $m=0$ | $m=1$ | $m=2$ | $m=3$ | $n_f=3$ | $m=0$ | $m=1$ | $m=2$ | $m=3$ |
|---|---|---|---|---|---|---|---|---|---|
| $n=1$ | 1 | – | – | – | $n=1$ | 1 | – | – | – |
| $n=2$ | 1.52453 | 25/12 | – | – | $n=2$ | 1.63982 | 9/4 | – | – |
| $n=3$ | -11.6856 | 9.56054 | 625/144 | – | $n=3$ | -10.2839 | 11.3792 | 81/16 | – |
| $n=4$ | -92.91 | -56.90 | 36.56 | $\frac{15625}{1728}$ | $n=4$ | -106.896 | -46.2379 | 47.4048 | 729/64 |

**Table 4.1:** $\overline{\mathrm{MS}}$-scheme coefficients $T_{n,m}$ within (4.51) for the imaginary part of the vector-current correlation function up to five-loop order for $n_f=4$ (left) and $n_f=3$ (right). The four-loop results are given in Ref. [199], the five-loop coefficient $T_{4,0}$ is from [192], and five-loop logarithmic coefficients $T_{4,1}$, $T_{4,2}$, and $T_{4,3}$ are generated from the renormalization group analysis of Ref. [199] via the four-loop ($n_f=4$ and $n_f=3$) $\overline{\mathrm{MS}}$-scheme $\beta$ function [201].

The FESR defined via (4.21) are now constructed up to five-loop order in perturbation theory in the chiral limit, LO in light-quark mass corrections, next-to-leading order (NLO) in dimension-four QCD condensates, and to LO in dimension-six QCD condensates. Using standard FESR methodology [124, 126, 176, 177], the resulting FESR $F_k$ for weights $k=$

| Parameter | Value | Source |
|---|---|---|
| $\alpha$ | $1/137.036$ | [108] |
| $\alpha_s\left(M_\tau\right)$ | $0.312 \pm 0.015$ | [108] |
| $m_u(2\,\mathrm{GeV})$ | $2.16^{+0.49}_{-0.26}\,\mathrm{MeV}$ | [108] |
| $m_d(2\,\mathrm{GeV})$ | $4.67^{+0.48}_{-0.17}\,\mathrm{MeV}$ | [108] |
| $m_s(2\,\mathrm{GeV})$ | $\left(0.0934^{+0.0086}_{-0.0034}\right)$ GeV | [108] |
| $f_\pi$ | $\left(0.13056 \pm 0.00019\right)/\sqrt{2}$ GeV | [108] |
| $m_n\langle\bar{n}n\rangle$ | $-\frac{1}{2}f_\pi^2 m_\pi^2$ | [98] |
| $m_s\langle\bar{s}s\rangle$ | $r_m r_c m_n\langle\overline{n}n\rangle$ | [202] |
| $r_c \equiv \langle\bar{s}s\rangle/\langle\bar{n}n\rangle$ | $0.66 \pm 0.10$ | [202] |
| $m_s/m_n = r_m$ | $27.33^{+0.67}_{-0.77}$ | [108] |
| $\langle\alpha G^2\rangle$ | $\left(0.0649 \pm 0.0035\right)$ GeV$^4$ | [203] |
| $\kappa$ | $3.22 \pm 0.5$ | [203] |
| $\alpha_s\langle\bar{n}n\rangle^2$ | $\kappa\left(1.8 \times 10^{-4}\right)$ GeV$^6$ | [202] |
| $\alpha_s\langle\bar{s}s\rangle^2$ | $r_c^2\alpha_s\langle\bar{n}n\rangle^2$ | [202] |

**Table 4.2:** QCD parameters and uncertainties used in our analysis. Here, $m_n = \left(m_u + m_d\right)/2$ and $\langle\bar{n}n\rangle = \langle\bar{u}u\rangle = \langle\bar{d}d\rangle$.

$\{0, 1, 2\}$ as needed for analysis of (4.31), (4.43), and (4.46) are given by

$$F_0\left(s_0\right) = \frac{1}{4\pi^2}\Bigg[1 + \frac{\alpha_s(\nu)}{\pi}T_{1,0} + \left(\frac{\alpha_s(\nu)}{\pi}\right)^2\left(T_{2,0} + T_{2,1}\right) + \left(\frac{\alpha_s(\nu)}{\pi}\right)^3\left(T_{3,0} + T_{3,1} + 2T_{3,2}\right) + \left(\frac{\alpha_s(\nu)}{\pi}\right)^4\left(T_{4,0} + T_{4,1} + 2T_{4,2} + 6T_{4,3}\right)\Bigg]s_0 - \frac{3}{2\pi^2}m_q(\nu)^2\,, \tag{4.53}$$

$$
\begin{aligned}
F_1\left(s_0\right) = \frac{1}{8\pi^2}\Bigg[ & 1+\frac{\alpha_s(\nu)}{\pi}T_{1,0}+\left(\frac{\alpha_s(\nu)}{\pi}\right)^2\left(T_{2,0}+\frac{1}{2}T_{2,1}\right) \\
& +\left(\frac{\alpha_s(\nu)}{\pi}\right)^3\left(T_{3,0}+\frac{1}{2}T_{3,1}+\frac{1}{2}T_{3,2}\right) \\
& +\left(\frac{\alpha_s(\nu)}{\pi}\right)^4\left(T_{4,0}+\frac{1}{2}T_{4,1}+\frac{1}{2}T_{4,2}+\frac{3}{4}T_{4,3}\right)\Bigg]s_0^2 \\
& -2\langle m_q\bar{q}q\rangle\left(1+\frac{1}{3}\frac{\alpha_s(\nu)}{\pi}\right)-\frac{1}{12\pi}\langle\alpha_s G^2\rangle\left(1+\frac{7}{6}\frac{\alpha_s(\nu)}{\pi}\right)\,, \qquad (4.54)
\end{aligned}
$$

$$
\begin{aligned}
F_2\left(s_0\right) = \frac{1}{12\pi^2}\Bigg[ & 1+\frac{\alpha_s(\nu)}{\pi}T_{1,0}+\left(\frac{\alpha_s(\nu)}{\pi}\right)^2\left(T_{2,0}+\frac{1}{3}T_{2,1}\right) \\
& +\left(\frac{\alpha_s(\nu)}{\pi}\right)^3\left(T_{3,0}+\frac{1}{3}T_{3,1}+\frac{2}{9}T_{3,2}\right) \\
& +\left(\frac{\alpha_s(\nu)}{\pi}\right)^4\left(T_{4,0}+\frac{1}{3}T_{4,1}+\frac{2}{9}T_{4,2}+\frac{2}{9}T_{4,3}\right)\Bigg]s_0^3-\frac{224}{81}\pi\alpha_s\langle\bar{q}\bar{q}qq\rangle\,. \qquad (4.55)
\end{aligned}
$$

Implicit in Eqs. (4.53)–(4.55) is a renormalization scale of $\nu=\sqrt{s_0}$ in both $\alpha_s$ and the running quark masses (see *e.g.,* Refs. [124, 126, 176, 177]). This can be understood as arising from the renormalization-group equation satisfied by (4.51)

$$
\left(-t\frac{\partial}{\partial t}+\alpha_s\beta(\alpha_s)\frac{\partial}{\partial\alpha_s}\right)\mathrm{Im}\Pi^{\mathrm{pert}}\left(t,\nu\right)=0\,, \qquad (4.56)
$$

where the canonical and anomalous mass dimensions are zero for the vector current. From (4.56) it follows that the FESRs satisfy the following renormalization-group equation [1]

$$
\left(-s_0\frac{\partial}{\partial s_0}+\alpha_s\beta(\alpha_s)\frac{\partial}{\partial\alpha_s}+(k+1)\right)F_k^{\mathrm{pert}}\left(s_0,\nu\right)=0\,, \qquad (4.57)
$$

$$
F_k^{\mathrm{pert}}\left(s_0,\nu\right)=\int_0^{s_0}t^k\frac{1}{\pi}\mathrm{Im}\Pi^{\mathrm{pert}}\left(t,\nu\right)\,dt\,. \qquad (4.58)
$$

Thus apart from the trivial $s_0^{k+1}$ canonical dimension prefactor, the solution of the renormalization-group equation for the QCD expressions (4.53)–(4.55) is obtained by the standard replace-

---

[1] Note that Eq. (4.56) and (4.57) are modified comparing to the published version to keep the consistency of the $\beta$ function definition throughout this thesis.

ment $\nu^2 = s_0$. For renormalization-group behaviour of the dimension-four NLO contributions, it is helpful to recall that $\langle m_q \bar{q} q \rangle$ and $\langle \beta G^2 \rangle + 4\gamma \langle m_q \bar{q} q \rangle$ are renormalization-group invariant (see *e.g.,* Ref. [44]).

In particular, because we are working to $\mathcal{O}\left(\alpha_s^4\right)$ in perturbation theory, we numerically solve the renormalization-group equation using the four-loop $\overline{\text{MS}}$-scheme $\beta$ function [201] with $n_f$ appropriate to the active flavours below $s_0$ and using $\alpha_s\left(M_\tau\right)$ as a boundary condition. For the running quark mass corrections, only the LO ($\overline{\text{MS}}$-scheme) anomalous mass dimension is needed. As outlined below, this $s_0$ energy region will span the range covered by $n_f = 4$ and $n_f = 3$. We do not implement flavour threshold matching conditions [204] (see *e.g.,* Ref. [205] for an example implementation) because such effects are insignificant compared to other sources of theoretical uncertainty. Finally, the generic light-flavour FESRs (4.53)–(4.55) require a pre-factor of their quark charge (*i.e.,* $Q_u^2 = 4/9$ and $Q_d^2 = Q_s^2 = 1/9$).

### 4.3.4 Analysis Methodology and Results

With the FESRs now defined in Eqs. (4.53)–(4.55), a lower bound on $a_\mu^{\text{QCD}}$ can be constructed via (4.37) [see also (4.49)]. The methodology seeks to optimize $s_0$ such that it simultaneously maximizes the ratio $F_0^3/F_1^2$ to obtain the strongest possible bound, while still satisfying the inequality (4.29) with $k = 1$. This ensures that the resulting $s_0^{\text{opt}}$ is in the region of validity for the FESRs because they satisfy the same inequality properties as an integrated hadronic spectral function. We start scanning $s_0$ from large energy (beginning near bottom threshold in $n_f = 4$ regime) and find that stronger bounds trend toward lower $s_0$. We then transition to $n_f = 3$ below the charm threshold (uncertainties associated with the Ref. [108] value for the $m_c\left(m_c\right) = 1.27\,\text{GeV}$ threshold are negligible) .

We use two different implementations of this optimization methodology. The flavour-separated approach applies the methodology to the FESRs (with each charge factor included) for each flavour separately, and then combines the individual optimized flavour contributions to obtain the final bound on $a_\mu^{\text{QCD}}$. In the flavour-combined approach, the methodology is applied to a combined FESR with a sum over flavours (with their charge factors included). The strongest bound from these two implementations is then used for our final prediction of the lower bound on $a_\mu^{\text{QCD}}$.

We find that the flavour-separated approach leads to the strongest bound, and Table 4.3 shows the results for the central values of the QCD input parameters of Table 4.2. There are a few key points in the interpretation of Table 4.3. First, it is important to remember that (4.37) is truly a bound, and the optimized $s_0^{\mathrm{opt}}$ represents the value which maximizes the bound while simultaneously satisfying the $k = 1$ inequality (4.29). It is therefore incorrect to interpret $s_0^{\mathrm{opt}}$ as a cut-off on the QCD contributions. Second, the only field-theoretical distinction between the $u$ and $d$ contributions arises from the very small effect of quark masses, and hence $s_0^{\mathrm{opt}}$ is the same in the non-strange channels and the bounds on $a_\mu^{\mathrm{QCD}}$ are in the ratio of quark charges $Q_u^2/Q_d^2 = 4$. Third, the strange contributions to the $a_\mu^{\mathrm{QCD}}$ bound are roughly an order of magnitude smaller than non-strange, a feature that aligns with the data-driven and LQCD approaches to $a_\mu^{\mathrm{HVP,LO}}$ [17, 206]. Finally, we note that the entire inequality analysis of Section 4.3.2 would also apply to Laplace sum-rules, leading to analogous expressions for Eq. (4.37). We have explored this possibility and find that the Laplace sum-rule bounds are considerably weaker than for FESRs, presumably because the Laplace sum-rule kernel $\exp(-t\tau)$ suppresses higher-energy contributions compared to the polynomial FESR kernels.

| Flavour | $s_0^{\mathrm{opt}}$ $\left(\mathrm{GeV}^2\right)$ | $a_\mu^{\mathrm{QCD}}$ (lower bound) | $a_\mu^{\mathrm{QCD}}$ (upper bound) |
|---|---|---|---|
| $u$ | 1.09 | $\geq 472.7 \times 10^{-10}$ | $\leq 567.2 \times 10^{-10}$ |
| $d$ | 1.09 | $\geq 118.1 \times 10^{-10}$ | $\leq 141.7 \times 10^{-10}$ |
| $s$ | 1.19 | $\geq 66.2 \times 10^{-10}$ | $\leq 79.5 \times 10^{-10}$ |
| Total | – | $\geq 657.0 \times 10^{-10}$ | $\leq 788.4 \times 10^{-10}$ |

**Table 4.3:** The optimized $s_0^{\mathrm{opt}}$ and corresponding bounds on $a_\mu^{\mathrm{QCD}}$ are shown for each flavour in the flavour-separated method for central values of the QCD input parameters of Table 4.2. The total entry represents the sum of the individual flavour contributions for the final predicted bounds on $a_\mu^{\mathrm{QCD}}$.

An uncertainty analysis was performed to determine the sensitivity of the Table 4.3 lower $a_\mu^{\mathrm{QCD}}$ bounds arising from the QCD input parameters in Table 4.2. The uncertainty of the $a_\mu^{\mathrm{QCD}}$ bound is dominated by changes in the vacuum saturation parameter $\kappa$ and in the uncertainty of the dimension-four gluon condensate parameter $\langle \alpha G^2 \rangle$ (the poorly known strange-quark condensate parameter $r_c$ is a sub-dominant effect because the strange contributions in Table 4.3 are much smaller than non-strange). Taking into account the combined effect of these uncertainties gives our final QCD prediction for the light-quark contributions lower bound

$$a_\mu^{\mathrm{QCD}} \geq (657.0 \pm 34.8) \times 10^{-10}\,. \tag{4.59}$$

A similar methodology is used to analyze the upper bounds associated with Eq. (4.48) [see also (4.49)] using either (4.43) or (4.46) for the upper bound on $F_{-2}$. We seek the strongest bound that simultaneously satisfies the $k = 1$ inequality (4.29) along with the conditions (4.41), (4.44), and (4.47). As in the lower bound analysis, the flavour-separated approach leads to the strongest bound, and the same $s_0^{\mathrm{opt}}$ is obtained because the $k = 1$ Cauchy-Schwarz inequality (4.29) turns out to be a limiting constraint in both cases. The results shown in Table 4.3 along with the theoretical uncertainty gives our final QCD prediction for the light-quark contributions upper bound

$$a_\mu^{\mathrm{QCD}} \leq (788.4 \pm 41.8) \times 10^{-10}\,. \tag{4.60}$$

For purposes of comparison with data-driven approaches, we first note that although we are calculating light-quark contributions (and ultimately using $n_f = 3$ virtual corrections in the final results), our determinations (4.59) and (4.60) still incorporate high-energy perturbative contributions to $a_\mu^{\mathrm{QCD}}$. We are thus underestimating the perturbative contributions above the charm threshold, and so our bounds remain valid. Thus we have to supplement our bounds with charmonium and bottomonium resonance contributions of $a_{\mu\,,\,\bar{c}c\,,\,\bar{b}b}^{\mathrm{HVP,LO}} = (7.93 \pm 0.19) \times 10^{-10}$ from [206] to obtain our total bound for comparison purposes

$$(664.9 \pm 34.8) \times 10^{-10} \leq a_\mu^{\mathrm{HVP,LO}} \leq (796.3 \pm 41.8) \times 10^{-10} \tag{4.61}$$

which should be compared with the data-driven Ref. [206] result

$$a_\mu^{\mathrm{HVP,LO}} = (692.78 \pm 2.42) \times 10^{-10}, \tag{4.62}$$

the data-driven result reported in the $(g-2)$ Theory Initiative Whitepaper [17]

$$a_\mu^{\mathrm{HVP,LO}} = (693.1 \pm 4.0) \times 10^{-10}, \tag{4.63}$$

as well as the result from LQCD reported in the $(g-2)$ Theory Initiative Whitepaper [17],

$$a_\mu^{\mathrm{HVP,LO}} = (711.6 \pm 18.4) \times 10^{-10}. \tag{4.64}$$

These values can been seen compared against our bounds in Figure 4.5.

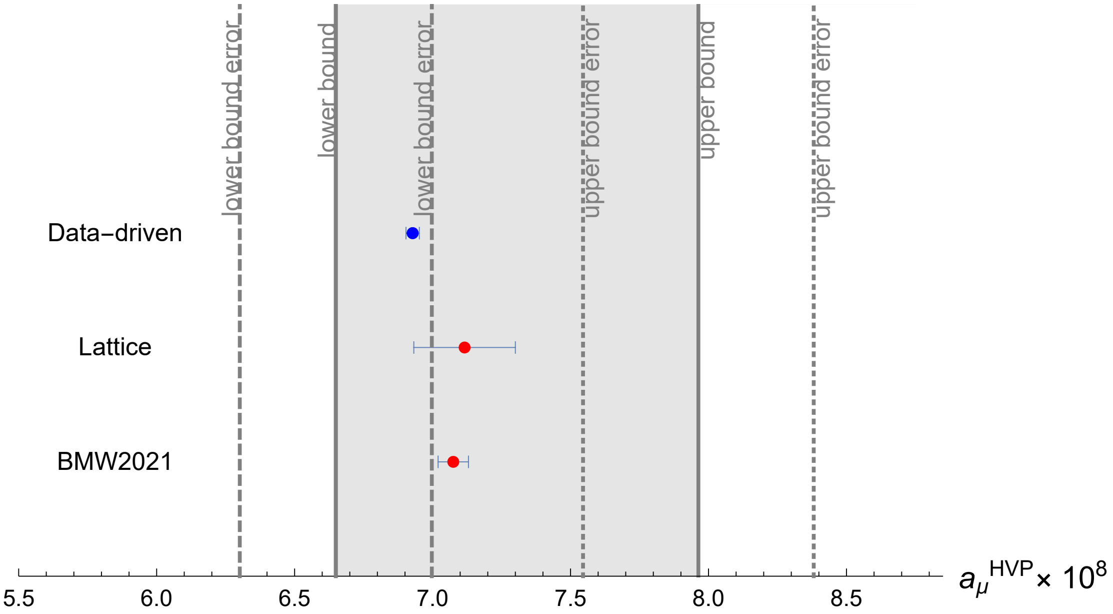

**Figure 4.5:** The $a_\mu^{\mathrm{QCD}}$ results (4.61) showing lower bound (long dashed lines reflecting theoretical uncertainties) and upper bound (short dashed lines reflecting theoretical uncertainties) in comparison to the $a_\mu^{\mathrm{HVP,LO}}$ world theoretical averages given in [17]. The blue indicates a data-driven methodology, while red indicates a value obtained via LQCD. Both the LQCD world average [17] and the sub-percent precision calculation from the BMW collaboration [19] are shown for comparison. The grey shaded region illustrates the allowed central-value range of our QCD predictions in Eq. (4.61).

In conclusion, we have constructed bounds on the QCD contributions to $a_\mu^{\mathrm{HVP,LO}}$ using a family of Hölder inequalities and related inequality constraints for QCD finite-energy sum-rules (FESRs). These fundamental inequalities are based on the requirement that the QCD FESRs are consistent with the relation (4.21) to an integrated hadronic spectral function, providing a novel methodology complementary to lattice QCD and data-driven approaches to determining $a_\mu^{\rm HVP,LO}$. Analyzing the light-quark $(u, d, s)$ contributions up to five-loop order in perturbation theory in the chiral limit, LO in light-quark mass corrections, NLO in dimension-four QCD condensates, and to LO in dimension-six QCD condensates leads to our QCD bounds in Eqs. (4.59) and (4.60), which can be supplemented with the well-known contributions from charmonium and bottomonium states to obtain the QCD bounds given in Eq. (4.61). As shown in the Appendix, these FESR bounds are more restrictive than the updated Laplace sum-rule bounds using the approach of Ref. [107]. As illustrated in Fig. 4.5, the central values of our total QCD bounds (4.61) thus bridge the region between LQCD and data-driven values, indicating a possible resolution of the tension between LQCD and data-driven determinations of $a_\mu^{\rm HVP,LO}$. Resolving this tension would provide better guidance to searches for new physics in measurements of the anomalous magnetic moment of the muon. In future work we will search for new methods and new fundamental inequalities to improve bounds on the QCD contributions to $a_\mu^{\rm HVP,LO}$.

## Acknowledgments

TGS is grateful for research funding from the Natural Sciences and Engineering Research Council of Canada (NSERC).

## Appendix: Laplace Sum Rule Approach

QCD Laplace sum-rules [82, 83] are similar to finite-energy sum-rules as defined in (4.21); however, they are constructed using a Borel (inverse Laplace) transform which introduces an exponential factor:

$$L_k\left(\tau\,, s_0\right) = \int_{t_0}^{s_0} \frac{1}{\pi} {\rm Im}\Pi^H\left(t\right) t^k\, e^{-t\tau}\, {\rm d}t\,. \tag{4.65}$$

In [107] it was shown that $a_\mu^{\rm HVP,LO}$, as defined in (4.18), can be expressed as a linear combination of QCD Laplace sum-rules (4.65). First, the exact kernel function (4.14) can be approximated near $t = t'$ as

$$K\left(t\right) \approx \mathcal{K}\left(t\,,t'\right) = K\left(t'\right) e^{\zeta} \left[a_1 \left(\frac{t}{t'}\right) + a_2 \left(\frac{t}{t'}\right)^2 + a_3 \left(\frac{t}{t'}\right)^3\right] e^{-\zeta t/t'}\,, \tag{4.66}$$

where $a_1 + a_2 + a_3 = 1$ so that $K\left(t'\right) = \mathcal{K}\left(t'\,,t'\right)$. Inserting (4.66) into (4.18) yields

$$a_\mu^{\mathrm{QCD}} \approx 4\alpha^2\, K\left(t'\right) \frac{e^{\zeta}}{t'} \int_{t_0}^{\infty} \frac{1}{\pi} \mathrm{Im}\Pi^H\left(t\right) \left[a_1 + a_2 \left(\frac{t}{t'}\right) + a_3 \left(\frac{t}{t'}\right)^2\right] e^{-\zeta t/t'} \mathrm{d}t\,, \tag{4.67}$$

where $t_0 = 4m_\pi^2$. Introducing the parameter $s_0$ as in (4.22) and defining $\tau = \zeta/t'$, (4.67) becomes

$$a_\mu^{\mathrm{QCD}} \approx 4\alpha^2\, K\left(\zeta/\tau\right) \frac{\tau}{\zeta} e^{\zeta} \int_{t_0}^{s_0} \frac{1}{\pi} \mathrm{Im}\Pi^H\left(t\right) \left[a_1 + a_2 \left(\frac{t}{t'}\right) + a_3 \left(\frac{t}{t'}\right)^2\right] e^{-t\tau} \mathrm{d}t\,. \tag{4.68}$$

Comparing (4.68) and the definition of the Laplace sum-rules in (4.65) shows that we may approximate $a_\mu^{\mathrm{HVP,LO}}$ as a linear combination of Laplace sum-rules:

$$a_\mu^{\mathrm{QCD}} \approx 4\alpha^2\, K\left(\zeta/\tau\right) \frac{\tau}{\zeta} e^{\zeta} \left[a_1 L_0\left(\tau\,,s_0\right) + a_2 \frac{\tau}{\zeta} L_1\left(\tau\,,s_0\right) + a_3 \left(\frac{\tau}{\zeta}\right)^2 L_2\left(\tau\,,s_0\right)\right]\,. \tag{4.69}$$

The approximation (4.66) is used because it makes a theoretical calculation of $a_\mu^{\mathrm{HVP,LO}}$ (using a QCD expression for the vacuum polarization function) amenable to a Laplace sum-rule analysis. In (4.66) the expansion is truncated at $\mathcal{O}(t^3)$ to avoid dependence on unknown higher dimension QCD condensates (a similar issue is encountered in the finite-energy sum-rule analysis in Section 4.3.2).

Although the approximation (4.66) is designed to be exact at $t = t'$ and is well suited to a Laplace sum-rule analysis, the approximation of the exact kernel function (4.14) decreases in accuracy away from $t = t'$. In order to gain some control over the theoretical uncertainty introduced by this approximation we will follow the approach of Ref. [107], wherein the approximation (4.66) was used to construct underestimates and overestimates of the exact kernel function (4.14), respectively denoted as $\mathcal{K}^{\downarrow}\left(t\,,t'\right)$ (corresponding to parameters $\{a_1 = 1.5700,\, a_2 = -1.75658,\, a_3 = 1.1958,\, \zeta = 2.6528\}$) and $\mathcal{K}^{\uparrow}\left(t\,,t'\right)$ (corresponding to parameters $\{a_1 = 6.0378,\ a_2 = -10.7006,\ a_3 = 5.6628,\ \zeta = 2.6528\}$), which are shown in Fig. 4.6. Using these underestimates and overestimates, a QCD Laplace sum-rule analysis can be performed to generate lower and upper bounds on $a_\mu^{\mathrm{HVP,LO}}$.

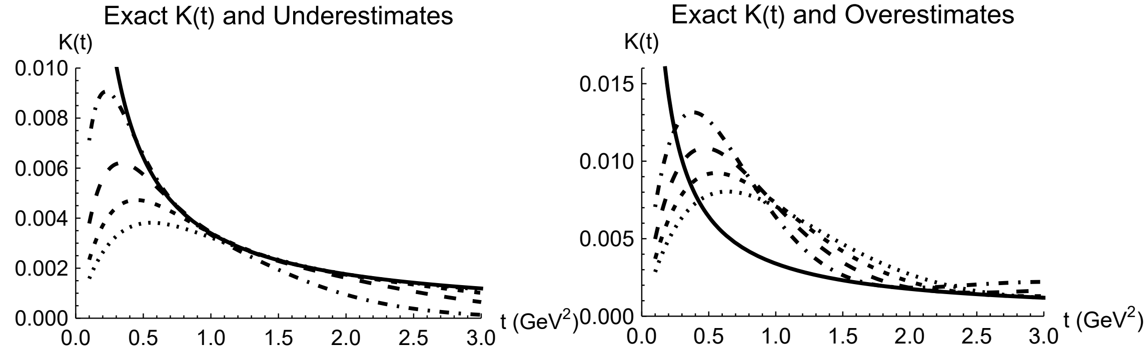

**Figure 4.6:** Left: the exact $K(t)$ (solid line) compared to underestimates $\mathcal{K}^{\downarrow}(t\,,t')$ with $t' \in \{0.8\,,\,1.2\,,\,1.6\,,\,2.0\}$ GeV$^2$, which are respectively represented by the dashed dotted, long dashed, short dashed, and dotted lines. Right: the exact $K(t)$ (solid line) compared to overestimates $\mathcal{K}^{\uparrow}(t\,,t')$ with $t' \in \{1.8\,,\,2.2\,,\,2.6\,,\,3.0\}$ GeV$^2$, which are respectively represented by dashed dotted, long dashed, short dashed, and dotted lines. The parameters used in equation (4.66) for the underestimates $\mathcal{K}^{\downarrow}(t\,,t')$ ($\{a_1 = 1.5700,\ a_2 = -1.75658,\ a_3 = 1.1958,\ \zeta = 2.6528\}$) and overestimates $\mathcal{K}^{\uparrow}(t\,,t')$ ($\{a_1 = 6.0378,\ a_2 = -10.7006,\ a_3 = 5.6628,\ \zeta = 2.6528\}$) are identical to those used in Ref. [107].

Using the results of Eqs. (4.50) and (4.51), the Laplace sum-rules (LSRs) for light-quark $(u, d, s)$ contributions up to five-loop order in perturbation theory in the chiral limit, LO in light-quark mass corrections, next-to-leading order (NLO) in dimension-four QCD condensates, and to LO in dimension-six QCD condensates are given for a generic light flavour by

$$
\begin{aligned}
L_0(\tau, s_0) = {}& \frac{1}{4\pi^2\tau}\left[f_{0,0}(\tau s_0) + \sum_{k=0}^{3} f_{0,k}(\tau s_0) \sum_{j=k+1}^{4} T_{j,k}\left(\frac{\alpha_s(\nu)}{\pi}\right)^j\right] - \frac{3}{2\pi^2} m_q(\nu)^2 \\
& + 2\langle m_q \bar{q} q\rangle\left(1 + \frac{1}{3}\frac{\alpha_s(\nu)}{\pi}\right)\tau + \frac{1}{12\pi}\langle \alpha_s G^2\rangle\left(1 + \frac{7}{6}\frac{\alpha_s(\nu)}{\pi}\right)\tau - \frac{112}{81}\pi\alpha_s\langle \bar{q}\bar{q}qq\rangle\tau^2\,, \quad (4.70)
\end{aligned}
$$

$$L_1(\tau, s_0) = \frac{1}{4\pi^2\tau^2}\left[f_{1,0}(\tau s_0) + \sum_{k=0}^{3} f_{1,k}(\tau s_0) \sum_{j=k+1}^{4} T_{j,k}\left(\frac{\alpha_s(\nu)}{\pi}\right)^j\right]$$
$$- 2\langle m_q\bar{q}q\rangle\left(1 + \frac{1}{3}\frac{\alpha_s(\nu)}{\pi}\right) - \frac{1}{12\pi}\langle\alpha_s G^2\rangle\left(1 + \frac{7}{6}\frac{\alpha_s(\nu)}{\pi}\right) + \frac{224}{81}\pi\alpha_s\langle\bar{q}\bar{q}qq\rangle\tau\,, \quad (4.71)$$

$$L_2(\tau, s_0) = \frac{1}{4\pi^2\tau^3}\left[f_{2,0}(\tau s_0) + \sum_{k=0}^{3} f_{2,k}(\tau s_0) \sum_{j=k+1}^{4} T_{j,k}\left(\frac{\alpha_s(\nu)}{\pi}\right)^j\right] - \frac{224}{81}\pi\alpha_s\langle\bar{q}\bar{q}qq\rangle\,, \quad (4.72)$$

where we have defined the quantity

$$f_{j,k}(\tau s_0) = \int_0^{\tau s_0} z^j\left[\log\left(\frac{1}{z}\right)\right]^k e^{-z}\,dz\,. \quad (4.73)$$

Implicit in Eqs. (4.70)–(4.72) is a renormalization scale of $\nu = 1/\sqrt{\tau}$ in both $\alpha_s$ and the running quark masses [117]. As in the QCD expressions (4.53)–(4.55) for the FESRs, the generic light-flavour LSRs (4.70)–(4.72) require a pre-factor of their quark charge.

Following the analysis methodology Ref. [107] for determining the upper and lower bounds on $a_\mu^{\rm QCD}$, $\tau$ stability [89,154,207] is used to determine the right-hand side of (4.69) for a fixed $s_0$, and then $s_0$ is varied until an asymptotic value is reached. The $\tau$-stability region naturally tends toward the $n_f = 3$ regime. As with the FESRs, this methodology can be applied to either a flavour-separated or flavour-combined case, but unlike the FESRs there is negligible difference in the two cases. Figure 4.7 shows the results for central values of the QCD input parameters, and leads to the bounds

$$369.5 \times 10^{-10} \le a_\mu^{\rm QCD} \le 930.2 \times 10^{-10}\,. \quad (4.74)$$

Comparing Eq. (4.74) with the FESR results in Eqs. (4.59) and (4.60) it is evident that the FESR bounds are stronger than those obtained from updated and extended QCD inputs in the Ref. [107] LSR methodology.

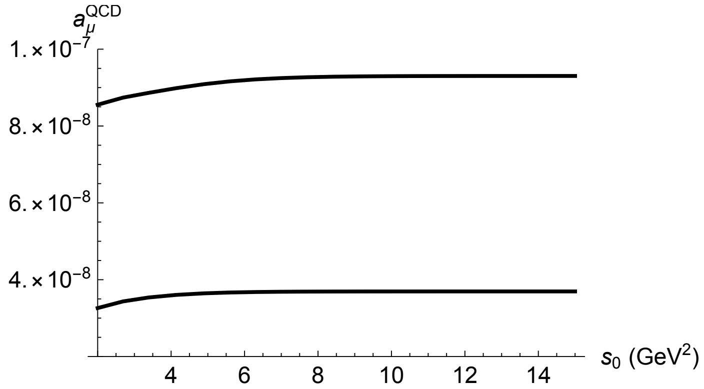

**Figure 4.7:** LSR upper bound (top curve) and lower bound (bottom curve) on light-quark contributions to $a_\mu^{\rm QCD}$ as a function of $s_0$.

## 4.4 Flavour Transition for running of $\alpha_s$ and $m_q$

One subtle aspect not explicitly detailed in Sec. 4.3.3 of the manuscript is the RG analysis when transitioning between flavour thresholds as we scan $s_0^{\rm opt}$ to obtain the strongest bounds. This involves moving from the $n_f = 4$ region to the $n_f = 3$ region at charm quark mass threshold as energy scales shift.

From $\beta$-function in Eq. (2.6) and boundary condition energy scale of $\tau$ lepton mass $\nu^{\rm th} = \sqrt{s_0^{\rm th}} = M_\tau$, the strong coupling $\alpha_s(\nu)$ can be computed to four-loop precision aligning with our FESR loop correction order in Sec 4.3.3 [199]:

$$\nu \frac{\mathrm{d}\left(\alpha_s(\nu)/\pi\right)}{\mathrm{d}\nu} = \beta_1\left(\frac{\alpha_s(\nu)}{\pi}\right) + \beta_2\left(\frac{\alpha_s(\nu)}{\pi}\right)^2 + \beta_3\left(\frac{\alpha_s(\nu)}{\pi}\right)^3 + \beta_4\left(\frac{\alpha_s(\nu)}{\pi}\right)^4, \qquad (4.75)$$

where $\alpha_s(\nu = M_\tau) = 0.312$ [108] at the energy scale of $M_\tau = 1.78\,\text{GeV}$, and has its uncertainty being recently updated in 2024 [7]. The values of the four-loop order $\overline{\text{MS}}$-scheme $\beta$-function depend on the number of active flavours [199]. Using data from Ref. [199] or numerically calculated four-loop beta functions from Ref. [201], we obtain the running of $\alpha_s(\nu)$, assuming a boundary condition at $\alpha_s(M_\tau)$, as shown in Fig. 4.8. This was achieved by numerically solving Eq. (4.75) using `MATHEMATICA`. The coupling increases more rapidly for larger $n_f$ values as $\nu$ decreases. It is important to note that the values from Ref. [199] cannot be directly applied to Eq.(4.75) due to inconsistencies in the $\beta$-function definitions across the literature. One must be cautious to appropriately transform between different conventions when comparing results.

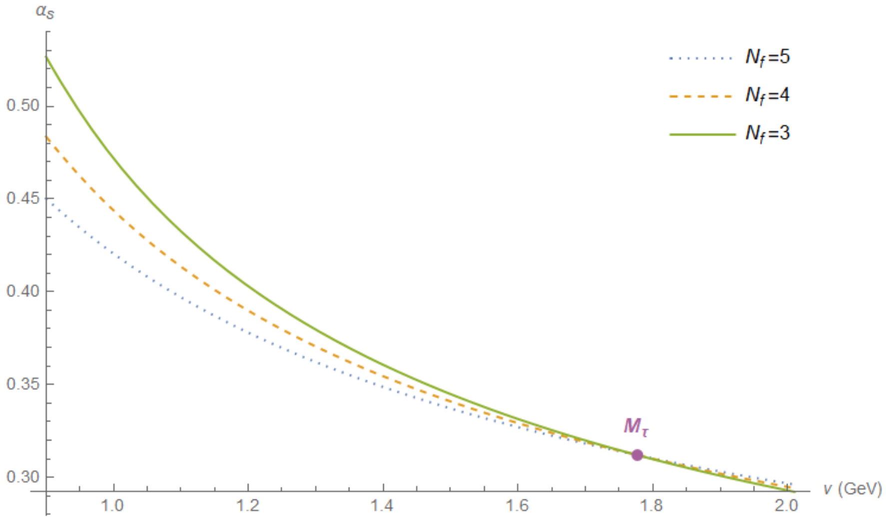

**Figure 4.8:** The running of strong coupling $\alpha_s$ with respect to energy scale $\nu$ for $n_f = 3, 4, 5$ (dotted, dashed, and solid lines, respectively). All curves are computed using the four-loop $\overline{MS}$-scheme $\beta$-functions with the boundary condition $\alpha_s(\nu = M_\tau) = 0.312$.

This reference energy scale at $M_\tau \gg m_q$ for $u, d, s$, and $c$ quarks is sufficiently large to activate the $c$ quark's degree of freedom while remaining below the $b$ quark mass, $m_b(\nu = m_b) = 4.18\,\text{GeV}$. This results in four active quark flavours ($n_f = 4$) at $s_0 = \nu^2$. However, as we lower $s_0$ to search for stronger bounds, the energy crosses the $c$ quark threshold at $M_c = m_c(\nu = m_c) = 1.27\,\text{GeV}$ [108], moving us into the $n_f = 3$ region. At this point, we must switch to the running coupling with $n_f = 3$, with a threshold energy scale at $\nu^{\text{th}} = M_c$. The transition is made by applying the relation from [205]:

$$\alpha_s^{(n_f-1)}(\nu^{\text{th}}) = \\ \alpha_s^{(n_f)}\left(\nu^{\text{th}}\right)\left[1 + 0.1528\left[\frac{\alpha_s^{(n_f)}\left(\nu^{\text{th}}\right)}{\pi}\right]^2 + \{0.9721 - 0.0847\,(n_f - 1)\}\left[\frac{\alpha_s^{(n_f)}\left(\nu^{\text{th}}\right)}{\pi}\right]^3\right]. \tag{4.76}$$

The difference in $\alpha_s^{(n_f=3)}(M_c)$ obtained from this matching condition is negligible (see Fig. 4.9), and will be overwhelmed by the uncertainty in $\alpha_s(M_\tau)$ alone. Thus, we ignore the effect of this small discontinuity and approximate:

$$\alpha_s^{(n_f=3)}(M_c) \simeq \alpha_s^{(n_f=4)}(M_c) = 0.376. \tag{4.77}$$

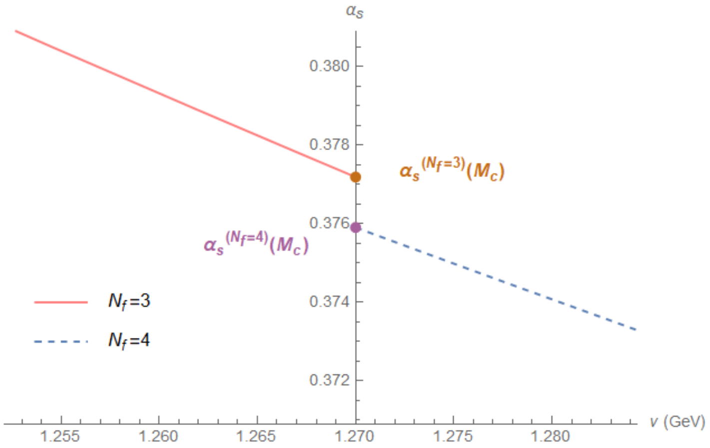

**Figure 4.9:** The small discontinuity in $\alpha_s(\nu)$ between $n_f = 4$ and $n_f = 3$ regions at charm quark threshold. The difference found using Eq. (4.76) is $\alpha_s^{(n_f=3)}(M_c) - \alpha_s^{(n_f=4)}(M_c) = 1.28 \times 10^{-3}$, which is an order of magnitude smaller than the uncertainty in $\alpha_s(M_\tau)$ [7].

Finally, using the four-loop beta function [199] and matching at the $c$ quark threshold, we obtain the combined running of $\alpha_s(\nu)$ in the energy range $1-2\,\text{GeV}$, which crosses between $n_f = 3$ and 4. The results are presented in Fig. 4.10.

A similar procedure is applied to the running of the light quark masses $(u, d, s)$ in $\overline{\text{MS}}$ scheme at the one-loop level, consistent with the order of corrections for quark masses in our FESRs, as discussed in Sec. 4.3.3. This follows the relation [74]:

$$m_q(\nu) = m_q(2\,\text{GeV}) \left[\frac{\alpha_s(\nu)}{\alpha_s(2\,\text{GeV})}\right]^{\frac{12}{33-2n_f}} \tag{4.78}$$

where $m_q(2\,\text{GeV})$ is the light quark mass at the reference scale of $\nu = 2\,\text{GeV}$ from Ref. [7], and $\alpha_s(\nu)$ is the running strong coupling. For $n_f = 4$ , we apply this to compute the running quark mass $m_q^{(n_f=4)}(\nu)$:

$$m_q^{(n_f=4)}(\nu) = m_q(2\,\text{GeV}) \left[\frac{\alpha_s^{(n_f=4)}(\nu)}{\alpha_s^{(n_f=4)}(2\,\text{GeV})}\right]^{\frac{12}{25}}, \tag{4.79}$$

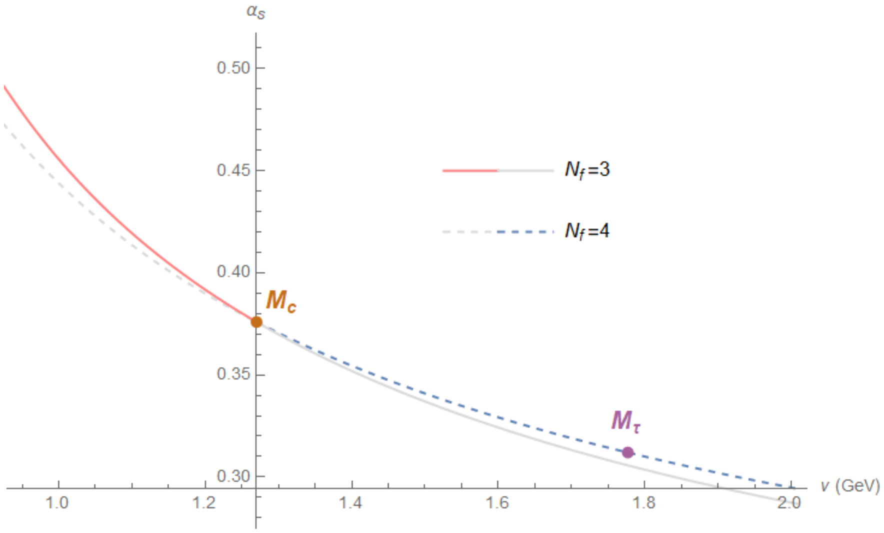

**Figure 4.10:** The complete running of $\alpha_s(\nu)$ transitions from the $n_f = 4$ (blue dashed line) to the $n_f = 3$ (red solid line) region as it crosses the charm quark mass threshold. $\alpha_s(s_0)$ is plotted in the energy range of interest from near $M_\tau$ to around 1 GeV near our $s_0^{\text{opt}}$ shown in Table. 4.3. Extension of $\alpha_s^{(n_f=3)}$ and $\alpha_s^{(n_f=4)}$ beyond their valid regions are shown in solid and dashed gray lines respectively for comparison, illustrating potential errors if the correct transition is not applied.

where the exponent $\frac{12}{25}$ is specific to four active flavors. At the $c$ quark mass threshold $M_c = 1.27\,\text{GeV}$, the quark masses in the $n_f = 3$ and $n_f = 4$ regions are matched giving the boundary condition:

$$\overline{m}_q = m_q^{(n_f=3)}(M_c) = m_q^{(n_f=4)}(M_c) = \begin{cases} 0.00243\,\text{GeV} & \text{up} \\ 0.00523\,\text{GeV} & \text{down} \\ 0.105\,\text{GeV} & \text{strange} \end{cases} \tag{4.80}$$

This boundary condition is then used to compute the running light quark mass in the $n_f = 3$ region:

$$m_q^{(n_f=3)}(\nu) = \overline{m}_q \left[ \frac{\alpha_s^{(n_f=3)}(\nu)}{\alpha_s^{(n_f=3)}(\overline{m}_q)} \right]^{\frac{12}{27}}, \tag{4.81}$$

where the exponent $\frac{12}{27}$ corresponds to three active flavours (one can refer to Eq. (2.60)). This approach ensures a smooth transition between the $n_f = 4$ and $n_f = 3$ regions, allowing us to accurately track the running of quark masses across energy thresholds. Combined functions of running $m_q(\nu)$ for light quarks are shown in Fig 4.11.

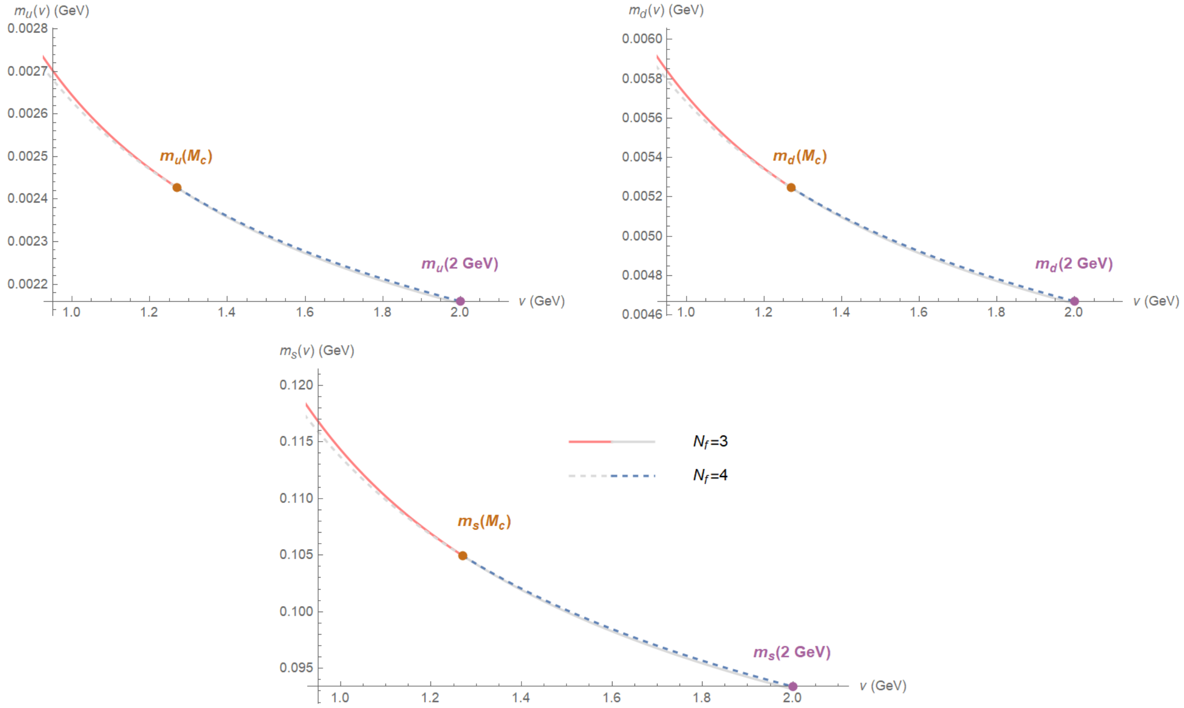

**Figure 4.11:** The running of light quark mass $m_q(\nu)$ for $m_u(\nu), m_d(\nu)$, and $m_s(\nu)$, showing the transitions from the $n_f = 4$ (blue dashed line) to the $n_f = 3$ (red solid line) as the energy scale crosses the charm quark mass threshold. The gray solid and dashed lines represent the extrapolations of the $m_q^{(n_f=3)}$ and $m_q^{(n_f=4)}$ quark masses, respectively, beyond their valid regions, highlighting potential errors if the appropriate transition is not applied at the threshold.

## 4.5 RG Effect on Condensate Contribution

In addition to ensuring proper transitions between regions with different active quark flavours, it is essential to verify that the FESRs are consistent with the RG equations. The RG equation for the perturbative contribution to FESRs is presented in Eqs. (4.57) and (4.58). However, the RG effects extend to the dimension-four condensate contributions at NLO.

Consider a simplified correlator of the form $\Pi = \langle \frac{\alpha_s}{\pi} G^2 \rangle \tilde{\mathcal{H}}$, where $\langle \beta G^2 \rangle$ is RG invariant while $\alpha_s\beta \equiv \nu\frac{\mathrm{d}\alpha_s}{\mathrm{d}\nu}$. If $\tilde{\mathcal{H}}$ satisfies the equation

$$\nu\frac{\mathrm{d}}{\mathrm{d}\nu}\left[\left\langle\beta G^2\right\rangle\tilde{\mathcal{H}}\right] = 0, \tag{4.82}$$

then $\tilde{\mathcal{H}}$, as well as $\Pi$ satisfies a homogeneous RG equation (*i.e.,* zero anomalous dimension). In order to maintain RG invariance for the condensate contributions, we start from Eq. (4.50), which includes the NLO dimension-four condensate contribution:

$$\Pi^{\mathrm{NLO}}_{(D=4)}\left(Q^2\right) = \frac{1}{Q^4}\left[\frac{1}{12\pi}\langle\alpha_s G^2\rangle\left(1+\frac{7}{6}\frac{\alpha_s(\nu)}{\pi}\right) + 2\langle m_q\bar{q}q\rangle\left(1+\frac{1}{3}\frac{\alpha_s(\nu)}{\pi}\right)\right]. \tag{4.83}$$

As discussed briefly in Sec. 4.3.3, we use the NLO perturbative expansion of the RG-invariant combination $\langle\beta G^2\rangle + 4\gamma\langle m_q\bar{q}q\rangle$ to construct a new RG-invariant [44]:

$$\langle\beta G^2\rangle + 4\gamma\langle m_q\bar{q}q\rangle = \frac{1}{\pi}\langle\alpha_s G^2\rangle\left(\beta_1+\beta_2\frac{\alpha_s}{\pi}\right) + \langle m_q\bar{q}q\rangle\left(4\gamma_1\frac{\alpha_s}{\pi}\right) + \mathcal{O}\left(\frac{\alpha_s}{\pi}\right)^2 \tag{4.84}$$

$$\to \frac{1}{\pi}\langle\alpha_s G^2\rangle\left(1+\frac{\beta_2}{\beta_1}\frac{\alpha_s}{\pi}\right) + \langle m_q\bar{q}q\rangle\left(4\frac{\gamma_1}{\beta_1}\frac{\alpha_s}{\pi}\right), \tag{4.85}$$

where, recall from Eq. (2.59), the anomalous dimension is

$$\gamma\left(\frac{\alpha_s}{\pi}\right) = \gamma_1\frac{\alpha_s}{\pi} + \mathcal{O}\left(\frac{\alpha_s}{\pi}\right)^2, \quad \gamma_1 = 2. \tag{4.86}$$

Expressing Eq. (4.83) in terms of these RG invariants: Eq. (4.85) and $\langle m_q\bar{q}q\rangle$ [44], we obtain:

$$\Pi^{\mathrm{NLO}}_{(D=4)}\left(Q^2\right) = \left[\frac{1}{\pi}\langle\alpha_s G^2\rangle\left(1+\frac{\beta_2}{\beta_1}\frac{\alpha}{\pi}\right) + \langle m_q\bar{q}q\rangle\left(4\frac{\gamma_1}{\beta_1}\frac{\alpha}{\pi}\right)\right]\frac{1}{12}\left(1+\frac{7}{6}\xi_g\frac{\alpha_s}{\pi}\right) + 2\langle m_q\bar{q}q\rangle\left(1+\frac{1}{3}\xi_q\frac{\alpha_s}{\pi}\right) \tag{4.87}$$

where $\xi_g = -\frac{11}{21}$ and $\xi_q = \frac{11}{9}$ for $n_f = 3$, and $\xi_g = -\frac{8}{25}$ and $\xi_q = \frac{31}{25}$ for $n_f = 4$. This modification ensures the RG consistency of the NLO correction to the dimension-four condensate contribution, which impacts $F_1$ (Eq. (4.54)) specifically among all FESRs we need.

# 5 Finite Temperature Loop Integrals Computation

So far, we have focused on using QCDSR in the framework of QCD, or more generally QFT, to predict correlations for particle observables. Standard QFT is formulated at zero temperature, where the temperature variable $T$ is not explicitly considered. However, numerous particle physics phenomena occur in thermal environments, which can be broadly categorized into two categories: cosmology (astrophysical generation) and heavy-ion collisions (laboratory reproduction). The former typically involves extremely high temperatures where weak interactions play a crucial role in topics such as the existence of dark matter and the equilibration processes after inflationary epoch, while the latter is dominated by strong interactions (see Ref. [54] for an overview). To analyse these thermal processes effectively, a computational framework for finite-temperature loop integrals becomes invaluable. Such a tool enables deeper exploration of thermal events within SM and beyond.

This chapter is based on the published research Ref. [23]:

***Numerically Computing Finite Temperature Loop Integrals using pySecDec***
**D. Harnett, Siyuan Li, T.G. Steele**
**Eur. Phys. J. A 60 (2024) 5, 107, doi:10.1140/epja/s10050-024-01323-5**

My contributions to this work began with retrieving and verifying the correlation function expressions from previous research outlined in Ref. [208]. Building on the application of inverse Wick rotation to correlators, I analysed the convergence efficiency of the zeta-function correction in the 3-point function scenario. For the 2-point function, I performed detailed analyses and calculations of the dimensional-regularized expressions under various parameter settings, conducted error analysis, generated data for visual representations, and actively contributed to the writing and editing of the manuscript.

The motivation of this research can be found in Sec. 5.1, followed by an introduction to finite-temperature field theory in Sec. 5.2. The full manuscript from [23] is included in Sec. 5.3.

## 5.1 Motivation for Computing Thermal Effects

pySecDec is a powerful Python and C++ program-based package that numerically calculates dimensionally-regulated loop integrals through the sector decomposition approach [209]. The package imposes no restrictions on loop orders, field masses or the number of external field lines in the topologies under study. As the complexity of evaluating loop integrals increases significantly with higher mass scales and loop orders in analytic methods, numerical approaches have become a more favoured option for providing experimental and theoretical predictions of Feynman integrals at high energy scales, aligning with the advancements in modern particle accelerators. All of the above factors collectively make pySecDec a valuable computational tool, forming a robust foundation for developing numerical methodologies.

We aim to use the computational capability of pySecDec for loop integrations in finite temperature field theory, thereby enhancing the understanding of particle processes under thermal effects and advancing studies in new physics, such as BSM phase transitions. With the introduction of an additional temperature dimension (which has the dimension of energy in natural units), the standard massive field content in loop diagrams significantly increases the difficulty of evaluating loop integrals. This necessitates the development of advanced calculational methodologies to seamlessly incorporate finite temperature field theory into tools traditionally designed for ordinary QFT.

Although there are extensive QCDSR studies for hot hadronic matter (see *e.g.,* Refs. [48, 210, 211]) and previous pySecDec adaptation for zero-temperature QCDSR calculations [212, 213], we choose to develop a computational methodology that applies to generic Feynman diagrams that is not restricted to the strong interactions. Our two-fold methodology extends the application of pySecDec to finite temperature loop integrals and tackles the divergence introduced by thermal field theory formalism using dimensional regularization.

## 5.2 Thermal Field Theory

Finite temperature field theory is also called thermal QFT or thermal field theory. It extends QFT to finite temperature and describes phenomena that emerge from the presence of a thermal bath, typically related to particle interactions at high temperatures (*e.g.,* the early universe) or high densities (*e.g.,* inside neutron stars).

For instance, quark-gluon plasma (or quark soup) is a phase that occurs when the temperature is above the Hagedorn temperature ($T_{\mathrm{H}} \gtrsim m_\pi$), where one expects chiral symmetry restoration [48] and colour deconfinement (where the hadronic matter is no longer colour confined and convert into quarks) [214–216]. Quark-gluon plasma is important in studying the early universe shortly after the Big Bang when temperature approaches $T_{\mathrm{H}}$. It is being experimentally studied through heavy-ion collisions and their debris energy distributions at RHIC in Brookhaven and LHC (see *e.g.,* Refs. [217–219] for reports). Baryogenesis is another physical process that relies on high temperature conditions. It introduces a mechanism for the matter-antimatter asymmetry observed in the universe using electroweak phase transition [220, 221]. Another example is gravitational waves which are spacetime ripples caused by accelerations of masses. It is often associated with events such as merging black holes, neutron stars, supernovae and the early universe expansion or first-order phase transition [222–224]. The thermal effects are also present in various topics including linear response theory (external perturbations), screening and plasma oscillation, spontaneous symmetry breaking and BSM dark matter models etc (see *e.g.,* Refs. [54, 225]).

Formalisms commonly used to investigate field theories at finite temperature include the Matsubara formalism, the real-time path formalism, and thermofield dynamics (see *e.g.,* Ref. [226]). Among these, the Matsubara formalism [227] is the most widely applied when discussing an equilibrium distribution of particles and will be the formalism of choice for this chapter.

### 5.2.1 Matsubara Formalism

The Matsubara formalism (also named the imaginary time formalism) describes the expectation value of an observable (operator) in a canonical ensemble as

$$\langle A\rangle = Z^{-1}(\beta)\,\mathrm{Tr}\left(e^{-\beta\mathcal{H}}A\right), \tag{5.1}$$

where $\mathcal{H} = H$ is the ensemble Hamiltonian, as well as the conventional dynamic Hamiltonian. If one is considering a grand canonical ensemble where particle exchange with an external reservoir is allowed, then the chemical potential $\mu$ should be taken into consideration giving Hamiltonian $\mathcal{H} = H - \mu\hat{N}$ where $\hat{N}$ is the associated conserved number operator (*e.g.,* additive quantum numbers such as strangeness) [48, 225, 226]. $Z(\beta)$ is the partition function of the ensemble acting as the normalization factor:

$$Z(\beta) = \mathrm{Tr}\left(e^{-\beta\mathcal{H}}\right). \tag{5.2}$$

With the natural units convention and Boltzmann constant $k_B = 1$, the new parameter $\beta = \hbar/\left(k_B T\right) \to 1/T$ stands for the inverse of temperature. One can easily reach the ground state expectation value of $A$ by taking the zero-temperature limit $T \to 0$ in Eq. (5.1).

The introduction of $\beta$ complicates the Feynman integral which is constructed through *path integral* formalism. The path integral describes a system through a functional integral (sum) over all possible field configurations, connecting from the initial state to the final state to find the transition matrix element or amplitude [30, 138]. One can find an example of path integral formalism application in Eq. (5.4) below. When $\beta$ enters the equation, the density operator $e^{-\beta\mathcal{H}}$ takes a similar form to the time evolution operator $e^{-it\mathcal{H}}$ in Euclidean spacetime. The replacement of $\beta \to it$ can be made and is called the *Wick rotation.*

Wick rotation is a very common technique in QFT to change time from real to imaginary and is usually applied to avoid poles in the temporal component: $x^0 = t$ or $p^0 = E$ depending on the variable of integration, where $E$ stands for relativistic energy. It also changes the square of the four-vector/momentum from Minkowski to Euclidean space:

$$p_M^2 = {p_M^0}^2 - \vec{p}^{\,2} = (ip_E^0)^2 - \vec{p}^{\,2} = -{p_E^0}^2 - \vec{p}^{\,2} = -p_E^2, \tag{5.3}$$

where the subscripts denote the spacetime of choice: $M$ for Minkowski and $E$ for Euclidean. Later in Sec. 5.3, the Minkowski notation is omitted and implied. The square of four vector $x$ goes analogously. Wick rotation is also the inspiration of the *inverse Wick rotation* method in our research which transforms Euclidean integrals into Minkowski spacetime to input in the pySecDec package.

In this application of Wick rotation on $\beta$ (*i.e.*, $\beta \to it$), the configuration in Eq. (5.1) propagates in the imaginary time of $\tau \equiv it \in [\,0, \beta\,]$. Hence the name of the imaginary time formalism [227]. The partition function Eq. (5.2) in the path integral formulation is [225,226]

$$Z = \text{normalization constant} \times \int \mathcal{D}[\phi]\, e^{-S_E[\phi]}, \tag{5.4}$$

where $\mathcal{D}[\phi]$ represents the functional integral measure over all possible configurations of field $\phi$. If the chemical potential $\mu \neq 0$, the Euclidean action $S_E[\phi]$ is defined as [226]:

$$S_E[\phi] = \int_0^\beta d\tau \left( \int \mathrm{d}^3x\, \mathcal{L}_E[\phi] + \mu \hat{N} \right) \tag{5.5}$$

with $\mathcal{L}_E[\phi]$ being the Euclidean Lagrangian density for the system in question. Referring to Eqs. (5.2) and (5.4), the trace operator in (5.2) presses boundary conditions on the fields over a full imaginary-time evolution, implying periodicity for bosonic fields

$$\phi(\tau) = \phi(\tau + \beta), \tag{5.6}$$

and anti-periodicity for fermionic fields

$$\psi(\tau) = -\psi(\tau + \beta) \tag{5.7}$$

due to the Pauli exclusion principle and Fermi-Dirac statistics. This (anti-)periodicity naturally extends to the Green's functions composed of bosonic and fermionic fields $\mathcal{G}(\tau) = \pm\mathcal{G}(\tau + \beta)$ with $\tau \in [-\beta, \beta]$ for the two-point function. The Fourier transform of $\mathcal{G}(x)$ can be written as

$$\mathcal{G}(\tau) = \frac{1}{\beta}\sum_{n} e^{i\omega_n \tau}\mathcal{G}(\omega_n) \Rightarrow \mathcal{G}(\tau, \vec{x}) = \frac{1}{\beta}\sum_{n}\int \frac{\mathrm{d}^3 p}{(2\pi)^3}\, e^{i(\omega_n \tau + \vec{p}\cdot\vec{x})}\,\mathcal{G}(\omega_n, \vec{p}), \tag{5.8}$$

where $\omega_n$ is the Matsubara frequency and defined as [227] (see also *e.g.,* Refs. [54, 225, 226])

$$\omega_n = \begin{cases} 2n\pi/\beta & \text{for bosons,} \\ (2n\pi + 1)/\beta & \text{for fermions,} \end{cases} \tag{5.9}$$

with $n = 0, \pm 1, \pm 2, \cdots$.

In our research, we will solely be using the bosonic fields for the purpose of demonstrating our computational method. However, the techniques can be adapted to fermionic Feynman diagrams. Equation (5.8) sets the replacement rules to transform Green's functions from Minkowski to Euclidean space in finite temperature:

$$\int_{-\infty}^{+\infty} \frac{\mathrm{d}^4 p}{(2\pi)^4} \to \frac{1}{\beta}\sum_{n=-\infty}^{+\infty}\int_{-\infty}^{+\infty}\frac{\mathrm{d}^3 p}{(2\pi)^3} \tag{5.10}$$

where the integral over temporal $p^0$ dimension is discretized to an infinite summation over $n$ as a result of incorporating the Matsubara frequencies and the integration over spatial dimensions $\vec{p}$ remain unchanged. Using the equation of motion, the Feynman rules for a massive (with mass $m$), scalar field propagator at finite temperature is found to be (see Ref. [226] for detailed derivation)

$$\mathcal{G}(\omega_n, \vec{p}) = \frac{1}{\omega_n^2 + |\vec{p}|^2 + m^2}, \tag{5.11}$$

which is heavily used in Sec. 5.3. With Eqs. (5.10), (5.9) and (5.11), one can construct a loop integral for any scalar Feynman loop diagram.

The Wick-rotated path integral (Euclidean path integral) enables one to calculate Feynman integrals within Euclidean spacetime with techniques and tools from standard QFT.

The new calculation difficulties lie in the shift of momentum definition from $p_M$ to $p_E$ (or the other way around in our case of the inverse Wick rotation) and the involvement of the parameters associated with temperature: $n$ and $\beta$.

In the following Sec. 5.3, one can find the manuscript of publication in *Eur. Phys. J. A* **60** (2024) 5, 107 (see also Ref. [23]).

## 5.3 Manuscript: Numerically Computing Finite Temperature Loop Integrals using pySecDec

**Abstract:** Finite-temperature quantum field theory provides the foundation for many important phenomena in the Standard Model and extensions, including phase transitions, baryogenesis, and gravitational waves. Methods are developed to enable application of pySecDec (a Python-language-based package designed for numerical calculation of dimensionally-regulated loop integrals) to numerically evaluate finite-temperature loop integrals in the imaginary time (Matsubara) formalism. These methods consist of two main elements: an inverse Wick rotation that converts a finite-temperature loop integral into a form applicable to pySecDec, and asymptotic techniques to regulate and accelerate convergence of the Matsubara frequency summations. Numerical pySecDec evaluation of finite-temperature, two-point and three-point, one-loop topologies for scalar fields is used to illustrate and validate these new methodologies. Advantages of these finite-temperature pySecDec numerical methods are illustrated by the inclusion of multiple mass and external momentum scales.

### 5.3.1 Introduction

Finite-temperature quantum field theory (see *e.g.,* Refs. [54, 210, 225, 226] for reviews) provides the foundation for many important phenomena in the Standard Model and beyond. In particular, finite temperature effects in the effective potential for studying phase transitions (see *e.g.,* Refs. [224, 228–230] for reviews, applications to the Standard Model [231,232] and extensions [233,234]) are an essential ingredient for studying baryogenesis (see *e.g.,* Refs. [224,235] for reviews) and gravitational waves (see *e.g.,* Refs. [224,230,236] for reviews).

Finite-temperature quantum field theory in the imaginary time (Matsubara) formalism amounts to a simple modification of zero-temperature propagators, replacing the temporal component of each four-momentum with a discretized Matsubara frequency [227]. The additional energy scale associated with temperature leads to greater calculational challenges in evaluating loop integrals, particularly in models with multiple mass scales. It is therefore valuable to develop new methods for evaluating finite-temperature loop integrals to enable the study of increasingly elaborate extensions of the Standard Model.

The computational program pySecDec [209,237] implements sector decomposition methods [238] to numerically calculate dimensionally-regularized integrals. pySecDec draws upon FORM [239–241], GSL [242], and the CUBA library [243,244]. It has previously been demonstrated that pySecDec can be adapted to QCD sum-rule calculations at leading- and next-to-leading order [212,213]. In this paper we develop methods to enable application of pySecDec to numerically evaluate finite-temperature loop integrals. One-loop bosonic two-point and three-point finite-temperature loop integrals (such as could emerge in scalar field theories) are used to develop and benchmark these new methodologies. As outlined below, two methodological elements are needed to apply pySecDec to finite-temperature loop integrals. The first methodological element is an inverse Wick rotation needed to convert a finite-temperature loop integral into a form applicable to pySecDec, and the second element is asymptotic techniques that accelerate or regulate the convergence of the sum over Matsubara frequencies.

In Section 5.3.2, three-point functions are first examined to establish the methodology in cases where the corresponding zero-temperature loop integral converges, but is overall complicated by the presence of multiple mass scales. Then, in Section 5.3.3, these methods are extended to the case where dimensional regularization is needed for the corresponding zero-temperature loop integral. A summary and discussion of the new pySecDec finite-temperature loop integration methodology is provided in Section 5.3.4.

### 5.3.2 The Finite-Temperature Three-Point Function

In the Matsubara formalism, the three-point vertex function for scalar fields in four spacetime dimensions at Euclidean external momenta $p_{1E} = (p^0_{1E},\, \vec{p}_1)$ and $p_{2E} = (p^0_{2E},\, \vec{p}_2)$ for propagator masses $\{m_i\}_{i=1}^3$ and finite inverse temperature $\beta = 1/T$ is given by (see *e.g.,* Ref. [226])

$$\Gamma_T\left(p_{1E}, p_{2E}\right) = \frac{1}{\beta}\sum_{n=-\infty}^{\infty}\int\frac{d^3k}{(2\pi)^3}\frac{1}{\left(\omega_n^2+|\vec{k}|^2+m_3^2\right)\left(\left(\omega_n+p_{2E}^0\right)^2+|\vec{k}+\vec{p}_2|^2+m_1^2\right)} \times\frac{1}{\left(\left(\omega_n-p_{1E}^0\right)^2+|\vec{k}-\vec{p}_1|^2+m_2^2\right)} \tag{5.12}$$

where

$$\omega_n = \frac{2n\pi}{\beta} \tag{5.13}$$

are the bosonic Matsubara frequencies (or energies) [227]. Note that $p_{1E}^0$ and $p_{2E}^0$ must also be Matsubara frequencies; the subscript "E" has been introduced for notational consistency between (5.12) and its zero-temperature limit (5.24) below. The Feynman diagram of the three-point vertex function Eq. (5.12) is shown in Fig. 5.1, where the external momenta can be interpreted as arising from either a single scalar field (*e.g.,* a $\phi^3$ interaction) or multiple fields (*e.g.,* a $\phi^4$ interaction). Defining the spatial integral

$$\mathcal{S}\left(\vec{p}_1,\vec{p}_2,\Delta_1,\Delta_2,\Delta_3\right) = \int\frac{d^3k}{(2\pi)^3}\frac{1}{\left(|\vec{k}|^2+\Delta_3\right)\left(|\vec{k}+\vec{p}_2|^2+\Delta_1\right)\left(|\vec{k}-\vec{p}_1|^2+\Delta_2\right)} \tag{5.14}$$

lets us write (5.12) as

$$\Gamma_T\left(p_{1E}, p_{2E}\right) = \frac{1}{\beta}\sum_{n=-\infty}^{\infty}\mathcal{S}\left(\vec{p}_1,\vec{p}_2,\omega_n^2+m_3^2,\left(\omega_n+p_{2E}^0\right)^2+m_1^2,\left(\omega_n-p_{1E}^0\right)^2+m_2^2\right). \tag{5.15}$$

Note that the spatial integral (5.14) converges as does the series in (5.15); thus, it is not necessary to use dimensional regularization in this (four-dimensional spacetime) case. Convergent or not, however, pySecDec can be used to efficiently numerically evaluate integrals like that of (5.14). Section 5.3.3 below presents an application for which dimensional regularization is necessary.

To apply pySecDec to the spatial integral (5.14), for an arbitrary spatial momentum $\vec{p}$,

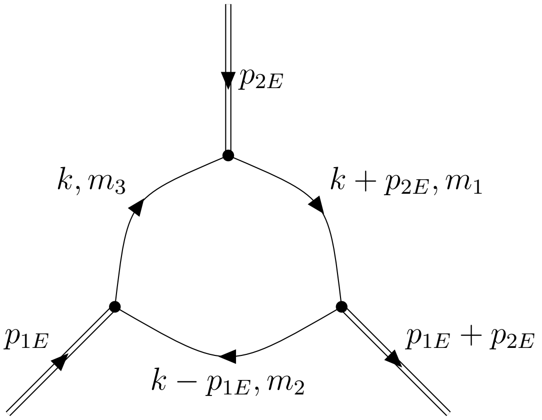

**Figure 5.1:** The 3-point function Feynman diagram where the double lines represent the total incoming momenta of the external fields within the model of interest (*e.g.,* single field for a $\phi^3$ interaction or two fields for a $\phi^4$ interaction).

we define a corresponding Minkowski $\vec{p}_M$ by

$$p^1_M = ip^1 \tag{5.16}$$

$$p^i_M = p^i \text{ for } i \neq 1. \tag{5.17}$$

The transformation (5.16)–(5.17) can be thought of as an inverse Wick rotation, but on the first spatial components rather than on the temporal components. Then, defining $\mathcal{P}$ such that

$$\mathcal{S}\left(\vec{p}_1, \vec{p}_2, \Delta_1, \Delta_2, \Delta_3\right) = \mathcal{P}\left(\vec{p}_{1M}, \vec{p}_{2M}, \Delta_1, \Delta_2, \Delta_3\right) \tag{5.18}$$

gives

$$\begin{aligned}
&\mathcal{P}\left(\vec{p}_{1M}, \vec{p}_{2M}, \Delta_1, \Delta_2, \Delta_3\right) \\
&= i \int \frac{d^3 k_M}{(2\pi)^3} \frac{1}{\left(\vec{k}_M \cdot \vec{k}_M - \Delta_3 + i0^+\right)\left((\vec{k}_M + \vec{p}_{2M}) \cdot (\vec{k}_M + \vec{p}_{2M}) - \Delta_1 + i0^+\right)} \\
&\qquad\qquad \times \frac{1}{\left((\vec{k}_M - \vec{p}_{1M}) \cdot (\vec{k}_M - \vec{p}_{1M}) - \Delta_2 + i0^+\right)}
\end{aligned} \tag{5.19}$$

where we have used (5.14) and (5.16)–(5.18). Throughout, we use the notation $\vec{u}_M \cdot \vec{v}_M$ to denote a Minkowski dot product of three-component vectors $\vec{u}_M,\ \vec{v}_M$, *e.g.*,

$$\vec{k}_M \cdot \vec{k}_M = (k_M^1)^2 - (k^2)^2 - (k^3)^2. \tag{5.20}$$

Note that the usual $i0^+$ limit within the propagators ensures that a Wick rotation of (5.19) in the first spatial components leads to (5.18), and hence Eqs. (5.16)–(5.17) constitute an inverse Wick rotation. The right-hand side of (5.19) has the form of a three-dimensional spacetime integral of a product of Minkowski-space propagators and, as such, is in a form suitable for numerical evaluation using pySecDec. Then, with

$$\Delta_1 = \omega_n^2 + m_3^2 \tag{5.21}$$

$$\Delta_2 = \left(\omega_n + p_{2E}^0\right)^2 + m_1^2 \tag{5.22}$$

$$\Delta_3 = \left(\omega_n - p_{1E}^0\right)^2 + m_2^2 \tag{5.23}$$

in (5.18)–(5.19), we can calculate $\Gamma_T(p_{1E}, p_{2E})$ using (5.15). Thus, the inverse Wick rotation as represented in Eqs. (5.16)–(5.17) and employed in (5.18)–(5.19) is the first methodological element needed to evaluate finite-temperature loop integrals with pySecDec.

The zero-temperature limit (*i.e.*, $\beta \to \infty$) of (5.12) is given by

$$\Gamma_0\left(p_{1E}, p_{2E}\right) = \int \frac{d^4 k_E}{(2\pi)^4} \frac{1}{\left(k_E^2 + m_3^2\right)\left((k_E + p_{2E})^2 + m_1^2\right)\left((k_E - p_{1E})^2 + m_2^2\right)} \tag{5.24}$$

where

$$k_E^2 = (k_E^0)^2 + |\vec{k}|^2 = (k_E^0)^2 + (k^1)^2 + (k^2)^2 + (k^3)^2 \tag{5.25}$$

with analogous expressions for $(k_E + p_{2E})^2$ and $(k_E - p_{1E})^2$. Alternatively, $\Gamma_0$ can be expressed in terms of Minkowski momenta by defining $\Lambda_0$ through

$$\Gamma_0\left(p_{1E}, p_{2E}\right) = \Lambda_0\left(p_1, p_2\right) \tag{5.26}$$

which gives

$$\Lambda_0\left(p_1, p_2\right) = i \int \frac{d^4 k}{(2\pi)^4} \frac{1}{\left(k^2 - m_3^2 + i0^+\right)\left((k+p_2)^2 - m_1^2 + i0^+\right)\left((k-p_1)^2 - m_2^2 + i0^+\right)} \tag{5.27}$$

where

$$k^0 = i k_E^0,\ p_1^0 = i p_{1E}^0,\ p_2^0 = i p_{2E}^0 \tag{5.28}$$

(note that spatial components are unaffected by such Wick rotations on temporal components) and where

$$k^2 = (k^0)^2 - |\vec{k}|^2 = (k^0)^2 - (k^1)^2 - (k^2)^2 - (k^3)^2 \tag{5.29}$$

with analogous expressions for $(k+p_2)^2$ and $(k-p_1)^2$. Equations (5.26)–(5.29) again represent an inverse Wick rotation. The right-hand side of (5.27) is in a form suitable for numerical evaluation using pySecDec because the $i0^+$ limit corresponds to standard Minkowski-space propagators.

As an aside, we note that (5.24) can be written in terms of the spatial integral (5.14) as

$$\Gamma_0\left(p_{1E}, p_{2E}\right) = \int_{-\infty}^{\infty} \frac{dk_E^0}{2\pi}\, \mathcal{S}\left(\vec{p}_1, \vec{p}_2, (k_E^0)^2 + m_3^2, (k_E^0 + p_{2E}^0)^2 + m_1^2, (k_E^0 - p_{1E}^0)^2 + m_2^2\right). \tag{5.30}$$

In (5.30), the integrand $\mathcal{S}$ can be numerically evaluated with pySecDec using (5.18)–(5.19) for $\Delta_1 = m_1^2$, $\Delta_2 = m_2^2$, and $\Delta_3 = m_3^2$ while the outside integral over $k_E^0$ can be numerically evaluated using a variety of one-dimensional techniques. Comparing $\Gamma_0$ as calculated using (5.26)–(5.27), a straightforward application of pySecDec to the entire spacetime integral, and (5.30) serves as a valuable consistency check on the inverse Wick rotation methodology (5.16)–(5.19) and the implementation of (5.14).

To identify the scaling behaviour of $\Gamma_T$ and $\Gamma_0$, we re-express both in terms of dimensionless quantities. In (5.12), we introduce a dimensionless integration variable $\vec{\kappa}$,

$$\vec{\kappa} = \frac{\beta}{2\pi}\vec{k} \implies \mathrm{d}^3\kappa = \left(\frac{\beta}{2\pi}\right)^3 \mathrm{d}^3 k. \tag{5.31}$$

Similarly, we define dimensionless variables $\ell_1$, $\vec{q}_1$, $\ell_2$, and $\vec{q}_2$,

$$\ell_i = \frac{\beta}{2\pi} p_{iE}^0, \;\; \vec{q}_i = \frac{\beta}{2\pi} \vec{p}_i \text{ for } i \in \{1, 2\}, \tag{5.32}$$

where $\ell_1$ and $\ell_2$ must be integers because $p_{1E}^0$ and $p_{2E}^0$ are Matsubara frequencies. With

$$M = \max\{m_i\}_{i=1}^3, \tag{5.33}$$

we define dimensionless mass parameters $\xi_i$,

$$\xi_i = \frac{m_i}{M}. \tag{5.34}$$

Then, we define $\tilde{\Gamma}_T$ through

$$\Gamma_T\left(p_{1E}, p_{2E}\right) = \frac{1}{M^2} \tilde{\Gamma}_T\left(\ell_1, \vec{q}_1; \ell_2, \vec{q}_2\right). \tag{5.35}$$

Substituting (5.31)–(5.34) into (5.12), we find, using (5.35),

$$\begin{aligned}
&\tilde{\Gamma}_T\left(\ell_1, \vec{q}_1; \ell_2, \vec{q}_2\right) \\
&= \frac{a^2}{2\pi} \sum_{n=-\infty}^{\infty} \int \frac{d^3\kappa}{(2\pi)^3} \frac{1}{\left(n^2 + |\vec{\kappa}\,|^2 + a^2\xi_3^2\right)\left((n+\ell_2)^2 + |\vec{\kappa} + \vec{q}_2|^2 + a^2\xi_1^2\right)} \\
&\qquad\qquad\qquad\qquad\qquad\qquad \times \frac{1}{\left((n-\ell_1)^2 + |\vec{\kappa} - \vec{q}_1|^2 + a^2\xi_2^2\right)}
\end{aligned} \tag{5.36}$$

where

$$a = \frac{\beta M}{2\pi} \tag{5.37}$$

is dimensionless. Therefore, $\tilde{\Gamma}_T$ is also dimensionless.

Next for $\Gamma_0$, in (5.24), we apply the change of variables

$$\kappa_E = \frac{k_E}{M} \implies \mathrm{d}^4\kappa_E = \frac{1}{M^4} \mathrm{d}^4 k_E \tag{5.38}$$

where $M$ is defined in (5.33). Analogous to (5.35), we define $\tilde{\Gamma}_0$ through

$$\Gamma_0\left(p_{1E}, p_{2E}\right) = \frac{1}{M^2}\tilde{\Gamma}_0\left(\ell_1, \vec{q}_1; \ell_2, \vec{q}_2\right) \tag{5.39}$$

where $\ell_i$ and $\vec{q}_i$ are defined in (5.32). Substituting (5.32), (5.34), and (5.38) into (5.24), we find, using (5.39),

$$\begin{aligned}\tilde{\Gamma}_0\left(\ell_1, \vec{q}_1; \ell_2, \vec{q}_2\right) = \int \frac{d^4\kappa_E}{(2\pi)^4} & \frac{1}{\left[\left(\kappa_E^0\right)^2 + \left|\vec{\kappa}\right|^2 + \xi_3^2\right]\left[\left(\kappa_E^0 + \frac{\ell_2}{a}\right)^2 + \left|\vec{\kappa} + \frac{\vec{q}_2}{a}\right|^2 + \xi_1^2\right]} \\ & \times \frac{1}{\left[\left(\kappa_E^0 - \frac{\ell_1}{a}\right)^2 + \left|\vec{\kappa} - \frac{\vec{q}_1}{a}\right|^2 + \xi_2^2\right]}\end{aligned} \tag{5.40}$$

which shows that $\tilde{\Gamma}_0$ is dimensionless. Strictly speaking, in (5.39)–(5.40), $\ell_1$ and $\ell_2$ need not be integers. Also note that (5.40) can be put into a Euclidean four-dimensional covariant form by associating $\ell_i/a$ and $\vec{q}_i/a$ for each $i$ with the temporal and spatial components respectively of a four-dimensional Euclidean vector.

The inverse Wick rotation methodology introduced above can be applied in a straightforward way to the rescaled integrals (5.35) and (5.36). It is also important to emphasize that pySecDec requires input of numeric values for all parameters within the loop integrals, and hence (apart from the scaling arguments), the masses $m_i$, inverse temperature $\beta$, and external momenta $p_{1E} = (p_{1E}^0, \vec{p}_1)$ and $p_{2E} = (p_{2E}^0, \vec{p}_2)$ are needed as numeric inputs to pySecDec.

In computing $\tilde{\Gamma}_T$, we generally need to truncate the series outside of $n \in \{-n_{\max}, -n_{\max}+1, \ldots, n_{\max}\}$ for some $n_{\max}$. We can, however, estimate the size of the corresponding truncation error. Suppressing function arguments, we write

$$\tilde{\Gamma}_T = \sum_{n=-\infty}^{\infty} \tilde{\Gamma}_{T,n} \tag{5.41}$$

$$= \sum_{n=-n_{\max}}^{n_{\max}} \tilde{\Gamma}_{T,n} + \sum_{n=n_{\max}+1}^{\infty} \tilde{\Gamma}_{T,n} + \sum_{n=-\infty}^{-(n_{\max}+1)} \tilde{\Gamma}_{T,n} \tag{5.42}$$

where, from (5.36) and (5.41),

$$\tilde{\Gamma}_{T,n} = \frac{a^2}{2\pi}\int \frac{d^3\kappa}{(2\pi)^3}\frac{1}{\left(n^2+|\vec{\kappa}\,|^2+a^2\xi_3^2\right)\left((n+\ell_2)^2+|\vec{\kappa}+\vec{q}_2|^2+a^2\xi_1^2\right)} \times \frac{1}{\left((n-\ell_1)^2+|\vec{\kappa}-\vec{q}_1|^2+a^2\xi_2^2\right)}. \tag{5.43}$$

If $n_{\max}$ is chosen large enough such that $|n| > n_{\max}$ implies that $|n| \gg a\xi_i$, $|n| \gg |\ell_i|$, and $|n| \gg |\vec{q}_i|$, then

$$\begin{aligned}
\tilde{\Gamma}_T &\approx \sum_{n=-n_{\max}}^{n_{\max}} \tilde{\Gamma}_{T,n} + 2\sum_{n=n_{\max}+1}^{\infty}\frac{a^2}{2\pi}\int\frac{\mathrm{d}^3\kappa}{(2\pi)^3}\frac{1}{(n^2+|\vec{\kappa}|^2)^3}\\
&= \sum_{n=-n_{\max}}^{n_{\max}} \tilde{\Gamma}_{T,n} + \frac{a^2}{32\pi^2}\sum_{n=n_{\max}+1}^{\infty}\frac{1}{n^3}\\
&= \sum_{n=-n_{\max}}^{n_{\max}} \tilde{\Gamma}_{T,n} + \frac{a^2}{32\pi^2}\left(\zeta(3)-\sum_{n=1}^{n_{\max}}\frac{1}{n^3}\right)\\
\implies \tilde{\Gamma}_T &\approx \sum_{n=-n_{\max}}^{n_{\max}} \tilde{\Gamma}_{T,n} + \frac{a^2}{32\pi^2}\,\zeta\left[3, n_{\max}+1\right]
\end{aligned} \tag{5.44}$$

where $\zeta[s,b]$ is the generalized Riemann zeta function

$$\zeta\left[s,b\right] = \sum_{k=0}^{\infty}\frac{1}{(k+b)^s}\ . \tag{5.45}$$

Accordingly, we refer to the final term on the right-hand side of (5.44) as the zeta-function correction. In general, including zeta-function corrections in calculations of $\tilde{\Gamma}_T$ allows for a significantly lower value of $n_{\max}$ to be used which speeds up computation times considerably. This is illustrated in Figure 5.2 where we plot (5.44) with and without the zeta-function correction for various values of $a$. The corrected versions converge more quickly than the uncorrected, and, hence, use of the large-$n$ asymptotic form of the finite-temperature loop integrals accelerates convergence of the Matsubara frequency summation. This asymptotic technique is the second element of our pySecDec methodology for finite-temperature loop integrals. In Section 5.3.3, asymptotic techniques are needed to regulate the Matsubara sum in addition to accelerating convergence. All calculations of $\tilde{\Gamma}_T$ in the rest of this section include the zeta-correction.

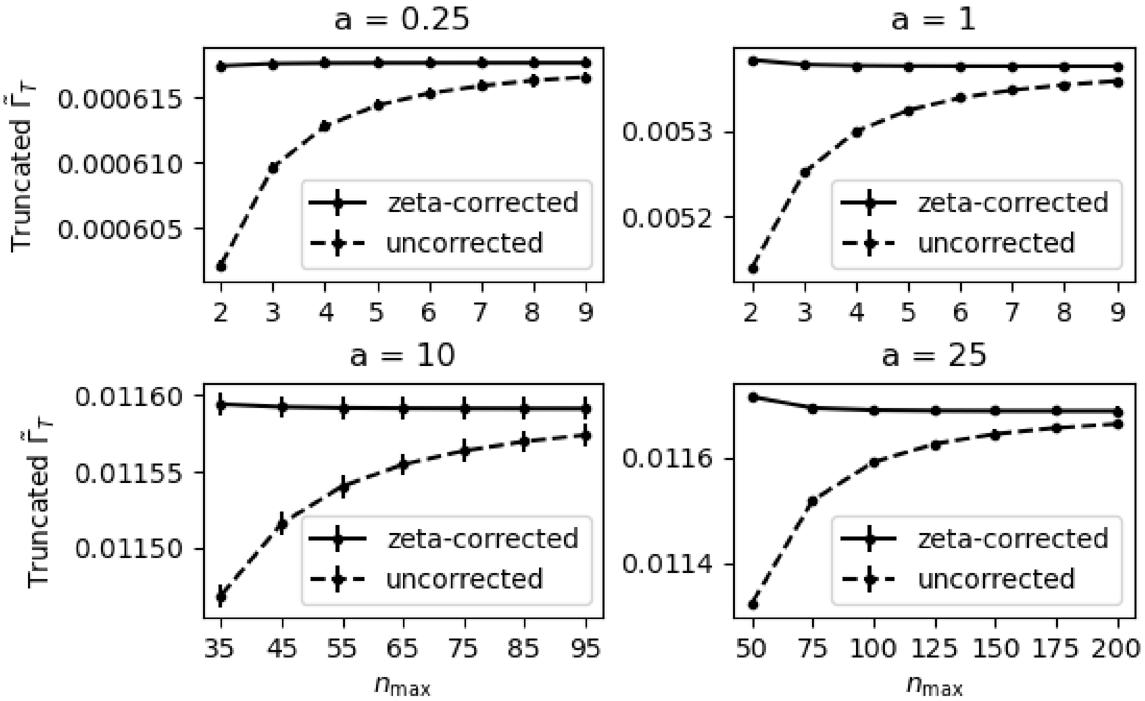

**Figure 5.2:** The right-hand side of (5.44) with and without the zeta-function correction versus $n_{\max}$ for $\ell_1 = \ell_2 = 1$, $\vec{q}_1 = \vec{q}_2 = 0$, $\xi_1 = 1$, $\xi_2 = 0.5$, and $\xi_3 = 0$ at various values of $a$.

To conclude this section, we show some plots of the dimensionless, zero-temperature vertex function $\tilde{\Gamma}_0$ (recall (5.39)–(5.40)) and the dimensionless, vertex function finite-temperature correction $\tilde{\Gamma}_T - \tilde{\Gamma}_0$ (recall (5.35)–(5.36)), both calculated using pySecDec. In Figure 5.3, we show $\tilde{\Gamma}_0$ as a function of $a$ for several values of $\ell = \ell_1 = \ell_2$. In obtaining Figure 5.3, it has been verified that the two approaches of (5.26)–(5.27) and (5.30) are identical, providing a robust self-consistency check on our methodology. In Figure 5.4, we show $\tilde{\Gamma}_T - \tilde{\Gamma}_0$ as a function of $a$ for the same values of $\ell$. In Figure 5.5, we show $\tilde{\Gamma}_0$ as a function of $q^1$ where $\vec{q}_1 = \vec{q}_2 = (q^1, 0, 0)$ for several values of $a$. In Figure 5.6, we show $\tilde{\Gamma}_T - \tilde{\Gamma}_0$ as a function of $q^1$ for the same values of $a$. In obtaining Figures 5.2–5.6 we have compared the pySecDec numerical results with an analytic calculation that is possible in the limiting case $\xi_2 = \xi_3 = 1$ and $\vec{q}_1 = \vec{q}_2 = 0$. Within the remaining $\{a, \ell_1, \ell_2\}$-parameter space, the difference between the analytic and pySecDec numerical results are smaller than the pySecDec-provided numerical errors, providing a validation of the methodology. The advantages and adaptability of our finite numerical pySecDec methodology are illustrated by the incredible diversity of physical scales (mass, temperature, momentum) encompassed by Figures 5.3–5.6.

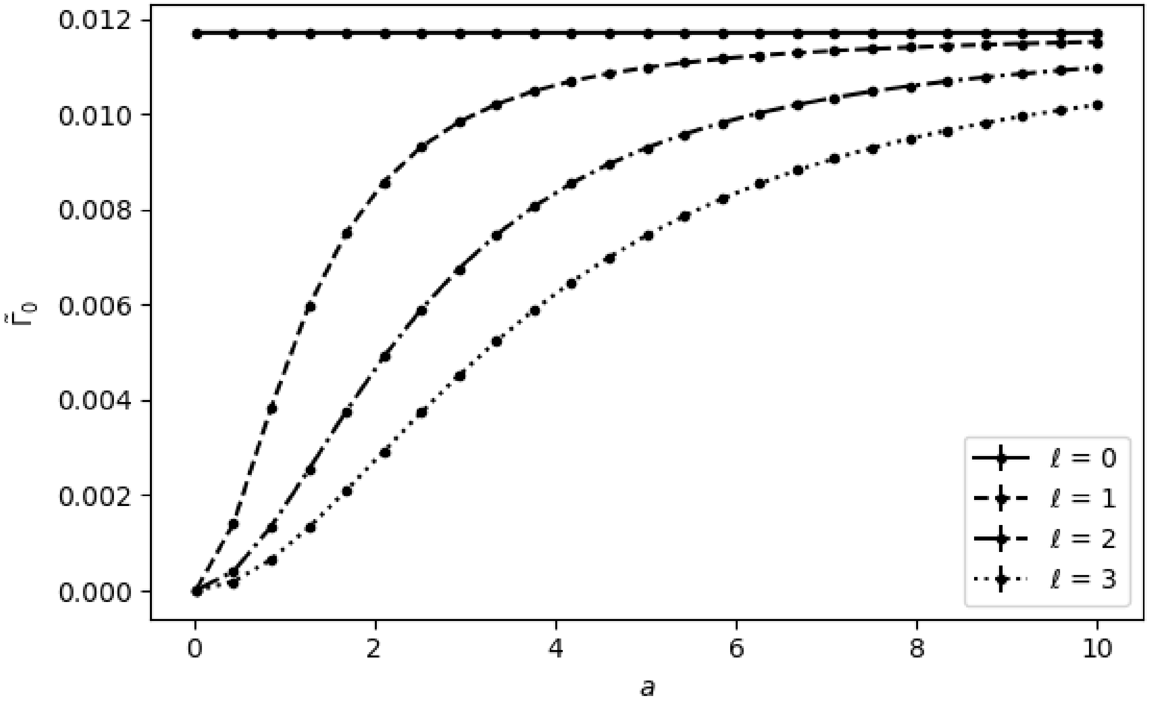

**Figure 5.3:** The dimensionless, zero-temperature vertex function $\tilde{\Gamma}_0$ versus $a$ for $\vec{q}_1 = \vec{q}_2 = 0$, $\xi_1 = 1$, $\xi_2 = 0.5$, and $\xi_3 = 0$ at various values of $\ell = \ell_1 = \ell_2$. Error bars reflecting the numerical uncertainty as determined by pySecDec are not visible.

### 5.3.3 The Finite-Temperature Two-Point Function

In this Section, we consider a case where dimensional regularization is needed within the finite-temperature loop integrals, which has implications for the Matsubara frequency summation.

Similar to the three-point function (5.12), the Matsubara formalism provides an expression for the two-point function in four spacetime dimensions with propagator masses $\{m_i\}_{i=1}^{2}$ at Euclidean external momentum $p_E = (p_E^0, \vec{p})$ (as in Section 5.3.2, the subscript "E" is used for notational consistency between (5.46) and its zero-temperature limit (5.49) below) and

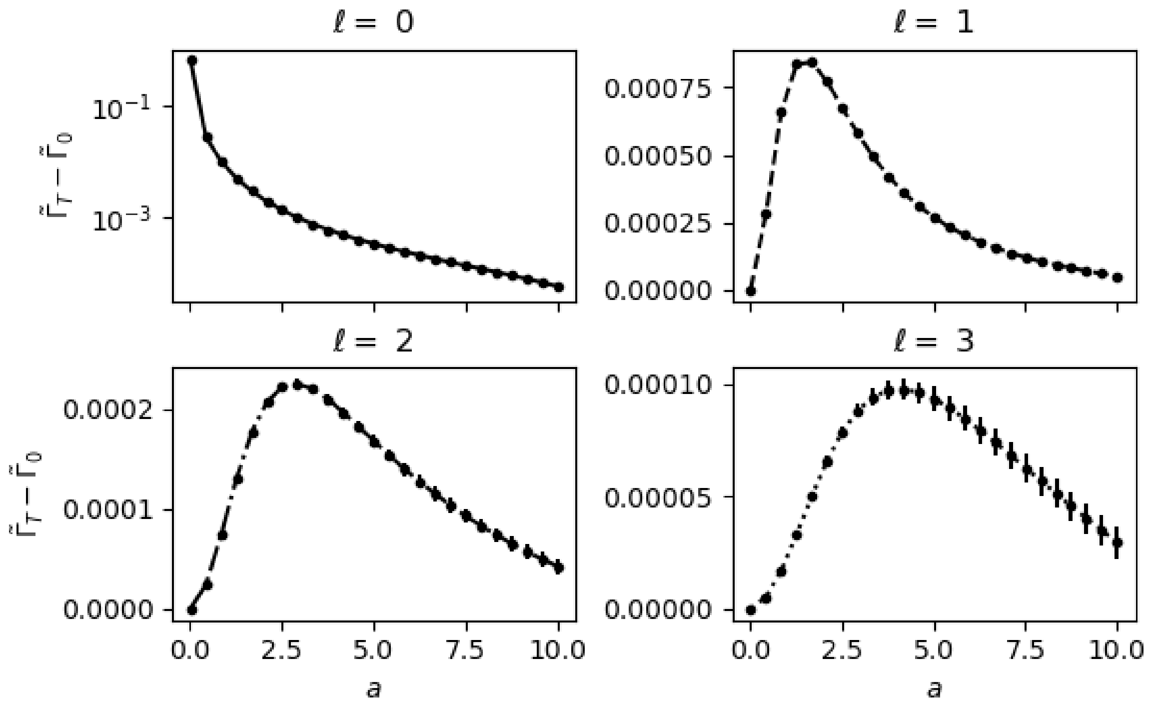

**Figure 5.4:** The dimensionless, finite-temperature vertex function correction $\tilde{\Gamma}_T - \tilde{\Gamma}_0$ versus $a$ for $\vec{q}_1 = \vec{q}_2 = 0$, $\xi_1 = 1$, $\xi_2 = 0.5$, and $\xi_3 = 0$ at various values of $\ell = \ell_1 = \ell_2$. Note that the vertical-axis scale of the $\ell = 0$ plot is logarithmic whereas the others are linear. Error bars (where visible) reflect the numerical uncertainty as determined by pySecDec.

finite inverse temperature $\beta = 1/T$ (see *e.g.,* Ref. [226]):

$$\Pi_T\left(p_E\right) = \frac{1}{2\beta} \sum_{n=-\infty}^{\infty} \int \frac{d^3k}{(2\pi)^3} \frac{1}{\left(\omega_n^2 + |\vec{k}|^2 + m_1^2\right)\left((\omega_n + p_E^0)^2 + |\vec{k} + \vec{p}|^2 + m_2^2\right)} \tag{5.46}$$

where $\omega_n$, the (bosonic) Matsubara frequencies (or energies) [227], are defined in (5.13) and where (5.46) contains a diagrammatic symmetry factor of $\frac{1}{2}$. Note that $p_E^0$ must be a Matsubara energy. The Feynman diagram corresponding to (5.46) is shown in Figure 5.7 where, again, the external momentum can be interpreted as arising from either a single scalar field (*e.g.,* a $\phi^3$ interaction) or multiple fields, *e.g.,* a $\phi^4$ interaction). In anticipation of the need to use dimensional regularization in $D = 4 - 2\epsilon$ spacetime dimensions, we define the

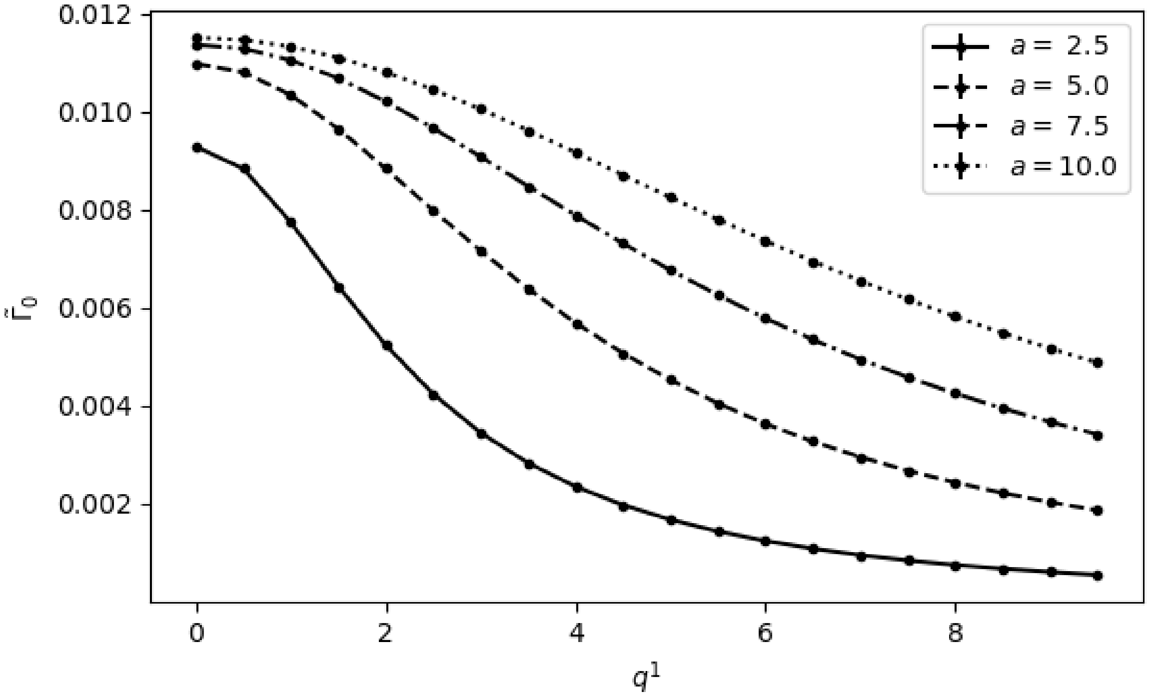

**Figure 5.5:** The dimensionless, zero-temperature vertex function $\tilde{\Gamma}_0$ versus $q^1$ for $\ell_1 = \ell_2 = 1$, $\xi_1 = 1$, $\xi_2 = 0.5$, and $\xi_3 = 0$ at various values of $a$. Error bars reflecting the numerical uncertainty as determined by pySecDec are not visible.

spatial integral

$$I\left(\vec{p}, \Delta_1, \Delta_2\right) = \frac{\nu^{2\epsilon}}{2\beta} \int \frac{d^{D-1}k}{(2\pi)^{D-1}} \frac{1}{\left(|\vec{k}|^2 + \Delta_1\right)\left(|\vec{k} + \vec{p}\,|^2 + \Delta_2\right)} \tag{5.47}$$

where $\nu$ is the renormalization scale. [Unlike in (5.14), here, we absorb a factor of $\beta^{-1}$ into the definition of the spatial integral (5.47).] Using (5.47) lets us express (5.46) as

$$\Pi_T(p_E) = \sum_{n=-\infty}^{\infty} I\left(\vec{p}, \omega_n^2 + m_1^2, (\omega_n + p_E^0)^2 + m_2^2\right). \tag{5.48}$$

Similarly, the dimensionally-regularized, zero-temperature ($\beta \to \infty$) two-point function is given by

$$\Pi_0\left(p_E\right) = \frac{\nu^{2\epsilon}}{2} \int \frac{d^D k_E}{(2\pi)^D} \frac{1}{(k_E^2 + m_1^2)\left((k_E + p_E)^2 + m_2^2\right)} \tag{5.49}$$

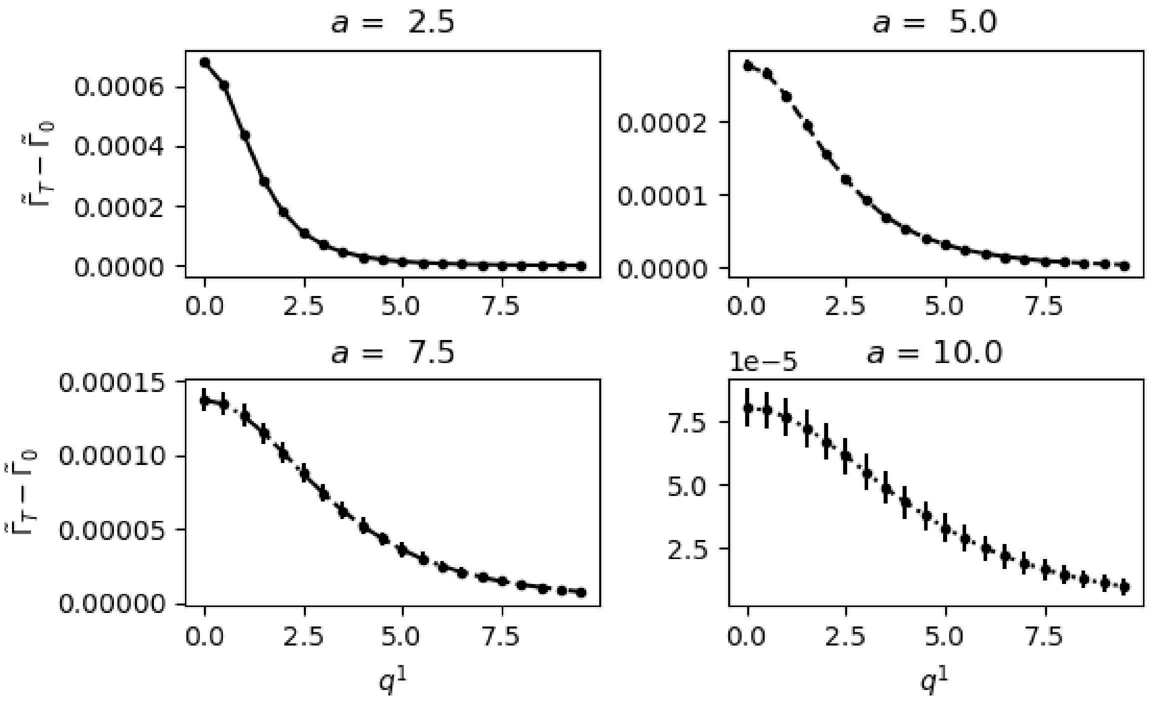

**Figure 5.6:** The dimensionless, finite-temperature vertex function correction $\tilde{\Gamma}_T - \tilde{\Gamma}_0$ versus $q^1$ for $\ell_1 = \ell_2 = 1$, $\xi_1 = 1$, $\xi_2 = 0.5$, and $\xi_3 = 0$ at various values of $a$. Error bars (where visible) reflect the numerical uncertainty as determined by pySecDec.

or, in terms of Minkowski momenta, by

$$\Pi_0(p) = -i\frac{\nu^{2\epsilon}}{2}\int \frac{d^Dk}{(2\pi)^D}\frac{1}{(k^2 - m_1^2 + i0^+)\left((k+p)^2 - m_2^2 + i0^+\right)}, \tag{5.50}$$

where $p_E^0$ and $p^0$ as well as $k_E^0$ and $k^0$ are related as in (5.28). Throughout this section, we denote the two-point, bosonic correlator as $\Pi$ regardless of the particular choice of function argument(s) such as $p_E$ in (5.49) or $p$ in (5.50).

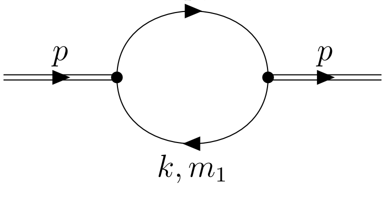

**Figure 5.7:** The 2-point function Feynman diagram where the double lines represent the total incoming momenta of the external fields within the model of interest (*e.g.,* a single field for a $\phi^3$ interaction or two fields for a $\phi^4$ interaction).

Compared to the three-point function, calculation of the two-point function is complicated by the fact that both (5.46) and (5.49) diverge in four spacetime dimensions. To see explicitly how the divergence in (5.46) arises and can be dimensionally-regulated, we consider the large-$|n|$ limit of (5.47) with $\Delta_1 = \omega_n^2 + m_1^2$ and $\Delta_2 = (\omega_n + p_E^0)^2 + m_2^2$ where $\omega_n$ is large in magnitude compared to the masses $m_1$, $m_2$ and all components of the external momentum $p_E$. Then,

$$I\left(\vec{p}, \omega_n^2 + m_1^2, (\omega_n + p_E^0)^2 + m_2^2\right) \approx \frac{\nu^{2\epsilon}}{2\beta} \int \frac{d^{D-1}k}{(2\pi)^{D-1}} \frac{1}{\left(|\vec{k}|^2 + \omega_n^2\right)^2}. \tag{5.51}$$

Using standard dimensional-regularization results (see *e.g.,* Refs. [44, 54]) we can rewrite (5.51) as

$$I\left(\vec{p}, \omega_n^2 + m_1^2, (\omega_n + p_E^0)^2 + m_2^2\right) \approx \frac{1}{32\pi^2}\left[1 + \epsilon\left(\log\left(\frac{\beta^2\nu^2}{4\pi^2}\right) - \gamma_E\right)\right] \frac{1}{(n^2)^{\frac{1}{2}+\epsilon}}. \tag{5.52}$$

Analogous to (5.41), we write

$$\Pi_T = \sum_{n=-\infty}^{\infty} \Pi_{T,n}\,, \tag{5.53}$$

$$\Pi_{T,n} = I\left(\vec{p}, \omega_n^2 + m_1^2, (\omega_n + p_E^0)^2 + m_2^2\right)\,, \tag{5.54}$$

where, from (5.48) and (5.52), we have for large $|n|$

$$\Pi_{T,n} \approx \frac{1}{32\pi^2}\left[1 + \epsilon\left(\log\left(\frac{\beta^2\nu^2}{4\pi}\right) - \gamma_E\right)\right] \frac{1}{|n|^{1+2\epsilon}}. \tag{5.55}$$

In the $\epsilon \to 0$ limit, we see from (5.53) and (5.55) that $\Pi_T$ is divergent. However, dimensional regularization does parameterize this divergence via the zeta function. As for the three-point function, this regularization is achieved by truncating the exact series (5.53) and replacing it with the large $n$ form (5.55) for $|n| > n_{\max}$

$$\begin{aligned}\Pi_T &\approx \sum_{n=-(n_{\max}-1)}^{n_{\max}-1} \Pi_{T,n} + \frac{1}{16\pi^2}\left[1+\epsilon\left(\log\left(\frac{\beta^2\nu^2}{4\pi}\right)-\gamma_E\right)\right]\sum_{n=n_{\max}}^{\infty}\frac{1}{n^{1+2\epsilon}} \\ &= \sum_{n=-(n_{\max}-1)}^{n_{\max}-1} \Pi_{T,n} + \frac{1}{16\pi^2}\left[1+\epsilon\left(\log\left(\frac{\beta^2\nu^2}{4\pi}\right)-\gamma_E\right)\right]\zeta\left[1+2\epsilon, n_{\max}\right] .\end{aligned} \tag{5.56}$$

Using the result

$$\zeta\left[1+2\epsilon, n_{\max}\right] = \frac{1}{2\epsilon} - \psi\left[n_{\max}\right] + \mathcal{O}(\epsilon)\,, \tag{5.57}$$

where $\psi(z)$ is the digamma function, leads to a dimensionally-regularized (divergent) expression for $\Pi_T$

$$\Pi_T \approx \sum_{n=-(n_{\max}-1)}^{n_{\max}-1} \Pi_{T,n} - \frac{1}{16\pi^2}\psi\left[n_{\max}\right] + \frac{1}{32\pi^2}\left[\frac{1}{\epsilon} - \gamma_E + \log\left(\frac{\beta^2\nu^2}{4\pi}\right)\right] , \tag{5.58}$$

where irrelevant terms of $\mathcal{O}(\epsilon)$ are omitted and the approximation can be improved by increasing $n_{\max}$ so that (5.52) becomes more accurate.

Although $\Pi_T$ and $\Pi_0$ separately diverge, their difference, *i.e.,* the finite-temperature correction $\Pi_s$,

$$\Pi_s = \Pi_T - \Pi_0 \tag{5.59}$$

is finite. This behaviour is expected in mass-independent regularization schemes like dimensional regularization. As shown in (5.58), the divergence in $\Pi_T$ comes from a series in $n$ whereas the divergence in $\Pi_0$ comes from an integral over $k_E$ (recall (5.49)). We can show analytically that these two divergences cancel in $\Pi_s$ defined by (5.59). Expressing (5.49) in terms of the dimensionless integration variable $\kappa_E = k_E/M$ gives

$$\Pi_0\left(p_E\right) = \left(\frac{\nu^2}{M^2}\right)^{\epsilon}\frac{1}{2}\int\frac{d^D\kappa_E}{(2\pi)^D}\frac{1}{\left(\kappa_E^2+\xi_1^2\right)\left(\left(\kappa_E+q_E\right)^2+\xi_2^2\right)}\,, \tag{5.60}$$

$$M = \max\{m_i\}_{i=1}^{2}\,,\ \xi_i = \frac{m_i}{M}\,,\ q_E = \frac{p_E}{M}\,,\ q_E^0 = \frac{\ell}{a} \tag{5.61}$$

where $a$ is defined in (5.37) and $\ell$ is the integer corresponding to the Matsubara energy $p_E^0 = 2\pi\ell/\beta$. Standard dimensional regularization methods (see *e.g.,* Ref. [44]) result in a divergence that is independent of $p_E$ and the parameters $\xi_i$

$$\Pi_0\left(p_E\right) = \frac{1}{32\pi^2}\left[\frac{1}{\epsilon} - \gamma_E + \log\left(4\pi\right) - \log\left(\frac{M^2}{\nu^2}\right)\right] + f_0^{\text{finite}}\left(q_E, \xi_i\right) \tag{5.62}$$

where $f_0^{\text{finite}}$ contains the remaining finite parts of $\Pi_0$. Having analytically extracted the divergences from both $\Pi_T$ and $\Pi_0$, we have shown explicitly that they are equal and, as expected, temperature-independent. Thus the divergences cancel from the finite-temperature correction (5.59) leading to the the result

$$\Pi_s = \sum_{n=-(n_{\max}-1)}^{n_{\max}-1} \Pi_{T,n} - \frac{1}{16\pi^2}\psi\left[n_{\max}\right] + \frac{1}{16\pi^2}\log\left(\frac{a}{2}\right) - f_0^{\text{finite}}\left(q_E, \xi_i\right) \; . \tag{5.63}$$

Because the divergent parts cancel in $\Pi_s$, the renormalization scale also cancels in (5.63) along with the usual dimensional-regularization terms $\gamma_E$ and $\log\left(4\pi\right)$. Thus, to apply pySecDec to (5.63), we use $\Pi_{T,n}$ as calculated in pySecDec, and extract only the finite part of $\Pi_0$ from the pySecDec calculation to give a slightly modified version of (5.63) suited to pySecDec,

$$\Pi_s = \sum_{n=-(n_{\max}-1)}^{n_{\max}-1} \Pi_{T,n} - \frac{1}{16\pi^2}\psi\left[n_{\max}\right] + \frac{1}{16\pi^2}\log\left(\frac{a}{2}\right) + \frac{1}{32\pi^2}\left[-\gamma_E + \log\left(4\pi\right)\right] - \tilde{\Pi}_0^{\text{finite}}\left(q_E, \xi_i\right) \; , \tag{5.64}$$

where $\tilde{\Pi}_0^{\text{finite}}$ is the finite part of the dimensionless integral (5.61) omitting the $\nu^2/M^2$ renormalization-scale pre-factor

$$\tilde{\Pi}_0\left(q_E, \xi_i\right) = \frac{1}{2}\int \frac{d^D\kappa_E}{(2\pi)^D}\frac{1}{\left(\kappa_E^2 + \xi_1^2\right)\left((k_E + q_E)^2 + \xi_2^2\right)} \; . \tag{5.65}$$

Note that the $\gamma_E$ and $\log\left(4\pi\right)$ terms have been restored in (5.64) because they cannot easily be separated out from the pySecDec finite part. As an important numerical benchmark, the divergent part of $\Pi_0$ should be calculated in pySecDec to verify the $1/(32\pi^2\epsilon)$-dependence in (5.62). The only remaining task is to develop a version of $\Pi_{T,n}$ suited to pySecDec.

As for the three-point function, we switch to dimensionless parameters. Based on our analytic result, we can anticipate the finiteness of (5.47) within dimensional regularization in $D = 4 - 2\epsilon$ spacetime dimensions. Also, in $\Pi_{T,n}$, we can set $\epsilon = 0$, introduce dimensionless $\vec{\kappa}$ as in (5.31), and define dimensionless quantities $\ell$, $\vec{q}$, and $a$ as follows:

$$\ell = \frac{\beta}{2\pi} p_E^0, \; \vec{q} = \frac{\beta}{2\pi} \vec{p}, \tag{5.66}$$

where $a$ is defined in (5.37) and $\ell$ is an integer because $p_E^0$ is a Matsubara energy. Then,

$$\Pi_{T,n}\left(\{l, \vec{q}\}\right) = \frac{1}{4\pi} \int \frac{d^3\kappa}{(2\pi)^3} \frac{1}{\left(n^2 + |\vec{\kappa}|^2 + \xi_1 a^2\right)\left((n+\ell)^2 + |\vec{\kappa} + \vec{q}|^2 + \xi_2 a^2\right)}. \tag{5.67}$$

For $\Pi_{T,n}$, we implement an inverse Wick rotation much as we did when calculating the finite-temperature three-point function. Following (5.16), we define $\kappa_M^1$ and $q_M^1$ as

$$\kappa^1 = -i\kappa_M^1, \; q^1 = -iq_M^1. \tag{5.68}$$

Then,

$$\begin{aligned} &\Pi_{T,n}\left(\{l, \vec{q}_M\}\right) \\ &\quad = \frac{-i}{4\pi} \int \frac{d^3\kappa_M}{(2\pi)^3} \frac{1}{\left(\vec{\kappa}_M \cdot \vec{\kappa}_M - \Delta_1 + i0^+\right)\left((\vec{q}_M + \vec{\kappa}_M) \cdot (\vec{q}_M + \vec{\kappa}_M) - \Delta_2 + i0^+\right)} \end{aligned} \tag{5.69}$$

where

$$\Delta_1 = n^2 + \xi_1 a^2 \tag{5.70}$$

$$\Delta_2 = (n+\ell)^2 + \xi_2 a^2 \tag{5.71}$$

and, as in (5.19), dot products in (5.69) are Minkowski [see Eq. (5.20)]. As discussed in Section 5.3.2, the right-hand side of (5.69) is in a form suitable for numerical evaluation with pySecDec. As for $\tilde{\Pi}_0$ in (5.65), its equivalent integral in terms of Minkowski-space propagators (in $D = 4 - 2\epsilon$ dimensions) is

$$\tilde{\Pi}_0\left(q,\xi_i\right) = \frac{1}{2}\int \frac{d^D\kappa}{(2\pi)^D}\frac{1}{\left(\kappa^2 - \xi_1 a^2 + i0^+\right)\left((\kappa+q)^2 - \xi_2 a^2 + i0^+\right)} \tag{5.72}$$

where

$$\kappa^0 = i\kappa_E^0 \text{ and } q^0 = i\ell. \tag{5.73}$$

The right-hand side of (5.72) is also in a form suitable for numerical calculation using pySecDec.

Before proceeding with some numerical results for the finite-temperature correction two-point function $\Pi_s$, we summarize some key aspects associated with the pySecDec evaluation of (5.64). First, analytic methods have been used to regulate the divergences in the finite-temperature Matsubara sum (5.53), and it has been demonstrated that these divergences cancel against the divergent zero-temperature result. As for the three-point function, these analytic methods also improve the numerical convergence of the Matsubara sum. Second, it should be verified that the pySecDec-computed values of (5.69) appearing in the sum are finite, and that the divergent part of (5.72) as computed with pySecDec is $1/(32\pi^2\epsilon)$ as needed to cancel the divergences. Finally, we also note that in (5.64), there is a natural cancellation of the $\gamma_E$ and $\log(4\pi)$ as shown analytically in (5.63).

As an example of results obtained from the procedure described above for numerically calculating $\Pi_s$, we plot $\Pi_s$ as a function of $a$ at $\vec{q} = 0$ for several values of $\ell$ in Figure 5.8. Also, in Figure 5.9, we plot $\Pi_s$ as a function of $q^1$ where $\vec{q} = (q^1, 0, 0)$ at $\ell = 1$ for several values of $a$. In obtaining these plots, it has been verified that the case where $\ell = 0$ and $\vec{q} = 0$ agrees with the results of Ref. [226] given in a considerably different form and approach, providing a robust validation of the regularization method used for the Matsubara sum. In obtaining Figure 5.8 we have also compared the pySecDec numerical results with an analytic version of our calculation that is possible in the limiting case $\xi_1 = \xi_2 = 1$ and $\vec{q} = 0$. Within the remaining $\{a, \ell\}$ parameter space, the difference between the analytic and pySecDec numerical results are smaller than the pySecDec-provided numerical errors, providing a validation of the methodology. As for the three-point function, the advantages and adaptability of our finite temperature numerical pySecDec methodology are illustrated by the incredible diversity of physical scales (mass, temperature, momentum) encompassed by Figures 5.8–5.9.

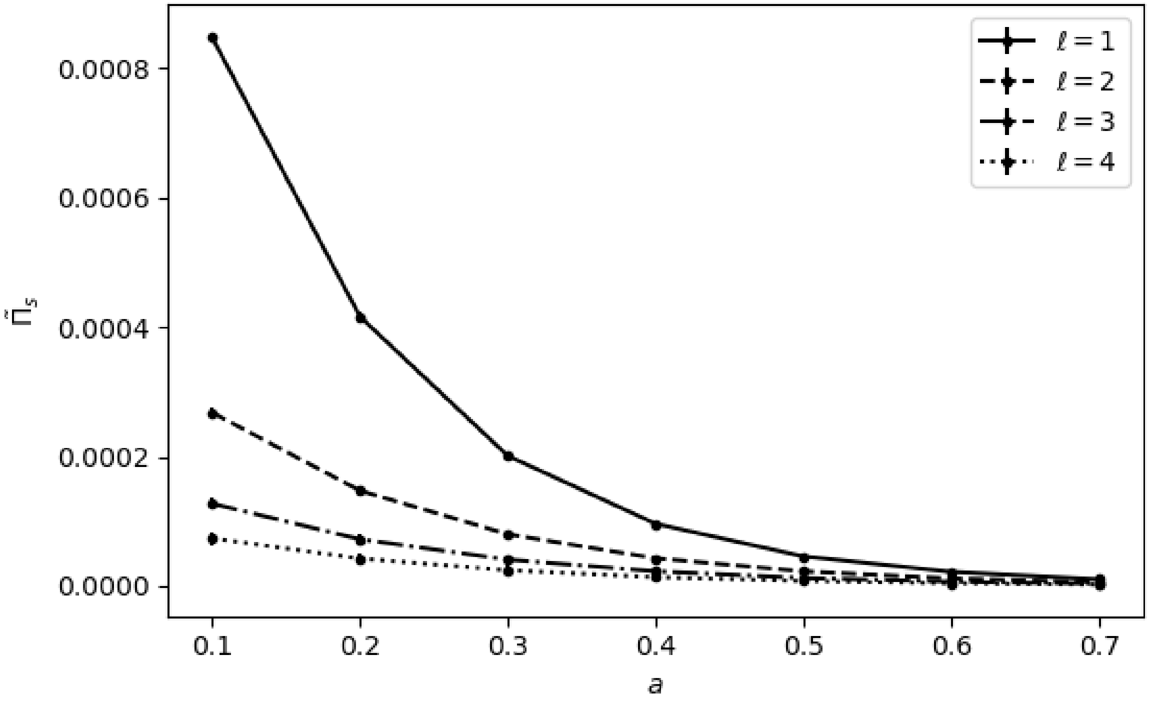

**Figure 5.8:** The dimensionless, finite-temperature 2-point function correction $\Pi_s$ versus $a$ for $\xi_1 = \xi_2 = 1$ and $\vec{q} = 0$ at various values of $\ell$. Error bars (where visible) reflect the numerical uncertainty as determined by pySecDec.

### 5.3.4 Discussion

In this paper we have developed methods to enable application of pySecDec [209, 237] to numerically evaluate dimensionally-regulated, finite-temperature bosonic loop integrals in the imaginary time (Matsubara) formalism. The methods are developed at one-loop order in four spacetime dimensions and consist of two main elements. The first element is an inverse Wick rotation of a spatial component that maps a finite-temperature spatial integral into a form that enables the use of pySecDec. This inverse Wick rotation is a generic methodology that can easily be extended to higher-loop integrals, various loop topologies, and to different choices of spacetime dimension. The second methodological element develops asymptotic forms that can be used to regulate and accelerate convergence of the Matsubara sum. In

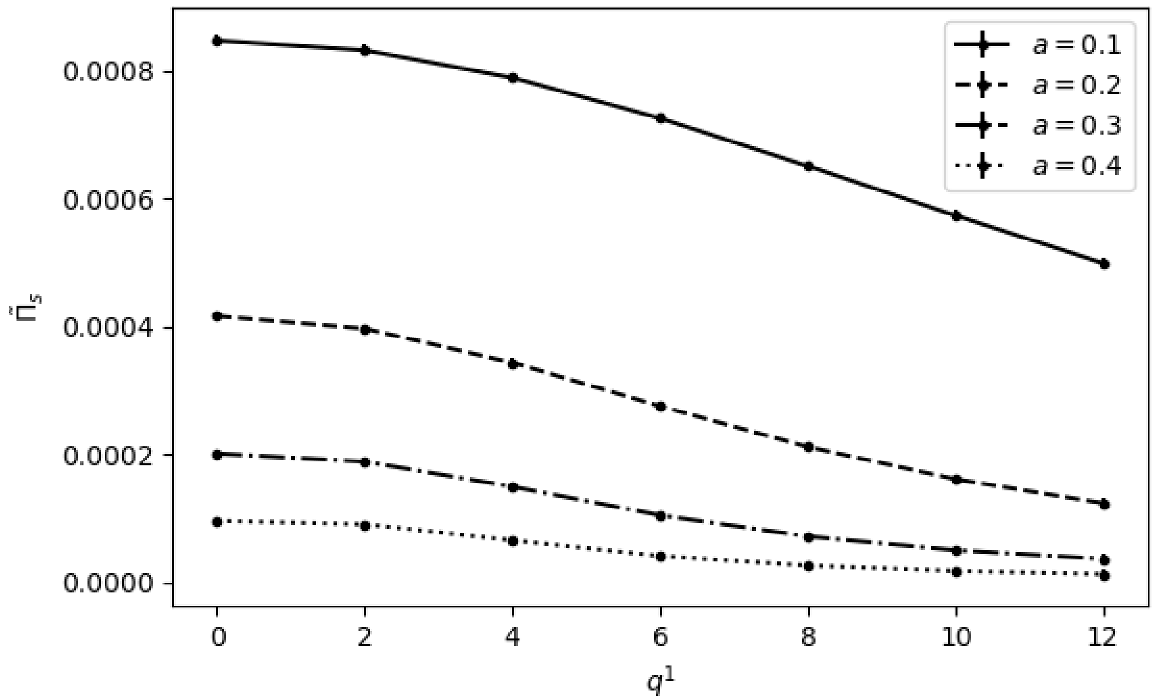

**Figure 5.9:** The dimensionless, finite-temperature 2-point function correction $\Pi_s$ versus $q^1$ where $\vec{q} = (q^1, 0, 0)$ for $\xi_1 = \xi_2 = 1$ and $\ell = 1$ at various values of $a$. Error bars (where visible) reflect the numerical uncertainty as determined by pySecDec.

principle, this asymptotic methodology could be extended to higher-loop calculations, but, of course, the analysis would become increasingly complicated with multiple Matsubara sums. Both of the methodological elements are easily adaptable to fermionic finite-temperature loop integrals.

Two examples were used to develop and illustrate our finite-temperature pySecDec methodology. The finite-temperature bosonic three-point function was first considered because in four spacetime dimensions, the loop integrals and Matsubara sum converge. However, although dimensional regularization is not strictly needed, we find that pySecDec still provides demonstrable advantages in computational efficiency compared with direct numerical integration using standard Python functions such as `tplquad` from `scipy.integrate` or Mathematica's `NIntegrate`. We thus conclude that pySecDec is particularly well optimized to loop integrals, and is capable of handling the full diversity of scales that could occur in a finite-temperature system. Despite this numerical efficiency, we also demonstrated that convergence of the Matsubara sum can be accelerated by using analytic methods for the asymptotic form of the finite-temperature series.

The second example of the finite-temperature bosonic two-point function in four spacetime dimensions has an additional complication of divergences in the Matsubara sum that we regulate using dimensional regularization combined with the asymptotic form of the finite-temperature series. We demonstrate that this divergence is identical to that of the zero-temperature two-point function, and hence the finite-temperature correction (5.59) is finite as expected. An algorithm was presented for applying pySecDec to the two-point finite-temperature correction by combining analytic methods and extracting specific portions of the zero-temperature loop integral in pySecDec. In the analysis of the two-point function, the numerical pySecDec results for the finite-temperature correction were compared against known results [226] in specific limiting cases.

In the various figures (see Figures 5.2–5.6 and Figures 5.8–5.9) used to demonstrate our pySecDec finite-temperature loop-integral methodology, we have shown the numerical uncertainties reported by pySecDec. In obtaining these figures, we have tested the pySecDec results against limiting cases where we can perform analytic calculations, and find the difference between the analytic and pySecDec numerical results are smaller than the pySecDec-provided numerical errors, and see no evidence of numerical noise in the data generated by pySecDec.

## Acknowledgments

TGS and DH are grateful for research funding from the Natural Sciences & Engineering Research Council of Canada (NSERC).

# 6 The End of the Beginning

In the Standard Model (SM), matter is composed of small constituents of fundamental particles whose interactions and combinations form the world we know of today (see *e.g.,* Ref. [6]). This thesis focuses on advancing theoretical particle physics predictions by improving precision in calculations and addressing open questions in QCD and physics beyond the SM (BSM). The research presented spans a broad spectrum, from exotic hadrons such as gluonia [14], experimental anomalies including muon $g-2$ [21], and advanced computational methodology development [23]. All of which aim at contributing to a deeper understanding of fundamental interactions.

In Chapter 3, we present a notable next-to-leading order (NLO) refinement to the QCD sum rules (QCDSR) theoretical predictions for $J^{PC} = 2^{++}$ tensor di-gluonium [14]. With both higher-energy perturbative and lower-energy non-perturbative contributions systematically evaluated, our results provide insights into the properties of $2^{++}$ tensor di-gluonium and support for future experimental and theoretical searches for gluonia. This research also lays the foundation for further collaborations on the theoretical predictions for the $J^{PC} = 2^{-+}$ tensor di-gluonium and $J^{PC} = 0^{++}$ scalar tri-gluonium. We aim to improve the theoretical precision of those exotic hadron properties and provide a more comprehensive understanding of the SM landscape.

In Chapter 4, we address the tension surrounding the leading order (LO) hadronic vacuum polarization (HVP) contributions to muon $g-2$ anomaly ($a_\mu^{\text{HVP,LO}}$) [21] (see also Ref. [22]). Using higher-order corrections to finite-energy QCD sum rules (FESR) and Hölder inequalities, we derive complementary and fundamental QCDSR bounds on hadronic contributions to $a_\mu^{\text{HVP,LO}}$ by incorporating light-quark contributions up to five-loop perturbative corrections within the chiral limit, LO light quark mass corrections, NLO dimension-four QCD condensates, and LO dimension-six QCD condensates. We also include the effect of flavour transitions as we move from higher to lower energy ranges, as well as the renormalization group effect on the condensate contributions. Our result offers a possible path to resolve the current tension in $a_\mu^{\text{HVP,LO}}$ theoretical predictions within and among data-driven [17, 18] and lattice QCD [19, 20] approaches to the experimental measurement [15], and potentially points towards new physics phenomena. Our novel methodology which combines FESR with the family of Hölder inequalities, can also improve predictions for other anomalous magnetic moments, such as those of the $\tau$ leptons, which motivates our ongoing research looking for the hadronic contribution to $a_\tau^{\text{HVP,LO}}$.

In Chapter 5, we develop computational methodologies to evaluate loop integrals in finite-temperature field theory via the pySecDec package. By expanding the functionality of pySecDec with an inverse Wick rotation method and dimensional regularization method for the thermal summation, we extend pySecDec's applicability to a wide range of Feynman diagram topologies in finite-temperature environments. Our methods offer the option of numerically calculating finite-temperature loop integrals, especially when the problem exceeds the capabilities of analytic approaches. These numerical computation techniques enable precise analyses of particle interactions in thermal environment and can be potentially applied to studies such as on quark-gluon plasma (see *e.g.,* Refs. [214–216]), baryongenesis [220, 221] and gravitational waves [222–224] etc.

Through theoretical innovations and computational advancements, this thesis addresses some of the key challenges in QCD and BSM physics, including theoretical studies of gluonia, muon $g-2$ anomaly and thermal loop integral calculation. By improving precision of theoretical predictions through means such as obtaining QCDSR higher-loop corrections and developing numerical computation methods, we extend our knowledge and insight on QCD and SM in general, making future searches and comparisons to experimental measurement more significant and paving the way for uncovering new physics beyond the known.

# References

[1] J. J. Thomson, Phil. Mag. Ser. 6 **7**, 237 (1904).

[2] I. Falconer, *Corpuscles to Electrons* (MIT Press, 2002), pp. 77–100.

[3] E. Rutherford, Phil. Mag. Ser. 6 **21**, 669 (1911).

[4] R. P. Feynman, Conf. Proc. C **690905**, 237 (1969).

[5] J. D. Bjorken and E. A. Paschos, Phys. Rev. **185**, 1975 (1969).

[6] D. Griffiths, *Introduction to elementary particles* (Wiley, 2008).

[7] Particle Data Group, S. Navas *et al.*, Phys. Rev. D **110**, 030001 (2024).

[8] F. Chadha-Day, J. Ellis, and D. J. E. Marsh, Sci. Adv. **8**, abj3618 (2022).

[9] M. Gell-Mann, Phys. Lett. **8**, 214 (1964).

[10] G. Zweig, *An SU(3) model for strong interaction symmetry and its breaking*, 2 ed. (Hadronic Press, 1964), pp. 22–101.

[11] V. Crede and C. A. Meyer, Prog. Part. Nucl. Phys. **63**, 74 (2009).

[12] V. Mathieu, N. Kochelev, and V. Vento, Int. J. Mod. Phys. E **18**, 1 (2009).

[13] W. Ochs, J. Phys. G **40**, 043001 (2013).

[14] S. Li, S. Narison, T. Steele, and D. Rabetiarivony, Phys. Lett. B **849**, 138454 (2024).

[15] Muon g-2, D. P. Aguillard *et al.*, Phys. Rev. Lett. **131**, 161802 (2023).

[16] Muon g-2, D. P. Aguillard *et al.*, Phys. Rev. D **110**, 032009 (2024).

[17] T. Aoyama *et al.*, Phys. Rept. **887**, 1 (2020).

[18] CMD-3, F. V. Ignatov *et al.*, Phys. Rev. Lett. **132**, 231903 (2024).

[19] S. Borsanyi *et al.*, Nature **593**, 51 (2021).

[20] S. Kuberski, PoS **LATTICE2023**, 125 (2024).

[21] S. Li *et al.*, Phys. Rev. D **110**, 014046 (2024).

[22] S. Li *et al.*, Nucl. Part. Phys. Proc. **347**, 6 (2024).

[23] D. Harnett, S. Li, and T. G. Steele, Eur. Phys. J. A **60**, 107 (2024).

[24] A. Einstein, Annalen Phys. **322**, 891 (1905).

[25] G. Aad, T. Abajyan, B. Abbott, J. Abdallah, and Others, Phys. Lett. B **716**, 1 (2012).

[26] S. Chatrchyan, V. Khachatryan, A. Sirunyan, and Others, Phys. Lett. B **716**, 30 (2012).

[27] E. Fermi, Rend. Lincei **3**, 145 (1926), [English Translation: arXiv:cond-mat/9912229].

[28] D. J. Griffiths and D. F. Schroeter, *Introduction to Quantum Mechanics*, 3 ed. (Cambridge University Press, 2018).

[29] P. W. Higgs, Phys. Lett. **12**, 132 (1964).

[30] L. H. Ryder, *Quantum Field Theory* (Cambridge University Press, 1996).

[31] M. E. Peskin and D. V. Schroeder, *An Introduction to quantum field theory* (Addison-Wesley, Reading, USA, 1995).

[32] S. Weinberg, Phys. Rev. Lett. **19**, 1264 (1967).

[33] A. Salam and J. Ward, Phys. Lett. **13**, 168 (1964).

[34] M. Gell-Mann, Phys. Rev. **125**, 1067 (1962).

[35] Y. Ne'eman, Nucl. Phys. **26**, 222 (1961).

[36] T. Nakano and K. Nishijima, Prog. Theor. Phys. **10**, 581 (1953).

[37] M. Gell-Mann, Nuovo Cim. **4**, 848 (1956).

[38] O. W. Greenberg, *Color Charge Degree of Freedom in Particle Physics* (Springer Berlin Heidelberg, 2009), pp. 109–111.

[39] M. Y. Han and Y. Nambu, Phys. Rev. **139**, B1006 (1965).

[40] M. Gell-Mann, Acta Phys. Austriaca Suppl. **9**, 733 (1972).

[41] H. Fritzsch and M. Gell-Mann, Current algebra: Quarks and what else? Vol. C720906V2, pp. 135–165, 1972.

[42] N. Brambilla *et al.*, Phys. Rept. **873**, 1 (2020).

[43] L. Faddeev and V. Popov, Phys. Lett. B **25**, 29 (1967).

[44] P. Pascual and R. Tarrach, *QCD: Renormalization for the Practitioner*, Lect. Notes Phys. Vol. 194 (Springer-Verlag, Berlin, Heidelberg, 1984).

[45] D. J. Gross and F. Wilczek, Phys. Rev. Lett. **30**, 1343 (1973).

[46] H. D. Politzer, Phys. Rev. Lett. **30**, 1346 (1973).

[47] S. Bethke, Prog. Part. Nucl. Phys. **58**, 351 (2007).

[48] S. Narison, *QCD as a Theory of Hadrons: From Partons to Confinement* (Oxford University Press, 2005).

[49] N. Isgur and J. E. Paton, Phys. Lett. B **124**, 247 (1983).

[50] T. Barnes, F. E. Close, and E. S. Swanson, Phys. Rev. D **52**, 5242 (1995).

[51] D. Harnett, R. T. Kleiv, T. G. Steele, and H.-Y. Jin, J. Phys. G **39**, 125003 (2012).

[52] M. Gell-Mann and F. Low, Phys. Rev. **84**, 350 (1951).

[53] G. 't Hooft and M. Veltman, Nucl. Phys. B **44**, 189 (1972).

[54] M. Laine and A. Vuorinen, *Basics of Thermal Field Theory*, Lect. Notes Phys. Vol. 925 (Springer, 2016).

[55] G. 't Hooft and M. J. G. Veltman, Nucl. Phys. B **153**, 365 (1979).

[56] G. Passarino and M. J. G. Veltman, Nucl. Phys. B **160**, 151 (1979).

[57] G. J. van Oldenborgh and J. A. M. Vermaseren, Z. Phys. C **46**, 425 (1990).

[58] R. Mertig and R. Scharf, Comput. Phys. Commun. **111**, 265 (1998).

[59] O. V. Tarasov, Phys. Rev. D **54**, 6479 (1996).

[60] O. Tarasov, Nucl. Phys. B **502**, 455 (1997).

[61] A. I. Davydychev, J. Math. Phys. **33**, 358 (1992).

[62] E. E. Boos and A. I. Davydychev, Theor. Math. Phys. **89**, 1052 (1991).

[63] G. 't Hooft and M. Veltman, Nucl. Phys. B **50**, 318 (1972).

[64] C. Becchi, A. Rouet, and R. Stora, Annals Phys. **98**, 287 (1976).

[65] G. 't Hooft, Nucl. Phys. B **61**, 455 (1973).

[66] S. Weinberg, Phys. Rev. D **8**, 3497 (1973).

[67] W. A. Bardeen, A. J. Buras, D. W. Duke, and T. Muta, Phys. Rev. D **18**, 3998 (1978).

[68] J. C. Collins, *Renormalization: An Introduction to Renormalization, the Renormalization Group and the Operator-Product Expansion,* Cambridge Monographs on Mathematical Physics (Cambridge University Press, 1984).

[69] J. A. Dixon and J. C. Taylor, Nucl. Phys. B **78**, 552 (1974).

[70] H. Kluberg-Stern and J. B. Zuber, Phys. Rev. D **12**, 467 (1975).

[71] S. D. Joglekar and B. W. Lee, Annals Phys. **97**, 160 (1976).

[72] T. de Oliveira, D. Harnett, A. Palameta, and T. G. Steele, Phys. Rev. D **106**, 114023 (2022).

[73] S. Narison, Phys. Rept. **84**, 263 (1982).

[74] J. Ho, D. Harnett, and T. G. Steele, JHEP **2017** (2017).

[75] K. G. Wilson, Phys. Rev. D **10**, 2445 (1974).

[76] HPQCD, UKQCD, MILC, Fermilab Lattice, C. T. H. Davies *et al.*, Phys. Rev. Lett. **92**, 022001 (2004).

[77] H. Leutwyler, Annals Phys. **235**, 165 (1994).

[78] H. Georgi, Phys. Lett. B **240**, 447 (1990).

[79] E. Eichten and B. R. Hill, Phys. Lett. B **234**, 511 (1990).

[80] T. Schäfer and E. V. Shuryak, Rev. Mod. Phys. **70**, 323 (1998).

[81] B. Zwiebach, *A first course in string theory* (Cambridge University Press, 2006).

[82] M. Shifman, A. Vainshtein, and V. Zakharov, Nucl. Phys. B **147**, 385 (1979).

[83] M. Shifman, A. Vainshtein, and V. Zakharov, Nucl. Phys. B **147**, 448 (1979).

[84] V. de Alfaro, S. Fubini, G. Furlan, and C. Rossetti, *Currents in Hadron Physics* (North-Holland, Amsterdam, 1973).

[85] S. Weinberg, Phys. Rev. Lett. **18**, 188 (1967).

[86] T. Das, V. S. Mathur, and S. Okubo, Phys. Rev. Lett. **19**, 1067 (1967).

[87] L. Reinders, H. Rubinstein, and S. Yazaki, Phys. Rept. **127**, 1 (1985).

[88] P. Colangelo and A. Khodjamirian, *QCD sum rules, a modern perspective* (World Scientific, 2000), pp. 1495–1576.

[89] S. Narison, (2023), [arXiv:2309.00258 [hep-ph]].

[90] K. G. Wilson, Phys. Rev. **179**, 1499 (1969).

[91] V. A. Novikov, M. A. Shifman, A. I. Vainshtein, and V. I. Zakharov, Fortsch. Phys. **32**, 585 (1984).

[92] C. Cronström, Phys. Lett. B **90**, 267 (1980).

[93] V. Elias, T. G. Steele, and M. D. Scadron, Phys. Rev. D **38**, 1584 (1988).

[94] E. Bagan, M. R. Ahmady, V. Elias, and T. G. Steele, Z. Phys. C **61**, 157 (1994).

[95] M. Neubert, Phys. Rept. **245**, 259–395 (1994).

[96] A. G. Grozin, Springer Tracts Mod. Phys. **201**, 1 (2004).

[97] R. Berg, D. Harnett, R. T. Kleiv, and T. G. Steele, Phys. Rev. D **86** (2012).

[98] M. Gell-Mann, R. J. Oakes, and B. Renner, Phys. Rev. **175**, 2195 (1968).

[99] M. A. Shifman, Nucl. Phys. B **173**, 13 (1980).

[100] R. Berg, *QCD Correlation Functions of Light Quarkonium and Strangeonium Hybrids*, Master's thesis, Saskatchewan U., 2015.

[101] J. N. E. Ho, *Beyond the Conventional Quark Model: Using QCD Sum Rules to Explore the Spectrum of Exotic Hadrons*, PhD thesis, Saskatchewan U., 2020.

[102] G. Kallen, Helv. Phys. Acta **25**, 417 (1952).

[103] H. Lehmann, Nuovo Cim. **11**, 342 (1954).

[104] R. Zwicky, A brief Introduction to Dispersion Relations and Analyticity, in *Quantum Field Theory at the Limits: from Strong Fields to Heavy Quarks*, pp. 93–120, 2017.

[105] G. Pólya and G. Latta, *Complex Variables* (Wiley, 1974).

[106] I. Caprini, J. Cole, and C. Verzegnassi, Nuovo Cim. A **83**, 121 (1984).

[107] T. G. Steele, N. C. A. Hill, V. Elias, and R. B. Mann, Phys. Rev. D **44**, 3610 (1991).

[108] Particle Data Group, R. L. Workman *et al.*, PTEP **2022**, 083C01 (2022).

[109] M. Lerch, Acta Mathematica **27**, 339 (1903).

[110] A. M. Cohen, *Inversion Formulae and Practical Results* (Springer US, Boston, MA, 2007), pp. 23–44.

[111] G. Breit and E. Wigner, Phys. Rev. **49**, 519 (1936).

[112] D. Harnett and T. G. Steele, Nucl. Phys. A **695**, 205 (2001), hep-ph/0011044.

[113] R. T. Kleiv, T. G. Steele, A. Zhang, and I. Blokland, Phys. Rev. D **87**, 125018 (2013), 1304.7816.

[114] M. Benmerrouche, G. Orlandini, and T. Steele, Phys. Lett. B **356**, 573–579 (1995).

[115] S. Narison, *QCD Spectral Sum Rules*, World Sci. Lect. Notes Phys. Vol. 26 (World Scienticfic, 1989).

[116] S. Narison, Nucl. Part. Phys. Proc. **324-329**, 94 (2023).

[117] S. Narison and E. de Rafael, Phys. Lett. B **103**, 57 (1981).

[118] S. Narison, Nucl. Part. Phys. Proc. **270-272**, 143 (2016).

[119] S. Narison, Int. J. Mod. Phys. A **30**, 1550116 (2015).

[120] A. A. Logunov, L. D. Soloviev, and A. N. Tavkhelidze, Phys. Lett. B **24**, 181 (1967).

[121] J. J. Sakurai, Phys. Lett. B **46**, 207 (1973).

[122] A. Bramon, E. Etim, and M. Greco, Phys. Lett. B **41**, 609 (1972).

[123] R. Shankar, Phys. Rev. D **15**, 755 (1977).

[124] E. G. Floratos, S. Narison, and E. de Rafael, Nucl. Phys. B **155**, 115 (1979).

[125] S. Narison and E. de Rafael, Nucl. Phys. B **169**, 253 (1980).

[126] R. A. Bertlmann, G. Launer, and E. de Rafael, Nucl. Phys. B **250**, 61 (1985).

[127] M. Suzuki, Phys. Rev. D **47**, 1043 (1993).

[128] E. Bagan, A. Bramon, and S. Narison, Phys. Lett. B **196**, 203 (1987).

[129] C. J. Morningstar and M. Peardon, Phys. Rev. D **60**, 034509 (1999).

[130] Y. Chen *et al.*, Phys. Rev. D **73**, 014516 (2006).

[131] S. Narison, Nucl. Phys. B 509 (1998) 312-356; Nucl. Phys. B, Proc. Suppl. 64 (1998) 210–219 .

[132] BESIII, M. Ablikim *et al.*, Phys. Rev. Lett. **132**, 181901 (2024), 2312.05324.

[133] V. Novikov, M. Shifman, A. Vainshtein, and V. Zakharov, Nucl. Phys. B **191**, 301 (1981).

[134] J. Govaerts, L. J. Reinders, P. Francken, X. Gonze, and J. Weyers, Nucl. Phys. B **284**, 674 (1987).

[135] R. Mertig, M. Bohm, and A. Denner, Comput. Phys. Commun. **64**, 345 (1991).

[136] V. Shtabovenko, R. Mertig, and F. Orellana, Comput. Phys. Commun. **207**, 432 (2016).

[137] V. Shtabovenko, R. Mertig, and F. Orellana, Comput. Phys. Commun. **256**, 107478 (2020).

[138] T. P. Cheng and L. F. Li, *Gauge theory of elementary particle physics* (Oxford University Press, Oxford, UK, 1984).

[139] R. D. Field, AIP Conf. Proc. **55**, 97 (1979).

[140] R. K. Ellis, Z. Kunszt, K. Melnikov, and G. Zanderighi, Phys. Rept. **518**, 141 (2012).

[141] L. Reinders, H. Rubinstein, and S. Yazaki, Phys. Rept. **127**, 1 (1985).

[142] M. Lavelle, *Non-Perturbative Propagators in QCD* (Springer US, Boston, MA, 1994), pp. 51–62.

[143] V. Elias, Can. J. Phys. **64**, 595 (1986).

[144] J. N. E. Ho, *QCD Correlation Functions of Heavy-light Hybrid Mesons ($J^P = 1^-$)*, Master's thesis, Saskatchewan U., 2015.

[145] D. Asner, R. Mann, J. Murison, and T. Steele, Phys. Lett. B **296**, 171 (1992).

[146] E. Bagan and T. Steele, Phys. Lett. B **234**, 135 (1990).

[147] S. Narison, Z. Phys. C **22**, 161 (1984).

[148] K. G. Chetyrkin, S. Narison, and V. I. Zakharov, Nucl. Phys. B **550**, 353 (1999).

[149] S. Narison, Nucl. Phys. A **1039**, 122744 (2023).

[150] S. Narison, N. Pak, and N. Paver, Phys. Lett. B **147**, 162 (1984).

[151] A. A. Pivovarov, Phys. At. Nucl. 63 (2000) 1646; Yad. Fiz. 63 (9) (2000) 1734 .

[152] V. Novikov, M. Shifman, A. Vainshtein, and V. Zakharov, Nucl. Phys. B **174**, 378 (1980).

[153] S. Narison and V. Zakharov, Phys. Lett. B **522**, 266 (2001).

[154] J. S. Bell and R. Bertlmann, Nucl. Phys. B **177**, 218 (1981).

[155] R. A. Bertlmann, Acta Phys. Austriaca **53**, 305 (1981).

[156] H.-X. Chen, W. Chen, and S.-L. Zhu, Nucl. Part. Phys. Proc. **318-323**, 122 (2022).

[157] J. Chen and J. Liu, Phys. Rev. D **95**, 014024 (2017).

[158] L. Zhang, C. Chen, Y. Chen, and M. Huang, Phys. Rev. D **105**, 026020 (2022).

[159] E. Gregory *et al.*, JHEP **10**, 170 (2012).

[160] A. Athenodorou and M. Teper, JHEP **11**, 172 (2020).

[161] E. Klempt, K. V. Nikonov, A. V. Sarantsev, and I. Denisenko, Phys. Lett. B **830**, 137171 (2022).

[162] W. Pauli, Z. Physik **43**, 601–623 (1927).

[163] W. Greiner, *Quantum mechanics: an introduction*, 4 ed. (Springer-Verlag, 1994), .

[164] G. Charpak *et al.*, *Results of the* $g-2$ *experiment* (World Scientific, 1994), p. 34.

[165] J. Bailey *et al.*, Nucl. Phys. B **150**, 1 (1979).

[166] Muon g-2 Collaboration, G. W. Bennett *et al.*, Phys. Rev. D **73**, 072003 (2006).

[167] X. Fan, T. G. Myers, B. A. D. Sukra, and G. Gabrielse, Phys. Rev. Lett. **130**, 071801 (2023).

[168] New (g-2), F. Gray, J. Phys. Conf. Ser. **312**, 102006 (2011).

[169] J. D. Jackson, *Classical Electrodynamics*, 3 ed. (Wiley, 1998).

[170] L. B. Okun, *Leptons and Quarks: Special Edition Commemorating the Discovery of the Higgs Boson* (North-Holland, Amsterdam, Netherlands, 1982).

[171] Muon g-2, K. S. Khaw *et al.*, Nucl. Instrum. Meth. A **945**, 162558 (2019).

[172] G. Degrassi and G. F. Giudice, Phys. Rev. D **58**, 053007 (1998).

[173] T. Ishikawa, N. Nakazawa, and Y. Yasui, Phys. Rev. D **99**, 073004 (2019).

[174] F. Jegerlehner, *The Anomalous Magnetic Moment of the Muon* Vol. 274 (Springer, Cham, 2017).

[175] B. E. Lautrup and E. de Rafael, Phys. Rev. **174**, 1835 (1968).

[176] W. Hubschmid and S. Mallik, Nucl. Phys. B **193**, 368 (1981).

[177] I. Caprini and C. Verzegnassi, Nuovo Cim. A **90**, 388 (1985).

[178] P. Gubler and D. Satow, Prog. Part. Nucl. Phys. **106**, 1 (2019).

[179] J. A. Casas, C. Lopez, and F. J. Yndurain, Phys. Rev. D **32**, 736 (1985).

[180] S. Narison, Nucl. Phys. A **1039**, 122744 (2023).

[181] J. Ho, R. Berg, W. Chen, D. Harnett, and T. G. Steele, Phys. Rev. D **98**, 096020 (2018).

[182] T. G. Steele, K. Kostuik, and J. Kwan, Phys. Lett. B **451**, 201 (1999).

[183] F. Shi *et al.*, Nucl. Phys. A **671**, 416 (2000).

[184] Q.-N. Wang, Z.-F. Zhang, T. G. Steele, H.-Y. Jin, and Z.-R. Huang, Chin. Phys. C **41**, 074107 (2017), 1612.00808.

[185] J.-M. Yuan, Z.-F. Zhang, T. G. Steele, H.-Y. Jin, and Z.-R. Huang, Phys. Rev. D **96**, 014034 (2017).

[186] E. F. Beckenbach and R. Bellman, *Inequalities* (Springer, Berlin, 1961).

[187] S. K. Berberian, *Measure and Integration* (MacMillan, New York, 1965).

[188] F. Dalfovo and S. Stringari, Phys. Rev. B **46**, 3991 (1992).

[189] L. J. Reinders and H. R. Rubinstein, Phys. Lett. B **145**, 108 (1984).

[190] L. R. Surguladze and F. V. Tkachov, Nucl. Phys. B **331**, 35 (1990).

[191] K. G. Chetyrkin, V. P. Spiridonov, and S. G. Gorishnii, Phys. Lett. B **160**, 149 (1985).

[192] P. A. Baikov, K. G. Chetyrkin, and J. H. Kühn, Phys. Rev. Lett. **101**, 012002 (2008).

[193] S. G. Gorishnii, A. L. Kataev, and S. A. Larin, Phys. Lett. B **259**, 144 (1991).

[194] L. R. Surguladze and M. A. Samuel, Phys. Rev. Lett. **66**, 560 (1991), [Erratum: Phys. Rev. Lett. **66**, 2416 (1991)].

[195] K. G. Chetyrkin, Phys. Lett. B **391**, 402 (1997).

[196] K. G. Chetyrkin, A. L. Kataev, and F. V. Tkachov, Phys. Lett. B **85**, 277 (1979).

[197] M. Dine and J. R. Sapirstein, Phys. Rev. Lett. **43**, 668 (1979).

[198] W. Celmaster and R. J. Gonsalves, Phys. Rev. Lett. **44**, 560 (1980).

[199] M. R. Ahmady *et al.*, Phys. Rev. D **67**, 034017 (2003).

[200] D. d'Enterria *et al.*, J. Phys. G **51**, 090501 (2024).

[201] T. van Ritbergen, J. A. M. Vermaseren, and S. A. Larin, Phys. Lett. B **400**, 379 (1997).

[202] D. Harnett, J. Ho, and T. G. Steele, Phys. Rev. D **103**, 114005 (2021).

[203] R. Albuquerque, S. Narison, and D. Rabetiarivony, Nucl. Phys. A **1039**, 122743 (2023).

[204] K. G. Chetyrkin, B. A. Kniehl, and M. Steinhauser, Nucl. Phys. B **510**, 61 (1998).

[205] T. G. Steele and V. Elias, Mod. Phys. Lett. A **13**, 3151 (1998).

[206] A. Keshavarzi, D. Nomura, and T. Teubner, Phys. Rev. D **101**, 014029 (2020).

[207] J. S. Bell and R. A. Bertlmann, Nucl. Phys. B **187**, 285 (1981).

[208] S. Li, *Numerical Methods for Finite Temperature Effects in Quantum Field Theory*, Master's thesis, University of Saskatchewan, 2021.

[209] S. Borowka *et al.*, Comput. Phys. Commun. **222**, 313 (2018).

[210] A. Ayala, C. A. Dominguez, and M. Loewe, Adv. High Energy Phys. **2017**, 9291623 (2017).

[211] A. Bochkarev and M. Shaposhnikov, Nucl. Phys. B **268**, 220 (1986).

[212] S. Esau and D. Harnett, Eur. Phys. J. A **55**, 31 (2019).

[213] K. Ray, D. Harnett, and T. G. Steele, Phys. Rev. D **108**, 034001 (2023).

[214] R. Hagedorn, Nuovo Cim. Suppl. **3**, 147 (1965).

[215] R. Hagedorn and J. Ranft, Nuovo Cim. Suppl. **6**, 169 (1968).

[216] M. Gaździcki and M. I. Gorenstein, *Hagedorn's Hadron Mass Spectrum and the Onset of Deconfinement* (Springer International Publishing, Cham, 2016), pp. 87–92.

[217] R. J. Fries, B. Müller, C. Nonaka, and S. A. Bass, Phys. Rev. C **68**, 044902 (2003).

[218] P. Foka and M. A. Janik, Rev. Phys. **1**, 154 (2016).

[219] LHCb, G. Graziani, J. Phys. Conf. Ser. **1271**, 012008 (2019).

[220] A. D. Sakharov, Pisma Zh. Eksp. Teor. Fiz. **5**, 32 (1967).

[221] M. Trodden, eConf **C040802**, L018 (2004).

[222] C. W. Misner, K. S. Thorne, and J. A. Wheeler, *Gravitation* (W. H. Freeman, San Francisco, 1973).

[223] J. Ellis, M. Lewicki, and J. M. No, JCAP **07**, 050 (2020).

[224] D. Croon, PoS **TASI2022**, 003 (2024).

[225] J. I. Kapusta and C. Gale, *Finite-temperature field theory: Principles and applications,* Cambridge Monographs on Mathematical Physics (Cambridge University Press, 2011).

[226] A. K. Das, *Finite Temperature Field Theory* (World Scientific, New York, 1997).

[227] T. Matsubara, Prog. Theor. Phys. **14**, 351 (1955).

[228] G. Aarts *et al.*, Prog. Part. Nucl. Phys. **133**, 104070 (2023).

[229] M. Quiros, Finite temperature field theory and phase transitions, in *ICTP Summer School in High-Energy Physics and Cosmology*, pp. 187–259, 1999.

[230] P. Athron, C. Balázs, A. Fowlie, L. Morris, and L. Wu, Prog. Part. Nucl. Phys. **135**, 104094 (2024).

[231] M. E. Carrington, Phys. Rev. D **45**, 2933 (1992).

[232] J. R. Espinosa, M. Quiros, and F. Zwirner, Phys. Lett. B **314**, 206 (1993).

[233] J. R. Espinosa, T. Konstandin, and F. Riva, Nucl. Phys. B **854**, 592 (2012).

[234] W.-C. Huang, F. Sannino, and Z.-W. Wang, Phys. Rev. D **102**, 095025 (2020).

[235] D. E. Morrissey and M. J. Ramsey-Musolf, New J. Phys. **14**, 125003 (2012).

[236] C. Caprini *et al.*, JCAP **03**, 024 (2020).

[237] G. Heinrich *et al.*, Comput. Phys. Commun. **295**, 108956 (2024), 2305.19768.

[238] G. Heinrich, Int. J. Mod. Phys. A **23**, 1457 (2008).

[239] J. A. M. Vermaseren, (2000), [arXiv:math-ph/0010025].

[240] J. Kuipers, T. Ueda, and J. A. M. Vermaseren, Comput. Phys. Commun. **189**, 1 (2015).

[241] B. Ruijl, T. Ueda, and J. Vermaseren, (2017), [arXiv:1707.06453 [hep-ph]].

[242] M. C. Galassi *et al.*, *GNU Scientific Library Reference Manual*, 3 ed. (Network Theory, Ltd., 2009).

[243] T. Hahn, Comput. Phys. Commun. **168**, 78 (2005).

[244] T. Hahn, J. Phys. Conf. Ser. **608**, 012066 (2015).

[245] A. Seiden, *Particle physics: A comprehensive introduction* (Pearson, 2004).

# Appendix A

# Conventions

This Appendix includes the basic algebra and convention choices (*e.g.,* for units). Reviews can be found in Refs. [6, 31].

- We are using the natural unit of $c = \hbar = 1$ to simplify the expressions. As a result, the mass and momentum are in the same dimension of energy, typically in the unit of electronvolt (eV). The distance and time have inverse energy unit ($\text{eV}^{-1}$).

- The Lorentz four vector, *e.g.,* position-time $x^\mu\,(\mu = 0, 1, 2, 3)$, in Minkowski space is defined as:

$$x^\mu = (x^0, x^1, x^2, x^3) = (ct, x^1, x^2, x^3) = (ct, \vec{x}). \tag{A.1}$$

  Similar definition also applies to other four vectors including momentum-time $p^\mu$. The derivative operator is defined as:

$$\partial_\mu = \frac{\partial}{\partial x^\mu} = \left(\frac{\partial}{\partial x^0}, \nabla\right). \tag{A.2}$$

- The Dirac metrics in $d = 4$ dimensional Minkowski space are defined as:

$$\gamma^0 = \begin{pmatrix} 0 & \mathbf{1} \\ \mathbf{1} & 0 \end{pmatrix}, \quad \gamma^i = \begin{pmatrix} 0 & \sigma^i \\ -\sigma^i & 0 \end{pmatrix}, \quad \gamma^5 = i\gamma_0\gamma_1\gamma_2\gamma_3 = \begin{pmatrix} 0 & \mathbf{1} \\ \mathbf{1} & 0 \end{pmatrix}, \tag{A.3}$$

  where $\mathbf{1}$ is $2 \times 2$ identity matrix, $\sigma^i\,(i = 1, 2, 3)$ are Pauli matrices:

$$\sigma^1 = \begin{pmatrix} 0 & 1 \\ 1 & 0 \end{pmatrix}, \quad \sigma^2 = \begin{pmatrix} 0 & -i \\ i & 0 \end{pmatrix}, \quad \sigma^3 = \begin{pmatrix} 1 & 0 \\ 0 & -1 \end{pmatrix}. \tag{A.4}$$

  The Minkowski space matrix tensor used is:

$$g_{\mu\nu} = \begin{pmatrix} 1 & 0 & 0 & 0 \\ 0 & -1 & 0 & 0 \\ 0 & 0 & -1 & 0 \\ 0 & 0 & 0 & -1 \end{pmatrix}. \tag{A.5}$$

  Hence satisfies $g_{\mu\nu}g^{\mu\nu} = D$ at $D$ spacetime dimension. $\gamma^\mu$ satisfies Dirac algebra:

$$\gamma^\mu\gamma_\mu = D\,\mathbf{1}_4, \quad \{\gamma^\mu, \gamma^\nu\} \equiv \gamma^\mu\gamma^\nu + \gamma^\nu\gamma^\mu = 2g^{\mu\nu}\mathbf{1}_4, \tag{A.6}$$

  with $\mathbf{I_4}$ being $4 \times 4$ identity matrix.

- The Einstein summation is implied throughout this thesis over repeated flavour, colour and metric indices. As in,

$$a^\mu = \sum_\nu \Lambda^\mu_\nu b^\nu \xrightarrow{\text{Einstein notation}} \Lambda^\mu_\nu b^\nu \tag{A.7}$$

For example,

$$p \cdot x = g_{\mu\nu} p^\mu x^\nu = p^0 x^0 - \vec{p} \cdot \vec{x}. \tag{A.8}$$

- The relationship between covariant four-vector $x_\mu$ and contravariant four-vector $x^\mu$ is:

  $$x_\mu \equiv g_{\mu\nu} x^\nu = (x^0, -\vec{x}), . \tag{A.9}$$

  However, `MATHEMATICA` package FeynCalc presumes its user can properly interpret the Lorentz indices appearing in Feynman integrals, it does not distinguish covariant and contravariant labels for Lorentz indices. Analogously in this thesis, the proper arrangement of indices is occasionally assumed to be implicit to provide the best visual formatting (*e.g.,* tensor $g^\mu_\nu = g_{\mu\nu}$ in this work).

- The "slashed" notation for operators and momenta are defined as:

  $$\not{D} = D_\mu \gamma^\mu, \quad \not{\partial} = \partial_\mu \gamma^\mu, \quad \not{p} = p_\mu \gamma^\mu. \tag{A.10}$$

# Appendix B

# SU(3) Colour Charge

This appendix includes the relevant properties of SU(3) colour charge of QCD that is introduced in Chapter 2 and is used throughout this thesis. The materials of this appendix refer to Refs. [6, 31, 44, 48, 245].

## B.1 SU(3) Colour Symmetry Group

QCD is a non-abelian gauge theory with special unitary group of degree $N = 3$ symmetry, denoted SU(3) symmetry given from the three degrees of freedom from the three colour charges. One can consider the three coloured quark states as:

$$|q_1\rangle = \begin{pmatrix}1\\0\\0\end{pmatrix}, \qquad |q_2\rangle = \begin{pmatrix}0\\1\\0\end{pmatrix}, \qquad |q_3\rangle = \begin{pmatrix}0\\0\\1\end{pmatrix} \tag{B.1}$$

There are $N^2 - 1 = 8$ Gell-Mann matrices $\lambda_a\,(a = 1, 2, \cdots, 8)$ for SU(3):

$$\begin{aligned}
&\lambda_1 = \begin{pmatrix}0&1&0\\1&0&0\\0&0&0\end{pmatrix}, \qquad \lambda_2 = \begin{pmatrix}0&-i&0\\i&0&0\\0&0&0\end{pmatrix}, \qquad \lambda_3 = \begin{pmatrix}1&0&0\\0&-1&0\\0&0&0\end{pmatrix},\\
&\lambda_4 = \begin{pmatrix}0&0&1\\0&0&0\\1&0&0\end{pmatrix}, \qquad \lambda_5 = \begin{pmatrix}0&0&-i\\0&0&0\\i&0&0\end{pmatrix}, \qquad \lambda_6 = \begin{pmatrix}0&0&0\\0&0&1\\0&1&0\end{pmatrix},\\
&\lambda_7 = \begin{pmatrix}0&0&0\\0&0&-i\\0&i&0\end{pmatrix}, \qquad \lambda_8 = \frac{1}{\sqrt{3}}\begin{pmatrix}1&0&0\\0&1&0\\0&0&-2\end{pmatrix}.
\end{aligned} \tag{B.2}$$

The Gall-Mann matrices are generalized Pauli matrices from SU(2) to SU(3). The shifts between the three coloured states, beyond the SU(2) subgroups of SU(3), can be created using linear combinations of the non-diagonal Gell-Mann matrices:

$$\begin{aligned}
&|q_1\rangle \rightleftarrows |q_2\rangle : \; I_{\mp} = \frac{1}{2}(\lambda_1 \mp i\lambda_2),\\
&|q_1\rangle \rightleftarrows |q_3\rangle : \; V_{\mp} = \frac{1}{2}(\lambda_4 \mp i\lambda_5),\\
&|q_2\rangle \rightleftarrows |q_3\rangle : \; U_{\mp} = \frac{1}{2}(\lambda_6 \mp i\lambda_7).
\end{aligned} \tag{B.3}$$

The $\lambda_a$ are hermitian and traceless, leading to the Lie group algebra

$$[\lambda_a, \lambda_b] = i\,2\,f_{abc}\lambda_c, \tag{B.4}$$

$$\mathrm{Tr}\,[\lambda_a\lambda_b] = 2\,\delta_{ab}, \tag{B.5}$$

where $f_{abc}$ is the totally antisymmetric structure constant with identity:

$$f_{abc}f_{dbc} = 3\,\delta_{ad}. \tag{B.6}$$

We let the generators $T_a$ for the quark states to be defined as $T_a = \lambda_a/2$, meaning they also obey

$$[T_a, T_b] = i f_{abc} T_c, \tag{B.7}$$

$$\mathrm{Tr}\ [T_a] = 0. \tag{B.8}$$

One can see that there are two diagonal generators $T_3$ and $T_8$. The non-diagonal operators in Eq. (B.3) does not generate a completely new state rather a linear combination of multiplet states. $T_3$ and $T_8$, on the other hand, will provide eigenvalues when apply to their eigenstates (instead of giving other eigenstates). One can visualize the multiplet's eigenvalues by those two diagonal operators, as shown in Fig. B.1 below.

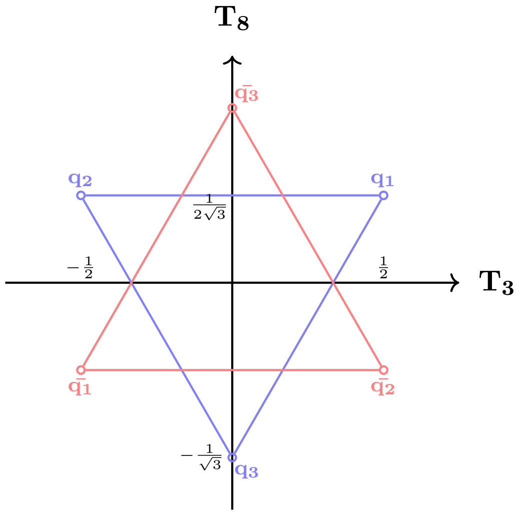

**Figure B.1:** Multiplets of quark ($q$) in red and antiquark ($\bar{q}$) in blue, are denoted as **3** and **3**$^*$ respectively.

In Fig. B.1, the fundamental representation of quarks is **3** and antiquarks **3**$^*$, with the gluons in the adjoint representation **8**. Using the representation theory of groups, we can find the irreducible representations for mesons:

$$\bar{q}q : \mathbf{3}^* \otimes \mathbf{3} = \mathbf{1} \oplus \mathbf{8}. \tag{B.9}$$

This leads to a different perspective of the example eightfold way in Fig. 2.2 for hadrons are viewed as colour singlets represented by **1**. And similarly, one can find the product representations for baryons:

$$qqq : \mathbf{3} \otimes \mathbf{3} \otimes \mathbf{3} = \mathbf{1} \oplus \mathbf{8} \oplus \mathbf{8} \oplus \mathbf{10}, \tag{B.10}$$

which also ensures hadrons being colour singlets to satisfy the colour confinement requirement for hadrons to be observed experimentally.

## B.2 Gluon Octet

In terms of SU(3) symmetry, the effective colour states — $r\bar{r}, r\bar{b}, r\bar{g}, b\bar{r}, b\bar{b}, b\bar{g}, g\bar{r}, g\bar{b}, g\bar{g}$ — exist only in principle. Instead, there are nine possible colour states of gluon, who are linearly independent, forming a “colour octet” equivalent to the Gell-Mann matrices [6]:

$$\begin{aligned}
|1\rangle &= \frac{1}{\sqrt{2}}(r\bar{b} + b\bar{r}) & |2\rangle &= -\frac{i}{\sqrt{2}}(r\bar{b} - b\bar{r}) \\
|3\rangle &= \frac{1}{\sqrt{2}}(r\bar{r} - b\bar{b}) & |4\rangle &= \frac{1}{\sqrt{2}}(r\bar{g} + g\bar{r}) \\
|5\rangle &= -\frac{i}{\sqrt{2}}(r\bar{g} - g\bar{r}) & |5\rangle &= \frac{1}{\sqrt{2}}(b\bar{g} + g\bar{b}) \\
|7\rangle &= -\frac{i}{\sqrt{2}}(b\bar{g} - g\bar{b}) & |8\rangle &= \frac{1}{\sqrt{6}}(r\bar{r} + b\bar{b} - g\bar{g})
\end{aligned} \tag{B.11}$$

and a “colour singlet”:

$$|9\rangle = \frac{1}{\sqrt{3}}(r\bar{r} + b\bar{b} + g\bar{g}), \tag{B.12}$$

among which $|3\rangle$ and $|9\rangle$ are colourless. However, the colour singlet $|9\rangle$ would suggest the existence of gluon as a free particle and it would allow long-range strong interaction which does not exist. Therefore, there are only eight colour states for gluons which are listed in Eq. (B.11).

# Appendix C

# Quantum Numbers

The frequently used quantum number combination of $J^{PC}$ reflects important properties and suggests possible parton constituents of a composite particle. One can find the basic definitions of orbital/spin/total angular momentum in Refs. [28, 31].

- $\vec{L}$: orbital angular momentum with magnitude $L$ where $L^2 = l(l+1)$. Here quantum number $l = 0, 1, 2, 3, \cdots$. The projection along $z$-axis is

  $$m_l = \underbrace{-l, -(l-1), \cdots, l-1, l}_{2l+1 \text{ terms}}. \tag{C.1}$$

- $\vec{S}$: spin angular momentum with magnitude $S$ where $S^2 = s(s+1)$. The quantum number of $s$ depends on the intrinsic form of the particle, *e.g.,* $s = 1/2$ for $e^-, n, p$ and $s = 1$ for gluon. The projection along $z$-axis is

  $$m_s = \underbrace{-s, -(s-1), \cdots, l-1, s}_{2s+1 \text{ terms}}. \tag{C.2}$$

  That means for spin-1/2 particles, $m_s = \pm 1/2$ (spin up or down).

- $\vec{J} = \vec{L} + \vec{S}$: total angular momentum with magnitude $J$ where $J^2 = j(j+1)$. The quantum number is

  $$j = |l-s|, |l-s|+1, \cdots, l+s \tag{C.3}$$

  with projection along $z$-axis $m_j = -j, -(j-1), \cdots, +j$.

- $P = (-1)^l$: parity, which reflects the symmetry under spatial inversion. For even (odd) $l$, one has even (odd) parity which is written as $+(-)$. Note for meson $q\bar{q}$ states, one need to account for the opposite intrinsic parities from $q$ and $\bar{q}$ resulting $P = (-1)^{l+1}$.

- $C = (-1)^{l+s}$: charge conjugation reflects the symmetry under particle to antiparticle changes. Similar to parity, the notation for $C = \pm 1$ is also $\pm$.

Quantum numbers $l$, $s$ and $j$ in this appendix are denoted as $L$, $S$ and $J$ in this thesis (following the Particle Data Group convention [7]) as there won't be confusion with the angular momentum magnitudes in the text. In Chapter 3, the target tensor digluonium has the quantum number of $J^{PC} = 2^{++}$ corresponds to the ground state of a system consist of two spin-1 gluons: $J = 2, L = 0, S = 2$.

## C.1 Gluonia Naming Scheme

Below we show the name conventions for gluonia that are relevant to this thesis by the Particle Data Group in Ref. [7]. Using an example,

$$f_2(2010)$$

- The first letter indicate the particle's Isospin $I$ and charge symmetry. Since gluonia are bosonic particles that have even total angular momentum ($J = 0, 2, 4, \cdots$), it is a more common fit for the $f$-states ($I = 0$ isoscalar with even $J$) than the others due to the gluonic composition. This naming scheme is borrowed from the naive quark model of light-flavoured mesons which also has $I = 0$ cases. Although in the case of triple-gluon glueballs can have $J = 1$ for vector boson or $J = 3$ for third-order tensor boson, we will not dig too deep in this work.
- The subscript number represents the total angular momentum $J$ of the mesons.
- The approximate mass of the particle is indicated in the parentheses in $\mathrm{MeV}/c^2$

$f_2(2010)$ represents a composite particle with quantum number: $I = 0$, $J^{PC} = 2^{++}$, and mass around 2010 MeV ($2011^{+62}_{-76}$ MeV to be precise [7]).

# Appendix D

# Sample Code for Usage of FeynCalc and TARCER

For reference, a sample calculation code for an NLO tensor di-gluonium bare diagram — specifically, diagram (e), which involves the gluon self-energy with a quark loop — is provided in the following pages. The primary software used for this thesis is `MATHEMATICA`, and the example calculation is implemented within this framework. Additionally, the example demonstrates the applications of two essential packages for this thesis: FeynCalc [135–137] and TARCER [58].

```
In[]:= Clear["Global`*"]
```

```
In[]:= $LoadTARCER = True;
```

```
In[]:= << FeynCalc`
```

**FeynCalc** 9.3.1 (stable version). For help, use the documentation center, check out the wiki or visit the forum.

To save your and our time, please check our FAQ for answers to some common FeynCalc questions.

See also the supplied examples. If you use FeynCalc in your research, please cite

- V. Shtabovenko, R. Mertig and F. Orellana, Comput.Phys.Commun. 256 (2020) 107478, arXiv:2001.04407.
- V. Shtabovenko, R. Mertig and F. Orellana, Comput.Phys.Commun. 207 (2016) 432–444, arXiv:1601.01167.
- R. Mertig, M. Böhm, and A. Denner, Comput. Phys. Commun. 64 (1991) 345–359.

**TARCER** 2.0, for more information see the accompanying publication. If you use TARCER in your research, please cite

- R. Mertig and R. Scharf, Comput. Phys. Commun., 111, 265–273, 1998, arXiv:hep–ph/9801383

# Calculation of 2- loop (NLO) tensor di-gluonium $2^{++}$current

# Diagram (e) Self Energy-fermion

## Feynman rules

gluonic-current-to-2-gluons

```
FD[i_, j_, μ_, ν_, ρ_, σ_, p_, q_] := -SUNDelta[i, j]
  ((-MTD[μ, σ] * MTD[ν, ρ] - MTD[μ, ρ] * MTD[ν, σ] + MTD[μ, ν] * MTD[σ, ρ]) * SPD[p, q] +
    MTD[μ, σ] * FVD[q, ρ] * FVD[p, ν] +
    MTD[μ, ρ] * FVD[p, σ] * FVD[q, ν] + MTD[ν, ρ] * FVD[q, μ] * FVD[p, σ] +
    MTD[ν, σ] * FVD[p, μ] * FVD[q, ρ] - MTD[σ, ρ] * FVD[q, μ] * FVD[p, ν] -
    MTD[ρ, σ] * FVD[p, μ] * FVD[q, ν] - MTD[μ, ν] * FVD[p, σ] * FVD[q, ρ] )
```

gluon propagator with arbitrary gauge, Pascaul & Tarrach, P35

```
Dg[i_, j_, μ_, ν_, a_, k_] :=
 -I * SUNDelta[i, j] * (MTD[μ, ν] * SPD[k] - (1 - a) * FVD[k, μ] * FVD[k, ν]) * FAD[{k, 0}, {k, 0}]
```

fermion propagator, Field convention

```
Df[i_, j_, k_] := I * SUNDelta[i, j].GSD[k] / SPD[k]
Dfnumeratornocolour[k_] := I.GSD[k]
Dfdenominator[k_] := FAD[{k, 0}]
```

Fermionic vertex $-ig\gamma^{\mu} T_{ij}{}^{a}$, where $T_a = \lambda_a / 2$,
$T_a$ will be included later with the colour factor
from fermion propagtor $\delta_{ij}$ together, as $\mathrm{Tr}[T_a\, T_b] = \frac{1}{2}\delta_{ab}$.

(*Field convention*)

```
FVnocolor[μ_] := -I * g.GAD[μ]
```

projection operator for $2{+}{+}$ term of the $2-$point function with the operators $J_1$ and $J_2$

$$\eta D[\mu\_,\nu\_,q\_] := \frac{FVD[q,\mu] * FVD[q,\nu]}{SPD[q]} - MTD[\mu,\nu]$$

```
P8D[μ_, ν_, ρ_, σ_, q_] :=
```

$$\eta D[\mu,\rho,q] * \eta D[\nu,\sigma,q] + \eta D[\mu,\sigma,q] * \eta D[\nu,\rho,q] - \frac{2}{D-1} * \eta D[\mu,\nu,q] * \eta D[\rho,\sigma,q]$$

from projection operator check (separate notebook) $R8 = \frac{2}{D-1}$

Include projection operator normalization factor

```
P8Dnorm = Contract[P8D[μ, ν, ρ, σ, p] * P8D[μ, ν, ρ, σ, p]];
```

---

# Diagram e : Quark /Fermion Self-Energy

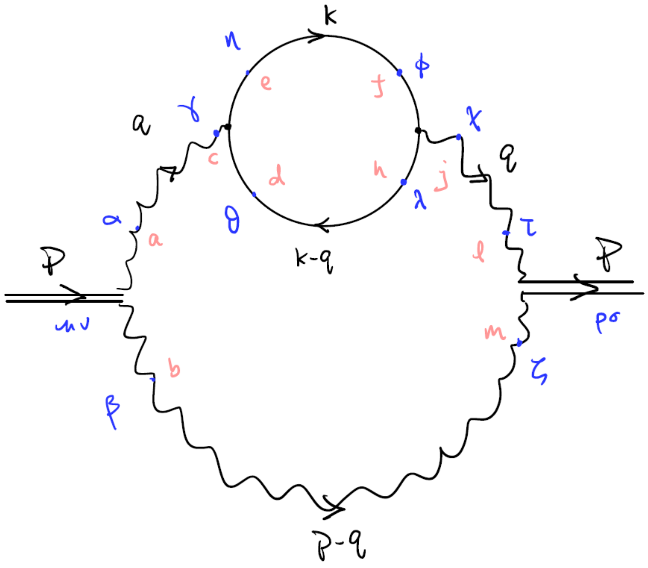

## Calculate amplitude (Arbitrary gauge: a=1 Feynman gauge; a=0 Landau gauge)

```
In[∘]:= fnumerator = (-1) *
    Contract[Tr[I * P8D[μ, ν, ρ, σ, p] * FD[a, b, μ, ν, α, β, q, p - q] * Dg[a, c, α, γ, a, q].
        FVnocolor[γ].Dfnumeratornocolour[k - q].FVnocolor[χ].Dfnumeratornocolour[k] *
       Dg[j, l, χ, τ, a, q] * Dg[b, m, β, ξ, a, p - q] * FD[l, m, ρ, σ, τ, ξ, -q, -p + q]]];
```

minus sign added for fermion field as it obeys fermionic statistics (-1 for every fermion loop), so it would disagree with P+T.

include denominators of the fermion propagator to find the amplitude

```
famp = fnumerator * Dfdenominator[k] * Dfdenominator[k - q];
```

TARCER principle function which reduces expressions to a set of basic integrals. In this case, $J^{(D)}$.

```
ansf1 = TarcerRecurse[ToTFI[famp, q, k, p]]
```

Out[∘]=

$$\frac{8\,(D-2)^2\,(D+1)\left(9\,D^3-40\,D^2+44\,D-16\right)g^2\,p^2\,\delta^{c\,j}\,\mathbf{J}^{(D)}_{\{1,0\}\,\{1,0\}\,\{1,0\}}}{3\,(D-4)\,(D-1)\,(3\,D-4)\,(3\,D-2)}$$

expansion with given rule of D → 4+2$\epsilon$ for $\epsilon$ around 0

```
ansf2 = TarcerExpand[ansf1 / P8Dnorm, D → 4 + 2 * ϵ];
```

expression simplification

```
ansf3 = ansf2 /. FCI[SEpsilon[4 + 2 * ϵ]] → 1;
ansf4 = ansf3 // DotSimplify;
```

substitutions for $P4 \equiv \left(-P^2\right)^2$, $L \equiv \mathrm{Log}\left[P^2\right]$

```
ansf5 = ansf4 /. (-Pair[Momentum[p, D], Momentum[p, D]]) ^ (2 * ϵ) *
      Pair[Momentum[p, D], Momentum[p, D]] ^2 → P4 * Exp[(2 ϵ) * L];
```

expand in series of $\epsilon$, and extract physical terms $L \equiv \mathrm{Log}\left[P^2\right]$

```
ansf6 = Series[ansf5, {ϵ, 0, 0}];
ansf7 = (L * Coefficient[ansf6, L, 1] + L^2 * Coefficient[ansf6, L, 2]);
```

## Colour factor for fermion propagator and vertex

denoting SU (3)

```
SUNN = 3;
ansf8 = SUNDeltaContract[SUNTrace[SUNT[c, j]] * ansf7];
```

## 2 - loop conversion factor between our loop convention and TFI definition

```
In[∘]:= conv = (4 * Pi) ^4;
```

## Diagrammatic symmetry factor

Refering to the formula presented in Cheng - Li p503

```
diagramsym = 1;
ansf9 = ansf8 / conv / diagramsym /. g → Sqrt[4 * Pi * αs] // Simplify;
ansf10 = (Coefficient[ansf9, L, 0] +
     L * Coefficient[ansf9, L, 1] + L^2 * Coefficient[ansf9, L, 2]) // Expand;
```

```
In[•]:= SEfermionresult = ansf10
```

Out[•]=

$$-\frac{L^2\,\mathrm{P4}\,\alpha_s}{60\,\pi^3}-\frac{L\,\mathrm{P4}\,\alpha_s}{60\,\pi^3\,\epsilon}+\frac{16\,L\,\mathrm{P4}\,\alpha_s}{225\,\pi^3}$$

The **P4** represents the external momentum to the power of 4, equivalent to the **(-$Q^4$)** in the thesis. The result is shown in Eq. (3.35).

# Appendix E

# Feynman Rules for QCD (non-abelian gauge theory)

To calculate the Feynman integrals of the Feynman diagrams corresponding to each NLO topology discussed in this document, one will need Feynman rules for each component involved in all Feynman diagrams (diagram a-h). Below are the QCD propagators and vertices needed for the tensor gluonium $2^{++}$ next-to-leading order Feynman diagrams.

Feynman rules for current-to-2-gluon (Eq. (3.14)) and current-to-3-gluon (Eq. (3.19)) are evaluated and found in this research, specifically in Sec. 3.2.1. The rest of the included Feynman rules (Eq. (E.3)-(E.9)) are referred and in agreement with literature [44, 138].

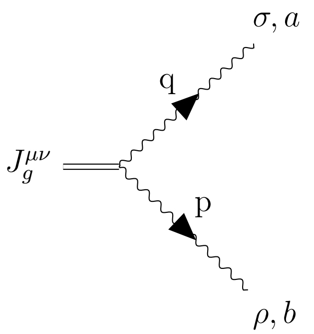

Current-to-2-gluon:

$$\begin{aligned} Z_{ab}^{\mu\nu\sigma\rho}(p,q) = \\ & -\delta_{ab}\left[\,(-g^{\mu\sigma}g^{\nu\rho} - g^{\mu\rho}g^{\nu\sigma} + g^{\mu\nu}g^{\sigma\rho})\;p\cdot q \right. \\ & + g^{\mu\sigma}\,q^{\rho}\,p^{\nu} + g^{\mu\rho}\,p^{\sigma}\,q^{\nu} + g^{\nu\rho}\,q^{\mu}\,p^{\sigma} \\ & \left. + g^{\nu\sigma}\,p^{\mu}\,q^{\rho} - g^{\sigma\rho}\,q^{\mu}\,p^{\nu} - g^{\rho\sigma}\,p^{\mu}\,q^{\nu} - g^{\mu\nu}\,p^{\sigma}\,q^{\rho}\,\right] \end{aligned} \tag{E.1}$$

Current-to-3-gluon:

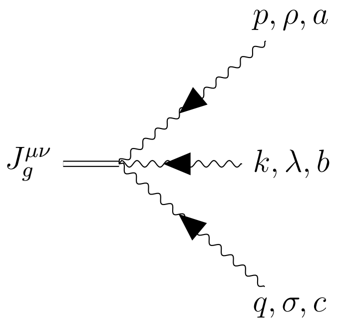

$$\begin{aligned} E_{abc}^{\mu\nu\rho\lambda\sigma}(p,q,k) = \\ & -igf_{abc}\Big[(p-q)^{\lambda}\left(g^{\mu\nu}g^{\rho\sigma} - g^{\rho\mu}g^{\sigma\nu} - g^{\sigma\mu}g^{\rho\nu}\right) \\ & + (k-p)^{\sigma}\left(g^{\mu\nu}g^{\lambda\rho} - g^{\rho\mu}g^{\lambda\nu} - g^{\lambda\mu}g^{\rho\nu}\right) \\ & + (q-k)^{\rho}\left(g^{\mu\nu}g^{\sigma\lambda} - g^{\lambda\mu}g^{\sigma\nu} - g^{\sigma\mu}g^{\lambda\nu}\right) \\ & + g^{\rho\lambda}\left(g^{\sigma\nu}\,(p-k)^{\mu} + g^{\sigma\mu}\,(p-k)^{\nu}\right) \\ & + g^{\rho\sigma}\left(g^{\lambda\nu}\,(q-p)^{\mu} + g^{\lambda\mu}\,(q-p)^{\nu}\right) \\ & + g^{\sigma\lambda}\left(g^{\rho\nu}\,(k-q)^{\mu} + g^{\rho\mu}\,(k-q)^{\nu}\right)\Big] \end{aligned} \tag{E.2}$$

Gluon propagator:

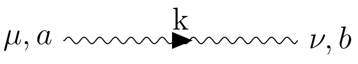

$$\begin{aligned} D_{ab}^{\mu\nu}(k) = -\frac{i\delta^{ab}}{k^2 + i\eta}\left(g^{\mu\nu} - (1-\xi)\frac{k^{\mu}k^{\nu}}{k^2 + i\eta}\right) \\ \xi = 1 \;\; \text{Feynman gauge} \\ \xi = 0 \;\; \text{Landau gauge} \end{aligned} \tag{E.3}$$

Fermion propagator:

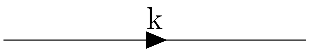

$$S(k) = \frac{i(\not{k} + m\mathbb{1})}{k^2 - m^2 + i\eta} \tag{E.4}$$

Ghost propagator:

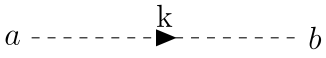

$$\Delta^{ab}(k) = \frac{-i\delta^{ab}}{k^2 + i\eta} \tag{E.5}$$

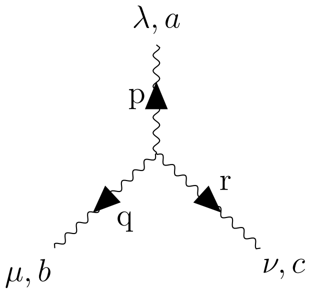

Triple-gluon vertex:

$$\begin{aligned} V^{\mu\nu\lambda}_{abc}(p,q,r) = -g f_{abc}\,[\,&(p-q)^\nu g^{\lambda\mu} \\ &+ (q-r)^\lambda g^{\mu\nu} + (r-p)^\mu g^{\nu\lambda}\,] \end{aligned} \tag{E.6}$$

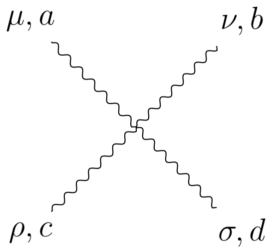

4-gluon vertex:

$$\begin{aligned} H^{\mu\nu\rho\sigma}_{abcd} = -\,ig^2\,\Big[&f^{abe}f^{cde}\,(g^{\mu\rho}g^{\nu\sigma} - g^{\mu\sigma}g^{\nu\rho}) \\ &+ f^{ace}f^{bde}\,(g^{\mu\nu}g^{\rho\sigma} - g^{\mu\sigma}g^{\nu\rho}) \\ &+ f^{ade}f^{bce}\,(g^{\mu\nu}g^{\rho\sigma} - g^{\mu\rho}g^{\nu\sigma})\Big] \end{aligned} \tag{E.7}$$

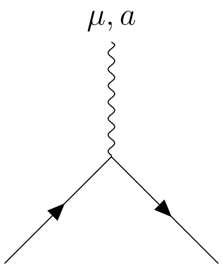

Gluon-fermion Vertex:

$$\Gamma^\mu_a = -ig\,\gamma^\mu\,\left(\frac{\lambda_a}{2}\right) \tag{E.8}$$

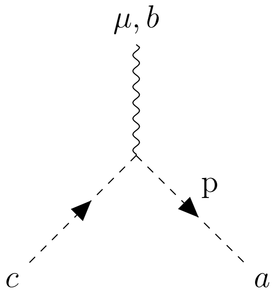

Gluon-ghost Vertex:

$$Y^\mu_{abc}(p) = g\,f_{abc}\,p^\mu \tag{E.9}$$